January 2015

Triplet Excitons in Natural Photosynthetic and Artificial Light Harvesting Systems: Measurement and Modeling.

Daniel Allen Hartzler
Purdue University

Graduate School Form 30
Updated 1/15/2015

PURDUE UNIVERSITY
GRADUATE SCHOOL
Thesis/Dissertation Acceptance

This is to certify that the thesis/dissertation prepared

By Daniel Allen Hartzler

Entitled

TRIPLET EXCITONS IN NATURAL PHOTOSYNTHETIC AND ARTIFICIAL LIGHT HARVESTING SYSTEMS: MEASUREMENT AND MODELING

For the degree of Doctor of Philosophy

Is approved by the final examining committee:

Sergei Savikhin
Chair

Yulia Pushkar

Ken P. Ritchie

Paul F. Muzikar

To the best of my knowledge and as understood by the student in the Thesis/Dissertation Agreement, Publication Delay, and Certification Disclaimer (Graduate School Form 32), this thesis/dissertation adheres to the provisions of Purdue University's "Policy of Integrity in Research" and the use of copyright material.

Approved by Major Professor(s): Sergei Savikhin

Approved by: John P. Finley 9/24/2015

Head of the Departmental Graduate Program Date

TRIPLET EXCITONS IN NATURAL PHOTOSYNTHETIC AND ARTIFICIAL LIGHT HARVESTING SYSTEMS: MEASUREMENT AND MODELING

A Dissertation

Submitted to the Faculty

of

Purdue University

Department of Physics and Astronomy

by

Daniel Allen Hartzler

In Partial Fulfillment of the

Requirements for the Degree

of

Doctor of Philosophy

December 2015

Purdue University

West Lafayette, Indiana

To my Mother who taught me kindness and compassion.

ACKNOWLEDGEMENTS

I would like to thank my family, Mom, Dad, Steve (Trudy, Coby, and Carson), and Sherry (Mike and Audrey) for their care, support, and strength in difficult times. To my wife Mona, thank you for your loving support, dedication, and encouragement. Without you I could not have seen this project through. I would also like to specifically thank my father for consultation on numerous electronic and electrical projects over the years and for teaching me which end of a screwdriver to hold. Your years of engineering experience and practical mechanical knowledge have been invaluable.

I would like to thank my advisor, Dr. Sergei Savikhin, for giving me this opportunity. I thank you for your patience and guidance over the course of my time in your laboratory. Your enthusiasm has always been a source of inspiration and your expertise and openness to discussion vital to my growth as a researcher.

I would also like to thank lab members Dr. Shige Kihara, for his help in sample preparation and measurement of the spectra of Chl *a* and BChl *a* dimers and aggregates (Figure 5.3 and Figure 5.10A and B), and Valentyn Stadnytskyi, for his help in sample preparation and measurement of the (microsecond) dynamics of BChl *c* artificial aggregates (Figure 7.4). Thanks to Professor Robert Blankenship and Dr. Dariusz Niedzwiedzki of the Photosynthetic Antenna Research Center (PARC) at Washington University, St. Louis MO and Professor Donald Bryant of the Pennsylvania State

University Department of Biochemistry & Molecular Biology for providing numerous samples of (Bacterio)Chlorophyll molecules and Dr. Gregory Orf also of PARC for providing samples of the Fenna-Matthews-Olson complex (Section 6.1). Thanks to Dr. Oleg Poluektov and Dr. Jens Niklas of Argonne National Laboratory for their help in measuring light induced changes in the EPR spectrum of *Chlorobaculum tepidum* chlorosomes (Figure 7.8 and Figure 7.9) and Dr. Yulia Pushkar of the Purdue Deparment of Physics and Astronomy for her help in a similar experiment with BChl *e* and BChl *f* artificial aggregates (Section 7.3). Finally I would like to thank Professor Lyudmila Slipchenko of the Purdue University Department of Chemistry for calculation of the triplet-triplet couplings of multiple dimeric porphyrin and chlorin systems (Figure 5.31, Figure 5.32, and Figure 5.36).

TABLE OF CONTENTS

Page

Page

Page

Page

Page

LIST OF FIGURES

Figure Page

Figure Page

Figure Page

Figure Page

Figure Page

Figure Page

Figure Page

Figure Page

Figure Page

Figure Page

Figure Page

Figure Page

Figure Page

Figure Page

Figure Page

Figure Page

Figure Page

Figure Page

Figure Page

Figure Page

LIST OF TABLES

Table Page

LIST OF ABBREVIATIONS

2-MeTHF	2-Methyl tetrahydrofuran
A	Ground state acceptor molecule / Absorbance
ADP	Adenosine diphosphate
ATP	Adenosine triphosphate
(B)Chl	(Bacterio)Chlorophyll
(B)Pheo	(Bacterio)Pheophytin
CI	Configuration interaction
CIS	CI theory for single excitations
Cr	Chromium
CT	Charge transfer
Cyt b_6f	Cytochrome b_6f
D	Excited state donor molecule
DC	Direct coupling
DFT	Density functional theory

EET	Excitation/Electronic Energy Transfer
EPR	Electron Paramagnetic Resonance
ESA	Excited State Absorption
eV	Electron volt
FC	Franck-Condon factor
FCWD	Franck-Condon Weighted Density
FD	Ferredoxin
FMO	Fenna-Matthews-Olson
FNR	ferredoxin-NADP+ reductase
FRET	Foerster Resonant Energy Transfer
FSD	Fragment spin difference
FWHM	Full width at half maximum
G3P	Glyceraldehyde-3-phosphate
Ga	Billion years before present
HOMO	Highest Occupied Molecular Orbital
IC	Internal conversion
ISC	Intersystem crossing

LN2	Liquid nitrogen
LUMO	Lowest Unoccupied Molecular Orbital
LWP	Long wave pass
M	Molar
meV	Milli-electron volt
mM, μM	Millimolar, micromolar
MeOH	Methanol
Mg	Magnesium
MO	Molecular orbital
NADPH	Nicotinamide adenine dinucleotide phosphate
Nd	Neodymium
NIR	Near infrared
NMR	Nuclear Magnetic Resonance
NPP	Net primary productivity
O_2	Molecular oxygen
$^1O_2$	Singlet oxygen
$^3O_2$	Triplet oxygen (ground state)
OEC	Oxygen evolving complex
P	RC special pair

P###	Specific RC special pair (### is the absorption max in nm)
P-P	Pump-Probe
PC	Plastocyanin
PDI	Perylene diimide
P_i	Inorganic phosphate
PPIX	Protoporphyrin IX
PSI	Photosystem I
PSII	Photosystem II
Q	Plastoquinone
QH2	Plastoquninol
Q-pool	Membrane bound plastoquinone / plastoquninol molecules
ROS	Reactive oxygen species
RC	Reaction center
S_0	Singlet ground state
S_1	1st excited singlet state
S_2	2nd excited singlet state
SE	Stimulated Emission
SF	Singlet fission
SHO	Simple harmonic oscillator
SOC	Spin-orbit coupling

T_1	Lowest triplet excited state
T_n	Higher triplet excited states
TD-DFT	Time dependent DFT
THF	Tetrahydrofuran
TTL	Transistor-transistor logic
TET	Triplet Energy/Excitation Transfer
T-T	Triplet-triplet
WT	Wild Type
Zn	Zinc
Zn-TPP	Zinc-tetraphenylporphyrin
Φ_P	Phosphorescence quantum yield
Φ_F	Fluorescence quantum yield

ABSTRACT

Hartzler, Daniel A. Ph.D. Purdue University, December 2015. Triplet Excitons in Natural Photosynthetic and Artificial Light Harvesting Systems: Measurement and Modeling. Major Professor: Sergei Savikhin

Under full sunlight, unprotected (Bacterio)Chlorophyll ((B)Chl) molecules photodegrade in a matter of minutes. This is the result of the generation of highly reactive singlet oxygen ($^1O_2$) by energy transfer from the (B)Chl triplet state (^{3}(B)Chl) to the oxygen ground state. Natural photosynthetic systems must protect themselves from $^1O_2$, typically done by positioning carotenoids within a few angstroms of each (B)Chl molecule to quench ^{3}(B)Chl states. Using phosphorescence spectroscopy and computational modeling, we investigated alternative, carotenoid independent, mechanisms which nature may employ to prevent $^1O_2$ sensitization by lowering the energy of ^{3}(B)Chl below that of $^1O_2$. The two proposed triplet lowering mechanisms investigated were: triplet state lowering by strong pigment-pigment interactions (i.e. triplet exciton formation) and triplet state lowering by pigment-protein interactions. Possible natural examples employing these mechanisms are two structures found in green sulfur bacteria: the chlorosome (an antenna containing ~100000 coupled BChl *c*, *d*, or *e* molecules with unexpectedly high photostability) and the Fenna-Matthews-Olson (FMO) complex (an auxiliary antenna containing eight seemingly unprotected BChl *a* molecules).

Measurements performed on linear aggregates of the dye perylene diimide (PDI) show that triplet exciton formation does reduce the triplet state energy. However, direct measurement of triplet state energies for the chlorosome and FMO complex proved experimentally difficult, thus an alternative approach was used to calculate these energies using empirical and excitonic models. Since the use of excitonic modeling requires knowledge of both the pigment site energies and the pigment-pigment interactions (i.e. couplings), work was performed to catalog the monomeric singlet and triplet state energies of all known natural (B)Chl pigments by direct measurement or computational modeling and to characterize the triplet-triplet (T-T) coupling in artificial (B)Chl and porphyrin dimers by experimental and computational methods. This data set obtained allowed for the development of an empirical model for prediction of the triplet state site energy from a given singlet site energy and for development and calibration of a T-T coupling model.

Use of these models shows that triplet state lowering by pigment-protein interaction provides photoprotection to the FMO complex, while triplet state lowering by triplet exciton formation is insufficient to provide protection to the chlorosome antenna. Additionally, the T-T coupling model shows that in dimers and other aggregates, the coupling is highly sensitive to relative monomer orientation and position, contrary to what was previously assumed. The simple exponential models used to estimate T-T couplings miss this orientation sensitivity, thus in systems with significant contact between adjacent monomers a more accurate approach is required.

PROLOG

The Sun is the main driver of life on Earth, with nearly every organism depending on photosynthesis or its products for energy. An estimated 10^{24}J of solar energy reaches the Earth's surface each year with photosynthetic organisms capturing just a fraction of the incoming radiation, the rest lost to surface heating or reflection (Ke 2001c). Of the captured light energy radiation, only a percentage is converted into the 10^{21}J of biomass (Ke 2001c) that sustains nearly all non-photosynthetic life on Earth. This includes the human population which is supported by 10^{19}J of foodstuff (Ke 2001c).

Photosynthesis, with its deceptively simple overall chemical formula (Stryer 1995):

$$6CO_2 + 6H_2O + h\nu \rightarrow C_6H_{12}O_6 + 6O_2 + heat$$

Equation 1.1

has had an incredible impact on the Earth, both throughout its history and in the present day. Each year photosynthetically active organisms capture approximately 105 petagrams of carbon (net primary productivity, NPP) (Field 1998) releasing approximately 140 petagrams ($1.4 \cdot 10^{11}$ metric ton) of molecular oxygen (O_2) (Equation 1.1). In addition to the nearly 10^{11} tons of captured carbon, numerous other inorganic (Desikachary & Dweltz 1961) and complex organic molecules are synthesized during growth and maintenance respiration (these plus NPP make up gross primary productivity, GPP).

Since life's beginning as early as 3.7 Ga (billion years before present) (Ohtomo et al. 2013) and the beginning of oxygenic photosynthesis possibly by 2.7 Ga (Buick 2008) the chemical processes of living organisms have fundamentally changed the atmospheric and surface geochemistry of our planet, raising the atmospheric oxygen concentration from near zero around 2.4 Ga (the beginning of the "Great Oxidation Event" (Catling 2014; Buick 2008) to its present day value. In fact, the quantity of chlorophyll is so great it can be observed from space as the so called Red Edge in the spectrum of reflected solar radiation (Kiang et al. 2007). Many minerals are biogenic in origin having either been directly laid down by living things such as limestone and chalk (Munnecke & Samtleben 1996) or been influenced by the byproducts of biological activity such as oxygen. These processes laid down great beds of material that are of economic importance today.

Ancient forests are believed to have laid down coal beds (Killops & Killops 2004) while algae and zooplankton are believed to have created oil and gas deposits (Killops & Killops 2004). This stored solar energy in the form of fossil fuels powers the majority of our industries today. According to the US Energy Information Administration, world energy consumption in 2000 was $4.2x10^{17}$ kJ, meaning mankind consumes the equivalent of one tenth of the energy stored by photosynthesis each year (EIA & United States Energy Infromation Administration 2013). With energy demand expected to double by 2040 along with carbon dioxide emissions (from ~25 to ~45 billion metric ton CO_2 from 2000 to 2040) (EIA & United States Energy Infromation Administration 2013), alternative energy sources are badly needed.

CHAPTER 1 – PHOTOSYNTHESIS: AN INTRODUCTION

1.1 Project Introduction and Goals

The goal of this project was to characterize the energies of triplet excited states relevant to natural photosynthetic systems and related artificial systems. In natural systems, control of the (Bacterio)Chlorophyll ((B)Chl) triplet states are essential to the survival of photosynthetic organisms since the (B)Chl triplet state readily transfers its energy to molecular oxygen, exciting it from its triplet ground state ($^3O_2$) to its singlet excited state ($^1O_2$, a powerful oxidizer). Nature has spent much effort to prevent the formation of the (B)Chl triplet state and safely dissipate its energy by positioning carotenoid molecules nearby each (B)Chl to quench the triplet states when they do form. Triplet states in artificial systems play a more varied role. Triplet states can be a destructive state, sensitizing singlet oxygen like in natural photosynthetic systems, or they can be a desired state, allowing for excited state quantum yields approaching 200% via the process of singlet exciton fission.

1.2 Photosynthesis: Structure and Chemistry

This overview will first review the major structures involved in the photosynthetic electron transport chain and their physical function. Then the chemistry performed by these structures will be examined and the overall chemical formula of photosynthesis, Equation 1.1, will be derived.

1.3 The Structures of Photosynthesis

The major molecular systems involved in photosynthesis are the reaction center complexes (photosystem I (PSI) and photosystem II (PSII)) and the antenna systems that form supercomplexes with them, the cytochrome b_6f complex, and ATP-synthase and the FNR enzyme. The next few sections will investigate them from a structural view point.

1.3.1 Photosynthetic Pigments

Photosynthesis must necessarily involve the capture of light which in turn must involve light absorbing pigments. These photosynthetic pigments come in three major classes (with further divisions within each group): chlorophylls, carotenoids, and phycobilins. Since chlorophylls will be the major focus of this work, the other pigment classes will only be covered in brief.

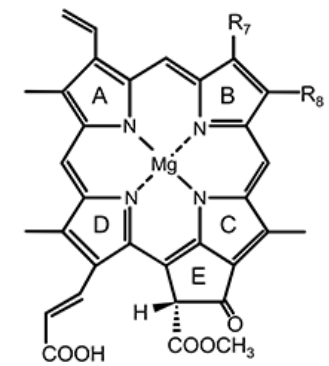

Porphyrin type

	R_7	R_8
Chl c_1	CH_3	C_2H_5
Chl c_2	CH_3	C_2H_3

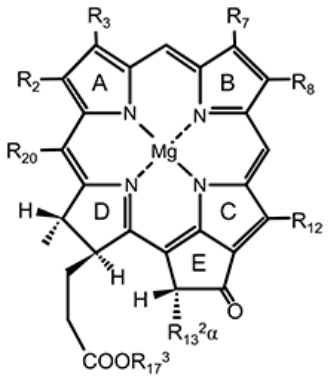

Chlorin type

	R_2	R_3	R_7	R_8	R_{12}	$R_{13}^2{}_\alpha$	R_{20}
Chl *a*	CH_3	C_2H_3	CH_3	C_2H_5	CH_3	$COOCH_3$	H
Chl *b*	CH_3	C_2H_3	CHO	C_2H_5	CH_3	$COOCH_3$	H
Chl *d*	CH_3	CHO	CH_3	C_2H_5	CH_3	$COOCH_3$	H
Chl *f*	CHO	C_2H_3	CH_3	C_2H_5	CH_3	$COOCH_3$	H
BChl *c*	CH_3	CHOH-CH_3	CH_3	$CH_2CH_n(CH_3)_{3-n}$	CH_3/C_2H_5	H	CH_3
BChl *d*	CH_3	CHOH-CH_3	CH_3	$CH_2CH_n(CH_3)_{3-n}$	CH_3/C_2H_5	H	H
BChl *e*	CH_3	CHOH-CH_3	CHO	$CH_2CH_n(CH_3)_{3-n}$	CH_3/C_2H_5	H	CH_3
BChl *f*	CH_3	CHOH-CH_3	CHO	$CH_2CH_n(CH_3)_{3-n}$	CH_3/C_2H_5	H	H

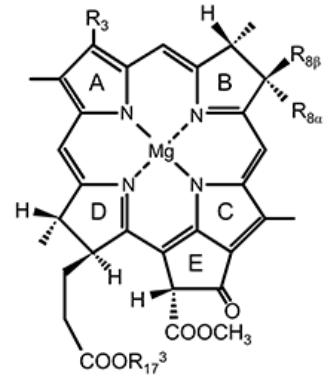

Bacteriochlorin type

	R_3	$R_{8\alpha}/R_{8\beta}$
BChl *a*	$COCH_3$	H/C_2H_5
BChl *b*	$COCH_3$	=CH-CH_3
BChl *g*	C_2H_3	=CH-CH_3

R_{17}^3 - phytyl (Chl *a*, Chl *b*,, Chl *d*,, Chl *f*, BChl *a*,, BChl *b*)
- geranylgeranyl (BChl *g*)
- farnesyl/others (BChl *c*, BChl *d*, BChl *e*, BChl *f*)

Figure 1.1: (Bacterio)Chlorophyll structures showing the IUPAC numbering system (Moss 1987) with the pyrrole rings labeled A-D and the isocyclic ring E. Reprinted with permission from (Hartzler et al. 2014). Copyright 2014 American Chemical Society.

Chlorophylls are the major photosynthetic pigment found in nature, which, in addition to gathering light, are also used in reaction centers to carry out charge separation

and transfer. All chlorophylls share the same basic structure of a tetrapyrrole macrocycle coordinated to a central metal ion (see Figure 1.1) which is almost exclusively an Mg^{2+}, although Zn^{2+} containing molecules have been found in nature (Wakao et al. 1996). The naturally occurring (B)Chl molecules can be divided into three major subgroups depending on the degree of saturation of the macrocycle (Gouterman 1961) (see Figure 1.1): the porphyrin type, chlorin type, and bacteriochlorin type. These subgroups broadly determine the spectral properties of the molecule, especially in terms of the intensity and location of the lowest energy electronic transitions (the Q-bands) which are one of two sets of intense absorption bands (Gouterman 1961; Gouterman et al. 1963) and will be investigated in detail in the theory section. Further spectral variation within these subgroups depends on various functional groups attached to the macrocycle (Figure 1.1).

Carotenoids are linear molecules (see Figure 1.2) that act as auxiliary antenna pigments, absorbing in the green part of the spectrum missed by (B)Chls, as well as energy dumps for dissipating the dangerous triplet states that (B)Chl molecules can enter (Ke 2001g). The dissipation of (B)Chl triplet state energy is perhaps the most important function of the carotenoids, as the triplet state can sensitize highly toxic singlet oxygen, a reactive oxygen species (ROS), and carotenoid free mutants of photosynthetic organisms typically suffer serious damage when illuminated (Glaeser & Klug 2005).

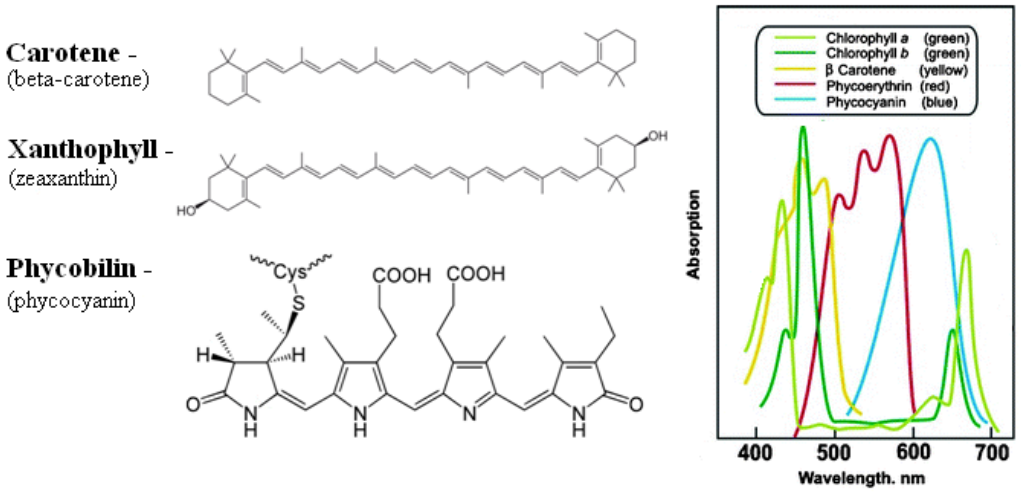

Figure 1.2: Carotenoids are auxiliary pigments and can be classified into Carotenes (containing only C and H) and into Xanthophylls (containing C, O, and H). Phycobilins are an alternative main antenna pigment based on an open tetra-pyrrole. Both types of molecules absorb in the spectral gap left by chlorophyll.

Phycobilins are an alternative pigment (as opposed to (B)Chl) used by some organisms such as cyanobacteria and red algae (Stryer 1995) as a major light gathering antenna pigment which absorb strongly in the green to red spectral region. These pigments all share the same basic structure of an open chain tetra-pyrrole, sort of like an unrolled chlorophyll (see Figure 1.2) and are covalently bonded to their respective antenna protein (Ke 2001f), unlike (B)Chls and carotenoids which are held in place by weaker non-covalent bonds (Ke 2001a). Spectral properties of phycobilins depend on the degree of saturation of the pyrrole subunits and methine (=CH-) bridges.

1.3.2 Antenna complexes

The role of antenna complexes are to gather light and provide a path for that energy to flow to the reaction center (RC) before it is lost to fluorescence or intersystem crossing (ISC), which is the major mechanism that allows for the formation of triplet

excited states from singlet excited states. In monomeric (B)Chls, both the decay of the singlet excited state (fluorescence) and ISC occur with approximately the same rate-constant of $(10ns)^{-1}$, for example Chl *b* has a measured fluorescence lifetime of 3.2 ns (Niedzwiedzki & Blankenship 2010) and an ISC rate of $(3.4\ ns)^{-1}$ (Schödel et al. 1998). Thus chlorophyll based antenna structures must gather the singlet state energy quickly to outcompete ISC, since the resulting triplet states waste energy (triplet states are not used for energy) and are harmful if allowed to sensitize singlet oxygen. As a result, energy transfer inside and between antenna complexes is quite fast and the whole process from light capture to RC excitation occurs within a few tens of picoseconds.

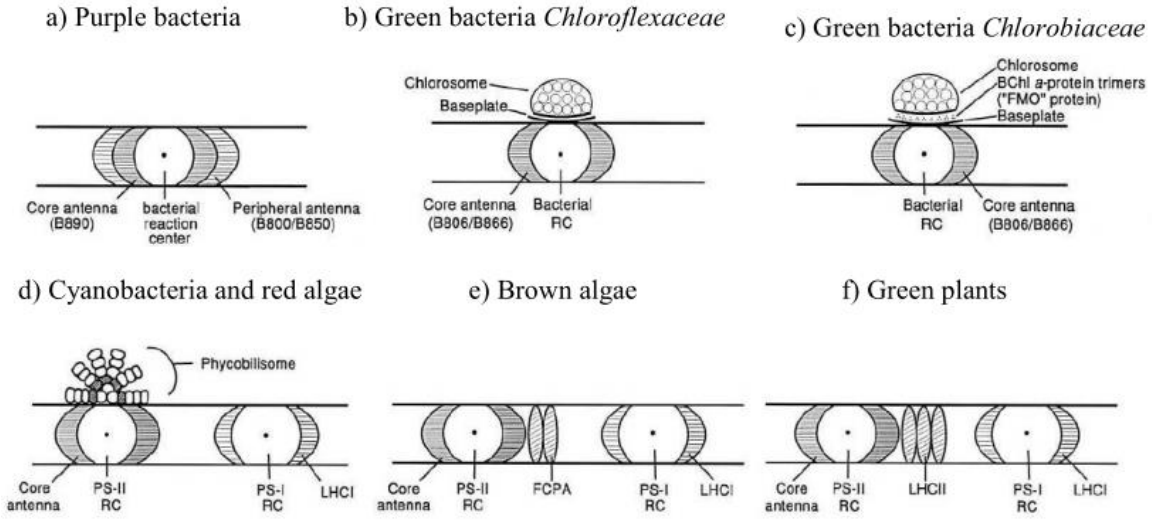

Figure 1.3: Simplified models of light harvesting machinery of various organisms. (Ke 2001c)

The antenna complexes that hold the photosynthetic pigments are varied and depend on the type of organism. Figure 1.3 shows simplified models of various classes of photosynthetic organisms with a, b, and c being anoxygenic and d, e, and f oxygenic (Ke 2001c). Each of these classes of organism feature core antenna tightly associated with

each of the RC as well as auxiliary antenna complexes which in the case of green plants and brown algae (LCHII and FCPa respectively) that are capable of dynamically associating with PSI or PSII depending on lighting conditions (Figure 1.4) (Iwai et al. 2010).

As can be seen in Figure 1.4, the LHCII is a trimer with a roughly elliptical arrangement of Chl a and b (cyan and green) in each LCHII monomer with carotenoids (yellow) arranged such that each Chl has access to one to quench the occasional Chl triplet state. These trimeric units associate with the RC core complexes where they can transfer captured energy via excitation energy transfer (EET) to the PSI or PSII core antenna then to the RC itself (Croce & van Amerongen 2011).

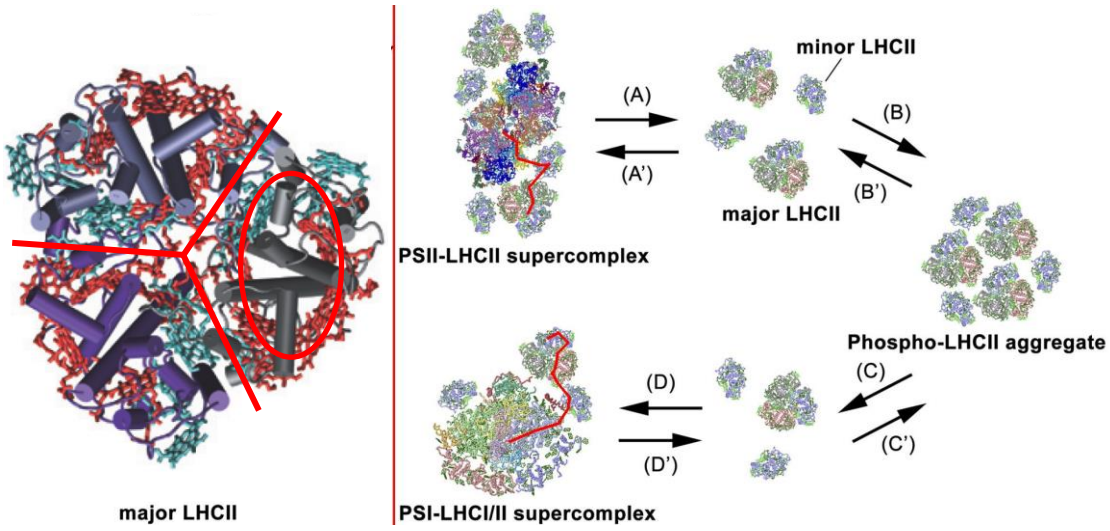

Figure 1.4: Trimeric structure of LHCII auxiliary antenna complex (Red pigments are Chl *a* and cyan are Chl *b*) (Scholes et al. 2011) and dynamic association of LHCII with PSI or PSII supercomplexes (Iwai et al. 2010).

Purple photosynthetic bacteria have a similar arrangement, with a RC surrounded by a core antenna (LH1) with loosely associated auxiliary antenna complexes (LH2) which funnel energy into the core antenna the same way as LCHII. As can be seen in

Figure 1.5, the structure of LH2 is quite dissimilar from LHCII. Instead of a trimer with loosely coupled Chl molecules, LH2 is a cylindrical structure with a ring of strongly coupled BChl a molecules (B850) and a second ring of weakly coupled BChl a molecules (B800). Additionally, as in LHCII, each BChl in the LH2 complex has access to a carotenoid to quench any triplet states that form. These ring shaped antenna associate with the core antenna (LH1, B875) to funnel energy to the RC (see Figure 1.5).

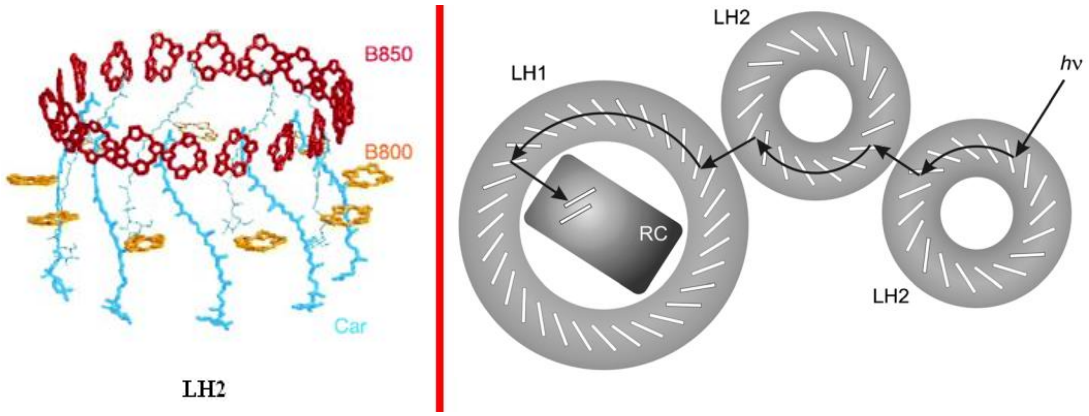

Figure 1.5: Arrangement of BChl molecules (macrocycle only) and carotenoid molecules within the LH2 complex (Herek et al. 2002) as well as the typical arrangement of the LH2, LH1, and RC complexes found in some purple photosynthetic bacteria (Balzani et al. 2011).

Cyanobacteria and green sulfur bacteria have vastly different auxiliary antenna systems compared to other organism. Cyanobacteria have large protein structures called phycobilisomes that contain covalently bound phycobilins as their antenna (Ke 2001f). Being that they contain no chlorophyll, they will not be explored.

Green sulfur bacteria have membrane bound organelles called chlorosomes that each contains hundreds of thousands of BChls. The chlorophylls (BChl *c*, *d*, or *e*) self-assemble into large tube or sheet like structures without the need for a protein scaffolding

(Orf & Blankenship 2013). These assemblies are very efficient light gathering antenna, allowing organisms that use them to grow under very low light intensities (Orf & Blankenship 2013). They have even been found living at a depth of ~2400 m near hydrothermal vents on the ocean floor, it is believed they are living off the blackbody radiation emitted by the hot water (Beatty et al. 2005).

Inside these large aggregates, the BChl molecules experience strong excitonic coupling to neighboring molecules resulting in a large energy shift in the absorption peaks (see Figure 1.6). This strong coupling aides in energy transfer (Orf & Blankenship 2013) as well as broadening and shifting the absorption peaks giving the organism access to a broader range of light, including the more penetrating near infrared (NIR) wavelengths. While these structures contain carotenoids, mutants lacking carotenoids and artificial aggregates of pure BChl c have been shown to have unexpectedly high photostability in the presence of light and oxygen (Kim et al. 2007). It has been suggested that tlarge wavefunction overlap between neighboring BChl molecules is giving rise to triplet excitons that shift the triplet state energy lower than that of singlet oxygen, thus preventing sensitization and subsequent destruction of the antenna (Kim et al. 2007). This possibility will be investigated in later chapters.

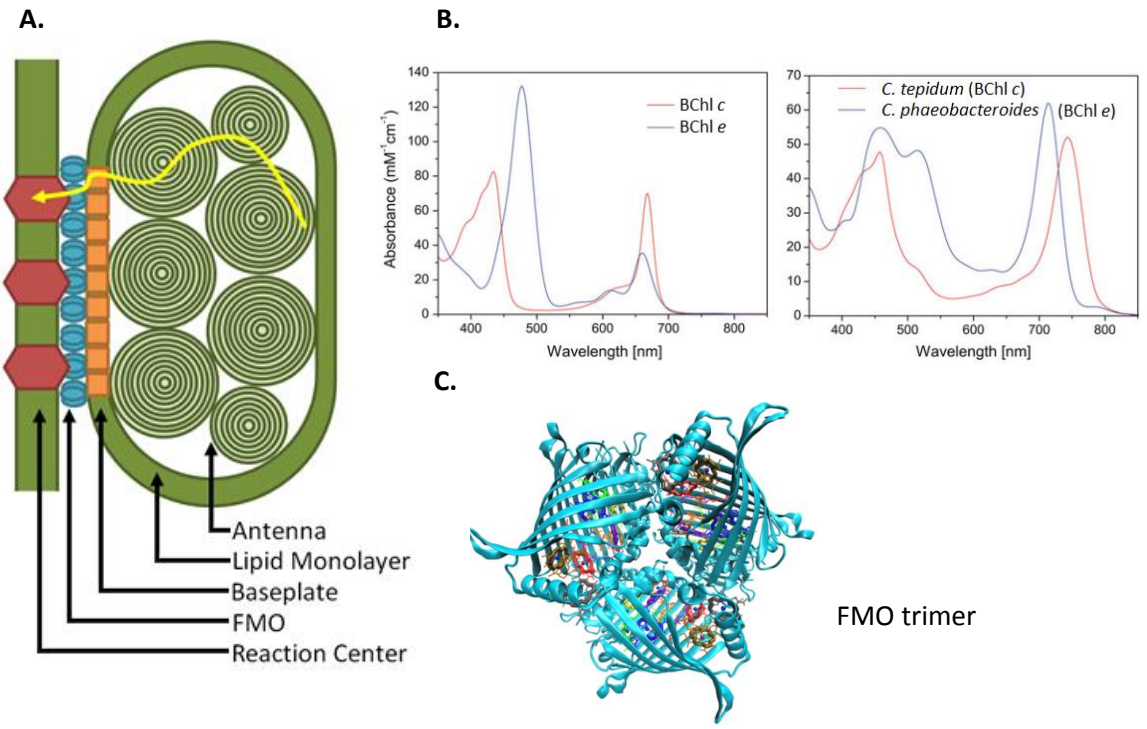

Figure 1.6: A- Basic structure of chlorosome antenna and bonding relation to FMO and RC. **B-** Absorption spectrum typical of many green sulfur bacteria. The left most absorption spectra are for BChl *c* and *e* monomers while the right most spectra are for the complete antenna (Pšenčík et al. 2014). **C-** Structure of FMO trimer with all eight pigments per monomer (Kihara et al. 2015).

In addition to the large chlorosomal antenna, some green sulfur bacteria contain an auxiliary antenna and energy conduit between the chlorosome and bacterial reaction center. This complex, the Fenna-Matthews-Olson (FMO) complex (Figure 1.6), consists of a trimer with each monomer containing seven coupled BChl a molecules as well as an eighth weakly bound BChl a between each monomer (Schmidt am Busch et al. 2011). Despite containing seven (eight) BChl molecules and no carotenoids (Li et al. 1997; Schmidt am Busch et al. 2011), the monomers are stable when exposed to light and oxygen (Kihara et al. 2015). This implies that the FMO complexes are unable to sensitize singlet oxygen. Evidence for this includes the complexes photostability and the fact that its triplet state dynamics are independent of oxygen concentration (Kihara et al. 2015). It

is speculated that either pigment-pigment or pigment-protein interactions have lowered the triplet state energy below that of singlet oxygen, preventing triplet state energy transfer (Hartzler et al. 2014). The FMO complex will also be investigated in a later chapter.

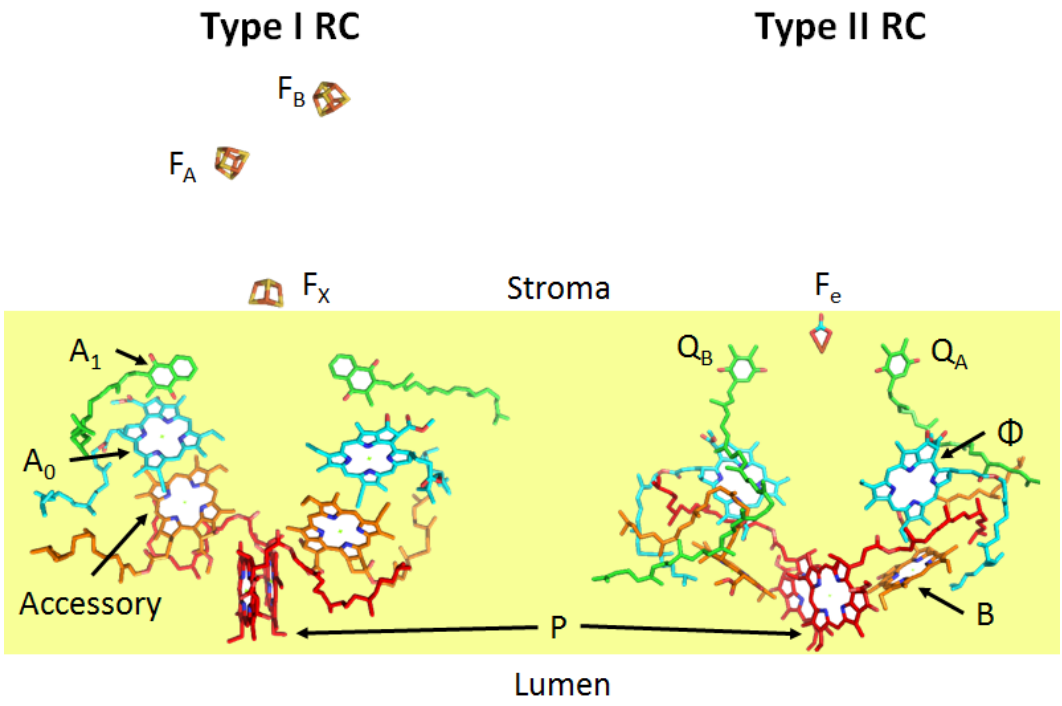

Figure 1.7: Type I and Type II reaction centers [PSI (PDB ID = 3LW5, (Amunts et al. 2010)) and PSII (PDB ID = 4UB6, (Suga et al. 2014)) respectively]. Note the differences in the primary and terminal electron acceptors between the two types. In the type I RC the primary acceptor (A_0) is a Chl and the terminal acceptor is an iron-sulfur cluster (F_B) while in the type II RC the primary acceptor (Φ) is a pheophytin and the terminal acceptor is a quinone (Q_b).

1.3.3 The Photosynthetic Reaction Centers

There are two types of reaction centers, type I and type II RC as pictured in Figure 1.7, each of which have defining electron transfer cofactors and terminal electron acceptors. The type I RC contains two active pathways leading from the special pair (P)

each with two Chls acting as primary electron acceptors (Accessory and A_0) and a quinone (A_1) as a secondary acceptor before the terminal acceptors, the iron-sulfur clusters ($F_{A/B}$). The type II RC has only one active electron transfer pathway (the a-branch) (Ke 2001e) which contains the primary electron acceptor (a pheophytin, Φ_A) with an accessory Chl, B_A, and quinones Q_A and Q_B as terminal electron acceptor. These are the only types of photosynthetic reaction centers found in nature. Since both type I and type II RCs are required for oxygenic photosynthesis (Blankenship 2010) and oxygenic bacteria are believed to have evolved about 2.7 billion years in the past (Buick 2008), both types of RC must have been around for at least 2.7 Ga, and likely evolved from a common ancestor some time before that (Blankenship 2010). Both RC types preform the same basic function, accepting energy from the antenna to carry out light-driven charge separation where a high energy electron is transferred away from the excited special pair, P (see Figure 1.7), to the terminal acceptors, $F_{A/B}$ or Q_B for type I and II RC respectively. Since the excited state of a (B)Chl is only on the order of 10ns (Niedzwiedzki & Blankenship 2010), the charge separation is the first step in the necessary process of converting this short living electronic excited state into a long living stable form.

1.3.4 Photosystem II

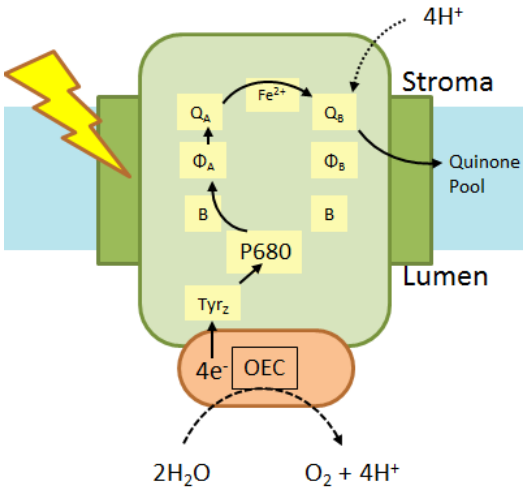

Figure 1.8: The electron transfer pathway through PSII. Light excites the special pair (P680) causing an electron to flow to the terminal acceptor (Q_B) where it can be accepted by the Q-pool. The oxidized special pair ($P680^+$) is then reduced by an electron removed from a water molecule by the oxygen evolving / water oxidizing complex (OEC / WOC).

Photosystem II (PSII) is a type II RC with the ability to extract electrons from water via the oxygen evolving / water-oxidizing complex (OEC / WOC) (see Figure 1.8) (Ke 2001e). After the special pair (P680) has been excited, either directly or by receiving energy from the antenna, an electron is transferred to the primary acceptor, $Pheo_A$, losing energy in the process. From $Pheo_A$, the electron is transferred to the terminal acceptor Q_B (a quinone) via Q_A and a non-heme iron, losing energy with each step(Ke 2001e). At Q_B, after two successive electrons are received from the RC, two protons are captured from the stroma and a plastoquninol is formed and released into the membrane bound Q-pool to transport the electrons to the next complex in the electron transport chain, cytochrome b_6f (Ke 2001e). The loss of energy with each step is needed to inhibit back transfer of the electron to the oxidized special pair ($P680^+$) where recombination with the high energy electron would take place, wasting energy and possibly creating triplet states (Ke 2001e).

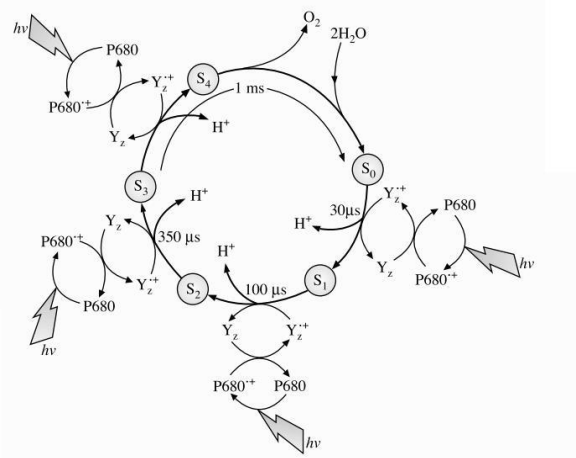

Figure 1.9: The five state S-cycle of the oxygen evolving complex (OEC). Shown, the light driven (*hν*) oxidation of the PSII special pair (P680) and subsequent reduction by tyrosine (Y_Z). The oxidized tyrosine (Y_Z^+) is then reduced by the OEC with an electron taken from a water molecule. (Barber 2004)

The low energy electron for reducing $P680^+$ to P680 is supplied by the OEC from the oxidation of water. This complex, the OEC, is a five state system that is capable of removing electrons one at a time from two bound water molecules to supply the needs of the RC (see Figure 1.9) (Ke 2001b; Barber 2004). Starting at state S_0 (note that S_1 is the dark adapted resting state (Ke 2001b)), the cycle begins with the light driven oxidation of P680, which is then reduced by an electron from a nearby amino acid residue, a tyrosine, labeled Y_Z in Figure 1.9 and Tyr_z in Figure 1.8. The oxidized tyrosine then receives an electron from the OEC, causing the complex to turn over to state S_1, releasing a proton into the lumen (the lumen being the inside of the photosynthetic membrane and the stroma the outside), and then waiting for the next light driven oxidation event. This process occurs a total of four times, turning the OEC over through the states $S_0 \rightarrow S_4$ (Ke 2001b). State S_4 is a transient state that will transition to S_0 automatically, assembling and releasing an oxygen molecule while also binding two more water molecules. To complete this cycle, the OEC must be capable of stabilizing and holding onto highly reactive

radicals such as OH (hydroxyl) and O (oxygen radical) without being damaged or destroyed (Ke 2001b; Barber 2004). It is not currently known how all the steps work since the final step, $S_4 \rightarrow S_0$ during which the oxygen-oxygen bond is formed, has not been stabilized for study (Ke 2001b).

1.3.5 The Cytochrome b_6f Complex

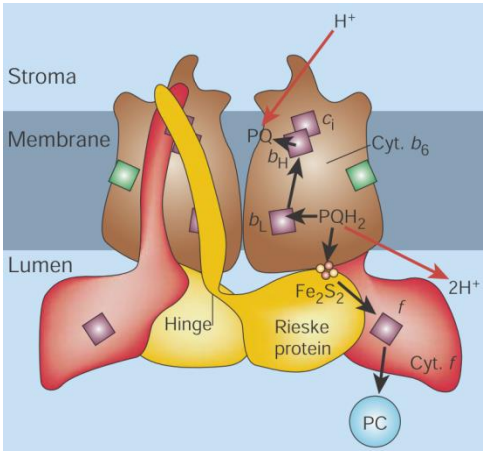

Figure 1.10: The split electron transport pathway through the cytochrome b_6f complex. Electrons enter the complex (donated by PQH_2) at the lumen side of the Cyt b_6 subunit and leave the complex either from the stroma side of Cyt b_6 or through the Cyt f subunit. (Kühlbrandt 2003)

In the electron transport chain, Cyt b_6f sits between PSII and PSI and uses the electrons available in the Q-pool to pump protons across the thylakoid membrane in addition to releasing the protons bound to QH_2 at PSII into the lumen (Ke 2001h). To facilitate proton pumping, the Cyt b_6f complex has two electron pathways (Figure 1.10). One path leads to Cyt f on the lumen side where the electron is transfer to plastocyanin (PC) for transport to PSI, while the other path leads to the stromal side of Cyt b_6 where a bound plastoquinone waits for two electrons (Ke 2001h). Once the plastoquinone has two electrons transferred to it, it captures two protons from the stroma and is released into the

Q-pool. There it will eventually bind to the lumal side of Cyt b_6, release its protons to the lumen and transfer its two electrons to the separate pathways of the Cyt b_6f complex. This split electron flow at Cyt b_6f results in an additional proton being pumped across the membrane for each electron generated by PSII (Ke 2001h), which can be represented with a geometric series: each e^- from PSII will release one proton into the lumen (+1), 50% of those e^- will return to the Q-pool to move an additional proton (+0.5), 50% of those e^- (i.e. 25%) will return to the pool to move an additional proton (+0.25), and so on.

$$1 + 0.5 + 0.25 + 0.125 + \cdots = \left(\sum_{n=0}^{\infty} \frac{1}{2^n}\right) = 2$$

Equation 1.2

1.3.6 Photosystem I

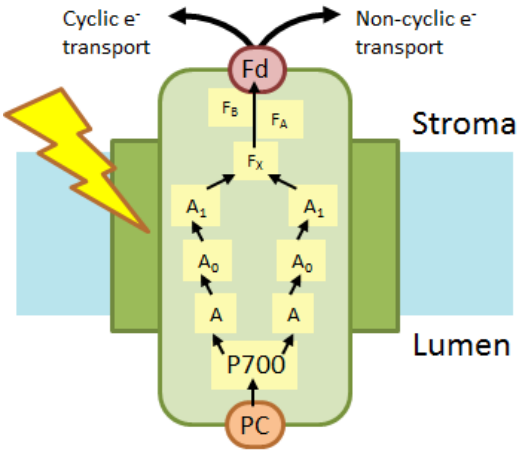

Figure 1.11: The electron transport pathway through the PSI complex. Light excites the special pair (P700) causing an electron to flow to the terminal acceptor (F_B) where it can be accepted by ferredoxin (Fd). The oxidized special pair ($P700^+$) is then reduced by an electron donated by plastocyanin (PC).

PSI is a type I RC, when its special pair (P700) is excited it transfers an electron to the primary acceptor A_0 (pheophytin) of one of the two active branches via the accessory pigment A (Chl), which then transfers it to the secondary acceptor A_1 (a

quinone) and then to the iron-sulfur clusters F_X, F_A, and the terminal acceptor F_B (Figure 1.11). The oxidized $P700^+$ will be reduced by an electron supplied by Cyt b_6f via the electron transport molecule PC (Ke 2001d).

1.4 The Chemistry of Photosynthesis

The chemistry of photosynthesis can be divided into two major categories, the light reactions and the dark reactions (i.e. light dependent and light independent processes), which work together to provide the organism with the sugars and other energetic molecules it needs for maintenance, growth, and reproduction. The light reactions work to supply a steady flow of energy in the form of adenosine triphosphate (ATP) and nicotinamide adenine dinucleotide phosphate (NADPH) to the dark reactions for carbon fixation and sugar synthesis. These two molecules, ATP and NADPH, act as rechargeable energy carriers that are broken down into ADP + P_i (adenosine diphosphate + inorganic phosphate) and $NADP^+$ + H^+ by the dark reactions and then reformed into ATP and NADPH by the light reaction.

1.4.1 The Dark Reactions

Also known as the Calvin cycle, the dark reactions use ATP and NADPH to synthesize glyceraldehyde-3-phosphate (G3P) from carbon dioxide, water, and inorganic phosphate ($H_2PO_4^-$ or HPO_4^- depending on pH) according to Equation 1.3:

$$3CO_2 + 5H_2O + 6NADPH + 9ATP \rightarrow G3P + 2H^+ + 6NADP^+ + 9ADP + 8P_i$$

Equation 1.3

G3P, a three-carbon sugar phosphate, is later used to create glucose and other six-carbon or longer sugars, releasing the inorganic phosphate in the process (Stryer 1995). Thus the overall reaction for photosynthesis can be given in general terms as:

$$nCO_2 + nH_2O + light \rightarrow (CH_2O)_n + nO_2 + heat$$

Equation 1.4

It should be noted that the reverse process, oxidizing an *n*-carbon sugar molecule to produce energy, consumes the same number of oxygen molecules (nO_2) that were created during the sugar's synthesis (Stryer 1995). So net oxygen production requires a percentage of the sugars created to not be oxidized. However, this is not a problem since cellulose and other structural materials used by plants and bacteria are constructed from these simple sugars (Stryer 1995) and these materials are, in some locations, buried in anoxic environments such as peat or ocean sediment where they later become coal, oil or natural gas (Killops & Killops 2004). It has been estimated that 0.1-0.2% of the organic carbon of NPP (Equation 1.4) is buried annually ensuring 10^{13} mol of O_2 is released to the atmosphere each year (Catling 2014).

1.4.2 The Light Reactions

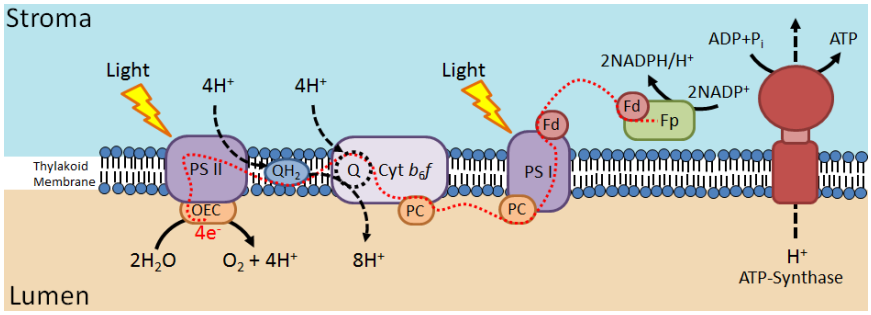

Figure 1.12: Thylakoid Membrane - The major systems involved in photosynthesis are shown: the reaction center complexes (PSI and PSII), the cytochrome b_6f complex, and ATP-synthase.

In plants, the light reactions primarily take place inside the thylakoid membrane (the photosynthetic membrane) and involve the progressive conversion of light energy into increasing more stable chemical forms via the electron transport chain. A sample thylakoid membrane, with electron transport chain, from an oxygenic phototroph is laid out in Figure 1.12. This membrane divides the cell or chloroplast into two distinct volumes, the volume enclosed by the thylakoid membrane, the lumen, and the volume outside the thylakoid membrane, the stroma.

The photosynthetic electron transport chain begins at PSII with the absorption of a photon by the antenna system. The excited state of the antenna pigment is transferred via EET to the RC where the excitation initiates charge separation at the special pair (P680). The resulting high energy electron is transferred out of the RC to the stromal side of the PSII protein complex. The oxidized reaction center ($P680^+$) will then be reduced by a low energy electron taken from a water molecule by the OEC, which, for every four electrons supplied to $P680^+$ transforms two water molecules into an oxygen molecule (O_2) while releasing four protons (H^+) into the lumen (Stryer 1995). On the stromal side of PSII a thylakoid membrane bound electron transport molecule, plastoquinone (Q), waits to accept two high energy electrons from the RC (Stryer 1995). Each Q, in addition to accepting two electrons from the RC, will bind two protons from the stromal side of the thylakoid membrane becoming a plastoquninol (QH_2) (Stryer 1995). The equation for the reaction thus far is:

$$2H_2O + 4h\nu + 2Q + 4H^+{}_{stroma} \rightarrow O_2 + 2QH_2 + 4H^+{}_{lumen}$$

Equation 1.5

From the RC, the plastoquninol is released into the membrane bound Q-pool where it diffuses until binding to a cytochrome b_6f (cyt b_6f) complex, to which it will transfer its two electrons while releasing the two protons into the lumen (Stryer 1995). Inside the cyt b_6f complex, one electron is directed to a transport molecule in the lumen, plastocyanin (PC), while the other electron is directed to a Q bound to the stromal side of cyt b_6f (Stryer 1995). Since half the total electron flow is redirected back into the Q-pool, where they will pick up protons from the stroma, cyt b_6f functions as a proton pump, moving a net of one additional proton from the stroma to the lumen for each electron produced by PSII (Ke 2001h). The net equation for the interaction of cyt b_6f with the Q-pool is:

$$QH_2 + 2H^+{}_{stroma} + 2PC \rightarrow Q + 4H^+{}_{lumen} + 2PC^-$$

Equation 1.6

Combining Equation 1.5 and Equation 1.6 shows that for each electron supplied by PSII a total of three protons are released into the lumen for a total of 12 protons for each molecule of O_2 produced by the OEC:

$$2H_2O + 4h\nu + 4PC + 8H^+{}_{stroma} \rightarrow O_2 + 4PC^- + 12H^+{}_{lumen}$$

Equation 1.7

In PSI, light absorbed by the antenna system is captured by the RC and used to initiate charge separation at the special pair (P). The high energy electron is then transferred out of the RC to an electron transport molecule in the stroma, ferredoxin (FD), which will take one of two paths. In non-cyclic electron transport, the reduced ferredoxin

(FD^-) binds to ferredoxin-$NADP^+$ reductase (FNR) which synthesizes NADPH according to the following reaction (Stryer 1995):

$$2FD^- + NADP^+ + H^+ \rightarrow 2FD + NADPH$$

Equation 1.8

For cyclic electron transport, FD^- binds to the stromal side of cyt b_6f where it transfers its electron back into the Q-pool to facilitate additional proton pumping (Stryer 1995). The oxidized PSI reaction center (P^+) is then reduced by an electron supplied by plastocyanin (PC^-).

Ignoring cyclic electron transport, the net yield of the oxygenic photosynthetic electron transport chain is:

$$2H_2O + 10H^+_{stroma} + 2NADP^+ \rightarrow O_2 + 2NADPH + 12H^+_{lumen}$$

Equation 1.9

It has been shown that to synthesize ATP from ADP and P_i, four protons pass through the ATP-synthase complex for each molecule of ATP created (Turina et al. 2003). Combining that with Equation 1.9, produces the equation for the net yield of the light reactions:

$$2H_2O + 3ADP + 3P_i + 2NADP^+ \rightarrow O_2 + 2NADPH + 3ATP + 2H^+_{stroma}$$

Equation 1.10

Cyclic electron transport from PSI serves to produce more ATP while requiring more photons to be supplied to PSI (Stryer 1995).

The light reactions are essentially light driven electron flow from water to NADPH which generates a proton gradient in the process. Energy flow through this system can be visualized as in Figure 1.13, called the Z-Scheme (Govindjee & Govindjee 2000) which shows the change in redox potential of an electron as it travels from water to FNR (where NADPH is created).

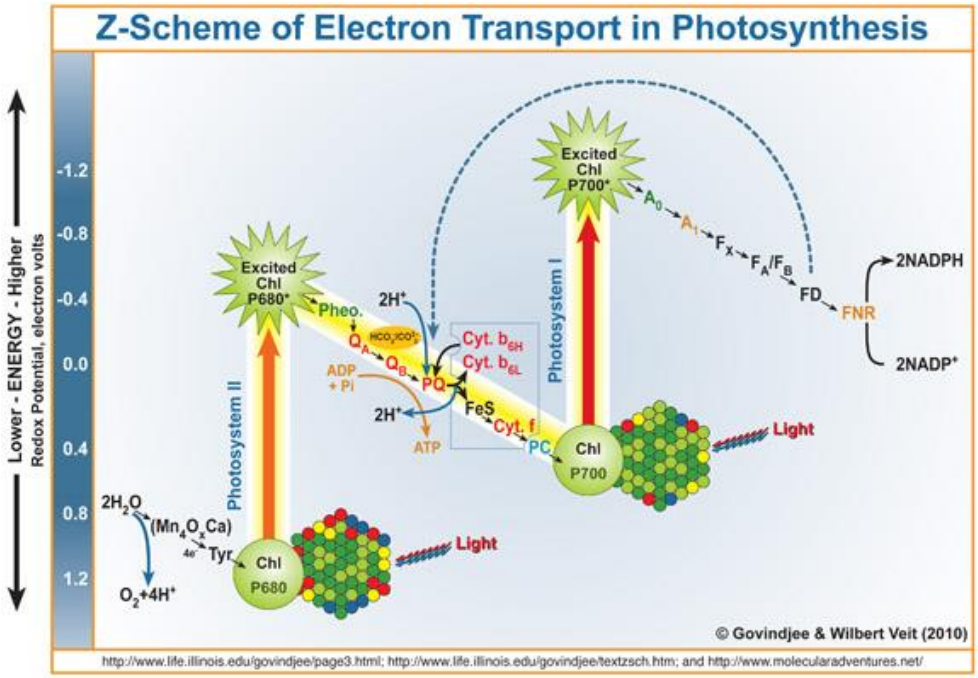

Figure 1.13: Z-Scheme of photosynthesis. (Govindjee & Veit 2010)

1.5 Artificial Photosynthetic Systems

In addition to natural systems, artificial systems are being explored for use in solar energy capture systems. New materials and chemical systems are being investigated for solar energy capture as either photovoltaic or photocatalytic systems. In conventional photovoltaic systems such as silicon, light absorption occurs in a bulk semiconducting layer creating weakly bound electron-hole pairs (Wannier-Mott exciton, (Bassani & Agranovich 2003)), which are separated by the electric field of the pn-junction (Kippelen

& Brédas 2009). Some organic photovoltaics (Figure 1.14A) function similarly to the conventional semiconductor (e.g. Si, CdTe, etc) based systems where light absorption occurs in a bulk organic dye film creating a tightly bound molecular exciton (Frenkel exciton, (Bassani & Agranovich 2003)) which is then separated into an electron/hole at the junction between two different organic layers, where the layer with the higher excited state redox potential (the donor layer) will transfer electrons to the layer with the lower redox potential (the acceptor layer) (Kippelen & Brédas 2009). More sophisticated approaches use covalently bound donor-acceptor pairs (a reaction center analog, Figure 1.14B) to either inject charge carriers directly into a semiconductor as in dye-sensitized solar cells or supply electrons to a catalyst.

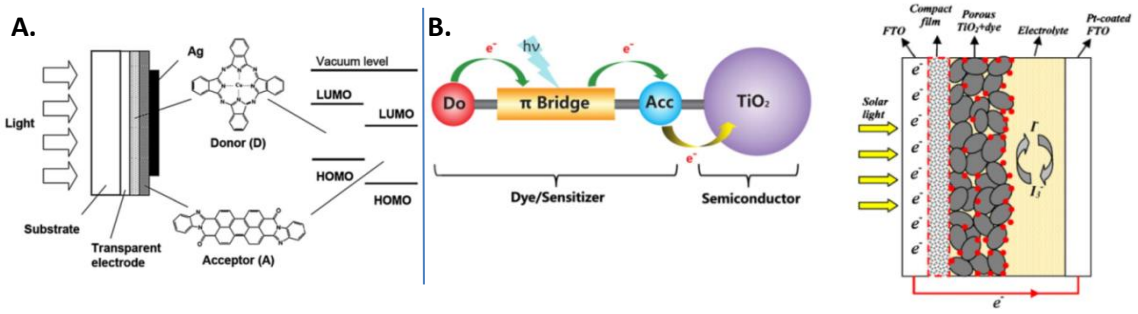

Figure 1.14: A – Organic photovoltaic cell consisting of two organic dye layers (Copper-Phthalocyanine and a perylene derivative (Kippelen & Brédas 2009). B – Dye-sensitized solar cell. Covalently bound donor and acceptor inject electrons into a semiconductor (TiO_2). The oxidized electron donor is then regenerated by a liquid electrolyte (Gong et al. 2012).

CHAPTER 2 – THEORY

The (B)Chl molecules studied have two major sets of optical transitions. One set of absorption bands (both X and Y polarization) lay in the blue spectral region and are known as the Soret, or B, bands while the other set lay in the red to near infrared (NIR) spectral region and are known as the Q bands. The locations, intensities, and splitting of the X and Y polarization of these bands depends strongly on the mixing of molecular orbitals via configuration interaction (CI), as such the orbitals and CI theory will be investigated by use of Gouterman's four orbital model of porphyrin.

A major focus of this study was to measure the triplet state energy of these molecules. The most direct method is to measure the phosphorescence emission spectrum, a spin-forbidden radiative transition from the first triplet excited state to the singlet ground state which must rely on spin-orbit coupling (SOC) to break the spin selection rule. These selection rules as well as SOC will also be investigated in brief.

2.1 Background

2.1.1 Molecular Orbitals

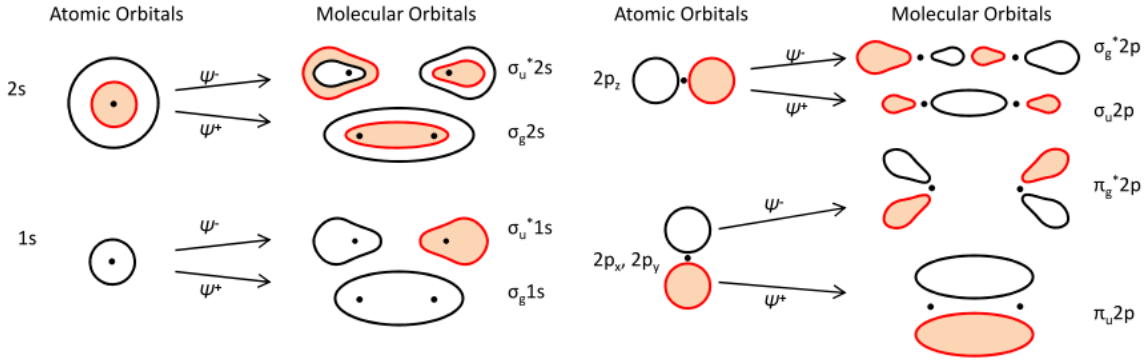

Figure 2.1: The formation of σ and π bonding and anti-bonding (*) molecular orbitals from atomic orbitals. Black dots represent atomic nuclei while color/shading of orbitals indicate phase.

The molecular orbitals (MO) discussed here were created using either the linear combination of atomic orbitals (LCAO) method or on an ad hoc basis (e.g. the four orbitals of Gouterman's Four Orbital Model of Porphyrin, (Gouterman 1961; Gouterman et al. 1963)). These orbitals, while quantitatively incorrect, possess the correct symmetries and bonding / anti-bonding characteristics (Figure 2.1) (Harris & Bertolucci 1978). Of particular importance are the orbitals containing π-bonds since in organic molecules the low lying electronic transitions in the visible and NIR are typically π-π* (bonding and anti-bonding) (Figure 2.2a) (Harris & Bertolucci 1978). In molecules with alternating co-planer single and multiple bonds (Figure 2.2a,b) the π-bonding electrons become delocalized into orbitals extending over large parts of the molecule, forming a conjugated π-electron system (Hornback 1998).

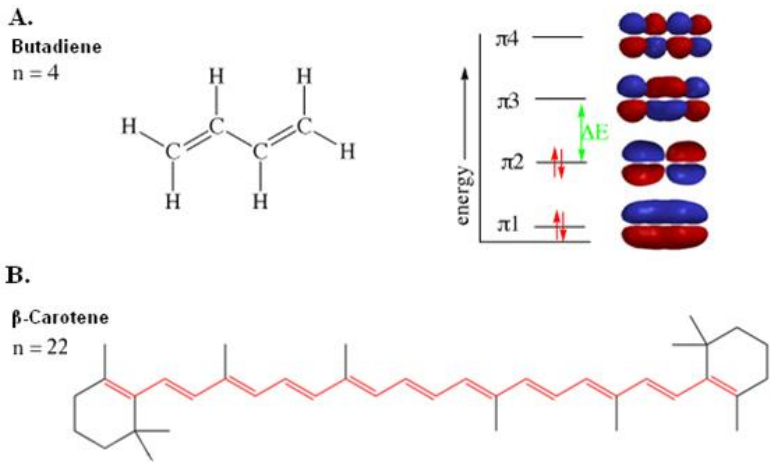

Figure 2.2: Alternating co-planar single (σ) and double (σ and π) bonds forming a conjugated π system for **A** - A four carbon system (1,3-Butadiene) **B** - A large 22 carbon linear conjugated π system (β-Carotene).

Examples of molecules with extensive conjugated π-systems include linear molecules like carotenoids (Figure 2.2b) and cyclic molecules like porphyrins, chlorins, and bacteriochlorins (Figure 2.3) which differ in the extent of the conjugation. Particular attention will be paid to porphyrin as both the chlorophylls and bacteriochlorophylls derive from it (see Figure 2.3, Figure 1.1).

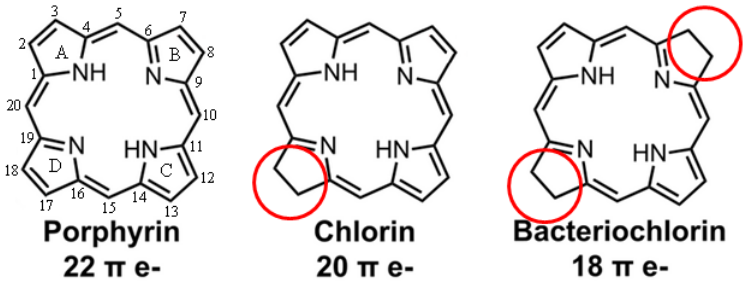

Figure 2.3: The porphyrin molecule and two derivatives, chlorin and bacteriochlorin. The conjugated π system of porphyrin involves 22 electrons and extends over all 20 carbon and 4 nitrogen atoms. The chlorin has a single bond between C7 and C8 while the bacteriochlorin has single bonds at C7-C8 and C17-C18 which means the conjugated π system does not extend over these atoms. Hydrogen atoms not shown.

2.1.2 Molecular Vibrations

The vibrational motion of each atomic bond can be treated as a quantum simple harmonic oscillator (SHO) (Hollas 2002; Harris & Bertolucci 1978). At low levels of vibration excitation, the SHO approximation is valid and the vibrational energy levels are evenly spaced with energies $E_v = \hbar\omega(v+½)$, while at higher vibrational levels the SHO approximation is not applicable (Hollas 2002; Harris & Bertolucci 1978). Additionally, complex motion of whole molecules can be decomposed into a superposition of normal modes (Harris & Bertolucci 1978) with each normal mode behaving approximately like a SHO (Harris & Bertolucci 1978). Each electronic configuration possesses its own set of vibrational levels which, within each electronic state, are orthogonal. Vibrational states between different electronic states are not orthogonal in general (Hollas 2002; Harris & Bertolucci 1978) and the overlap between them is defined as $S_{v,v'} = \int \psi_v \psi_{v'} d\tau_v$ (Franck-Condon factor, Figure 2.4) (Harris & Bertolucci 1978).

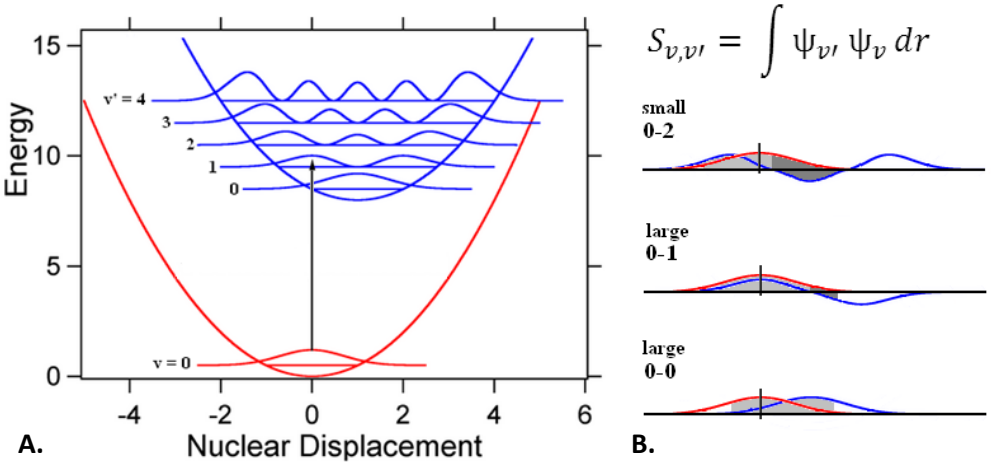

Figure 2.4: A- The vibrational wavefunctions (magnitude squared) associated with particular electronic states (red = ground, blue = 1st excited) are shown. **B** – $S_{v,v'}$ is the overlap integral of vibrational wavefunctions. Regions where the integral is positive are marked in light grey while regions were the integral is negative are marked in dark grey.

The magnitude of the overlap modulates the intensity of the elctronic transition. Figure 2.4 demonstrates this for absorption. The vertical transition from the electronic and vibrational ground state (v = 0) will have larger amplitude with the v' = 0 and v' = 1 than with the v' = 2 state due to the larger overlap.

2.1.3 State Transitions and Selection Rules

The probability of a transition occurring between states can be approximated using Fermi's Golden Rule:

$$P_{i\to f} = \frac{2\pi}{\hbar}|M|^2\rho(E_f)\,\delta(E_f - E_i)$$
$$M = \langle f|\boldsymbol{H}'|i\rangle$$

Equation 2.1

Where M is called the Transition Moment Integral (Harris & Bertolucci 1978), $\boldsymbol{H}'$ is the Interaction Hamiltonian (Harris & Bertolucci 1978), |f> and |i> represent the initial and final states of the system, and $\rho(E_f)$ is the density of final states at energy E_f. The delta function is to ensure conservation of energy.

If the rotation, vibration, electronic, and spin components of the system are uncoupled, then the total wavefunction may be factorized as $\varphi_{tot} = \varphi_r\,\varphi_v\,\varphi_e\,\varphi_s$. If it is assumed the system is interacting with an external electromagnetic field, the interaction Hamiltonian is $\mathbf{H' \sim \mu_n + \mu_e}$ (transition dipole for nuclear and electronic motions) and the transition moment integral can be factored as (Harris & Bertolucci 1978):

$$M = \int \varphi_{v'}\varphi_v d\tau_n \int \varphi_{e'}\hat{\mu}_e\varphi_e d\tau_e \int \varphi_{s'}\varphi_s d\tau_s$$

Equation 2.2

$$M = (FC) * (Orbital\ Symmetry) * (Spin)$$

Equation 2.3

Where rotational motion and the nuclear motion transition dipole have been neglected as these are only important for microwave, IR, and Raman spectroscopies.

If any of the factors in Equation 2.3 are zero, the transition is forbidden. In terms of relative strength, the spin selection rule is the strongest followed by orbital symmetry selections rules (Table 2.1) while the Franck-Condon factor (FC) modulates the transition probabilities by a small amount (see Figure 2.4) (Harris & Bertolucci 1978).

Table 2.1 Approximate expected absorption characteristics for spin and orbital symmetry selection rules. 'X' means the parameter is not relevant. Extinction coefficient values in (M^{-1} cm^{-1}) (Harris & Bertolucci 1978)

Spin selection rule	Orbital symmetry rule	Extinction coefficient (approx.)
Spin-forbidden	X	$10^{-5} – 1$
Spin-allowed	Orbital symmetry forbidden	$1 – 10^{3}$
Spin-allowed	Orbital symmetry allowed	$10^{3} – 10^{5}$

2.2 Porphyrin Physical and Electronic Structure

The physical structure of porphyrin is shown in Figure 2.3 (hydrogen atoms not shown). The macrocycle is approximately 1 nm in diameter and the conjugated π-system, containing 22 electrons, extends across all carbon and nitrogen atoms. Additionally, each nitrogen atom possesses a pair of non-bonding electrons facing the inner pocket of the porphyrin. These non-bonding electron pairs are vitally important for binding the metals present in many biologically important porphyrins and porphyrin derivatives (F. P. Dwyer 1964).

2.2.1 The Four Orbital Model

The electronic structure of porphyrin and related molecules can be described by application of the Gouterman Four Orbital Model. Of the MOs present, only the four frontier MOs (involving four electrons) are responsible for the optical properties of these molecules. These orbitals are the near degenerate HOMO and HOMO-1 (Highest Occupied Molecular Orbital) and doubly degenerate LUMO (Lowest Unoccupied Molecular Orbital) as seen in Figure 2.5.

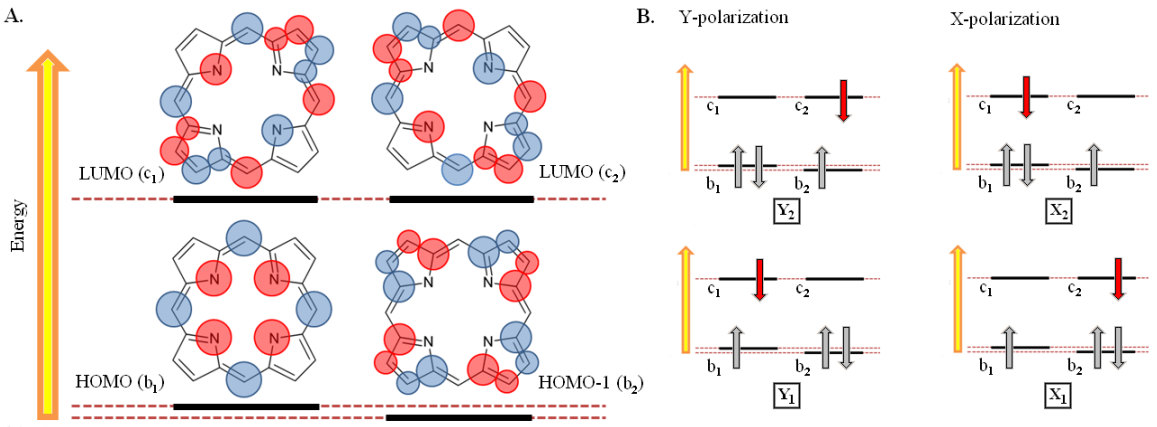

Figure 2.5: A - The four orbitals of the Gouterman Four Orbital Model. **B** – Single electron excited state configurations for each polarization.

The degeneracy of the LUMO (c_1 and c_2) and near degeneracy of the HOMO and HOMO-1 (b_1 and b_2) results in significant configuration interaction between the single electron excited state configurations. The ground state configuration is written as $b_2^{\,2}\ c_2^{\,0}\ b_1^{\,2}\ c_1^{\,0}$ (called $\mathbf{G_0}$ from here on), with the orbitals b_1 and b_2 occupied by two electrons each and c_1 and c_2 both empty. The four single electron excited states (Figure 2.5) are written as: $b_2^{\,2}\ c_2^{\,0}\ b_1^{\,1}\ c_1^{\,1}$ ($\mathbf{Y_1}$), $b_2^{\,1}\ c_2^{\,1}\ b_1^{\,2}\ c_1^{\,0}$ ($\mathbf{Y_2}$), $b_2^{\,1}\ c_2^{\,0}\ b_1^{\,2}\ c_1^{\,1}$ ($\mathbf{X_1}$), and $b_2^{\,2}\ c_2^{\,1}\ b_1^{\,1}\ c_1^{\,0}$ ($\mathbf{X_2}$). It must be noted that the configurations are constructed from Slater Determinants to

introduce proper electron anti-symmetry. Physically, while these configurations respect electron anti-symmetry, they neglect electron-electron Coulomb interactions and must be corrected, which is accomplished by applying configuration interaction (CI) theory for single excitations (CIS). Note that CIS, by Brillouin's theorem, cannot mix the ground state, G_0, with single excited state configurations (Bauche & Klapisch 1972), so the ground state will be ignored in the following calculation.

Looking at just the Y polarization, mixing between the Y_1 and Y_2 states results in a new wavefunction for the excited state:

$$\psi = c_1 Y_1 + c_2 Y_2$$

Equation 2.4

Where the coefficients c_1 and c_2 are found by solving the Schrodinger equation for the system:

$$\begin{bmatrix} H^{11} & H^{12} \\ H^{12} & H^{22} \end{bmatrix} \begin{bmatrix} c_1 \\ c_2 \end{bmatrix} = E_n \begin{bmatrix} c_1 \\ c_2 \end{bmatrix}$$

Equation 2.5

Where $H^{ij} = \langle Y_i | H | Y_j \rangle$, H^{11} and H^{22} are the $b_1 \rightarrow c_1$ and $b_2 \rightarrow c_2$ transition energies (Figure 2.5), and H^{12} is the interaction between Y_1 and Y_2. The solution gives two new states ($\psi_{\alpha,\beta}$) with energies and expansion coefficients:

$$E_{\alpha,\beta} = \frac{(H^{11} + H^{22}) \mp \sqrt{(H^{11} - H^{22})^2 + 4(H^{12})^2}}{2}$$

$$[c_1, \quad c_2]_{\alpha,\beta} = \left[\frac{(H^{11} + H^{22}) \mp \sqrt{(H^{11} - H^{22})^2 + 4(H^{12})^2}}{H^{12}}, \quad 1 \right]$$

Equation 2.6

2.2.2 Special Cases of the Four Orbital Model

It is instructive to define the quantity $\Delta \equiv (H^{11} - H^{22})$ and expand the square roots in Equation 2.6 in terms of Δ for two limiting cases (all terms of order Δ^2 or higher were dropped).

Case one: $\Delta/H^{12} \ll 1$ (i.e. small Δ)

$$E_\alpha \approx \tfrac{1}{2}(H^{11} + H^{22}) - H^{12} \qquad [c_1, \quad c_2]_\alpha = \left[-1 - \frac{\Delta}{2H^{12}}, \quad 1\right]$$

$$E_\beta \approx \tfrac{1}{2}(H^{11} + H^{22}) + H^{12} \qquad [c_1, \quad c_2]_\beta = \left[+1 - \frac{\Delta}{2H^{12}}, \quad 1\right]$$

Equation 2.7

Case two: $H^{12}/\Delta \ll 1$ (i.e. large Δ)

$$E_\alpha \approx H^{11} - \frac{(H^{12})^2}{\Delta} \qquad [c_1, \quad c_2]_\alpha = \left[1, \quad -\frac{H^{12}}{\Delta}\right]$$

$$E_\beta \approx H^{22} + \frac{(H^{12})^2}{\Delta} \qquad [c_1, \quad c_2]_\beta = \left[+\frac{H^{12}}{\Delta}, \quad 1\right]$$

Equation 2.8

Case one most closely corresponds to the simple porphyrin molecule with its high symmetry and degenerate MOs. With $H^{11} \approx H^{22}$ the excited state energies experience a large amount of splitting, approximately $2H^{12}$, while the excited state configurations consist of a near 1:1 mixture of the amplitudes of the Y_1 and Y_2 configurations. Even though both the α and β states consist of near equal mixtures of Y_1 and Y_2, the low energy state (α) has a ~180º phase difference between the Y_1 and Y_2 components while

the high energy state (β) has ~0º phase difference. The phase differences manifest themselves in the dipole moments of the α and β transitions. The transition dipole moment, μ, is defined as (van Amerongen et al. 2000):

$$\vec{\mu} = e\langle f|\vec{\boldsymbol{r}}|i\rangle$$
$$d = |\vec{\mu}|^2$$

Equation 2.9

Where d is the oscillator strength. Plugging $\langle \boldsymbol{\alpha}| = \frac{1}{\sqrt{2}}(-\langle \boldsymbol{Y_1}| + \langle \boldsymbol{Y_2}|)$ and $\langle \boldsymbol{\beta}| = \frac{1}{\sqrt{2}}(\langle \boldsymbol{Y_1}| + \langle \boldsymbol{Y_2}|)$ for $\langle \boldsymbol{f}|$ into Equation 2.9 and letting $|i\rangle$ be the ground state yields:

$$\vec{\mu}_\alpha = \frac{e}{\sqrt{2}}(-\langle Y_1|\vec{\boldsymbol{r}}|i\rangle + \langle Y_2|\vec{\boldsymbol{r}}|i\rangle) = \frac{1}{\sqrt{2}}(-\vec{\mu}_1 + \vec{\mu}_2) \approx \vec{0}$$
$$\vec{\mu}_\beta = \frac{e}{\sqrt{2}}(\langle Y_1|\vec{\boldsymbol{r}}|i\rangle + \langle Y_2|\vec{\boldsymbol{r}}|i\rangle) = \frac{1}{\sqrt{2}}(\vec{\mu}_1 + \vec{\mu}_2) \approx \sqrt{2}\,\vec{\mu}$$

Equation 2.10

In the limiting case of $\boldsymbol{\mu_1} = \boldsymbol{\mu_2}$, the oscillator strength for the α transition is zero ($D_\alpha = 0$) while for the β transition the oscillator strength is doubled ($D_\beta = 2|\boldsymbol{\mu}|^2$).

Case two best corresponds to the bacteriochlorin molecules with their significantly reduced symmetry (see Figure 2.3). With $H^{11} \gg H^{22}$ or $H^{12} \approx 0$ the transition energies experience only minor shifts from their original values and the excited state configurations mix only slightly. Using the α and β expansion coefficients from case two (Equation 2.8), we arrive at the following dipole moments for the low and high energy transitions (where $N = (1 + (H^{12}/\Delta)^2)^{-\frac{1}{2}}$):

$$\vec{\mu}_\alpha = Ne\left(\langle Y_1|\vec{\boldsymbol{r}}|i\rangle - \frac{H^{12}}{\Delta}\langle Y_2|\vec{\boldsymbol{r}}|i\rangle\right) = N\left(\vec{\mu}_1 - \frac{H^{12}}{\Delta}\vec{\mu}_2\right) \approx \vec{\mu}_1$$
$$\vec{\mu}_\beta = Ne\left(\frac{H^{12}}{\Delta}\langle Y_1|\vec{\boldsymbol{r}}|i\rangle + \langle Y_2|\vec{\boldsymbol{r}}|i\rangle\right) = N\left(\frac{H^{12}}{\Delta}\vec{\mu}_1 + \vec{\mu}_2\right) \approx \vec{\mu}_2$$

Equation 2.11

Thus the oscillator strengths of these two transitions are unchanged in the limiting case of $H^{12}/\Delta = 0$.

Vibrations can modify the molecular symmetry and partially reduce the forbidden nature of a transition, this can be clearly seen in the Q-band absorption of a symmetric metallo-porphyrin where the (0-1') transition is more intense than the (0-0') transition (Harris & Bertolucci 1978). The saturation of the C7-C8 bond in chlorins and C7-C8 & C17-C18 bonds in bacteriochlorins removes the degeneracy of the LUMO and near degeneracy of the HOMO and HOMO-1 resulting in significantly reduced configuration interaction and strongly allowed Q transitions (Gouterman 1961; Gouterman et al. 1963; Adar 1978).

Being eigenfunctions of the molecular Hamiltonian (H_0) these MOs (ψ_n = b_1, b_2, c_1, c_2) represent stationary states with time evolution of the form: $\psi_n(t) \sim \exp\left(-i\, {E_n}/{\hbar}\, t\right)$. If an external perturbation is applied, e.g. an oscillating electric field, the system Hamiltonian becomes H' = H_0 + V_{ext} and the MOs must now be constructed from a linear combination of the previous eigenfunctions (ψ_n) using perturbation theory. This mixing causes beating between the eigenfunctions of the original Hamiltonian resulting in the electron density oscillating with a frequency of $(E_{LUMO} - E_{HOMO})$ / ħ. It is this oscillating electron density that gives rise to the electric transition dipole moment and the oscillation frequency defines the excitation wavelength.

2.3 Fate of the Excited State

2.3.1 Intra-Molecular Transitions

An atom or molecule can become excited by a number of means including collisions, energy transfer, chemical changes, or photon absorption ('A' Figure 2.6). Once a molecule is in an excited state, it will return to the ground state through a variety of mechanisms. Intra-molecular transitions (i.e. transition happening within a single molecule) include vibrational relaxation (R), internal conversion (IC), fluorescence (F), intersystem crossing (ISC), and phosphorescence (P) (Figure 2.6) as well as a few others not mentioned here.

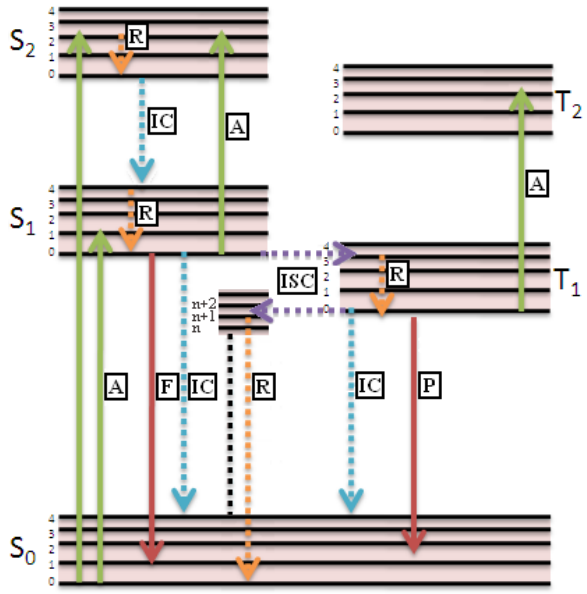

Figure 2.6: (A) - Absorption. (F) – Fluorescence. (P) – Phosphorescence.
(R) - Vibrational relaxation. (IC) - Internal Conversion. (ISC) - Intersystem Crossing .

Vibrational relaxation is the rapid (10^{-11} – 10^{-9} s) (Harris & Bertolucci 1978) transition between the vibrational levels of a single electronic state until reaching the ground or thermally populated vibrational states. Energy is given up to other vibrational

modes (for large molecules) or to solvent molecules via collisions (Harris & Bertolucci 1978). Internal conversion is a spin-conserving, iso-energetic, non-radiative transition between different electronic states (Harris & Bertolucci 1978). It occurs between the vibrational ground state of an electronic excited state and an excited vibrational state of a lower electronic state, for example between $S_{1,v'=0}$ and $S_{0,v=n}$ where $n > 0$ (Figure 2.4 and Figure 2.6). Vibrational relaxation then brings the molecule to the vibrational ground state. Fluorescence is a rapid (<10ns for (B)Chls (Niedzwiedzki & Blankenship 2010)), spin-allowed, spontaneous radiative transition between electronic states. The fluorescence emission spectrum approximately mirrors the absorption spectrum for the lowest lying electronic transition, although it is not exactly mirror symmetric (Figure 2.7). The fluorescence typically experiences a Stokes shift (the absorption 0-0 transition (Figure 2.4) occurring at a higher energy compared to the fluorescence 0-0 transition (Figure 2.7)) and different relative intensities of vibrationally excited transitions (see inset Figure 2.7). These are due to changes in nuclear equilibrium positions between the electronic ground and excited states and solvent shell / solid matrix reorganization altering the ground and excited state energy levels and the vibrational couplings (Harris & Bertolucci 1978). Intersystem crossing is an iso-energetic, non-radiative transition between states of differing spin multiplicity. It occurs between the vibrational ground state of an electronic excited state and an excited vibrational state of an electronic state with different multiplicity, for example between $S_{1,v'=0}$ and $T_{1,v=n}$ where $n > 0$ (Figure 2.6). Phosphorescence is the radiative transition between states of different spin multiplicity, for example and $T_{1,v'=0}$., $S_{0,v=n}$ where $n \geq 0$.

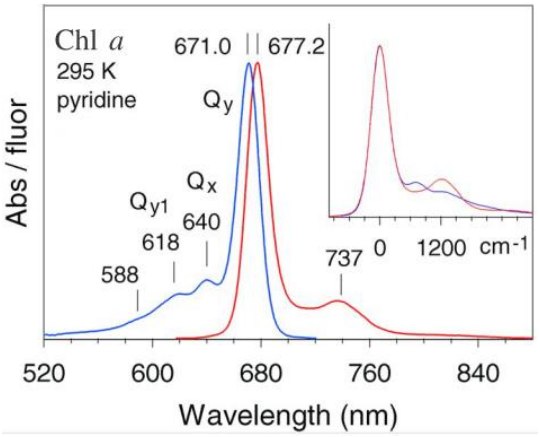

Figure 2.7: Absorption and fluorescence spectra for Chl *a* showing the Stokes shift and approximate mirror symmetry between the fluorescence and Q_y abs band. The insets show the overlap of the absorption and emission spectra in the transition dipole moment representation (Rätsep et al. 2009).

2.3.2 Relativity and Spin-Orbit Coupling

Being transitions between states of different multiplicity, ISC and phosphorescence must rely on relativistic effects to break the spin selection rule (Table 2.1) (Fontana & Meath 1968; Marian 2012). These relativistic effects can be treated as a perturbation in typical organic molecules and can be understood by examining the Breit-Pauli Hamiltonian (Fontana & Meath 1968):

$$\boldsymbol{H} = \boldsymbol{H_{mol}} + \alpha^2 \boldsymbol{H_{rel}}$$

Equation 2.12

Where H_{mol} = non-relativistic molecular Hamiltonian and α = fine structure constant. While H_{rel}, relativistic Hamiltonian, can be broken down into:

$$\boldsymbol{H_{rel} = H_{LL} + H_{SS} + H_{SL} + H_P + H_D}$$

Equation 2.13

Where, $\mathbf{H_{LL}}$ = orbit-orbit coupling, $\mathbf{H_{SS}}$ = spin-spin coupling, $\mathbf{H_{SL}}$ = spin-orbit coupling, $\mathbf{H_P}$ = relativistic mass correction, and $\mathbf{H_D}$ = "Darwin term" from Dirac theory. Only the

spin-orbit term is important for understanding ICS and phosphorescence in molecules like (B)Chl, so the other terms will be ignored. It should be noted that spin-spin coupling is important when paramagnetic species are present, however, since natural (B)Chls contain Mg^{2+} (occasionally Zn^{2+}) which is not paramagnetic, one need not consider spin-spin interactions.

The spin-orbit coupling (SOC) Hamiltonian has the form:

$$H_{SL} = \frac{1}{2}\sum_{\beta,j}\frac{Z_\beta}{r_{j\beta}^3}(\hat{r}_{j\beta}\times\hat{p}_j)\bullet\hat{s}_j - \frac{1}{2}\sum_{k\neq j}\frac{1}{r_{jk}^3}[(\hat{r}_{jk}\times\hat{p}_j)\bullet\hat{s}_j - 2\cdot(\hat{r}_{jk}\times\hat{p}_k)\bullet\hat{s}_j]$$

Equation 2.14

Where the first term is the result of the electrons orbiting in the field of the nuclei (with charge 'Z') while the second term is the result of electrons orbiting in the field of the other electrons. Many authors refer to only the first term while ignoring the second when discussing SOC, which is not even approximately correct as demonstrated by the triplet state lifetimes of Pheophytin *a* (Pheo *a*, a Chl *a* molecule lacking the central Mg^{2+} ion), Mg-Pheo *a* (Chl *a*), Zn-Pheo *a*, and Pt-Pheo *a* (Drzewiecka-Matuszek et al. 2005). The (argon purged) room temperature triplet state lifetimes of Pheo *a*, Mg-Pheo *a*, Zn-Pheo *a* vary at most by a factor of two with no dependence on Z, while the triplet state lifetime of Pt-Pheo *a* is consistently over a factor of ten shorter. This indicates that the presence nuclei up to Z=30 (i.e. Zn) have little effect on SOC in the experimental conditions used by Drzewiecka- Matuszek et al.

The effect of the relativistic perturbation is to cause a mixing of the singlet and triplet eigenfunctions of the non-relativistic Hamiltonian. The new eigenfunctions of the perturbed system contain contributions from multiple singlet and triplet state orbitals as

well as some non-bonding (n) orbitals. For example, the singlet ground state becomes (Hameka 1967):

$$^1\Phi_0 = {}^1\Psi_0 - \sum_{k\neq 0} \frac{\langle {}^1\Psi_k | H_{SL} | {}^1\Psi_0 \rangle {}^1\Psi_k}{({}^1E_k - {}^1E_0)} - \sum_n \sum_{i=-1,0,1} \frac{\langle {}^3\Psi_{n,i} | H_{SL} | {}^1\Psi_0 \rangle {}^3\Psi_{n,i}}{({}^3E_n - {}^1E_0)}$$

Equation 2.15

Where the first term is the original singlet ground state while the second term corresponds to mixing with other singlet states ($^1\Psi_k$) and the third term is mixing with the triplet states ($^3\Psi_n$). The excited singlet and triplet states are similarly mixed (Hameka 1967).

The apparent spin non-conserving transitions are actually taking place from the singlet character of the triplet state or the triplet character of the singlet state with the "extra" unit of angular momentum coming from or going to the orbital momentum. Time dependent density functional theory calculations (TD-DFT) predict the major contribution to the phosphorescence emission dipole moment in free-base porphyrins comes from an out of plane (i.e. perpendicular to the macrocycle) n→π* singlet-singlet transition (Minaev 2004). However, little experimental data exist on the exact nature of the phosphorescence dipole moment (Minaev 2004).

2.3.3 Inter-Molecular Energy Transfer

Energy can be transferred between different molecules in a number of ways. Perhaps the simplest is radiative energy transfer, which is the emission of a photon by one molecule followed by the absorption of the photon by another molecule. There also exist non-radiative energy transfer, which relies on direct coupling between two

molecules and not an intermediate photon to carry the energy. These processes can involve transfer of the excited state, electron exchange, net transfer of charge, or even chemical reactions that modify structure. Only the excited state transfer and electron exchange mechanisms will be discussed here.

If two molecules (one in the excited state, the donor "D", and one in the ground state, the acceptor "A") are allowed to interact, then there is a probability of energy transfer between them which can be examined in terms of Fermi's Golden Rule (Equation 2.1) (Dexter 1953). The fully anti-symmetric initial and final states, |i> and |f>, are (Dexter 1953):

$$|i\rangle = \frac{1}{\sqrt{2}}(|D'(r_1)\rangle|A\,(r_2)\rangle - |D'(r_2)\rangle|A\,(r_1)\rangle)$$
$$|f\rangle = \frac{1}{\sqrt{2}}(|D\,(r_1)\rangle|A'(r_2)\rangle - |D\,(r_2)\rangle|A'(r_1)\rangle)$$

Equation 2.16

If **H'**, the interaction Hamiltonian (Equation 2.1), acts only on the spatial components and not the spin components, then the wavefunctions in Equation 2.16 can be factored as:

$$|D'(r_1)\rangle = |\varphi'_D(r_1)\rangle|D'_1\rangle$$
$$|A(r_2)\rangle = |\varphi_A(r_2)\rangle|A_2\rangle$$

Equation 2.17

These equations correspond to electron one in excited state of D and electron two in ground state of A. There are eight total of these equations, one for each combination of electron, molecule, and electronic state, they will not all be written out. Substituting Equation 2.16 and Equation 2.17 into M from Equation 2.1 and factoring out the spin components yields (Dexter 1953):

$$M = \int ([\varphi'_D(r_1)\varphi_A(r_2)\ \boldsymbol{H_I}\ \varphi_D(r_1)\varphi'_A(r_2)][\langle D'_1|D_1\rangle\langle A_2|A'_2\rangle] - [\varphi'_D(r_1)\varphi_A(r_2)\ \boldsymbol{H_I}\ \varphi_D(r_2)\varphi'_A(r_1)][\langle D'_1|A'_1\rangle\langle D_2|A_2\rangle])d\tau$$

Equation 2.18

The first term of Equation 2.20 can be recognized as the Foerster Resonant Energy Transfer (FRET) mechanism while the second term of the integral can be recognized as the Dexter electron exchange mechanism.

2.3.4 Foerster Resonant Energy Transfer

The FRET component of Equation 2.18 is:

$$\int ([\varphi'_D(r_1)\varphi_A(r_2)\ \boldsymbol{H_I}\ \varphi_D(r_1)\varphi'_A(r_2)][\langle D'_1|D_1\rangle\langle A_2|A'_2\rangle])d\tau$$

Equation 2.19

Examining just the spin component of the Foerster term reveals that the spin of each molecule (donor and acceptor) must be individually conserved since:

$$\langle D'_1|D_1\rangle = \delta_{D',D}$$
$$\langle A_2|A'_2\rangle = \delta_{A',A}$$

Equation 2.20

That is, the spin of electron one in the ground and excited states of D (A) must be the same (Dexter 1953). This energy transfer process can occur between molecules of any spin multiplicity provided the intra-molecular transitions involved are spin-allowed (Hofkens et al. 2003).

If it is assumed that the interaction Hamiltonian, $\mathbf{H_I}$, is Coulombic:

$$V_I = \sum_{i\in D, j\in A}^{All\ pairs} q_i q_j / r_{ij}$$

Equation 2.21

(where $\mathbf{H_I}$=$\mathbf{V_I}$), then the spatial component of the Foerster term can be expanded in terms of a multi-pole expansion, $V_I = \sum_{n=1}^{\infty} \frac{V_n}{R^n}$, where V_n = multi-pole moment of order 'n' (Struve 1995; Dexter 1953). Since the interacting molecules are neutral, the lowest order non-zero term of the multi-pole expansion will be the dipole-dipole term (n = 3). Using only the dipole-dipole term is valid in the weak coupling limit, strongly coupled cases must either use higher order terms or a different calculation method. The dipole-dipole term is (Struve 1995; Dexter 1953):

$$V_I \approx \frac{\mu_{\boldsymbol{D}} \bullet \mu_{\boldsymbol{A}} - 3\left(\mu_{\boldsymbol{D}} \bullet \widehat{\boldsymbol{R}}\right)\left(\mu_{\boldsymbol{A}} \bullet \widehat{\boldsymbol{R}}\right)}{R^3} = \frac{\mu_D \mu_A}{R^3}\kappa$$

Equation 2.22

Where R = center to center separation of D and A while κ, the orientation factor, is defined as (Struve 1995):

$$\kappa = \left[\hat{\mu}_{\boldsymbol{D}} \bullet \hat{\mu}_{\boldsymbol{A}} - 3\left(\hat{\mu}_{\boldsymbol{D}} \bullet \widehat{\boldsymbol{R}}\right)\left(\hat{\mu}_{\boldsymbol{A}} \bullet \widehat{\boldsymbol{R}}\right)\right]$$

Equation 2.23

Thus, not only does FRET depend on the pigment-pigment separation distance, it also depends on the relative orientation of the interacting molecules. Plugging this expression for V_I into the first term of Equation 2.18 and Fermi's Golden Rule, Equation 2.1, gives (Struve 1995; Dexter 1953):

$$P_{i\to f} = \frac{2\pi}{\hbar}\left|\int \varphi'_D(r_1)\varphi_A(r_2)\,\frac{\mu_D\mu_A}{R^3}\kappa\,\varphi_D(r_1)\varphi'_A(r_2)\,dr_1dr_2\right|^2 \delta(E_f - E_i)$$

Equation 2.24

Rearranging yields:

$$P_{i\to f} = \frac{2\pi}{\hbar}\frac{\kappa^2}{R^6}\left|\int \varphi'_D(r_1)\,\mu_D\,\varphi_D(r_1)\,dr_1\right|^2\left|\int \varphi_A(r_2)\mu_A\varphi'_A(r_2)dr_2\right|^2 \delta(E_f - E_i)$$

$$P_{i\to f} = \frac{2\pi}{\hbar}\frac{\kappa^2}{R^6}|M_D|^2|M_A|^2\,\delta(E_f - E_i)$$

Equation 2.25

The above expression is the transition probability at a specific energy and orientation for one initial and one final state. To obtain a total probability, one must integrate over all possible orientations and energies and over all initial and final states. For a chromophore coupled to environmental vibrations, the initial and final state energies (of each chromophore) are not well defined and we must introduce a probability factor for finding the molecule in a particular energy state, $p(\varepsilon)$ (Dexter 1953).

$$P_{I\to F} = \frac{2\pi}{\hbar}\frac{\kappa^2}{g'_D g_A R^6}\int d\varepsilon'_A\int d\varepsilon_D\int d\varepsilon_A\,p_A(\varepsilon_A)|M_A|^2\int d\varepsilon'_D\,p'_D(\varepsilon'_D)|M_D|^2\,\delta(E_f - E_i)$$

Equation 2.26

Where g'_D (g_A) is the degeneracy of the excited (ground) state of D (A). The integrals, $\int p'_D(\varepsilon'_D)d\varepsilon'_D|M_D|^2$ and $\int p_A(\varepsilon_A)d\varepsilon_A|M_A|^2$, can be related to the emission and absorption spectra by the Einstein A and B coefficients. It can be shown that the probability for an excited atom (in this case the donor 'D') to spontaneously emit a photon with energy E is proportional to the Einstein A coefficient (Struve 1995):

$$A_D(E) = \frac{4E^3n^3}{3\hbar^4c^3g_D'}\left(\int p_D'(\varepsilon_D')d\varepsilon_D'|M_D|^2\right)$$

Equation 2.27

While the probability for an atom (the acceptor 'A') to absorb a photon with energy E is proportional to the Einstein B coefficient (Struve 1995):

$$B_A(E) = \frac{2\pi}{3\hbar^2 g_A}\left(\int p_A(\varepsilon_A)d\varepsilon_A|M_A|^2\right)$$

Equation 2.28

The Einstein A coefficient is related to the radiative lifetime, τ_0, and normalized emission spectrum, $f(E)$, by (Struve 1995; Dexter 1953):

$$A_D(E) = \frac{1}{\tau_{D,0}} f_D(E)$$

Equation 2.29

The Einstein B coefficient is related to the absorption cross section, $\sigma(E)$, by (Struve 1995):

$$B_A(E) = \frac{c}{nhE}\sigma_A(E)$$

Equation 2.30

Substituting these expressions into Equation 2.26, integrating, and setting $E = (\varepsilon_A' - \varepsilon_A) = (\varepsilon_D' - \varepsilon_D)$ yields (Struve 1995):

$$P_{I\to F} = \frac{9}{8\pi}\frac{\hbar^4c^3\kappa^2\varphi_D}{n^4R^6\tau_D}\int dE\ \frac{f_D(E)\sigma_A(E)}{E^4} \equiv \frac{3}{2}\frac{\kappa^2}{\tau_D}\left(\frac{R_0}{R}\right)^6$$

Equation 2.31

Averaging over all orientations yields the usual Foester rate equation (Struve 1995):

$$k_{I\to F} \equiv \frac{1}{\tau_D}\left(\frac{R_0}{R}\right)^6$$

Equation 2.32

Where R_0 is defined as the Foerster critical radius, that is, the distance at which the FRET efficiency is half its maximum value. This value is typically in the 1-10 nm range though its exact value depends on the particular donor and acceptor molecules involved and their environment.

2.3.5 Dexter Electron Exchange Mechanism

The Dexter electron exchange component of Equation 2.18 is:

$$\int ([\varphi'_D(r_1)\varphi_A(r_2)\, \boldsymbol{H_I}\, \varphi_D(r_2)\varphi'_A(r_1)][\langle D'_1|A'_1\rangle\langle D_2|A_2\rangle])d\tau$$

Equation 2.33

Examining just the spin component of the Dexter exchange mechanism reveals that the spin of each electron must be preserved, but the spin state of the molecules involved may interchange.

$$\langle D'_1|A'_1\rangle = \delta_{D(1)',A(1)'}$$

$$\langle A_2|D_2\rangle = \delta_{A(2),D(2)}$$

Equation 2.34

That is, before and after exchange, the excited states of D and A must have the same spin and the ground states of D and A must have the same spin. Thus the spin state of D will transfer to A and vice versa. This energy transfer mechanism can occur between

molecules of the same or different spin-multiplicity provided there is no net transfer of charge.

The Dexter exchange mechanism is more difficult to analyze in the same detail as the FRET mechanism due to the need to work directly with the molecular orbitals even in the first order approximation (Dexter 1953). However, some general approximations can be made. If the singlet-triplet absorption and triplet-singlet emission (phosphorescence) processes are dominated by the SOC mechanism described earlier (as opposed to spin-orbit-vibronic coupling (Struve 1995)), then the triplet-triplet energy transfer rate can be described by (Struve 1995; Dexter 1953):

$$k_{I\to F} = \frac{2\pi}{\hbar}\frac{e^4}{g_D' g_A}\left|\int \varphi_D'(r_1)\varphi_A(r_2)\frac{1}{r_{12}}\varphi_D(r_2)\varphi_A'(r_1)\right|^2 \int f_D(E)F_A(E)dE$$

Equation 2.35

Where $f_D(E)$ is the normalized phosphorescence spectrum of the donor, $F_A(E)$ is the normalized $S_0 \rightarrow T_1$ absorption spectrum of the acceptor (Struve 1995), and the center integral of Equation 2.35 can be represented as (Dexter 1953):

$$\frac{e^4}{g_D' g_A}\left|\int \varphi_D'(r_1)\varphi_A(r_2)\frac{1}{r_{12}}\varphi_D(r_2)\varphi_A'(r_1)\right|^2 \approx Y\frac{e^4}{{R_0}^2}exp\left(\frac{-2R}{L}\right)$$

Equation 2.36

Where Y is a dimensionless parameter (<< 1) depending on the oscillatory behavior of the wavefunctions (i.e. how oscillations tend to cancel during integration), R_0 is the center to center separation of the donor and acceptor, and L is a parameter on the order of the size of D and A (i.e. the effective Bohr radius of the excited and ground states of D and A) (Dexter 1953).

Thus the Dexter exchange mechanism, while not dependent on the relative orientations of D and A, is effective only over short distances comparable to the molecular sizes of the chromophors, i.e. a few angstrom.

2.4 Excitonic Interactions.

Molecular excitons occur when the electronic state of a molecule is coupled with the electronic state of the neighboring molecules, typically in photosynthetic systems the coupling of an excited state with a ground state. Electrostatic force is the dominant interaction that gives rise to the coupling between molecules and has the form of Equation 2.21 which, in the case of spin allowed transition of neutral molecules, can be approximated as the dipole-dipole interaction term (Equation 2.22) in the weak coupling limit, while in the case of spin-forbidden transitions of neutral molecules, the coupling must be evaluated directly from the Hamiltonian. For these coupled systems, the Hamiltonian is (Savikhin, Buck, et al. 1999):

$$H = \sum_{i=1}^{N} \left(H_i + \sum_{j=1}^{N} V_{ij} \right)$$

Equation 2.37

In matrix form (van Amerongen et al. 2000):

$$H_{ij} = \delta_{ij} H_i + V_{ij}$$

Equation 2.38

Where H_i is the molecular Hamiltonian for the i'th monomer and V_{ij}, for $i \neq j$, is the interaction energy (i.e. the coupling) between molecules i and j which for the case of a dimer has the form of Equation 2.18. For i = j, V_{ij} it is the displacement of the i'th excited state energy level (displacement energy / site energy offset). The eigenstates for the coupled system can be constructed out of the eigenstates of the monomeric system using the following basis (van Amerongen et al. 2000):

$$|n\rangle = \left||\psi_1\rangle, \cdots, |\psi_n'\rangle, \cdots, |\psi_N\rangle\right|$$

Equation 2.39

Where $|n\rangle$ is a Slater determinant of ground state spin-orbitals, $|\psi_j\rangle$, with $|\psi_n'\rangle$ corresponding to the excited state of molecule 'n'. The eigenstates of Equation 2.37 then have the form:

$$|\Psi\rangle = \sum_{n=1}^{N} c_n |n\rangle$$

Equation 2.40

Where the expansion coefficients, the c_n's, are found by solving the system's Schroedinger equation as was done with Equation 2.5. For a system of N pigments, the Hamiltonian will always have N solutions composed of superposition of the original N pigment states. Thus excitonic coupling cannot increase or decrease the number of electronic transitions of a pigment system.

The transition dipole moment for a particular excitonic excitation, say E_α, can be calculated using the expansion coefficients of the eigenstate, $|\Psi_\alpha\rangle$, and the dipole

moments for each individual pigment involved in the exciton (van Amerongen et al. 2000):

$$\boldsymbol{\mu_\alpha} = \sum_{n=1}^{N} c_{\alpha,n}\boldsymbol{\mu_n}$$

Equation 2.41

It should be noted that the sum of the oscillator strengths of the excitonic system, $D_\alpha=|\boldsymbol{\mu_\alpha}|^2$, is equal to the sum of the oscillator strengths, d_n (Equation 2.9), of the individual pigments, i.e.:

$$\sum_{\alpha=1}^{N} D_\alpha = \sum_{n=1}^{N} d_n$$

Equation 2.42

Thus excitonic coupling cannot increase the integrated absorbance of a set of pigments, rather it can only change the relative intensities and energies of the electronic transitions (van Amerongen et al. 2000).

2.5 Molecular Coupling

As stated in the previous section, the intermolecular coupling is given by the off diagonal terms of the Hamiltonian, Equation 2.38 ($V_{i,j\neq i}$), which contain the following components for the singlet (V_S) and triplet (V_T) couplings (You & Hsu 2010):

$$V_S = V_{coul} + V_{exch} + V_{ovlp}$$

$$V_T = V_{exch} + V_{ovlp}$$

Equation 2.43

Where V_{coul} is the Coulomb term (Equation 2.19), V_{exch} is the exchange term (Equation 2.33), and V_{ovlp} is the overlap integral given by (You & Hsu 2010; Hsu et al. 2001):

$$V_{ovlp} = \omega_0 \int \varphi'_D(r)\varphi_D(r)\varphi_A(r)\varphi'_A(r)\, dr$$

Equation 2.44

Where $\omega_0$is the transition frequency (You & Hsu 2010).

For singlet state coupling, when the intermolecular distance is large (a nanometer or more) the contributions from the exchange and overlap are negligible. With triplet state coupling, both the exchange (the Dexter component) and the overlap contribute to the coupling and neglecting the contribution of the overlap term results in an underestimate of the triplet coupling (You & Hsu 2010).

2.6 Optical Signals.

2.6.1 Rates of Absorption and Emission

Optical signals are used to probe a number of properties of molecular systems such as state energies (both vibrational and electronic), excited state energy transfer among molecules, and chemical changes such as electron transfer. The energies of electronic states are often determined by the absorption or emission of photons via absorption, fluorescence, or phosphorescence spectroscopy, although, transitions that are optically forbidden or that experience spectral interference from other emitters or

absorbers can require more sophisticated techniques to study (for an example, see (Polívka & Sundström 2004) for the determination of the carotenoid S_1 state).

The probability of an atom or molecule absorbing a photon and transitioning from state 1 to state 2 is related to the Einstein B_{12} coefficient which is given by Equation 2.28. This Einstein coefficient is related to two others, the A_{21} coefficient (Equation 2.27) which describes spontaneous emission of a photon and the B_{21} coefficient which describes the stimulated emission of a photon. The three Einstein coefficients are related by the following (Hilborn 2002):

$$B_{21} = \left(\frac{\pi^2 \hbar^2 c^3}{E_{21}^3}\right) A_{21}$$

$$B_{12} = \left(\frac{g_2}{g_1}\right) B_{21}$$

Equation 2.45

Where $E_{21}$is the state 2 to state 1 transition energy and $g_1$and $g_2$are the degeneracies of states 1 and 2 respectively. These quantities are directly related to the rates of photon emission and absorption by (Hilborn 2002):

$$W_{21}^{Sp.E.} = A_{21} N_2$$

$$W_{12}^{A} = B_{12} \rho_E N_1$$

$$W_{21}^{S.E.} = B_{21} \rho_E N_2$$

Equation 2.46

Where $W_{21}^{Sp.E.}$, W_{12}^{A}, and $W_{21}^{S.E.}$ are the rates (units s^{-1}) of spontaneous emission, absorption, and stimulated emission respectively, N_1 and N_2 are ground and excited state

populations respectively and $\rho_E$is the energy density per unit ħω (i.e. the photon density at energy E=ħω) in the volume containing N_1 or N_2 (Hilborn 2002). Each coefficient depends on the transition dipole moment through the oscillator strength (Equation 2.27, Equation 2.28), thus the Einstein coefficients (Equation 2.45) and their corresponding rates (Equation 2.46) are wavelength dependent.

The absorbance (A) of a sample is defined in terms of incident (I_0) and transmitted (I) light intensity after passing through the sample and is related to the absorption rate, W_{12}^A, given by Equation 2.46:

$$A = \varepsilon cl = -log_{10}\left(\frac{I}{I_0}\right)$$

Equation 2.47

Where A = εcl is the Beer-Lambert Law with 'ε' being the molar extinction coefficient, 'c' the chromophore molar concentration, and 'l' the optical path-length. It's clear that $\varepsilon \sim B_{12}$, and since B_{12} depends on the transition dipole moment (|M|, Equation 2.28), the absorption spectrum can function as a probe of the transition moment allowing assessment of both the transition energy and strength. Transitions with little to no dipole moment will have little to no absorbance (e.g. $S_0 \rightarrow T_1$ transition in (B)Chl, Figure 2.6). It's also clear that $c \sim N_1$, so processes that increase or decrease the absorbing state populations will correspondingly increase or decrease the sample absorbance. Thus the absorption can function as a probe of the population dynamics of the absorbing states, for both excited and ground states.

The emission of light from a sample, either fluorescence or phosphorescence, is related to $W_{21}^{Sp.E.}$ and $W_{21}^{S.E.}$ (Equation 2.46). Spontaneous emission, $W_{21}^{Sp.E.}$, depends primarily on the excited state population, N_2, and the transition dipole strength through A_{21} (see Equation 2.27). Thus states with low dipole strength and states with low population (or that become depopulated quickly with respect to the emission lifetime) will have little emission intensity (e.g. emission from the (B)Chl T_1 and S_2 states). Conversely, states that are well populated and have a large transition dipole moment will emit significant radiation. Stimulated emission, $W_{21}^{S.E.}$, depends on the same transition dipole moment and excited state populations as spontaneous emission, however, the rate of stimulated emission also depends on the intensity of external radiation. High excited state populations with high radiation intensity can result in significant stimulated emission; this can result in spectral distortion when spontaneous emissions from the sample are amplified by stimulated emission (amplified spontaneous emission, ASE). When coupled with optical feedback this process forms the basis of a laser. For transitions with little to no dipole moment (e.g. (B)Chl phosphorescence), there will be little to no stimulated emission. Since both spontaneous and stimulated emission depend on the excited state populations as well as the transition dipole moments, they can function as probes of excited state properties and population dynamics.

2.6.2 Excited State Population Dynamics

As discussed above and in section 2.3, an excited molecule has a number of deactivation pathways available to it (e.g. fluorescence, ISC, FRET, Dexter exchange, etc) with each pathway having a probability associated with it. If this molecule or

molecular system is part of a large collection of identical systems (i.e. an ensemble), then these transition probabilities become rates at which the various excited state populations will evolve. The time rate of change of a particular population can be expressed as the sum of the number of excitations entering this state from other states and the number of excitation leaving this state for other states (per unit time):

$$\dot{N}_x = \sum_n k_{nx} N_n - \sum_m k_{xm} N_x$$

Equation 2.48

Where k_{ij} is the transition / transfer rate from state 'i' to state 'j' and $N_k$is the population of state 'k'. The positive term on the right hand side of Equation 2.48 is the rate at which excitations are entering state 'x' while the negative term is the rate at which excitations are leaving state 'x'.

For a molecular system, each state involved will have a rate equation like Equation 2.48 associated with it, and the solution to the resulting system of differential equations will give the time evolution of all excited and ground states of the ensemble.

2.6.3 Signals in Pump-Probe Spectroscopy

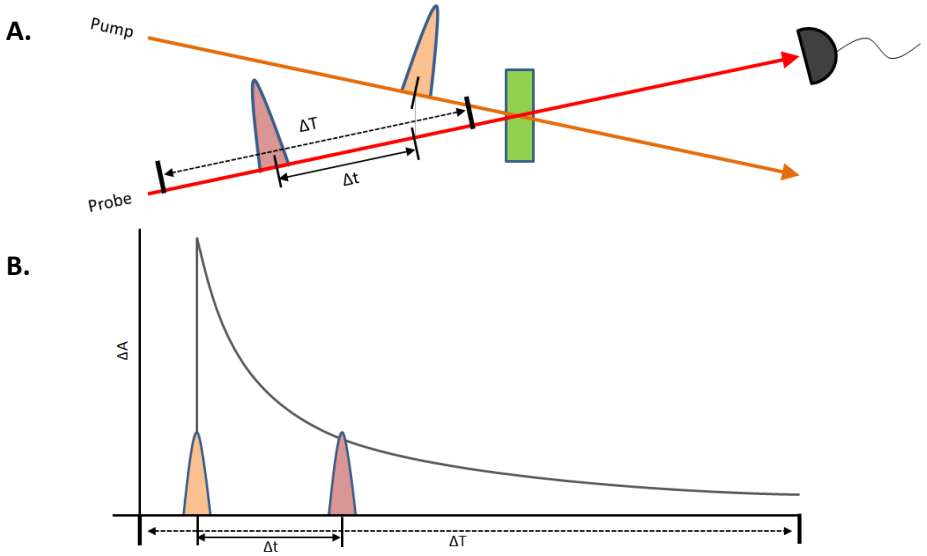

Figure 2.8: A - Schematic representation of an ultrafast pump-probe experiment. B - Simulated transient absorption trace (total ΔA as a function of probe delay, Δt, for a single probe wavelength). The pump pulse excites the sample while the probe pulse probes the optical properties of the sample after a time delay Δt. The delay time is varied across a large range, ΔT, to measure the dynamics of the system.

In ultrafast pump-probe spectroscopy (specifically transient absorption spectroscopy), a sample is excited by a light pulse (the pump) and then after a time delay, Δt, a second light pulse (the probe) passes through the sample (Figure 2.8A,B). The difference between the sample absorbance in the exited state (A_E, i.e. with pump) and the absorbance of the ground state (A_G, i.e. without pump) gives the transient absorption signal ($\Delta A = A_E - A_G$, Figure 2.8B), which can be related to the transmitted intensities of the probe via the Beer-Lambert law (Equation 2.47):

$$\Delta A = -log_{10}\left[\frac{I_E}{I_G}\right]$$

Where I_E = transmitted probe intensity with pump and I_G = transmitted probe intensity without pump excitation.

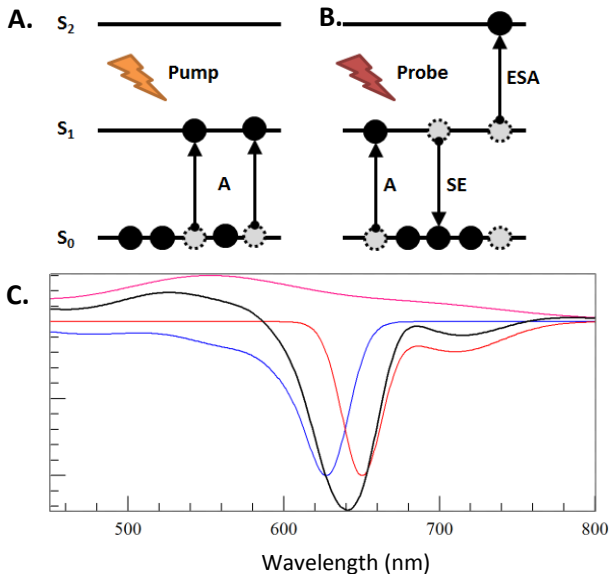

Figure 2.9: An ensemble of absorbing molecules with two excited states. A – Ground state bleaching after excitation by pump. B – Signals measured by probe; ground state absorption (A), excited state absorption (ESA), and stimulated emission (SE). C – Simulated transient absorption spectrum: bleaching (Blue), SE (Red), ESA (Magenta), total ΔA (Black)

The transient absorption signal typically has four major components (Figure 2.9); ground state bleaching, stimulated emission (SE), excited state absorption (ESA), and photoproduct absorption (not shown) (Berera et al. 2009). Bleaching occurs due to depletion of the ground state population by the pump pulse (Figure 2.9A,B) and results in a decrease of the sample absorption, i.e. a negative ΔA. The spectrum of the bleaching signal should match the absorption spectrum of the excited species (Figure 2.9C) (Berera et al. 2009). SE occurs when the wavelength of the probe matches the transition wavelength between the excited state and a lower energy state (often the ground state, Figure 2.9B). If the transition is allowed, SE causes an additional photon to be emitted in the same direction, and with the same wavelength, as the pump photon. The result is an apparent decrease in the sample absorption (negative ΔA) which should spectrally match the fluorescence spectrum of the excited species (Figure 2.9C) (Berera et al. 2009). ESA

occurs when the probe wavelength matches a transition between the current electronic state of an excited species and a higher excited state (Figure 2.9B). If this transition is allowed, additional light will be absorbed, resulting in an increase of the sample absorption (positive ΔA). The ESA spectrum will be the absorption spectrum of the electronically excited species, e.g. Chl *a**, or ^{3}BChl *a* (Figure 2.9C) and will increase the sample absorption (positive ΔA). Finally, photoproduct absorption occurs when a chemical change, such as electron transfer, is induced by the absorption of the pump (as occurs with reaction centers, see Figure 1.7 and Figure 1.13). The photoproduct absorption spectrum will be the absorption spectrum of the chemically modified species, such as P^{+} and A_0^{-} or Φ^{-} (Figure 1.7), and will result in an increase in sample absorption (positive ΔA) (Berera et al. 2009).

The excited state population created by the pump will evolve in time according to Equation 2.48 as energy is transferred to and from the various components of the system. This will result in evolution of the four signal components (Figure 2.9B,C) giving a ΔA trace like Figure 2.8B. Interpreting this data requires fitting it to a model of the system being investigated, such as the simple system represented by Figure 2.6 (transitions within a (B)Chl monomer) or a more complex system such as FMO (e,g, (Kihara et al. 2015)). This allows extraction of important information such as energy transfer rates and direction of energy flow within complex photosynthetic systems (Berera et al. 2009).

2.7 Singlet Oxygen Sensitization

In its ground state, molecular oxygen (O_2) is has two unpaired electrons (a diradical) with parallel spins (a triplet state, $^{3}O_2$), which severely reduces its reactivity

especially considering its radical nature (Briviba et al. 1997). This limit to its reactivity can be most easily understood by appealing to the law of conservation of angular momentum. Most organic molecules possess a singlet ground state, as do the byproducts of combustion (i.e. water and carbon dioxide). Since the reactants possess a total spin of one and the products possess a total spin of zero, there is an overall spin forbidden aspect to the reaction and significant activation energy must be supplied or compounds with significant SOC must be added (e.g. tetraethyl lead additive in gasoline) to start a self-sustaining combustion reaction.

The first electronic excited state of O_2 is a singlet state ($^1O_2$), which both removes the spin restriction discusses above (Briviba et al. 1997) and increases its oxidizing potential by ~1V (DeRosa & Crutchley 2002). States higher that the first excited state are not biologically important since they rapidly decay (10^{-11} -10^{-9} s in solution, (DeRosa & Crutchley 2002)) into the first excited state which is relatively long lived (10^{-6} -10^{-3} s in solution, (DeRosa & Crutchley 2002)) due to the spin forbidden nature of the transition to the ground state. Molecular oxygen can be exited into its singlet state by interactions with other molecules either chemically or via direct electronic energy transfer (i.e. singlet oxygen sensitization, (Briviba et al. 1997; DeRosa & Crutchley 2002)) which occurs when a molecule must make a spin-forbidden transition back to the ground state and the energy released by the transition is larger than the energy absorbed by the $^3O_2 \rightarrow {}^1O_2$ transition (Figure 2.10). Molecules that satisfy these two conditions can be good sensitizers of singlet oxygen.

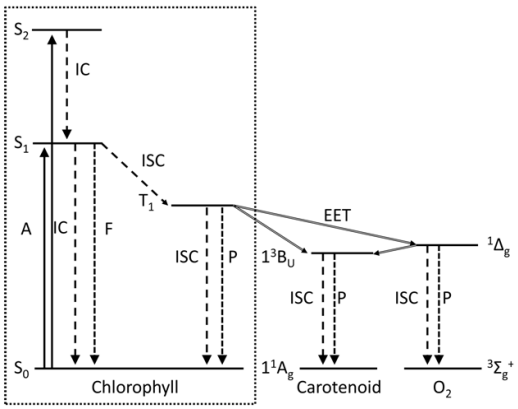

Figure 2.10: Simplified (B)Chl energy level diagram showing the formation of the (B)Chl triplet state (T1) from the excited singlet state (S1) followed by electronic energy transfer (EET) from the (B)Chl triplet state to a carotenoid molecule or an oxygen molecule. A - absorption, F -fluorescence, P - phosphorescence, IC - internal conversion, ISC - intersystem crossing. Reprinted with permission from (Hartzler et al. 2014). Copyright 2014 American Chemical Society.

(B)Chl molecules are highly efficient sensitizers of singlet oxygen. In (B)Chls, the triplet state (T_1) is populated from the 1st excited singlet (S_1) state via intersystem crossing (ISC) (Figure 2.10, Figure 2.6), which occurs with a high quantum yield of ~50% (Bowers & Porter 1967; Borland et al. 1987). This high yield for a forbidden process comes from strong SOC (Equation 2.14) that causes mixing of the S_1 and T_1 states (Equation 2.15) and from considerable overlap of the vibrational levels of S_1 and T_1 (Maggiora & Ingraham 1967; Hameka 1967; van der Waals & de Groot 1967; Marian 2012). Once in triplet excited state, a (B)Chl molecule can decay to the ground state through several pathways including ISC, phosphorescence, and quenching by oxygen or other molecules (Fujimori & Livingston 1957). Monomeric (B)Chl molecules in an air-saturated solution will transfer their triplet energy to oxygen molecules within ~1 μs, resulting in the formation of the highly reactive singlet oxygen as discussed previously. The quantum yield of such energy transfer approaches 100%, because the natural lifetime

of (B)Chl triplet state is ~500 µs (Niedzwiedzki & Blankenship 2010). To prevent singlet oxygen formation in photosynthetic proteins, a carotenoid molecule is typically positioned near (B)Chl molecules, allowing for rapid triplet energy transfer (TET) from the (B)Chl to the carotenoid. Since the energy of the carotenoid triplet state is below that of the singlet oxygen, the carotenoid can safely return to the ground state, dissipating the energy as heat (Figure 2.10).

2.8 Artificial Photosynthetic Systems

As discussed in the Introduction, artificial systems can initiate charge separation between bulk films of donor and acceptor molecules or covalently bound reaction center analogs (Figure 1.14). Both systems depend on the redox potentials of the molecules used, i.e. the energy needed to add (reduce) or remove (oxidize) electrons. Since optical spectroscopies, such as absorption or fluorescence spectroscopy, can only give differences in the energy levels within a chromophore, they are of limited use when predicting electron transfer, which depends on the difference between energy levels of different molecules. Additional information about the relative energies of the ground or excited states must be obtained either for one molecule relative to the other or, more likely, each molecule relative to an external standard. Cyclic voltammetry (CV) is one such technique that can give the HOMO and / or LUMO energies with respect to a reference electrode such as a standard hydrogen electrode (SHE), saturated calomel electrode (SCE), etc (see (Kissinger & Heineman 1983) for an explanation of the technique).

An example RC analog is the covalently bound zinc-tetraphenylporphyrin (Zn-TPP) and perylene diimide (PDI) system shown in Figure 2.11A. Cyclic voltammetry gives the oxidation and reduction potentials of Zn-TPP as approximately 0.8V and -1.4V vs. SCE respectively (Terazono et al. 2002; Ahrens et al. 2007) and PDI as approximately 1.6V and -0.6V vs. SCE respectively (depending on substituents (Lee et al. 1999; Ahrens et al. 2007)), indicating electron transfer can occur from Zn-TPP to PDI (Figure 2.11B). Absorption spectroscopy gives the lowest energy absorption band of PDI as 530nm (2.34eV) and Zn-TPP as 588nm (2.11eV) indicating excited state energy transfer can occur from PDI to Zn-TPP via the FRET mechanism.

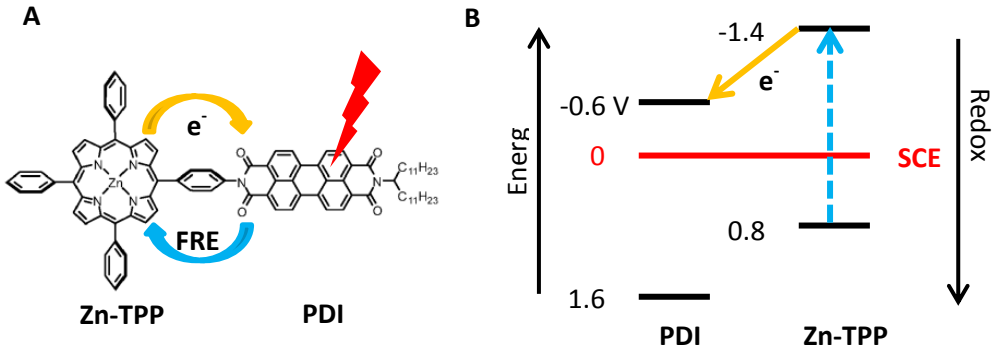

Figure 2.11: A – Covalently linked RC analog. Energy directly absorbed by Zn-TPP or transferred from PDI can initiate electron transfer from TPP to PDI. B – The energy levels of PDI and Zn-TPP vs. a saturated calomel electrode (SCE) and electron transfer (orange/grey solid arrow) to PDI after electronic excitation of Zn-TPP (blue/dashed arrow).

This RC analog functions as follows: Zn-TPP becomes excited, either by direct absorption of a photon or via energy transfer from PDI, which then donates an electron from its excited state to the LUMO of PDI (see Figure 2.11A,B). The same process occurs at the hetero-junction presented in Figure 1.14A.

CHAPTER 3 – EXPERIMENTAL SETUP

Experiments probing several different optical properties were performed using a variety of experimental techniques. Some of these techniques rely on unmodified commercial spectroscopic instruments (absorption and fluorescence spectrometers) or preexisting experimental instruments (nanosecond and ultrafast pump-prope spectrometers and an EPR spectrometer), thus only the relevant details will be discussed in brief.

One of the major goals of the project is the characterization of the triplet state energies of several pigments, natural and artificial, which involved the construction of a new measurement system for the detection of phosphorescence. Since this spectrometer was constructed by the author, it will be described in detail.

3.1 Absorption Spectrometer

In a typical absorption spectrometer (Figure 3.1), a nearly monochromatic beam is split between two different pathways by a beam splitter (a mirrored chopper in this example).

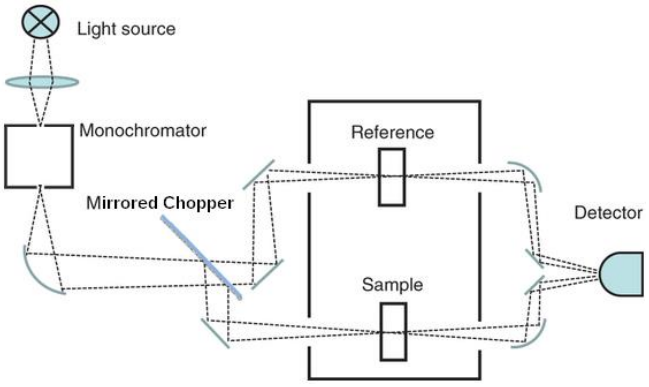

Figure 3.1: Schematic of a typical steady state absorption spectrometer.
One beam passes through the sample cell while the other either passes through free space (air) or a reference cell, the intensities are divided to remove intensity fluctuations of the light source and background absorbance originating from the sample cell and buffers or solvents (the reference cell). In a typical experiment, this instrument was used to verify sample integrity and measure sample concentration. It was also used to observe changes in a sample's chemical state, such as the aggregation state of (B)Chl molecules in solution, by changes in the absorption profile (i.e. the appearance, disappearance, or shifting of absorption bands, see also Figure 1.6B). It can also be augmented with an external excitation source and be used for low temporal resolution pump-probe experiments. Note that this instrument can only measure the total absorbance of a sample, that is, it cannot selectively probe a single chemical species, only the summed absorbance of all species present.

3.2 Fluorescence Spectrometer

In a typical fluorescence spectrometer (Figure 3.2), a near monochromatic excitation beam is passed through a sample while the sample emission is monitored at 90º

with respect to the excitation beam. Monochromators in both the excitation and emission beam paths allow selection of both the excitation and emission wavelengths.

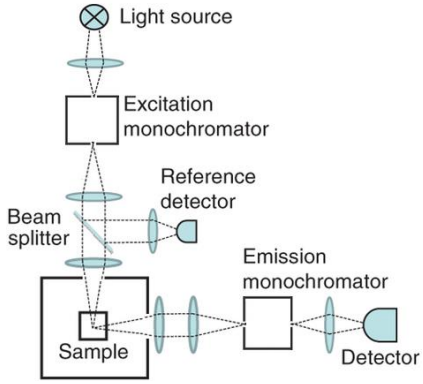

Figure 3.2: Schematic of a typical fluorimeter.

One powerful technique a fluorimeter can perform is measuring the fluorescence excitation spectrum of a sample containing multiple absorbing and/or fluorescing chemical species. In an excitation spectrum, the emission wavelength is fixed while the excitation wavelength is scanned. The excitation spectrum should approximately follow the absorption spectrum of the particular fluorescing species and if the emission spectra of two chemical species are well separated, then the absorption of each can be probed separately. This is important when deciding where to pump in a pump-probe or phosphorescence experiment since an optimum excitation wavelength, where only one emitting or absorbing species is excited, can be easily found.

3.3 Phosphorescence Spectrometer

Since the most direct method to measure the energy of the (B)Chl triplet excited state is by its phosphorescence spectrum (Figure 3.3), a phosphorescence spectrometer was constructed. Phosphorimeters can take on a variety of forms depending on the

quantum yield of phosphorescence. However, the optical transition from the T_1 state of (B)Chl to the singlet ground state (phosphorescence) has very low quantum yield, being 10^4 to 10^6 times lower than the fluorescence quantum yield (see Chapter 4), so a high-sensitivity, time-gated design was chosen. Due to the difficulty in detecting such signals (discussed throughout Chapter 3), there were still several (B)Chls for which phosphorescence spectra had not been measured. In the course of this work, the phosphorescence spectra for ten major (B)Chl species found in nature were measured with spectra for Chl c_2, BChl *e* and BChl *g* as well as BPheo *g* measured for the first time.

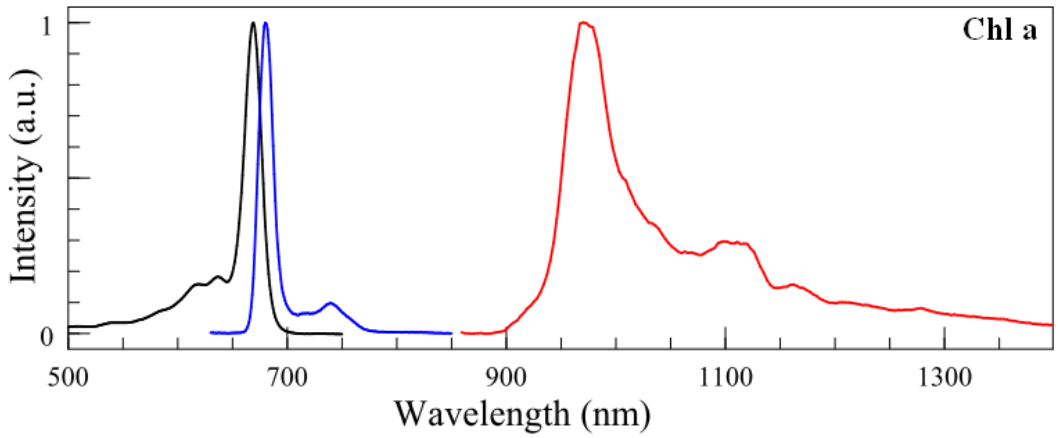

Figure 3.3: Representative spectra of chlorophyll absorption, fluorescence, and phosphorescence. Show are the Q-band absorption (Black / Left), the fluorescence (Blue / Center), and the phosphorescence (Red / Right) spectra for Chl *a*. All spectra have been normalized to one at their maxima.

Because all samples were measured under analogous conditions, the triplet state energies for these (B)Chl molecules can now be directly compared. The triplet state energies for these molecules were also determined by quantum chemical calculations and compared with experimental values. These computational methods were also used to predict the triplet state energies of three additional molecules: Chl c_1, Chl *f*, and BChl *f*.

3.3.1 The Phosphorimeter: Major Experimental Considerations

As discussed, (B)Chl molecules, have a phosphorescence quantum yield 10^4 to 10^6 times lower than the fluorescence quantum yield (Takiff & Boxer 1988b; Hartzler et al. 2014). Even at the phosphorescence emission maximum, which is shifted by 300-400nm toward longer wavelengths relative to the fluorescence emission maximum (e.g. Figure 3.3), the intensity of the long wavelength tail of the fluorescence emission can be one to two orders of magnitude higher than the phosphorescence intensity (Figure 3.4). Thus the fluorescence effectively masks the phosphorescence despite the spectral separation of the emission maxima.

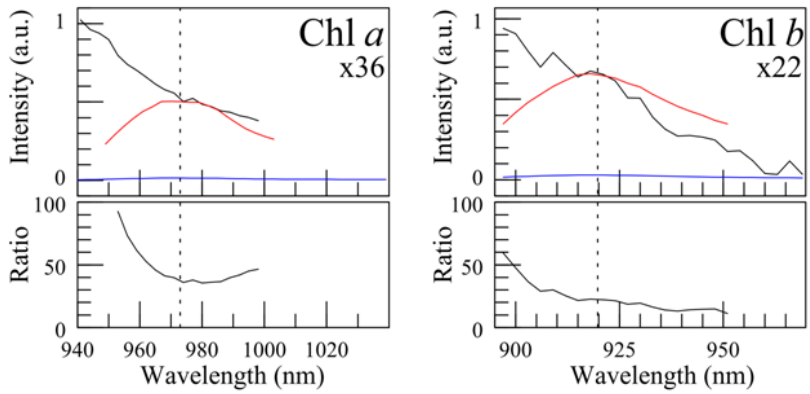

Figure 3.4: The long wavelength tail of the fluorescence compared directly to the phosphorescence signal for Chl a and Chl b molecules. Top frames: the long wavelength tail of the fluorescence emission spectrum (black line) and the maximum of the phosphorescence emission spectrum (blue line) measured in identical conditions with the fluorescence eliminated by the time gate. Red line corresponds to the phosphorescence magnified 36 or 22 times for Chl a and b, respectively. Lower frames: the ratio of fluorescence to phosphorescence. Reprinted with permission from (Hartzler et al. 2014). Copyright 2014 American Chemical Society.

However, the triplet state lifetime of monomeric (B)Chl molecules exceeds the singlet state lifetime by 4 to 6 orders of magnitude with the fluorescence lifetimes all below 10ns and triplet state lifetimes between 0.1-5 ms (Niedzwiedzki & Blankenship

2010; Hartzler et al. 2014). This allows for effective gating of the fluorescence emission in the time domain by means of a fast optical shutter (Takiff & Boxer 1988a; Dvornikov et al. 1979; Krasnovsky Jr 1979; Hartzler et al. 2014).

3.3.2 The Phosphorimeter: Construction

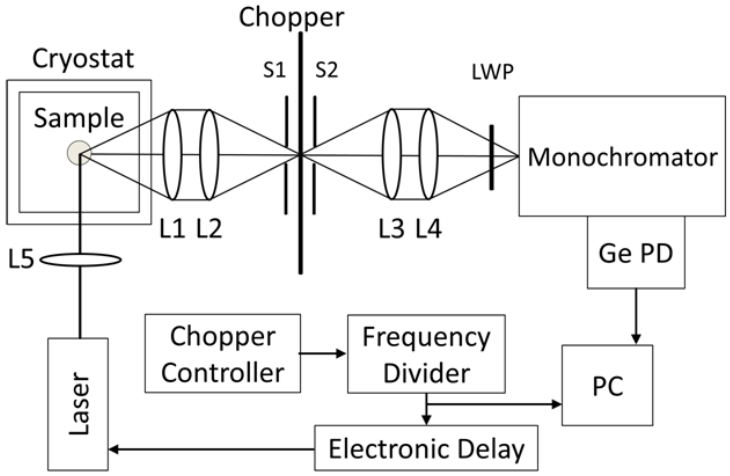

Figure 3.5: Block-diagram of the home-built phosphorimeter. Sample in a cryostat is excited by ~5 ns laser pulse. Lenses L1 and L2 collect emission from the sample and focus it on the mechanical shutter consisting of slits S1, S2 and the chopper wheel. Light transmitted by the gate is collimated (L4-L5) and filtered by a long wave pass filter (LWP) and monochromator (~10-nm bandwidth) before detection by the cryogenically cooled germanium photodetector (Ge PD). Reprinted with permission from (Hartzler et al. 2014). Copyright 2014 American Chemical Society.

A time-gated phosphorescence spectrometer (Figure 3.5) was built using a sensitive, liquid nitrogen-cooled germanium photodetector (North Coast Scientific Corp., EO-817L) with a measured noise equivalent power (NEP) of 7 $fW/\sqrt{Hz}$. Samples were placed into quartz EPR tubes and loaded into a cryostat at 77K (Oxford Instruments, Optistat DN).

Samples were excited by a 0.5-4 mJ, 5 ns laser pulse at a 10 Hz repetition rate (Ekspla NT 342B) into the Q_y absorption band for Chl *a* (660 nm), Chl *b* (640 nm), Chl

c_2 (650 nm), Chl *d* (690 nm), BChl *a* (770 nm), BChl *b* (795 nm), BChl *c* (660 nm), BChl *d* (660 nm), BChl *e* (670 nm), and BPheo *g* (770 nm), while BChl *g* was excited in the Q_x band (600 nm). This ensured dominant excitation of the molecules of interest.

The laser pulses were focused onto the samples with a cylindrical lens (L5) and the sample emission was collected and collimated onto a fast optical gate consisting of an optical chopper (Scitech, 300CD) closely flanked by slits, S1 and S2, to reduce scattered light and ensure fast gating (Figure 3.5). With a 10 cm diameter wheel rotating at 6000 rpm (100 rps), this arrangement allowed the gate to open in approximately 20 μs. A 700 nm or 800 nm long wave pass (LWP) interference filter (Edmund Optics, 62-987 or 66-235, respectively) was placed in front of the monochromator (Oriel, MS257) to reduce scattered laser light and fluorescence further. Note that the 950 nm IR timing LED in the chopper head was replaced with a red 630 nm LED (RadioShack, model 276-020) to avoid spectral interference with the phosphorescence (Figure 3.9A).

All phosphorescence spectra were corrected for the spectral sensitivity of the spectrometer (Figure 3.6A). A drawback of the germanium detector is its high cross-section for interaction with cosmic-rays. These appear as large spikes in the detector output (Figure 3.6B) that occur randomly at a rate of approximately 0.1 s^{-1}. These spikes were automatically excluded by the data acquisition software.

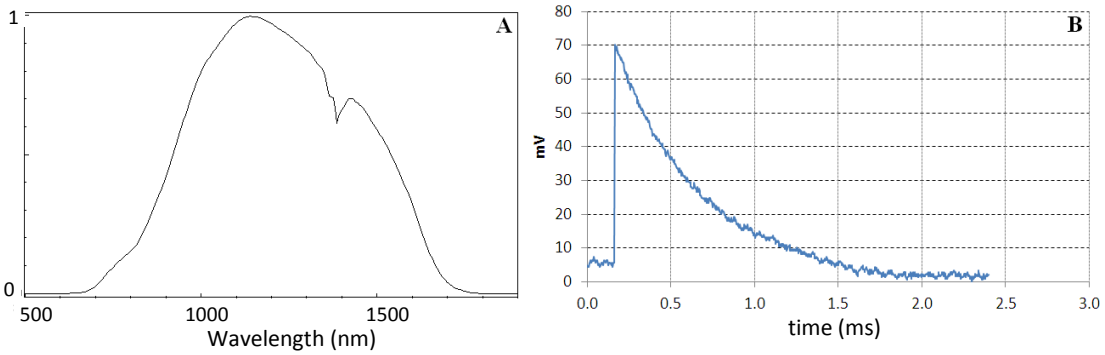

Figure 3.6: A – Spectral response of detection system which includes spectral characteristics of lens system, Monochromator with grating #3 (Oriel Grating Assembly 77745), and the Ge photodetector. Vertical axis of 'A' is proportional to photons per mV. B – Response of Ge photodetector to gamma ray from Americium.

3.3.3 The Phosphorimeter: Major Experimental Challenges

Choice of solvent and excitation wavelength was critical for experimental success. Certain solvent combinations, particularly water containing solvent systems, lead to significant sample aggregation at low temperatures causing a large shift of the Q_y absorption band to longer wavelengths upon cooling. Since all absorption spectra were measured at room temperature due to poor optical quality at low temperature, excitation wavelengths based off the room temperature absorption spectra proved to be poor choices due to the shifting of the Q_y absorption band. Additionally, the (B)Chl triplet state exhibits a relatively high excited state absorbance in the spectral region spanning the UV to approximately the Q_y absorption band (Figure 3.7) (Niedzwiedzki & Blankenship 2010; Asano & Koningstein 1981). Exciting a (B)Chl sample into this spectral range with a ~10-100 ns pulse will create triplet states that will absorb a significant fraction of the laser excitation pulse. It was observed that exciting a Chl *a* sample with a ~100 ns 532

nm pulse produced no measurable phosphorescence while a ~10 ns 660 nm pulse produced significant signal.

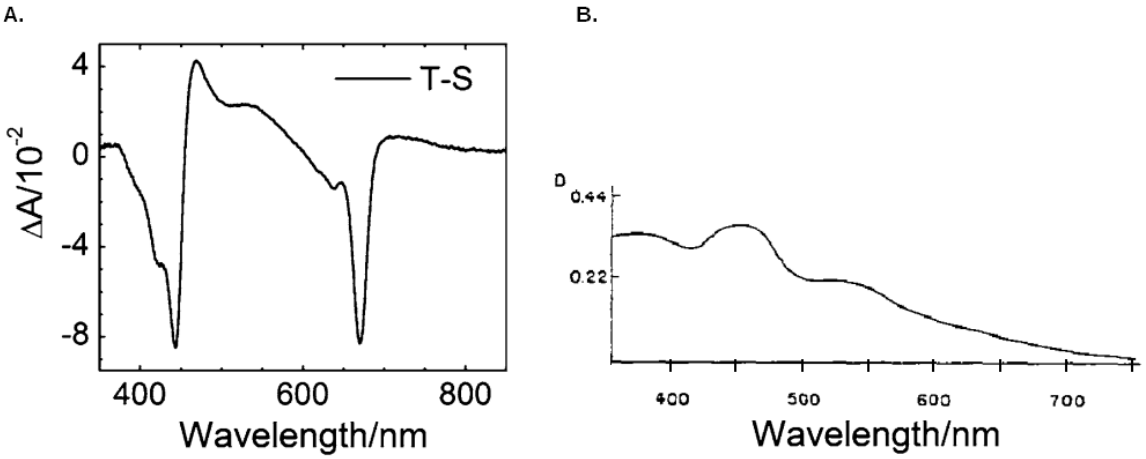

Figure 3.7: A - Triplet-Singlet (triplet minus singlet) transient absorption spectrum for Chl *a* in pyridine showing both singlet state bleaching and triplet-triplet excited state absorption (ESA) (Niedzwiedzki & Blankenship 2010). **B** – Triplet-triplet ESA absorption of Chl *a* in pyridine with the singlet bleaching removed (Asano & Koningstein 1981). Vertical scale on B is the ESA relative to the Chl *a* Soret absorption max at 443 nm.

Another challenge was avoiding contamination of the frozen sample by atmospheric oxygen. Special care had to be taken to avoid condensation of liquid oxygen into the sample upon cooling, as its presence resulted in a strong singlet oxygen signal via direct laser excitation of the liquid oxygen (Figure 3.8A) (Jockusch et al. 2008). This was accomplished by warming the cryostat and sample to a temperature above the boiling point of liquid oxygen (90K) and purging the cryostat with nitrogen gas through a custom sample holder for 1 to 3 minutes.

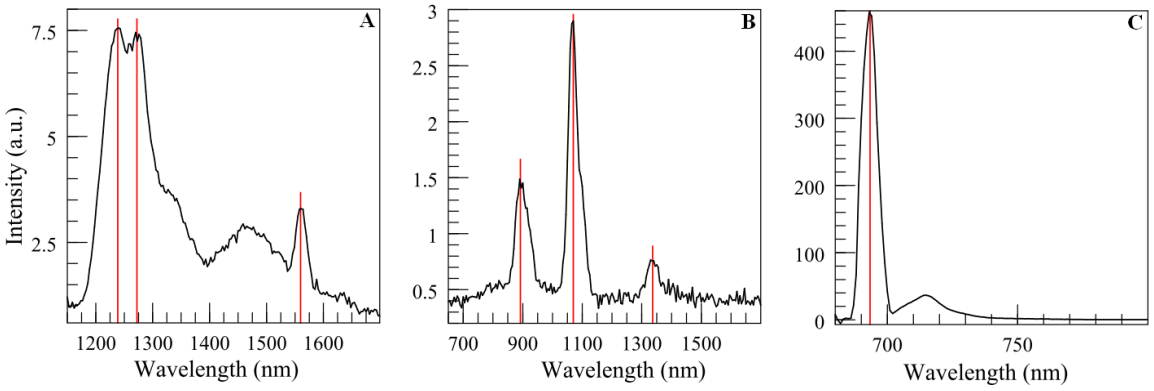

Figure 3.8: A - Phosphorescence of BChl b at 1240nm with the emissions of singlet oxygen at 1270nm and the 2nd order diffraction maximum of the scattered laser excitation (780nm) at 1560nm. B – Emission of Nd^{3+} contaminated glass at 900nm, 1070nm, and 1340nm. C – Emission of Cr^{3+} contaminated sapphire at 693nm.

Spectral contamination by stray light from external sources as well as emissions from chemical impurities in sample cells, optical elements, and structural members of the spectrometer also caused significant problems. For sample cells, quartz or fused silica cells are essential, as some glass cells were found to have trace Nd^{3+} impurities producing emission bands at ~900, ~1070, and ~1340 nm (Figure 3.8B), while some sapphire cells were found to have trace Cr^{3+} impurities, which produces emission at ~693 nm. (Figure 3.8C). Also paints, dyes, glues, and absorbing glass filters are to be avoided as well since they are capable of producing emissions that overlap the spectral region of interest (700-1600nm) (Figure 3.9B). As such, only interference based optical filters should be used in the beam path. Additionally, it is known that the metals stainless steel, aluminum, copper, and brass as well as their surface oxides (and chemically blackened brass/copper, i.e. CuO) do not produce measurable emission in the 700-1600nm range. Thus, all structures and spatial filters (e.g. slits) in the optical path should be made of these metals.

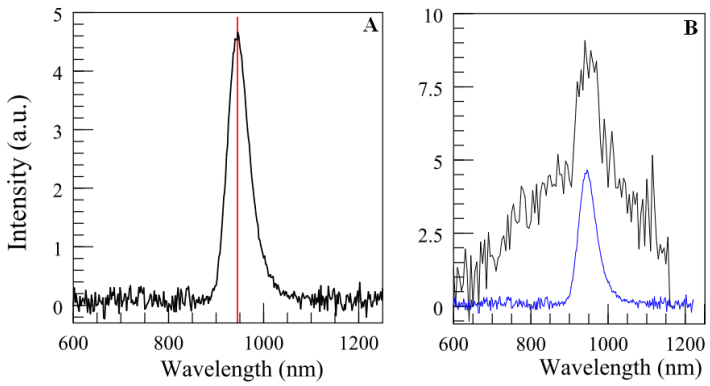

Figure 3.9: A - Spectral interference from a 950nm timing LED built into the chopper. **B –** 950nm LED and phosphorescence emission from an absorbing glass filter (red sharp cutoff filter).

3.3.4 Data accusation

Data accusation was performed by a fast analog to digital converter (National Instruments, AT-MIO-16XE-10) and a software based boxcar integrator. The voltage signal coming from the photodetector looks similar to Figure 3.10. With a two slot chopper wheel spinning at 100 rps, the chopping frequency is 200 Hz resulting in the gate opening for 2.5 ms before closing again. In Figure 3.10 the gate opens at approximately 3.5-4 ms and closes at 6-6.5 ms during which time the detector integrates the signal and then returns to the baseline with the intrinsic RC time constant of the detection system.

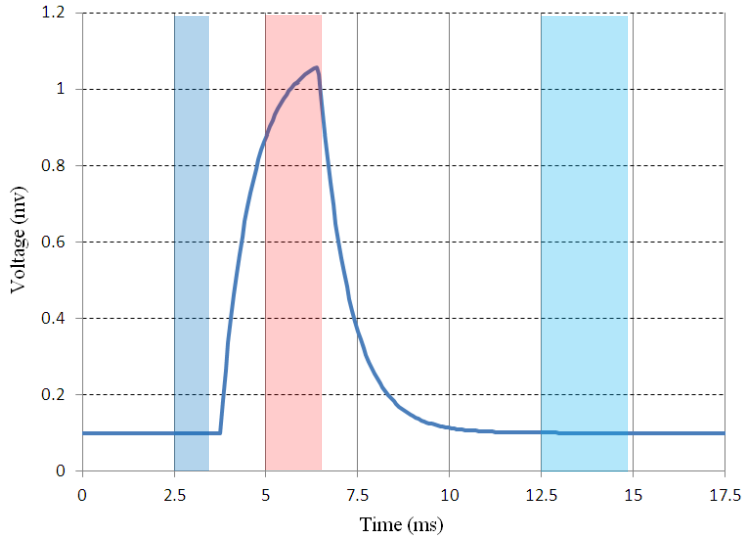

Figure 3.10: Simulated voltage signal as generated by the phosphorescence detection system. Shown are the three signal gates used by the boxcar integrator. The Left and Right gates (BLUE and CYAN) for background and noise subtraction and the Signal gate (RED) for capturing the absolute signal level. The actual signal is the difference between the average value of these three gates.

The boxcar integrator has three internal temporal gates that can be set with individual widths and start times, these are the Left and Right gates (blue and cyan respectively, Figure 3.10) used for background subtraction and noise removal and the Signal gate (red, Figure 3.10) for capturing the absolute signal level. The actual signal (d_i) is calculated as the difference between the average value across the Signal gate (s_i) and across both the Left and Right gates (b_i): $d_i = s_i - b_i$. Random noise can be suppressed by setting the signal gate to integrate only over regions with the highest signal (e.g. from 5-6.5 ms in Figure 3.10) thus incorporating only the points with the highest signal to noise, while non-random noise like mechanical vibrations from the chopper can be suppressed by appropriate placement of the left and right gates (e.g. if the chopper noise is at 100 Hz, separate the gates by a multiple of 10 ms with the left gate narrow and close to the signal gate).

The cosmic ray noise filter used by the data accusation software is type of chi-squared filter that examines the rate of change of chi-squared as data points are removed. Chi-squared is defined as:

$$\bar{d} = average(d_i)$$

$$\chi^2 = \sum_{i=1}^{N} \left(d_i - \bar{d}\right)^2$$

Equation 3.1

Since the signals originating from cosmic rays are large with relatively high slope (Figure 3.6B actual, Figure 3.11 simulated), we expect the magnitude of 'd' originating from regions with cosmic ray spikes to be large compared to 'd' originating from regions without cosmic ray spikes (see Figure 3.11).

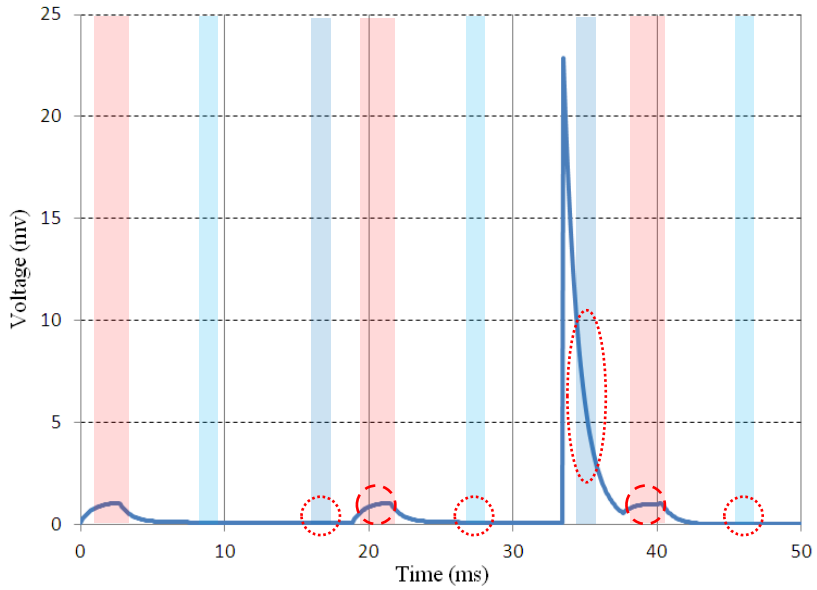

Figure 3.11: Simulated voltage signal showing the effect of cosmic ray noise. Shown are the three gates used to calculate the optical signal as well as the voltages within these gates. Left and Right gates (background level) are circled in red dots while the Signal gate is circled in red dashes.

Thus cosmic ray spikes will have a large effect on the value of chi-squared and removing a spike will lower the chi-squared value significantly. By removing the data point with the largest value of $|d_i - \bar{d}|$, chi-squared can be recalculated (χ_n^2) and compared to the previous value (χ_{n-1}^2). If the relative change (the slope) of chi-squared is below a user defined threshold, the filtering is completed.

$$|\chi_n^2 - \chi_{n-1}^2| < threshold$$

Equation 3.2

3.3.5 Phosphorescence Emission Lifetime and Relative Quantum Yield

Phosphorescence emission lifetimes were estimated by varying the electronic time delay (Berkeley Nucleonics, Model 7040) and measuring the emission intensity at different delay times, where delay time is defined as the time difference between the firing of the laser and the opening of the optical gate in Figure 3.5. The measured signal (*S*) as a function of delay time (*t*) was approximated using a single exponential (Takiff & Boxer 1988a):

$$S(t) = S_0 e^{-t/\tau}$$

Equation 3.3

Where S_0 is a constant and τ is the emission lifetime. For each sample studied, the phosphorescence intensity was measured at three to four different delay times at several wavelengths flanking the phosphorescence emission maximum. This data was then fit globally for all wavelengths using a mono-exponential function (Equation 3.3). However,

due to the small number of points used, the lifetimes determined by this method are not expected to be accurate beyond one significant digit.

The ratios of the fluorescence and phosphorescence quantum yields (see Chapter 4) were computed using the integrated photon flux of the fluorescence and phosphorescence spectra. The fluorescence spectra were measured using the described phosphorescence spectrometer with a zero time delay. Calibrated neutral density filters were used to reduce the fluorescence signal intensity while all other parameters were kept the same as in the phosphorescence measurements. When measuring phosphorescence emission spectra there was an approximately 20 μs minimum delay time due to the optical gating. This was corrected by using the measured lifetimes to project the phosphorescence emission intensity to its value at zero time delay.

The high sample concentrations used to acquire the phosphorescence emission spectra caused significant reabsorption of the fluorescence, resulting in a truncated emission peak (Figure 3.12). To account for reabsorption of the fluorescence emission peak, fluorescence emission spectra were also recorded with a fluorimeter (Cary Eclipse) at 77K in the same solvents but at a lower sample concentration in the range of 1 – 5 μM. These spectra were then scaled to match the long wavelength vibrational bands of the fluorescence recorded with the phosphorescence spectrometer and used to estimate the relative quantum yield of phosphorescence (Figure 3.12). The long wavelength tail of the fluorescence does not overlap with the Q_y absorption band and its shape is not affected by high sample concentration, thus this approach effectively corrects for the reabsorption (Penzkofer & Leupacher 1987).

The location of emission maxima were determined by fitting a Gaussian function to the top 30% of peak amplitude (for example, 952-991 nm for Chl a). This range was chosen to minimize the influence of the vibrational bands. The major source of uncertainty in fluorescence and phosphorescence emission maxima originates from misalignment of the sample with the optical beam path of the instrument (e.g., the straight line in Figure 3.5 connecting the sample with the monochromator through the center of lenses L1-L4). Offset from this line was noted to shift the emission peak by up to 10 nm, depending on the monochromator bandwidth. To counteract this, the phosphorimeter was aligned by reducing the bandwidth to approximately 3 nm and translating the sample perpendicular to the beam path until the prompt fluorescence signal is maximized. The fluorimeter was aligned in a similar way.

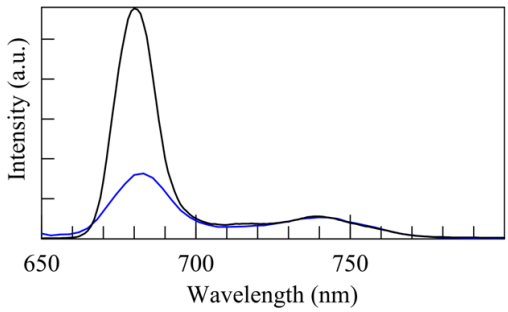

Figure 3.12: Chl a showing reabsorption of fluorescence Q_y emission. Black– low concentration (~5 µM). Blue/Grey – high concentration (~100 µM). These spectra were scaled to match on their long wavelength tails. Reprinted with permission from (Hartzler et al. 2014). Copyright 2014 American Chemical Society.

3.3.6 Electronics

Several custom circuits were built in the course of this study. All digital logic devices were made to conform to the TTL standard with a logical LOW registered for voltages between 0-0.8V and a logical HIGH registered for voltages between 2.2-5V.

3.3.6.1 Line Driver

Certain pieces of laboratory equipment do not have the ability to drive a 50Ω or even 200Ω load to the TTL HIGH level. This required a TTL line driver with relatively high input impedance and the ability to dive a 50Ω load to over 2.2V.

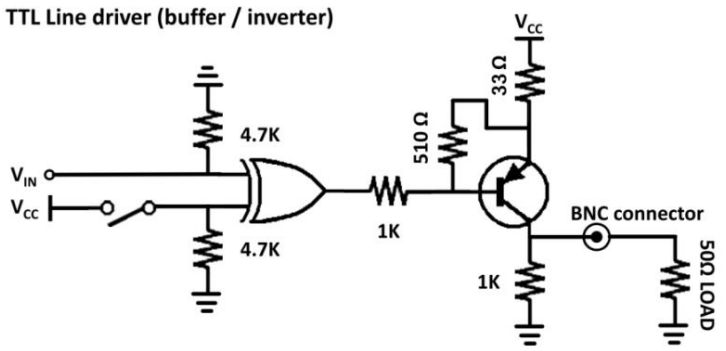

Figure 3.13: One of four TTL line drivers with a switchable inverter and input impedance of ~4.7kΩ.

An XOR logic gate was chosen as the input stage to force adherence to the TTL input standard and allow the device to function as either an inverting or non-inverting buffer (via an onboard DIP switch). A simple single PNP transistor circuit was chosen for the output stage (Figure 3.13). This driver has an unloaded cutoff frequency of over 20MHz (the limit of the oscilloscope used for testing).

3.3.6.2 Laser External Trigger Module (Ekspla NT 342B)

Since the optical gating depends on the timing of the laser pulse relative to the opening of the gate (i.e. the chopper swinging out of the beam path), the laser must be triggered from the chopper to ensure it fires at the proper time. To trigger the laser (Ekspla NT 342B) externally, the controller is set to accept an external trigger and a fixed width pulse must be supplied to the external trigger input. The rising edge of this pulse

triggers the laser flash lamp while the falling edge triggers the electro-optic Q-switch (firing the laser). The length of this trigger pulse determines the output power / pulse energy of the laser (see manual for Ekspla NT 342B). If the trigger pulse is too short, the laser pulse energy can exceed the damage threshold of the internal optics and cause serious damage to the system, so the trigger pulse width must be well controlled. Additionally, the laser is designed to fire the flash lamp at a rate of 10Hz, too slow and the reduced thermal lensing negatively effects output power, triggering too fast increases the thermal load and can damage the laser. Thus, the external trigger needs to ensure the trigger rate is 10Hz.

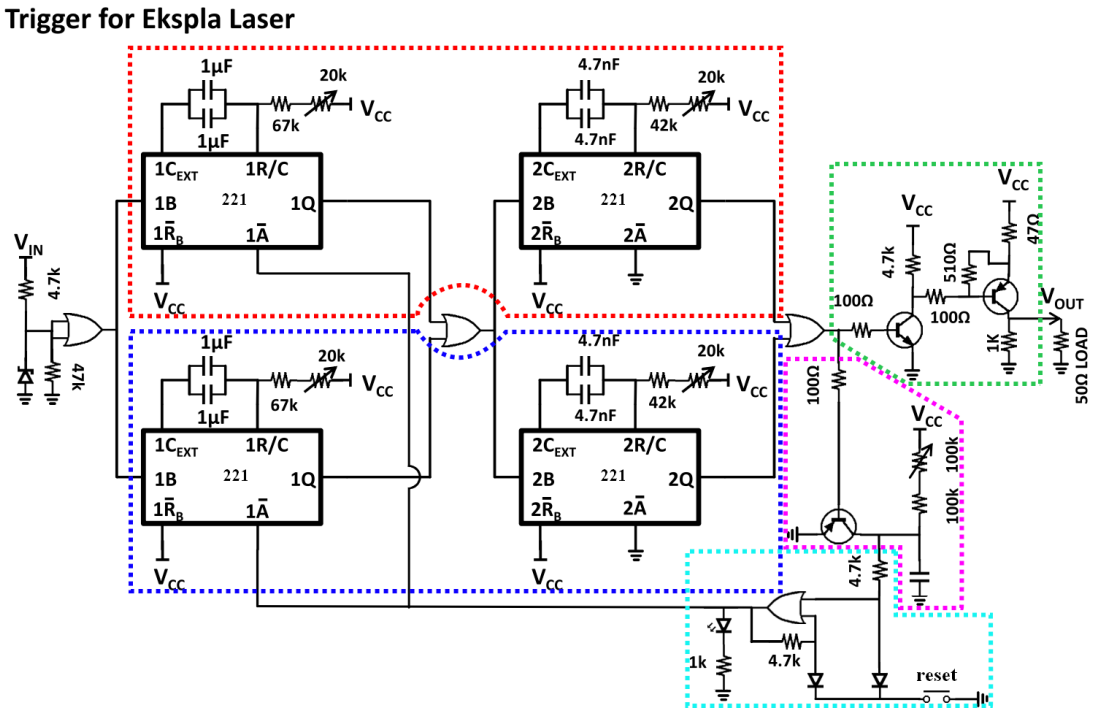

Figure 3.14: Triggering circuit for Ekspla laser. RED – Channel A, adjustable channel. BLUE – Channel B, non-adjustable channel. GREEN – output stage. MAGENTA and CYAN – Timer (magenta) and latch (cyan) to lock the input if the circuit is triggered too fast or too slow.

A two channel design based on the 221 non-retriggerable one-shot timer was chosen to meet the triggering requirements. Each channel consists of two timers, one to protect the laser from being triggered significantly over 10Hz (up to 10.5Hz, 95ms), and a second timer to provide a stable trigger pulse to control the laser pulse energy (approximately 300μs, see manual for exact value) (Figure 3.14). Two channels (A and B, Red and Blue in Figure 3.14) are used to protect the system from being damaged during adjustment of the triggering rate and laser pulse energy. This is accomplished by fixing one channel (B) at the MAXIMUM safe values for frequency and laser pulse energy (i.e. MINIMUM timer values) and only adjusting the other channel (A). If, for instance, the laser energy trigger pulse of channel A is made shorter than B, the logical OR combining channels A and B will ensure channel B controls the output. When A's trigger pulse is longer than B's, then A will control the output. Additionally, if the circuit is triggered much above or below 10Hz, a simple timer and latch is included to lock the input and light an LED as a warning. Improvements can be made to the output stage (Green, Figure 3.14) and the latch timer (Magenta, Figure 3.14) since the output stage uses two inverting stages and the latch timer lacks significant adjustability (due to physical limitations of the components used).

3.3.6.3 Frequency Divider

The conflicting needs to gate the optical signal as fast as possible (requiring a high chopper speed) and to trigger the laser at 10Hz necessitated building a frequency divider. Two dividers were built, one four stage ripple divider based on type-D flop-flops (division by 2, 4, 8, 16, Figure 3.15A) and another based on a 4017B decade counter

(division by 1-9, Figure 3.15B). The combination of these two dividers allow for division by 28 unique, non-trivial values in the range 2-144. Since the maximum speed of the chopper is 100 revolutions per second (rps) or 6000 rpm, using a two slot chopper wheel requires division by 20 (4 times 5).

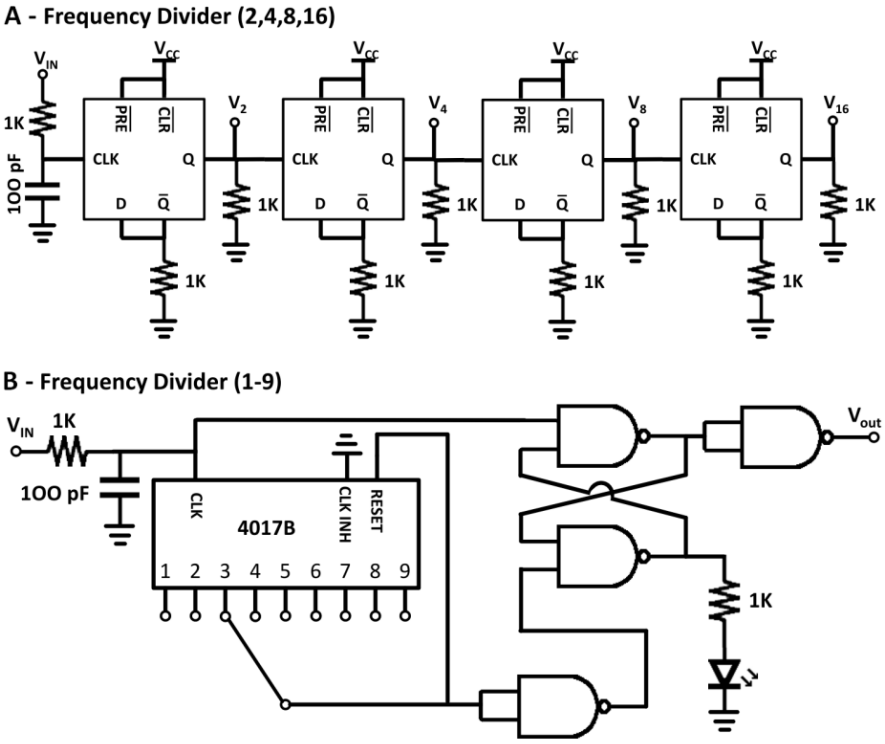

Figure 3.15: Frequency dividers. A – 4 stage ripple divider. B – Decade counter based divider.

3.4 Pump-probe techniques

Two pump-probe transient absorption spectrometers were used in the course of this study. One is a high sensitivity ultrafast system used to measure dynamics in the sub-picosecond to several hundred picosecond time scale while the other is a nanosecond system used to measure dynamics in the nanosecond to millisecond time scale.

3.4.1 Ultrafast pump-probe spectrometer

The ultrafast pump-probe spectrometer (the "MHz system", (Savikhin 1995)) functions on the same principle as the technique described in Section 2.6.3 (the "kHz system") except for the modulation. Instead of the modulation technique described in Section 2.6.3, where every other pump pulse is blocked and ΔA is computed from the difference between the probe intensity with and without the pump, the MHz system employs a high frequency double modulation scheme where both the pump and probe are modulated separately at different frequencies. This modulation scheme allows for high sensitivity detection of ΔA on the order of 1 part in 10^6 while the kHz system can detect a change in absorbance of 1 part in 10^4.

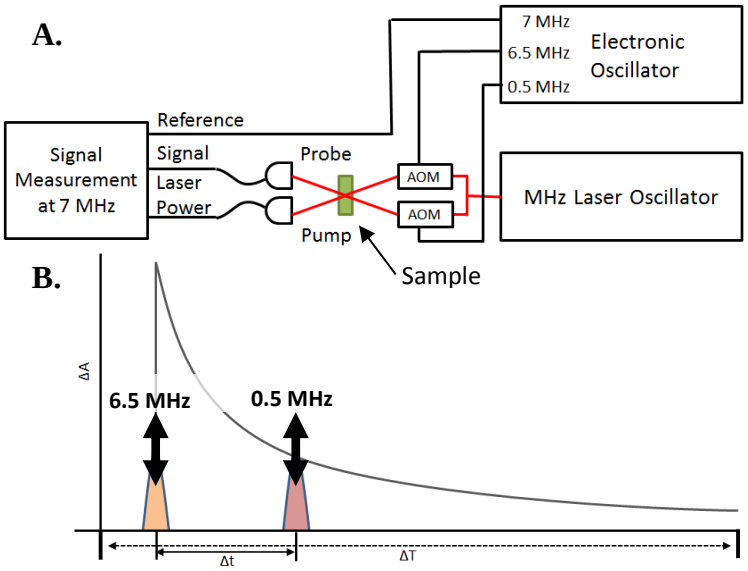

Figure 3.16: A – Laser oscillator produces an ~80 MHz pulse train which is then split and modulated to produce the pump and probe. The pump and probe combine in the sample to produce a sum frequency (7 MHz) which is then detected. **B –** Time trace showing the amplitude modulation of the pump (6.5 MHz) and probe (0.5 MHz).

In the MHz system, the ~80 MHz pulse train of the pump and probe are modulated by $\cos(\omega_1 t)$ and $\cos(\omega_2 t)$ respectively ($f_1 = \omega_1/2\pi$ = 6.5 MHz and $f_2 = \omega_2/2\pi$ =

0.5 MHz, see Figure 3.16). Through absorption of the pump, the ground and excited state populations are modulated at a frequency of ω_1 which in turn modulates the sample absorbance at the same frequency. The modulation depth of 'A' is proportional to the pump intensity and, crucially, the ground and excited state populations.

$$I_{pump}(t) \propto \cos(\omega_1 t)$$
$$A(t) \propto \cos(\omega_1 t)$$

Equation 3.4

The incident probe intensity is modulated at a frequency of ω_2, while the transmitted probe intensity is also modulated by the absorption according to the Beer-Lambert law (Equation 2.47).

$$I_{probe}(t) \propto \cos(\omega_2 t)$$
$$I_{trans}(t) = I_{prob}(t)e^{-A(t)}$$

Equation 3.5

Expanding the exponential as a series to 1st order gives:

$$I_{trans}(t) \approx I_{prob}(t) * \big(1 - A(t)\big)$$
$$I_{trans}(t) \propto \cos(\omega_2 t) * (1 - k\cos(\omega_1 t))$$

Equation 3.6

Where 'k' is a constant proportional to the ground and excited state populations.

The product of cosines in Equation 3.6 produces sum and difference frequencies at 7 and 6 MHz of which the detection system is designed to select only the sum frequency, the amplitude of which is proportional to ΔA (through the constant 'k'). By varying the delay time (Δt in Figure 3.16 B), ΔA can be measured as a function of time since excitation. The reason for this detection scheme is that, in the frequency range containing 7 MHz the free running ultrafast titanium:sapphire laser possess a minimum in

its noise which allows for shot noise (photon statistics) limited detection (Savikhin 1995; Mulder et al. 2008). Detection at the sum-frequency also eliminates a possible background signal due to the scattering of the modulated pump beam onto detector, which, even in the case of a sample with excellent optical quality is >> 10^{-6} and would limit the sensitivity of the spectrometer.

3.4.2 Nanosecond pump-probe spectrometer

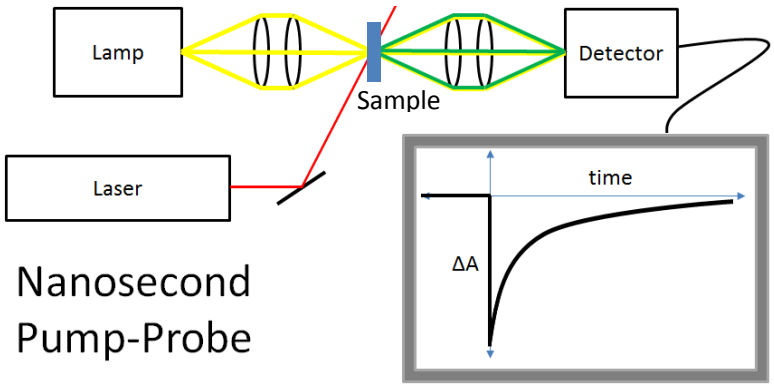

Figure 3.17: Nanosecond p-p spectrometer. At t=0, while the probe (yellow / light grey) is passing through the sample, the ns laser fires, and the transmitted intensity (green / grey) of the lamp is measured in real time by a fast detection system and is used to calculate ΔA.

The nanosecond pump-probe spectrometer (Figure 3.17) is simpler than the ultrafast systems owing to the fact that electronics exist that are capable of detecting signals changing on the ns time scale, while no electronics exist that can detect changes on the femtosecond time scale (thus the individual femtosecond pump and probe pulses). This system functions by passing continuous radiation from a lamp (the probe) through the sample while exciting the sample with a short (~5 ns) laser pulse (the pump). The transmitted probe intensity is measured in real time by a fast detection system and,

together with the transmitted probe intensity without the pump, used to calculate ΔA as a function of time (see (Kim 2007)).

3.5 Electron Paramagnetic Resonance

Electron Paramagnetic Resonance (EPR) is a spectroscopic technique that measures the microwave absorption of paramagnetic chemical species (i.e. species with non-zero spin) in an external magnetic field (Brudvig 1995). The applied external field, **H**, splits the spin energy levels into discrete states whose energies are linearly proportional to the applied field strength (H) and the z-component of the spin state with respect to the field direction (i.e. the Zeeman effect) (Brudvig 1995).

$$Zeeman\ energy = g\beta H m_s$$

Where β is the Bohr magneton (a constant), H is the magnitude of the external field, m_s is the spin quantum number (1/2, -1/2 for a free electron or 1,0,-1 for a triplet), and g is the 'g-factor' (to be discussed later).

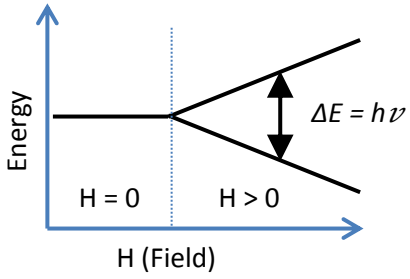

Figure 3.18: Zeeman splitting of the spin state of an unpaired electron with transition energy, ΔE, at unspecified field strength.

Transitions between these states can be induced by microwave radiation much like optical transitions except that the transition frequency (and thus the energy, $h\nu$)

depends on the external magnetic field strength (see Figure 3.18). For technical reasons, in a typical EPR spectrometer the magnetic field strength is swept to measure spectra instead of the microwave frequency (which is fixed). For an unpaired electron (with m_s = 1/2, -1/2), the transition energy (ΔE from Figure 3.18) follows Equation 3.7.

$$hv = g\beta H$$

Equation 3.7

The frequency of the transition depends on both the g-factor and the applied magnetic field (Equation 3.7). Since the external field is not a property of the chemical system being studied, rather a machine setting, the microwave transition frequency is not a fundamental property of the system either. The g-value defined in Equation 3.7 is, however, a property of the chemical system that is sensitive to electronic spin state, local magnetic field effects (e.g. from nearby non-zero spin atomic nuclei), etc (see Ioanitescu (Ioanitescu et al. 2009) and Lauricella (Lauricella et al. 2010) for examples of such effects). So to compare EPR spectra taken with different microwave frequencies, one must convert into g-value by using Equation 3.8.

$$g = \frac{hv}{\beta H}$$

Equation 3.8

3.6 Computational Methods

Quantum chemical calculations were performed by Gaussian 09 (Frisch et al. 2010) on eight cores of a Dell compute node (four 2.3 GHz 12-Core AMD Opteron 6176) operated as part of a cluster by the Purdue Rosen Center for Advanced Computing

(RCAC). These calculations were performed using unrestricted DFT utilizing the B3LYP functional and 6-31G(d,p) basis in the vacuum state, that is, with no solvation model or explicit solvent molecules in the calculation unless specified otherwise (Godbout et al. 1992). Ground state geometry optimization and vibrational frequency calculations were performed for both the singlet and triplet state of each of the ten (B)Chl molecules measured in this study as well as for an additional three (B)Chls not experimentally measured. The final energy of the triplet state was taken as the difference between the predicted total electronic and thermal free energies for the singlet and triplet ground states.

The specific molecules used in the calculations of Chapter 4 were Chl *a*, Chl *b*, Chl c_1, Chl c_2, Chl *d*, Chl *f*, BChl *a*, BChl *b*, 8-ethyl-12-methyl-BChl *c*, 8-ethyl-12-methyl-BChl *d*, 8-ethyl-12-ethyl-BChl *e*, 8-ethyl-12-ethyl-BChl *f*, and BChl *g* (Figure 1.1). All molecules (except Chl c_1 and Chl c_2) possessed the same esterifying alcohol at R_{17}^3 which consisted of a phytyl truncated at the fifth carbon atom and terminated with a methyl group (Figure 3.19). Truncation at carbon number five produces the same esterifying alcohol ($-C_6H_{10}-CH_3$) regardless of whether the starting point is a phytyl, farnesyl, or geranylgeranyl.

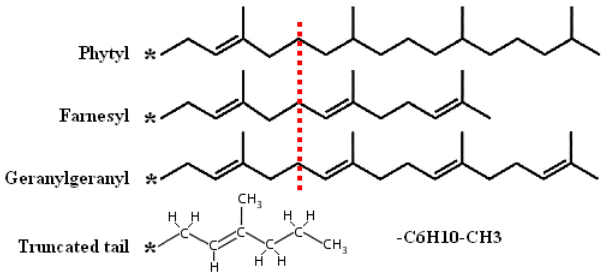

Figure 3.19: Three common tails found on (B)Chl molecules and the truncated tail (hydrogens explicitly shown) used for DFT calculations. Tails were truncated at the vertical dashed line. All tails were terminated with a methyl ($-CH_3$) after the truncation.

CHAPTER 4 – MAPPING THE TRIPLET STATE ENERGIES OF (BACTERIO)CHLOROPHYLLS

The singlet and triplet state energies of ten naturally occurring (B)Chl molecules as well as one BPheo in similar chemical environments were successfully determined by fluorescence and phosphorescence spectroscopy. Also, the relative quantum yield of emission from these states (Φ_P / Φ_F) was determined for each molecule.

4.1 Sample Preparation

Chl *a* and *b* were obtained from Sigma-Aldrich Corporation and used with no further purification. The other chlorophyll pigments were extracted with 100% technical grade methanol from cells of the following bacterial or algal species: Chl c_2 from *Symbiodinium*, Chl *d* from *Acaryochloris marina*, BChl *a* from *Rhodobacter sphaeroides*, BChl *b* from *Blastochloris viridis*, BChl *c* from *Chlorobaculcum tepidum*, BChl *e* from *Pelodictyon phaeum*, BChl *g* from *Heliobacterium modesticaldum*. Purification was done using an Agilent 1100 HPLC system equipped with a Zorbax Eclipse XDB-C18 reverse phase column (250 mm x 4.6 mm) with an isocratic flow rate of 1mL/min and acetonitrile:methanol:tetrahydrofuran (60:36:4, v/v/v) as a mobile phase. These samples were prepared by the research group of Robert E. Blankenship.

BChl *d* was extracted from the *bchQRU* mutant chlorosomes of *Chlorobaculcum tepidum* (Gomez Maqueo Chew et al. 2007) (provided by Donald A. Bryant). In an anaerobic atmosphere, 30 μL of the isolated chlorosomes (optical density of ~1000 cm^{-1}) were added to 1 mL of hexane and 1 mL of aqueous buffer (1 M NaCl, 0.1 M KH_2PO_4, pH 7; both were deoxygenated). The sample was mixed vigorously using a vortex mixer and centrifuged for 10 minutes under 7,200*g* until the phases were separated, with the upper layer being hexane and the lower layer being aqueous buffer. The carotenoids and quinones remained dissolved in the hexane phase and BChl *d* precipitated between the phases. The hexane and the aqueous phases were carefully removed and discarded (This step was repeated to obtain higher purity.). Once more, 1mL each of hexane and aqueous buffer are added, the mixture was then mixed and centrifuged until the solution separated into two phases. The hexane phase (top) was removed and discarded on this last repeat of this manipulation, and 1 mL of deoxygenated chloroform was added to the remaining solution, which was then vigorously mixed. Because BChl *d* dissolves in chloroform, another centrifugation separated the BChl *d* solution in chloroform and the aqueous buffer into two phases. The BChl *d* solution in chloroform is removed and dried under anaerobic conditions (Kim 2007). Absorption spectra taken after purification show the final carotenoid to BChl *d* molar ratio can be at most 1:70, a reduction by a factor of approximately 5.4 compared to wild type chlorosomes (Takaichi & Oh-oka 1999). In the frozen solvent used for phosphorescence measurements, molecular diffusion is precluded and given the low concentration it is highly unlikely any carotenoids were close enough to quench the BChl *d* triplet states.

BPheo *g* was produced in large quantities during sample storage as a natural breakdown product of BChl *g*. It was identified as such by its absorption spectrum, with maxima at 530, 670, and 757 nm. Spectral interference in the short wavelength region with chlorin type breakdown products (Brockmann Jr. & Lipinski 1983; Michalski et al. 1987) prevented accurate identification of the BPheo *g* Soret peaks, however a major peak was observed at 361 nm with a shoulder at 390 nm. These absorption peaks are consistent with BPheo *g* (Michalski et al. 1987; Brockmann Jr. & Lipinski 1983).

The central magnesium ion (Mg^{2+}) of a (B)Chl molecule can accept up to 6 ligands, four provided by the nitrogen atoms of the macrocycle and up to two more can be provided by the environment (e.g. solvents or protein residues). It has been shown that the coordination state of the central ion can influence the fluorescence and phosphorescence properties of the molecules with higher coordination states shifted to longer wavelengths (Solov'ev et al. 1983; Takiff & Boxer 1988b). Although, it is not possible in general to identify a specific Q_y absorption or fluorescence maximum with a particular coordination state given that solvent effects have been shown to shift the Q_y absorption maximum by up to 40 meV (milli-eV), independent of coordination state (Krawczyk 1989; Callahan & Cotton 1987), while also causing a solvent dependent fluorescence Stokes shift of 20 – 50 meV (Szalay et al. 1974). Additionally, for a particular solvent the direction of the Q_y maximum shift can depend on the central metal ion, as seen with metal substituted BChl molecules (Hartwich et al. 1998; Noy et al. 2000). However, data from Rätsep et. al. (Rätsep et al. 2009) suggests that in solvents where the (B)Chl coordination state is temperature dependent its absorption and fluorescence Q_y maxima shift toward longer wavelength upon changing from 5- to 6-

coordinate state, and that shift is larger than the observed temperature dependent shift in other (B)Chl and solvent systems (Rätsep et al. 2009).

4.2 Sample Coordination State

While, in nature, (B)Chl molecules are known to exist in both the 5- and 6-coordinated state (Fiedor 2006; Evans & Katz 1975), in this study, care was taken to ensure that all molecules were in the 6-coordinate state since this proved to be the most straightforward to achieve as a pure state. Raman and fluorescence line narrowing experiments have shown that at room or low temperature (B)Chl molecules in pyridine, methanol (MeOH), and tetrahydrofuran (THF) are either entirely or predominantly 6-coordinated (Fujiwara & Tasumi 1986; Koyama et al. 2006; Callahan & Cotton 1987; Telfer et al. 2010). For the spectroscopic measurements of the present study, all samples were dissolved in toluene:pyridine (4:1, v/v) with the exception of Chl c_2, which was dissolved in MeOH:THF (4:1, v/v), because of its chemical instability in pyridine (Niedzwiedzki & Blankenship 2010). Sample concentrations were approximately 20 – 100 μM during phosphorescence measurements.

4.3 Sample Integrity

To ensure sample integrity during experiments, room temperature absorption spectra were recorded before and after the measurements. These indicated that the porphyrin and chlorin type samples had not changed during measurements and the Q_y absorption bands of the bacteriochlorin type samples (BChl *a*, BChl *b*, and BChl *g*) had dropped in intensity by no more than 5%, with no apparent change in spectral shape. The

drop in the bacteriochlorin Q_y absorbance was accompanied by the appearance of chlorin type byproducts that absorb in the 660-680 nm range (Steiner et al. 1983; Brockmann Jr. & Lipinski 1983; Michalski et al. 1987). These byproducts do not spectrally overlap the bacteriochlorin Q_y bands, thus selective excitation of only the bacteriochlorin type molecules is possible, ensuring the small fraction of these products did not affect the shape of the phosphorescence spectra. This was also supported by phosphorescence spectra measured in the beginning and at the end of each experiment; no noticeable changes in shape and position of the phosphorescence band were observed.

4.4 Experimental Results

The phosphorescence spectra, along with the fluorescence spectra measured at 77K, are shown in Figure 4.1, and the data on the fluorescence and phosphorescence emission maxima and relative quantum yields are summarized in Table 4.1. The table also lists data obtained by other groups.

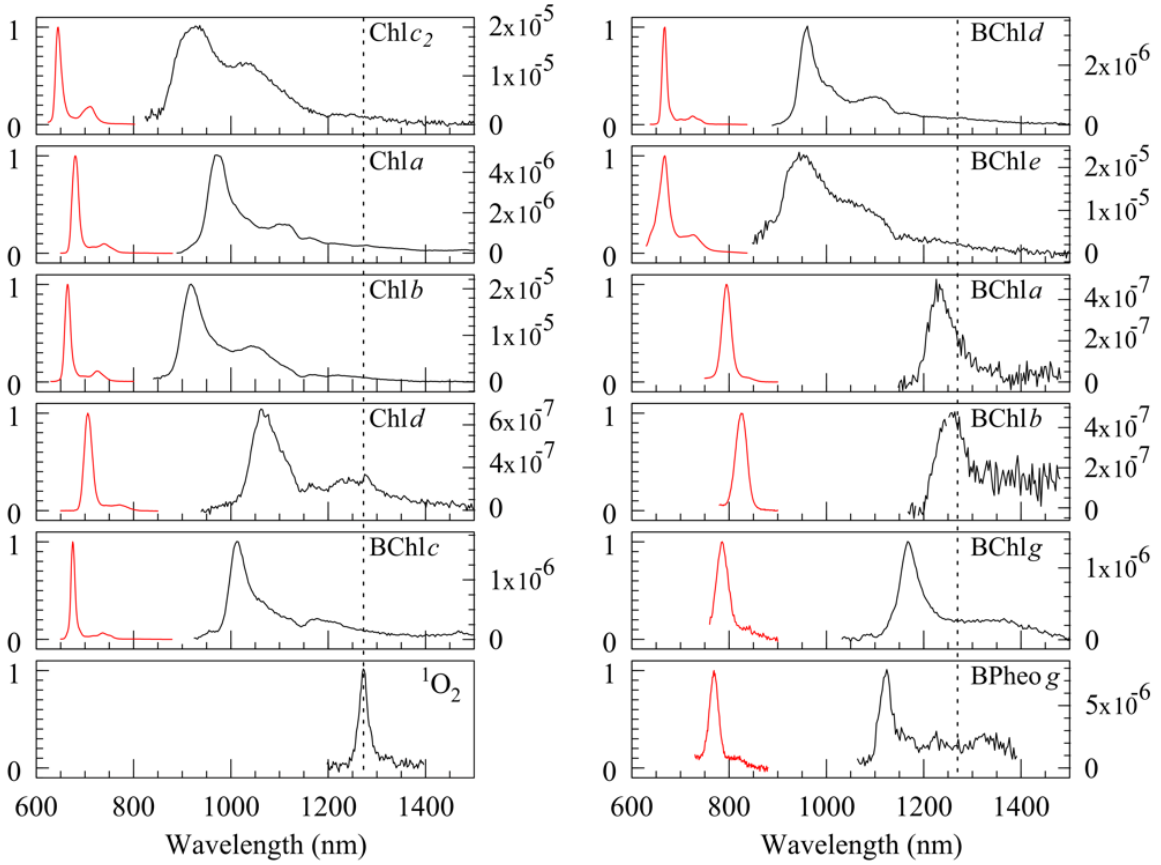

Figure 4.1: Fluorescence (RED/GREY) and phosphorescence (BLACK) emission spectra. The left hand scale is the fluorescence intensity normalized to one while the right hand scale is the phosphorescence intensity relative to the fluorescence intensity. The vertical dotted line corresponds to the emission maximum of singlet oxygen ($^1O_2$). Reprinted with permission from (Hartzler et al. 2014). Copyright 2014 American Chemical Society.

Table 4.1 - Experimental and theoretical values of ten types of (B)Chl and one BPheo, including fluorescence and phosphorescence emission maxima (λ_F and λ_P respectively), the approximate phosphorescence emission lifetime (τ_P), the relative phosphorescence / fluorescence quantum yield (Φ_P / Φ_F), and the coordination state and solvent used during measurement. Reprinted with permission from (Hartzler et al. 2014). Copyright 2014 American Chemical Society.

molecule	λ_F (nm)[A]	λ_P (nm)[A]	τ_P (μs)	Φ_P / Φ_F	coord. state	solvent[B]	ref
porphyrin type							
Chl c_2	**645**	**927**	**4000**	**1.6×10^{-4}**	**6**	**Me/THF**	***C***
	640	(967)[D]	833	—	6	THF (RT)	*E*
chlorin type							
Chl *a*	**680**	**973**	**2000**	**2.6×10^{-5}**	**6**	**T/P**	***C***
	677	(1079)[D]	413	—	6	P (RT)	*E*
	672	925	2500	9.9×10^{-5}	[5][F]	DE	*G*
	675	970	1200	2.6×10^{-5}	[6][F]	DE/PE	*G*
	—	930	2400	—	[5][F]	DE	*H*
	—	980	1800	—	6	P	*H*
	—	965	—	—	6	T/P (1%)	*I*
Chl *b*	**664**	**920**	**3000**	**1.2×10^{-4}**	**6**	**T/P**	***C***
	662	(1028)[D]	556	—	6	P (RT)	*E*
	654	875	5100	2.6×10^{-4}	[5][F]	DE	*G*
	660	920	2800	2.0×10^{-4}	[6][F]	DE/PE	*G*
	—	890	4300	—	[5][F]	DE	*H*
	—	930	3100	—	6	P	*H*
Chl *d*	**706**	**1068**	**1000**	**5.3×10^{-6}**	**6**	**T/P**	***C***
	705	(1132)[D]	312	—	6	P (RT)	*E*
	699	978	1050	—	[5][F]	DE	*J*
	—	981	1100	$\Phi_P=(1.5\text{-}3.5)\times10^{-5}$	[5][F]	Water/Triton	*J*
BChl *c*	**675**	**1014**	**1000**	**1.2×10^{-5}**	**6**	**T/P**	***C***
	674	(1055)[D]	474	—	6	P	*E*
	—	960	1600	—	5	DE	*K*
	—	1040	1100	—	6	P	*H*
BChl *d*	**667**	**960**	**1000**	**1.9×10^{-5}**	**6**	**T/P**	***C***
	663	(1065)[D]	448	—	6	P (RT)	*E*
	—	920	2100	—	5	DE	*K*
	—	960-980	1500	—	6	P	*H*
BChl *e*	**667**	**953**	**1000**	**1.0×10^{-4}**	**6**	**T/P**	***C***
	—	**912**	—	—	**5**	**T/P**	***C***
	670	(1060)[D]	461	—	6	P (RT)	*E*
bacteriochlorin type							
BChl *a*	**795**	**1232**	**200**	**1.2×10^{-6}**	**6**	**T/P**	***C***
	795	(1415)[D]	99	—	6	P (RT)	*E*

	778	1214	—	$\Phi_P \sim 10^{-7}$	5	Triethylamine	*I*
	785	1221	—	$\Phi_P \sim 10^{-7}$	6	2MeTHF/P (10%)	*I*
BChl *b*	**825**	**1256**	**100**	**1.5×10^{-6}**	**6**	**T/P**	***C***
	822	(1415) *D*	99	—	6	P (RT)	*E*
	821	1255	—	—	6	T/P (16%)	*I*
BChl *g*	**786**	**1169**	**400**	**3.7×10^{-6}**	**6**	**T/P**	***C***
	792	(1336) *D*	130	—	6	P (RT)	*E*
BPheo *g*	**769**	**1122**	**200**	**2.6×10^{-5}**	**N/A**	**T/P**	***C***
singlet O_2		**1272**	**—**	**—**	**N/A**	**—**	***C***
		1270	—	—	N/A	—	*L*

A Experimental uncertainties in peak wavelengths (Δλ) are defined as ½ the instrument bandwidth: $\Delta\lambda_F = \pm 2.5$ nm, $\Delta\lambda_p = \pm 4$ nm. ***B*** Solvent temperature at 77K unless stated otherwise (RT → room temperature). T/P = toluene:pyridine (4:1 v/v). Me/THF = methanol:tetrahydrofuran (4:1 v/v). DE/PE = diethyl ether:petroleum ether (1:1 v/v). 2MeTHF/P (10%) = 2 methyl-tetrahydrofuran + 10% pyridine. Water/Triton = water+2% Triton X100. DE = diethyl ether, P = pyridine;

C (This work); ***D*** values in brackets are calculated using Eq. 7 from ref (Niedzwiedzki & Blankenship 2010) [$\Delta E(T_1 - S_0)(cm^{-1}) = 21258 - 1539 \cdot \ln k_{int}$] and data from Table 1 of ref (Niedzwiedzki & Blankenship 2010).

E (Niedzwiedzki & Blankenship 2010); ***F*** Coordination state inferred from phosphorescence emission maximum;

G (Solov'ev et al. 1983); ***H*** (Krasnovsky Jr 1982); ***I*** (Takiff & Boxer 1988b); ***J*** (Neverov et al. 2011); ***K*** (Krasnovsky Jr et al. 1993); ***L*** (Krasnovsky Jr 1979)

4.4.1 Porphyrin-type molecule: Chl *c_2*

Chl *c_2*, the lone porphyrin-type Chl among the studied samples, exhibits the shortest wavelength fluorescence of any of the other Chls measured and the second shortest wavelength phosphorescence, just a few nanometers longer than Chl *b* (Table 4.1). The relative quantum yield of Chl *c_2* phosphorescence is relatively high (10^{-4}) for a (B)Chl and comparable to the upper range of chlorin-type Chls (Table 4.1). The phosphorescence spectrum of Chl *c_2* possesses a major vibronic band at 1029 nm with a relative intensity of 0.60 (relative intensity is defined as the ratio of emission intensity at

the vibronic peak maximum to the intensity at the emission maximum listed in Table 4.1).

This molecule was the only sample to be dissolved in a different solvent (MeOH / THF) due to its chemical instability in pyridine under illumination (Niedzwiedzki & Blankenship 2010). It should be noted that this sample contained different phosphorescing species, likely a mixture of 5- and 6-coordinate molecules. Effort was made to excite the longest wavelength absorbing species (see *Discussion*).

4.4.2 Chlorin-type moleules: Chl *a*, Chl *b*, Chl *d*, BChl *c*, BChl *d*, BChl *e*

These molecules fluoresce in the range 664 – 706 nm and phosphoresce in the range 918 – 1012 nm with Chl *b* emitting at the shortest wavelength and Chl *d* emitting at the longest wavelength (Table 4.1). Relative quantum yields spanned two orders of magnitude, 10^{-4} – 10^{-6}, with Chl *b* having the highest and Chl *d* having the lowest relative quantum yield of this group (Table 4.1). The phosphorescence spectrum of Chl *a* possesses a major vibronic band clearly resolved at 1109 nm with a relative intensity of 0.30. The wavelength and relative intensities of the major vibronic bands for the other chlorin type molecules are: Chl *b* (1045 nm, 0.36), Chl *d* (1275 nm, 0.32), BChl *c* (1186 nm, 0.20), BChl *d* (1093 nm, 0.29), and BChl *e* (1042 nm, 0.52).

The BChl *e* sample contained a mixture of 5- and 6-coordination states. However this sample allowed for predominate excitation of either the 5- or 6-coordinated states with proper choice of the excitation wavelength, allowing extraction of the phosphorescence emission maximum for both species (Figure 4.2). The 41-nm shift in the phosphorescence emission peak is consistent with the difference observed between the 5-

and 6-coordinate states of Chl *a* and Chl *b*. The difference between the fluorescence maxima could not be resolved with this method.

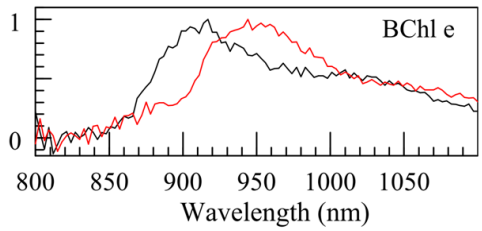

Figure 4.2: Different species (5 and 6-coordinated states) in BChl e sample. BChl e excited at 640 nm (black) and 670 nm (red/grey). Reprinted with permission from (Hartzler et al. 2014). Copyright 2014 American Chemical Society.

4.4.3 Bacteriochlorin-type molecules: BChl *a*, BChl *b*, BChl *g*, BPheo *g*

These molecules exhibit the longest wavelength emission maxima of all the molecules studied in this work. The fluorescence emission maxima were in the range 786 – 825 nm and the phosphorescence maxima occurred in the range 1170 – 1255 nm with BChl *g* emitting at the shortest wavelength and BChl *b* emitting at the longest wavelength in both cases (Table 4.1). The BChls of this group exhibit the lowest relative quantum yields of all molecules in this study, all three being in the order of 10^{-6} (Table 4.1). Due to their tendency to produce chlorin-type molecules care had to be taken to avoid exciting these breakdown products.

The phosphorescence spectrum of BChl *g* does not possess well resolved vibronic bands. Instead, a broad feature is present that extends from approximately 1200 – 1500 nm and is best fit with two Gaussian components in addition to the main maximum at 1169 nm (amplitude of 0.86 and full width at half max (FWHM) of 45 nm), one vibronic component is centered at 1215 nm (amplitude of 0.15 and FWHM of 36 nm), while the second component is centered at 1296 nm (amplitude of 0.19 and a FWHM of 245 nm).

The other bacteriochlorin type molecules show evidence of similar broad vibronic features, in particular BChl *b* and BPheo *g*, however the poor signal to noise of these spectra does not allow meaningful fits to be made.

BPheo *g* was the molecule with the shortest emission wavelength and with the highest relative quantum yield of this class, which may be due to the absence of a coordinating metal ion.

4.4.4 Singlet Oxygen

The singlet oxygen emission spectrum (Table 4.1, Figure 4.1) was measured by immersing an EPR tube into an unsilvered optical dewar (KGW-Isotherm) filled with liquid nitrogen and allowing atmospheric oxygen to condense into the tube. This liquid was excited directly with a laser pulse in the 600-700 nm range (Jockusch et al. 2008).

4.4.5 Quantum Yield

The fluorescence quantum yields (Φ_F) of many of the (B)Chl molecules used in this study have been measured at room temperature in various solvents. However, the fluorescence quantum yield depends on solvents (Hindman et al. 1978; Seely & Connolly 1986) and temperature (Broyde & Brody 1967; Pospísil 1998), (e.g. Φ_F of Chl *a* in ethanol increases by 64% between 300K and 77K (Broyde & Brody 1967)). Since all the phosphorescence measurements in this study have been performed at 77K, the fluorescence quantum yield at this temperature should be used to compute the absolute phosphorescence quantum yield. Therefore, only the relative phosphorescence / fluorescence quantum yields at 77K are given in Table 4.1.

4.5 Computational Results

The results of the DFT calculations were compared to the measured values for ten (B)Chls (Table 4.2, Figure 4.3). These calculations produced excellent agreement with experiment with an average deviation of 0.03 eV from experimentally measured values for the porphyrin and chlorin type molecules and an average deviation of 0.22 eV from experiment for bacteriochlorin type molecules (BChl *a*, *b*, and *g*). The correlations observed between the experimental and calculated values (Figure 4.3) now allow for prediction, by use of a standard computational package, of the triplet states of molecules not directly measured. Triplet state energies for Chl c_1, Chl *f*, and BChl *f* were estimated using this method (

Table 4.3, Figure 4.3).

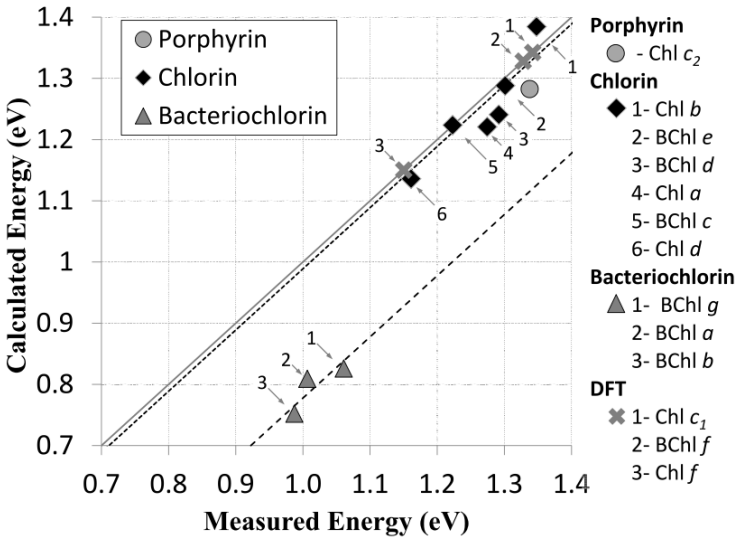

Figure 4.3: Triplet state energies calculated by DFT plotted against experimentally measured values. Dotted (Dashed) line: least squares fit with slope constrained to one for chlorin (bacteriochlorin) type molecules. Reprinted with permission from (Hartzler et al. 2014). Copyright 2014 American Chemical Society.

Table 4.2 – Comparison of triplet state energies predicted by DFT to the measured values. Reprinted with permission from (Hartzler et al. 2014). Copyright 2014 American Chemical Society.

molecule	experimental eV (nm)	calculation eV (nm)	Difference meV
Porphyrin type			
Chl c_2	1.338 (927)	1.283 (966)	55
Chlorin type			
Chl *a*	1.274 (973)	1.221 (1016)	54
Chl *b*	1.348 (920)	1.385 (896)	-37
Chl *d*	1.161 (1068)	1.136 (1091)	35
BChl *c*	1.223 (1014)	1.224 (1013)	-1
BChl *d*	1.292 (960)	1.241 (999)	51
BChl *e*	1.301 (953)	1.289 (962)	12
Bacteriochlorin type			
BChl *a*	1.006 (1232)	0.809 (1532)	197
BChl *b*	0.987 (1256)	0.752 (1649)	235
BChl *g*	1.061 (1169)	0.826 (1501)	235

Table 4.3 – Triplet state energies of Chl c_1, Chl *f*, and BChl *f* predicted by DFT. Reprinted with permission from (Hartzler et al. 2014). Copyright 2014 American Chemical Society.

molecule	DFT calculation eV (nm)	corrected value[A] eV (nm)
Porphyrin type		
Chl c_1	1.34 (925)	
Chlorin type		
Chl *f*	1.15 (1078)	1.16 (1069)
BChl *f*	1.33 (932)	1.34 (925)

[A]The correction model derived in *Discussion* (Eq. 2) has been applied.

4.6 Discussion

4.6.1 Coordination State

Table 4.1 indicates that the fluorescence and phosphorescence emission maxima of the 5-coordinate state tend to be shifted towards shorter wavelengths compared to the 6-coordinate state (see Table 4.4). However, as discussed in *Sample Preparation* (this chapter), it is unknown if the observed shift in fluorescence is due to a change in

coordination state or due to other solvent effect. The differences between triplet state energies for the same species measured in this paper and in the literature (and differences within the literature) are likely to stem from coordination number and solvent effects.

Table 4.4 – The effect of molecule coordination state on the emission properties. A clear trend among the chlorin type molecules is visible in the phosphorescence and S_1-T_1 energy gap (see Figure 2.10) upon changing the coordination state from five to six. Reprinted with permission from (Hartzler et al. 2014). Copyright 2014 American Chemical Society.

	coord.[A] state	fluor. (eV)	phos. (eV)	energy gap (eV)	ref.
Chl *a*	5	1.85	1.34	0.51	B
	6	1.84	1.28	0.56	B
	Δ[C]	0.01	0.06	-0.05	
Chl *b*	5	1.90	1.42	0.48	B
	6	1.88	1.35	0.53	B
	Δ	0.02	0.07	-0.05	
Chl *d*	5	1.78	1.27	0.51	D
	6	1.76	1.16	0.60	E
	Δ	0.02	0.11	-0.09	
BChl *c*	5	--	1.29	--	F
	6	1.84	1.22	0.62	E
	Δ	--	0.07	--	
BChl *d*	5	--	1.35	--	F
	6	1.86	1.29	0.57	E
	Δ	--	0.06	--	
BChl e	5	--	1.35	--	E
	6	1.86	1.30	0.55	E
	Δ	--	0.05	--	
BChl *a*	5	1.60	1.02	0.58	G
	6	1.56	1.01	0.55	E
	Δ	0.04	0.01	0.03	

[A] Note, different coordination states are achieved, in general, by use of different solvents (Krawczyk 1989; Callahan & Cotton 1987);
[B] (Solov'ev et al. 1983); [C] Δ denotes the difference between 5 and 6 coordinated states;
[D] (Neverov et al. 2011); [E] (This work); [F] (Krasnovsky Jr et al. 1993); [G] (Takiff & Boxer 1988b)

In the course of this study it was observed that a diethyl ether:petroleum ether (1:1, v/v) solvent resulted in a uncontrolled mixture of 5- and 6-coordinate molecules, while a toluene:pyrinine (4:1, v/v) solvent nearly universally resulted in 6-coordinate

molecules. The exceptions were Chl *c*$_2$ and BChl *e* molecules, which were likely mixtures of coordination states. By exciting the Chl *c*$_2$ and BChl *e* samples on the long wavelength side of the Q_y absorption band the 6-coordinated states could be predominantly excited, diminishing the influence of the other states. Note, Chl *c*$_2$ was dissolved in MeOH:THF rather than toluene:pyridine, as described in *Sample Preparation*. Control of coordination state, either through choice of solvents or selective excitation, is important since mixtures of these states can produce emission maxima intermediate to the different coordination states. One side effect of the selective excitation procedure used in this study is a reduced signal to noise due to exciting the sample in a spectral region where its absorbance is intrinsically low (see Chl *c*$_2$ and BChl *e* in Figure 4.1).

The data of Table 4.4, in addition to clearly demonstrating that the local chemical environment can have a significant effect on the triplet state energy, suggest that an empirical relationship exists between the energies of the fluorescence and phosphorescence maxima. Both the fluorescence and phosphorescence bands shift to lower energies as the coordination number increases from 5 to 6 with the singlet excited state shifting ~10 meV and the chlorin type triplet excited state shifting 60 to 110 meV (Table 4.4). However, it is not as simple as a constant energy difference between the singlet excited and triplet excited states, because the fluorescence to phosphorescence energy difference is larger for 6-coodinate chlorin type molecules compared to 5-coordinated molecules of the same kind (Table 4.4). As discussed earlier, it is unknown if the changes in the singlet state emissions (fluorescence) are due to differences in coordination state or other solvent effects. However, we can confidently say that the

coordination state affects the triplet state energy since our experiment shows that BChl *e* possessed two phosphorescence emitting species in the same solvent that are consistent with the 5- and 6- coordinated states (Figure 4.2). The long wavelength form of BChl e possessed a phosphorescence emission peak at 953 nm, consistent with the value predicted by DFT (Figure 4.3, Table 4.2), while the phosphorescence emission peak of the short wavelength form was shifted by 41 nm (50 meV) to 912 nm, a difference consistent with the values reported in the literature for the 5- and 6- coordination states of other molecules (Table 4.4).

4.6.2 Pigment Environment

It is known that the local pigment environment, whether it is a solvent or protein environment, can shift the singlet state energies of (B)Chl molecules as observed through absorption and fluorescence. The Q_y absorption maximum of Chl *a* monomers in pyridine is 671 nm (Niedzwiedzki & Blankenship 2010) while the Q_y absorption maximum of Chl *a* bound in the cytochrome b_6f complex of spinach and *Mastigocladus laminosus* are 668 nm and 673 nm respectively (Zhang et al. 1999) and in photosystem I (PSI) Chl *a* molecules have absorption maxima between about 670 and 720 nm (Savikhin, Xu, et al. 1999). For BChl *a*, the Q_y absorption maximum of monomers in pyridine is 781 nm (Niedzwiedzki & Blankenship 2010) while bound in the CmsA pigment-protein complex of *Chloroflexus aurantiacus* the Q_y absorption maximum is shifted to 795 nm (Sakuragi et al. 1999). Both PSI and the CmsA complex show that a ~10 to 30 meV shift in the absorption maximum is possible due to pigment-pigment and pigment-protein interactions. This shift is comparable to the fluorescence maxima shift (~10 to 20 meV)

between the 5- and 6-coordinated states from Table 4.4. Since the pigment-solvent interactions explored in Table 4.4 are known to shift the singlet state energies of (B)Chl molecules by approximately the same amount as pigment-pigment or pigment-protein interactions, it may stand to reason that the triplet state energies also experience a shift due to pigment-pigment or pigment-protein interactions on the order of ~50 meV, similar to the shift observed in Table 4.4**.**

The energies of the 6-coordinate BChl *a* and BChl *b* triplet states are only ~30 meV and ~10 meV higher than the energy of singlet oxygen (0.96 eV). Given that pigment-solvent interactions (via change of coordination state) has been shown to shift the triplet state energies of several chlorin type molecules by up to 110 meV (Table 4.4), it is possible that pigment-protein interactions could shift the triplet state energies of BChl *a* and BChl *b* below the energy of singlet oxygen, which would inhibit energy transfer from the BChl triplet state to O_2 and thereby eliminate the need for carotenoids for photoprotection. This is possibly the reason why, for example, the Fenna-Matthews-Olson (FMO) complex contains a number of BChl *a* molecules but no carotenoids (Li et al. 1997).

As mentioned, the triplet excited state energy could also be affected by pigment-pigment interactions. For example, BChl *c*, BChl *d* and BChl *e* are known to self-assemble into highly aggregated, semi-crystalline structures in the chlorosomes of green sulfur bacteria (Orf & Blankenship 2013). The triplet state energies of monomeric 6-coordinate BChl *c*, *d*, and *e* are 250 meV, 320 meV, and 330 meV, respectively, higher than the energy of singlet oxygen. Thus these molecules, in their monomeric state, could

readily sensitize the formation of singlet oxygen. However, in a study involving carotenoid-free mutants of BChl *c* containing chlorosomes, Kim et. al. (Kim et al. 2007) demonstrated the existence of a novel photoprotection mechanism that is not based on carotenoids in these highly aggregated antenna structures.

In the aggregated state, these molecules experience strong pigment-pigment interactions resulting in a 60 to 80-nm red shift of the Q_y absorption maximum by singlet exciton coupling (Orf & Blankenship 2013). The close proximity of each pigment molecule to its neighbors (Orf & Blankenship 2013; Ganapathy et al. 2009) also results in strong π-π interactions which may allow the formation of triplet excitons (Kim et al. 2007). It was suggested that the formation of the triplet excitons in the BChl aggregates can be sufficient to lower the triplet excited state energy below that of singlet oxygen, resulting in the enhanced photoprotection observed in the BChl *c* aggregates of the carotenoid-less mutant (Kim et al. 2007). Evidence for the formation of triplet excitons in pigment aggregates has recently been demonstrated by Eaton et. al. (Eaton et al. 2013) using a derivative of the artificial pigment PDI. In the closely packed PDI aggregates, the triplet state energy was observed, by phosphorescence spectroscopy (next part of this chapter), to drop by 140 meV relative to the monomer (Eaton et al. 2013). Triplet exciton formation will be investigated in detail in a later chapter.

Two known natural systems where either triplet coupling between BChl molecules or pigment-protein interactions have lowered the triplet states energies below that of singlet oxygen are the RC special pairs of *Rhodobacter sphaeroides* and *Blastochloris viridis* (formerly *Rhodopseudomonas viridis* (Hiraishi 1997)) (Takiff &

Boxer 1988a). These special pairs, which consist of two tightly coupled BChl molecules, show phosphorescence at 1318 nm (0.94 eV) and 1497 nm (0.83 eV) for the BChl *a* and BChl *b* containing species, *R. sphaeroides* and *B. viridis* respectively (Takiff & Boxer 1988a). Thus the triplet state energies of these BChl *a* and BChl *b* special pairs are significantly lowered with respect to the corresponding monomers and even below the level of singlet oxygen (0.975 eV). It is unknown if this offers any photoprotection to these organisms, however, it is known that *B. viridis* does not tolerate oxygen (Lang & Oesterhelt 1989). Both organisms still require carotenoid protection for the pigments of their light harvesting antenna and other RC pigments (Ziegelhoffer & Donohue 2009).

4.6.3 Vibrational levels of fluorescence and phosphorescence

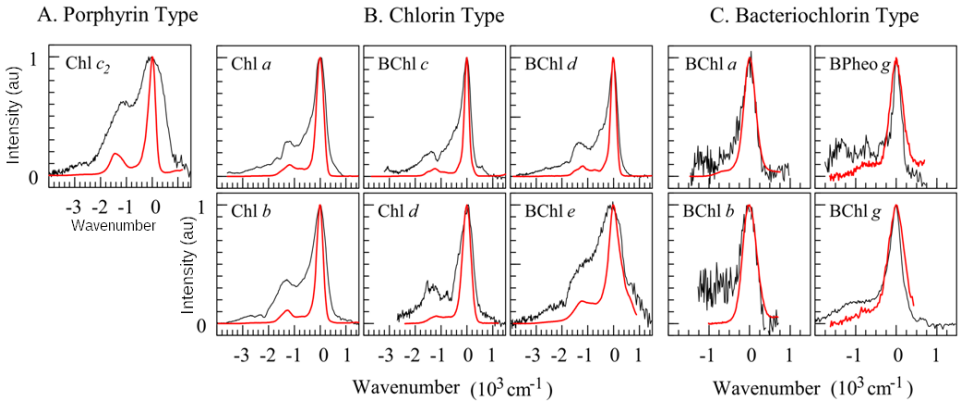

Figure 4.4: The vibrational structure of the fluorescence emission (red) and phosphorescence emission (black) are highlited by plotting both on an energy scale and aligning the origin bands (i.e. the 0-0 transition). Adapted with permission from (Hartzler et al. 2014). Copyright 2014 American Chemical Society.

Inspection of the emission spectra (fluorescence and phosphorescence) on an energy scale (Figure 4.4) reveals that for the chlorin- and porphyrin-type molecules the locations of the major vibrational peaks are approximately the same, except for a shoulder on the low energy side of the main phosphorescence peak. The bacteriochlorin-

type molecules show a much larger deviation for the higher vibrational modes, especially BChl *b* with a large (but poorly resolved) vibrational band in the phosphorescence that has no corresponding band in the fluorescence. However, the vibrational bands are much more intense with respect to the main band (the 0-0 transition) in phosphorescence compared to fluorescence (Figure 4.1) so the "missing" bands in the fluorescence may be present, but not visible. This intensity difference indicates a different coupling strength between the vibrational modes and the electronic transition in triplet and singlet excited states.

4.6.4 DFT calculations

DFT calculations were performed with several simplifications such as truncated phytyl tails and in vacuum with no axial ligands to Mg^{2+} ion. Nevertheless almost perfect agreement of calculated energy differences with the measurements for the porphyrin and chlorin types (all with deviations within 5% of the measured values) was found (Table 4.2, Figure 4.3). At the same time, it is not clear why DFT consistently over-stabilizes the triplet states of bacteriochlorin type molecules.

The good linear correlation between the experimental values and DFT predicted values, however, allows one to propose corrections for the DFT calculations (Figure 4.3). We grouped molecules into two classes according to their structures (chlorin and bacteriochlorin types) and assumed a constant offset between the DFT calculated and experimental values. A linear least squares fit with the slope constrained to one yielded the following corrections of the calculated energies, E_{DFT}, and measured energies, $E_{triplet}$

for each class of molecule (error is defined as the standard deviation from the fit) (Hartzler et al. 2014):

$$E_{\text{triplet, chlorin}} = E_{\text{DFT}} + 0.01\ (\pm 0.03)\ \text{eV}$$

$$E_{\text{triplet, bacteriochlorin}} = E_{\text{DFT}} + 0.22\ (\pm 0.02)\ \text{eV}$$

Equation 4.1

While other, more sophisticated, correction models may produce better results, the small number of data points precludes a more detailed analysis. The results of these calculations can be found in Table 4.2 and Figure 4.3.

Subsequent measurement of the phosphorescence spectrum of BChl *f* (Figure 4.5) has verified the predictive power of the model. BChl *f* was extracted from the bchU mutant of *Chlorobaculum limnaeum* (Vogl et al. 2012), using the same method as BChl *d*, and measured using the previously described phosphorescence spectrometer. The measured triplet state energy of BChl *f* in the 6-coordinate state is 1.355 eV (+/- 14 meV), while the predicted value from Equation 4.1 is 1.34 eV (+/- 30 meV) (

Table 4.3). The full uncertainty range of the measured value falls within the error bounds of the predicted value, showing good agreement with the model.

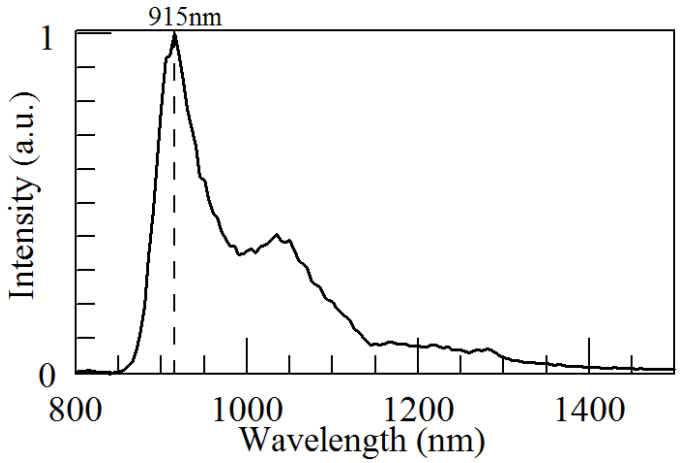

Figure 4.5: Phosphorescence emission spectrum of 6-coordianted BChl *f* in 4:1 (v/v) toluene/pyridine at 77K. Measured at ~20 nm bandwidth (expected error +/- 10 nm).

4.7 Conclusion

The triplet state energies of ten natural chlorophyll (Chl *a*, *b*, c_2, *d*) and bacteriochlorophyll (BChl *a*, *b*, *c*, *d*, *e*, *g*) molecules and one bacteriopheophytin (BPheo *g*) have been directly determined under comparable conditions from their phosphorescence spectra. Additionally, calculation of the triplet state energies of these molecules with a commonly used DFT functional and basis allowed for empirical calibration of the method, which in turn allowed for prediction of the triplet state energies of three additional molecules – Chl c_1, Chl *f* and BChl *f*. Subsequent measurement of BChl *f* confirmed the strength of this method.

The major contribution to the spectral properties of a (B)Chl molecule comes from the macrocycle structure (i.e. porphyrin, chlorin, or bacteriochlorin type) and both the fluorescence and phosphorescence (Figure 4.1, Table 4.1) of the chlorin and bacteriochlorin type molecules can be broadly grouped into their respective categories with the lowest energy singlet and triplet transitions associated with the bacteriochlorin

type while the one porphyrin type aligns with the upper range of the chlorin type molecules. Furthermore, both the relative quantum yield and the phosphorescence emission lifetime can also be grouped in this manner, with the chlorin-type molecules possessing longer phosphorescence emission lifetimes and higher relative quantum yields compared to the bacteriochlorin types (Table 4.1). The one porphyrin-type molecule studied, again, aligns with the upper range of the chlorin-type molecules. Variations within these subgroups depend on the location and type of functional groups attached to the macrocycle, with electron donating or withdrawing groups having a strong effect.

The results show that it is energetically favorable for each of the molecules studied to sensitize the formation of singlet oxygen. However, the results also suggest it may be possible for pigment-pigment or pigment-protein interactions to lower the (B)Chl triplet state energy below that of singlet oxygen, making sensitization energetically unfavorable. This lowering of the triplet state energy could confer a novel type of photoprotection.

CHAPTER 5 – TRIPLET-TRIPLET COUPLING

The effects of triplet-triplet (T-T) state couplings between nearby molecules were investigated by phosphorescence spectroscopy and computational methods. Experimentally measured systems were Chl *a* and protoporphyrin IX (PPIX) dimers as well as linear aggregates of (derivatives of) the molecule perylene-3,4:9,10-bis(dicarboximide) (PDI). Computational modeling allowed for extraction of T-T coupling from other effects (like solvation) for chlorin systems in addition to the development of a general T-T coupling model in porphyrin and chlorin systems.

5.1 Triplet-Triplet Coupling in Dimeric Systems

Homodimers were successfully formed with two different molecules, Chl *a* and PPIX, while limited success was achieved with BChl *a*.

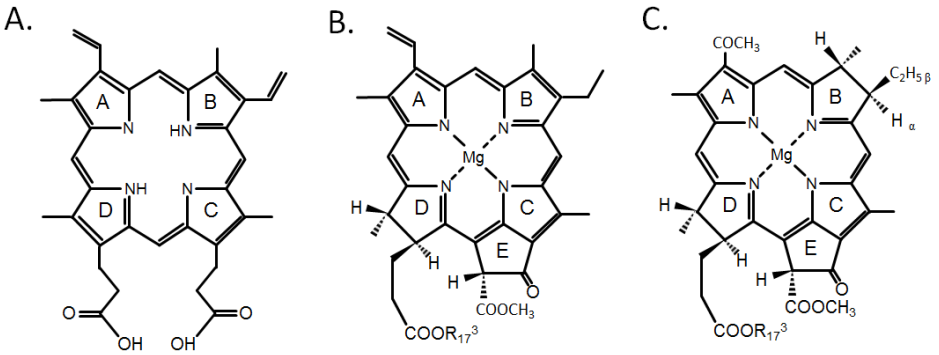

Figure 5.1: Chemical Structures of: A – Protophophyrin IX (PPIX). B - Chlorophyll *a* (Chl *a*). C – Bacteriochloropyll *a* (BChl *a*)

5.1.1 Sample Preparation

PPIX disodium salt, BChl *a*, and Chl *a* were purchased from Sigma-Aldrich and used without further purification. PPIX monomers and dimers were prepared similar to Scolaro (Monsù Scolaro et al. 2002). Dimers were made by injecting a concentrated stock solution of PPIX in dimethyl sulfoxide (DMSO) into a solution of sodium hydroxide with pH = 11.5 (solution contained approximately 5% DMSO by volume). Monomers were made by injection of stock solution into a solution of hydrochloric acid (HCl) with pH = 1.2 which produced a sample consisting primarily of monomers with a small amount of aggregate (solution contained approximately 5% DMSO by volume). Methanol (MeOH) was added to the acid solution to disrupt the aggregates. Both samples were then mixed with glycerin before freezing. For the sample consisting of dimers the final mixture was 40% NaOH solution with 60% glycerin (by volume), while for the monomers the final mixture was 40% HCl solution with 15% MeOH and 45% glycerin (by volume). No significant differences were noted in the absorption spectrum at 77K when compared to the room temperature absorption (Figure 5.2).

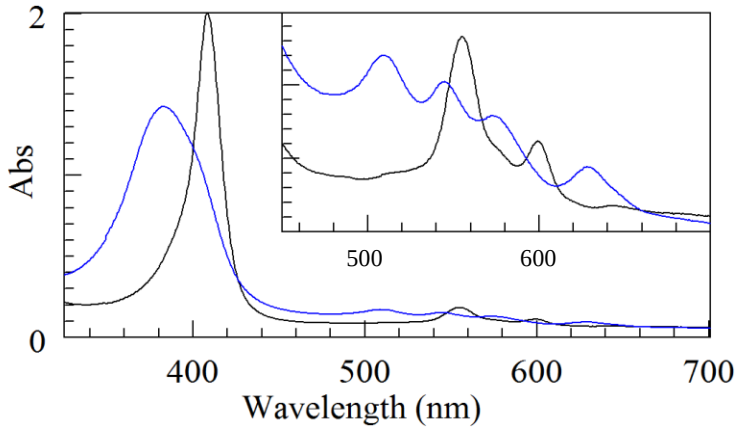

Figure 5.2: Absorption spectrum of PPIX monomers (BLACK) and dimers (BLUE) at room temperature.

Chl *a* dimers were prepared by dissolving the sample into room temperature water saturated toluene and plunging into liquid nitrogen (LN2). The toluene was saturated by adding an excess of water (500 uL water in 2-3 mL toluene) to the vial, which was then mixed with a vortex mixer and allowed to sit overnight. Upon freezing an additional absorption band centered at 708 nm was observed to the red of the monomeric Q_y absorption band (centered at 673nm) (see Figure 5.3). Analysis of the data of Figure 5.3 shows convincing evidence that the 708 nm absorbing species is indeed a dimer, as opposed to another type of aggregate.

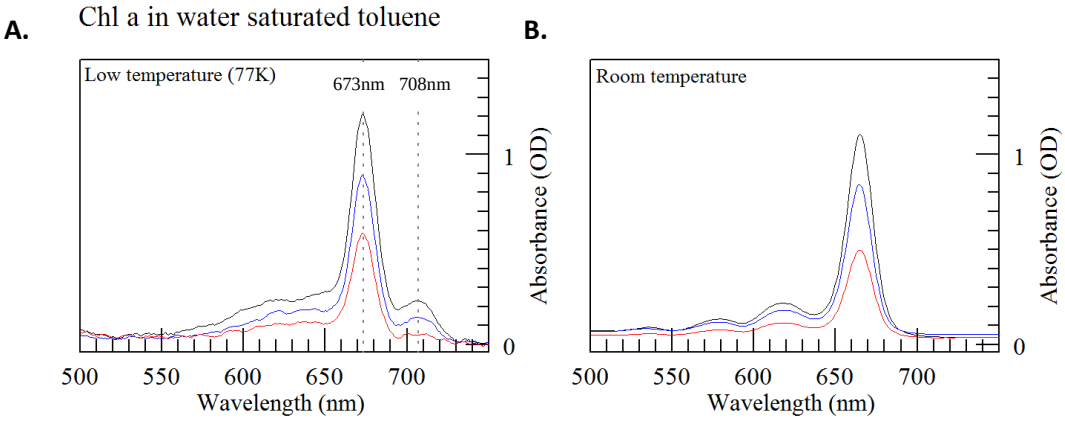

Figure 5.3: Chl *a* absorption spectrum at three concentrations and at room temperature **(B)** and 77K **(A)**. Note the appearance of the peak at 708 nm. [In collaboration with Dr. Shigeharu Kihara]

5.1.2 Evidence of dimers

If the additional absorption band belongs to a dimeric species that is in equilibrium with the monomer, its concentration is related to the monomer concentration by:

$$k = \frac{c_D}{{c_M}^2}$$

Equation 5.1

Where ‘k’ is the equilibrium constant. Taking the log of Equation 5.1 shows that one would expect a plot of $\log(c_D)$ vs. $\log(c_M)$ to have a slope of two if the new species is a dimer.

$$log(c_D) = 2 * \log(c_M) + \log(k)$$

Equation 5.2

The concentration of the monomeric and dimeric species can be related to the intensity of their absorption bands by the Beer-Lambert law (Equation 2.47):

$$A = \varepsilon l c$$

Equation 2.47

Solving the Beer-Lambert law (Equation 2.47) for *c* and inserting it into Equation 5.2 (for the monomer and dimer) gives:

$$log(A_D) = 2 * log(A_M) + const.$$

Equation 5.3

Where ‘const.’ includes the constant "$log(\varepsilon l)$" term from each absorbing species.

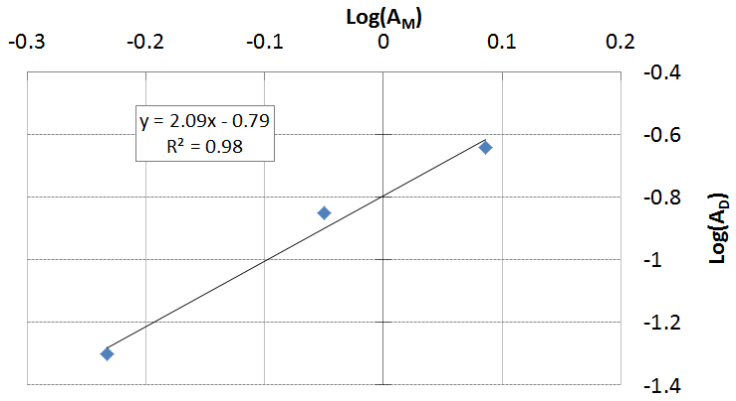

Figure 5.4: Log base 10 of 708 nm absorption vs log of 673 nm absorption from Figure 5.3 (77K)

Plotting the log of the 708 nm absorption maximum verses the log of the 673 nm maximum for three concentrations gives a line with a slope of approximately 2 (Figure 5.4), which is consistent with a dimer. It is understood that absorbance originating from the dimeric species underlies the 673 nm absorption peak, but it is assumed to be a minor contributor to the full amplitude.

5.1.3 Extraction of Dimeric Chl *a* Absorption Spectrum

In Figure 5.3A we see the composite absorption spectrum of a mixture of Chl *a* monomers and dimers. Given the absorption spectra of a concentration series, like in Figure 5.3A, it is possible to extract the spectrum of the individual absorbing species using the method of West & Pearce and Rohatgi & Mukhopadhyay (West & Pearce 1965; Rohatgi & Mukhopadhyay 1971) (see APPENDIX for code), assuming that the relative concentration of each species is dependent on the total concentration and the total absorbance of the sample is a linear combination of the absorbance of each species (instrument errors, like clipping, can affect this). The first condition is met by the dimer-

monomer equilibrium in Equation 5.1 and assuming the second condition is true we get from the Beer-Lambert law (Equation 2.47):

$$A = \varepsilon_M c_M l + \varepsilon_D c_D l$$

Equation 5.4

Letting *c* equal the total concentration ($c = c_M + 2c_D$), Equation 5.4 can be rewritten so that the reduced absorbance, $A' = {}^{A}/_{cl}$, is linear function of the reduced monomer concentration, $c' = {}^{c_M}/_{c}$.

$$A' = \left(\varepsilon_M - \tfrac{1}{2}\varepsilon_D\right) c' + \tfrac{1}{2}\varepsilon_D$$

Equation 5.5

Thus knowing the total initial concentration, *c*, and the monomer mole fraction, *c'*, for each spectrum in Figure 5.3A one can simply compute the slope and intercept at each wavelength to extract the unique monomeric and dimeric extinction coefficients. In the absence of direct knowledge of the monomeric mole fraction, the monomer concentration (c_M) and total concentration (*c*) for each absorption curve can be used as global fitting parameters. The resulting spectra when this technique is applied to Figure 5.3A are shown in Figure 5.5. An interesting result of this analysis is that the singlet excitonic bands have been shifted significantly to the red. Additionally, the Soret band is also shifted by approximately 10 nm (compared to the monomer) from 445 nm to 455 nm, a fact easily identifiable in fluorescence excitation spectra (data not shown).

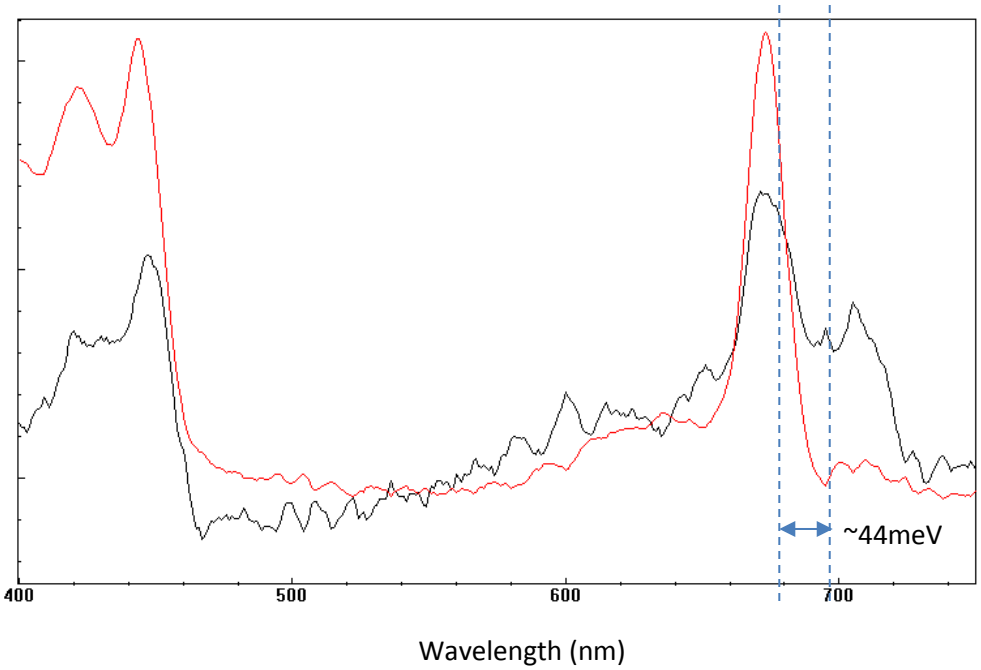

Figure 5.5: Extracted monomeric (**RED**) and dimeric (**BLACK**) absorption spectra. Note the red shift of the Soret (~10 nm to 455 nm) and the two excitonic bands at approximately 674 nm and 707 nm.

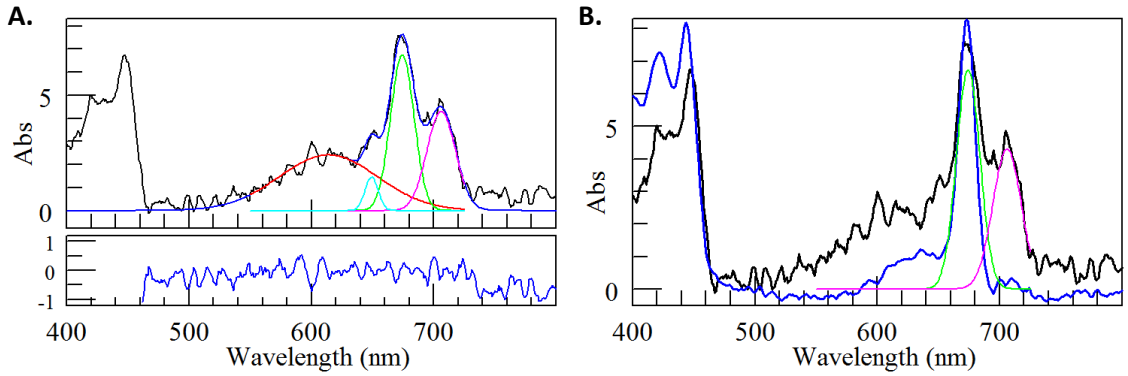

Figure 5.6: A – Extracted dimer absorption spectrum (BLACK) with fit (BLUE) and four Gaussian components (RED, CYAN, GREEN, MAGENTA). Only the Green and Magenta components can be used with any confidence, as the Red and Cyan components likely correspond to a collection of overlapping bands whose features are masked by the noise. B – Dimer (BLACK) with two long wavelength fit components and the monomer (BLUE).

Decomposing the dimer spectrum into its component Gaussian bands shows the two low energy excitonic bands lay at 674 nm and 706 nm (Figure 5.6). Comparing these two bands to the monomer peak (673 nm), we see the excitonic system has experienced a significant shift compared to the monomer with the average position of the bands lying at 690 nm, a 17 nm red shift or ~44 meV drop in energy with respect to the monomer.

5.1.4 Dimer structures

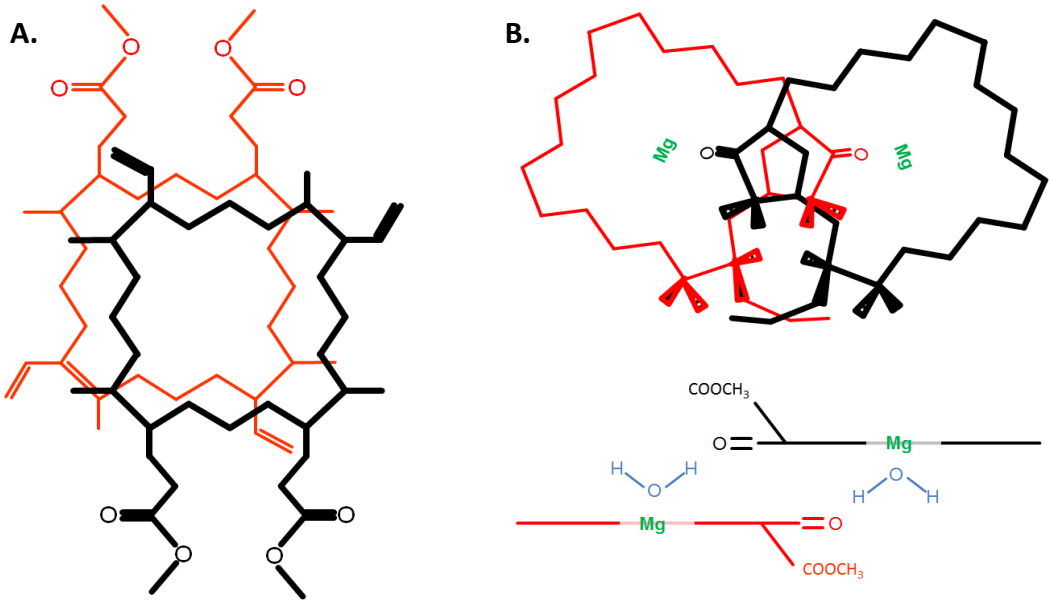

Figure 5.7: Structure of PPIX and Chl *a* dimer (Black is on top) A - PPIX dimer (face view). B –Chl *a* dimer (face view and size view). Note the involvement of water in the formation of the Chl *a* dimer.

The structure of the PPIX dimer (Figure 5.7A) is obtained from the ^{1}H-NMR (proton Nuclear Magnetic Resonance) data of Janson (Janson & Katz 1972). Proton chemical shifts are measured as a function of aggregate concentration, revealing which protons are strongly shielded by the porphyrin macrocycle upon dimer or aggregate formation and which protons are least affected (producing an aggregation map, Figure 5.8).

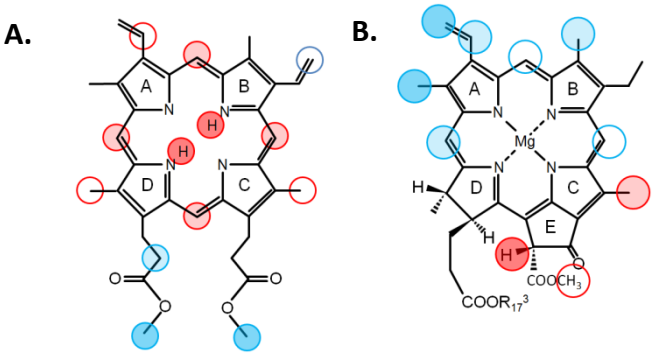

Figure 5.8: ^{1}H-NMR aggregation map of **A -** PPIX (Janson & Katz 1972) and **B -** Chl *a* (Katz & Brown 1983). Maps are produced by titration of an aggregate with an aggregate disrupting solvent. Proton chemical shifts are color coded as percentage of maximum shift. 100-30% maximum shift (filled red → open red). 15-2% maximum shift (open blue → filled blue).

The Chl *a* dimer structure (Figure 5.7B) is inferred from data collected by a variety of methods. NMR (Figure 5.8B) and x-ray crystallography work (Figure 5.9) with aggregates of Chl *a* and Chl *a* like molecules (usually lacking part of the tail (R_{17}) and sometimes the R_{13}^{2} methyl ester) (Abraham et al. 1989; Abraham & Rowan 1991; Katz & Brown 1983; Strouse 1974), show that the monomers primarily overlap at the E and C rings (Figure 5.8 B and Figure 5.9) while x-ray crystallography and Raman data show water molecules are bound as shown in Figure 5.7B (the oxygen coordinated to the Mg^{2+} and one hydrogen bonded to R_{13}^{1} ketone of the neighboring Chl) (Shipman et al. 1976b; Strouse 1974). However, the crystalline aggregate is unlikely to have the same relative monomer orientation as the free dimer.

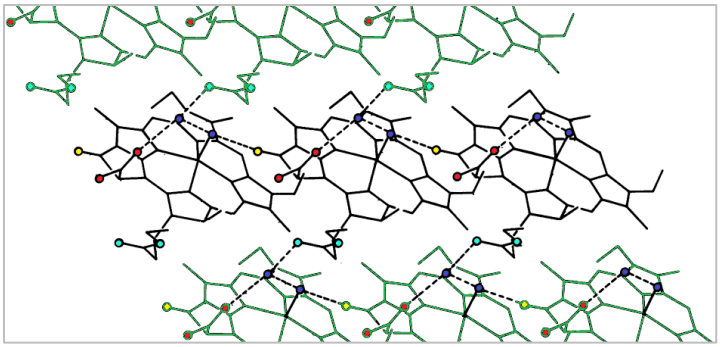

Figure 5.9: X-ray crystal structure of ethyl Chorophillide *a* (Strouse 1974). Oxygen atoms are color coded as follows: Water - Dark Blue, R_{13}^1 ketone – Yellow, R_{13}^2 methyl ester – Red, R_{17} (tail) ethyl ester – Cyan. Hydrogen bonds are dashed lines.

Chl a is known to form two dimer types, a non-fluorescent dimer with only a slight red shift of the Q_y absorption maximum (~680 nm) and a fluorescent dimer with a more significant Q_y red shift (to ~700-710 nm) (Livingston & Weil 1952; Amster & Porter 1967; Cotton et al. 1978). The non-fluorescent dimer only forms in very dry "soft" non-polar solvents (non-polar, but polarizable) while the fluorescent dimer forms in soft non-polar solvents with a small amount of polar solvent containing an OH group (or equivalent). Fluorescence can be returned to the non-fluorescent dimers by adding a small amount (1:1 or higher molar ratio) of nucleophilic solvent (i.e. one that will coordinate to the Mg^{2+}), however only adding a solvent containing an OH or equivalent (coordinating and h-bonding) will produce the ~700-nm absorbing dimer (Cotton et al. 1978). Addition of a solvent like pyridine (coordinating only) will produce only monomers (Cotton et al. 1978).

Shipmann et. al. proposed the model shown in Figure 5.7B based on excitonic calculations and IR absorption data on the 700-nm absorbing Chl *a* dimer and x-ray crystallography on Chl *a* like molecules (Shipman et al. 1976b). Their data shows that the 700-nm dimer forms in dry toluene only after the addition of an approximately 1.5 molar

ratio of ethanol and the R_{13}^1 ketone experiences a large shift in its IR absorption indicating hydrogen bonding upon dimer formation. The other oxygen containing groups, the R_{13}^2 and R_{17}^3 esters, show no h-bonding upon dimer formation (unlike in the crystalline aggregates, Figure 5.9). Excitonic calculations, using the point transition dipole approximation, are consistent with the model (Figure 5.7B) derived from IR, NMR, and x-ray data (Shipman et al. 1976b; Shipman et al. 1976a).

5.1.5 BChl *a* and BChl *c*

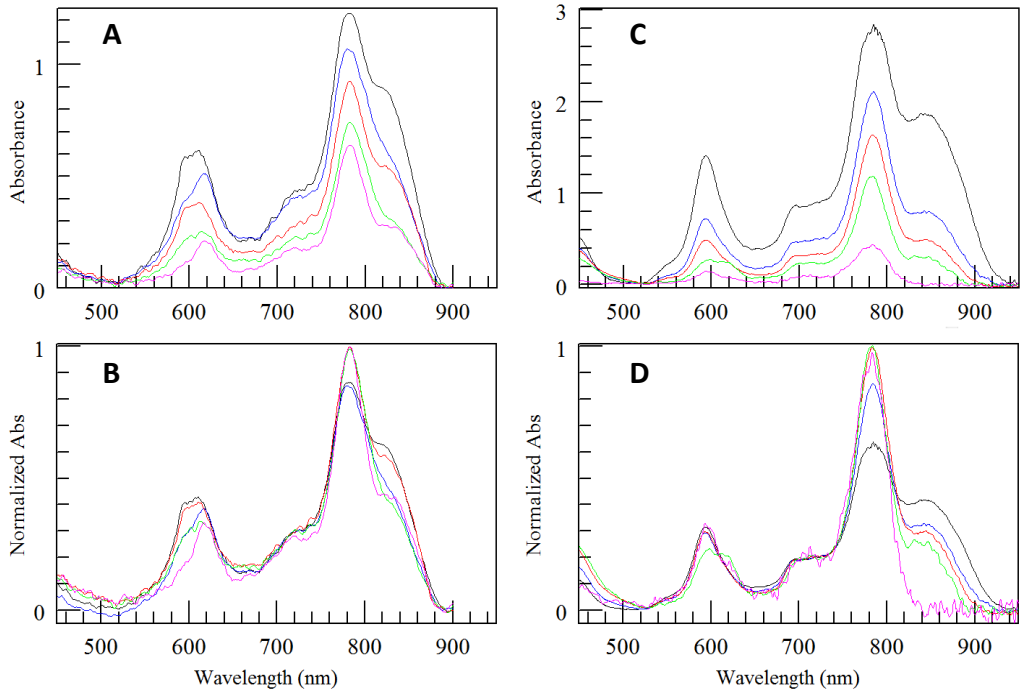

Figure 5.10: Absorption spectrum of BChl *a* in water saturated toluene at 77K. **A,B –** Low concentration series. Samples were plunge frozen in LN2 starting from room temperature. **C,D –** High concentration series. Samples were precooled to -80 °C before plunge freezing in LN2. All spectra were taken in 1 mm path length borosilicate cells. The Spectra in B and D were normalized at 700 nm to avoid the effects of saturation (Black and Blue spectra). [In collaboration with Dr. Shigeharu Kihara]

Attempts to produce dimers of BChl *a* using the same method used for Chl *a* produced poor, difficult to reproduce results. In the course of trying to prepare this

sample, it was discovered that BChl *a* dimerization is highly sensitive to the conditions before and during freezing. It was noticed that BChl *a* samples in near identical conditions produced different results depending on which (handmade) cell they were housed in (note the variations in the 595 and 825 nm bands in Figure 5.10B). The cooling rate likely influences the final product as sample volume and the cell size/geometry change the volume of solvent and glass to be cooled, thus some cells cooled faster than others.

In Figure 5.10A are the absorption spectra for five different concentrations of BChl *a*, frozen by plunging into LN2 directly from room temperature. It is known that the Q_x band is a sensitive probe of the BChl *a* coordination state with the (room temperature) 5-cooridnate state Q_x band peaked at 580 nm and the 6-coordinate peak at 610 nm (Kania & Fiedor 2006). In Figure 5.10A the appearance of a band at ~595 nm with increasing BChl *a* concentration suggest that the population of 5-coordinate molecules grows with increasing BChl *a* concentration concurrently with the growth of a band at ~825 nm. Additionally, if the same kind of analysis as in Figure 5.4 is applied to the absorption amplitudes at 625 and 590 nm in Figure 5.10A, the resulting slope is approximately 1.5 (as opposed to two, Equation 5.3) which is suggestive that the 625 nm and 590 nm bands correspond to a monomer and dimer respectively. This, together with the constant spectral width of the peak at ~825 nm (Figure 5.10B), suggest that a dimer forms in a 5-coordinated state with a Q_y absorption maximum at 825 nm.

Figure 5.10C and D demonstrate the formation of a higher order aggregate. These were formed by precooling high concentration samples to -80 °C before plunging in to

LN2. Notice that the samples are primarily in the 5-coordinated state while the long wavelength band widens and shifts to longer wavelength with increasing concentration. Interestingly, the lowest concentration sample (purple, Figure 5.10C & D) shows evidence of being in a 5-coordinated state as opposed to the 6-coordinated state dominating in Figure 5.10A and B. This difference is likely due to the precooling of the sample before plunge freezing in LN2, suggesting that the cooling rate may be important for the final product.

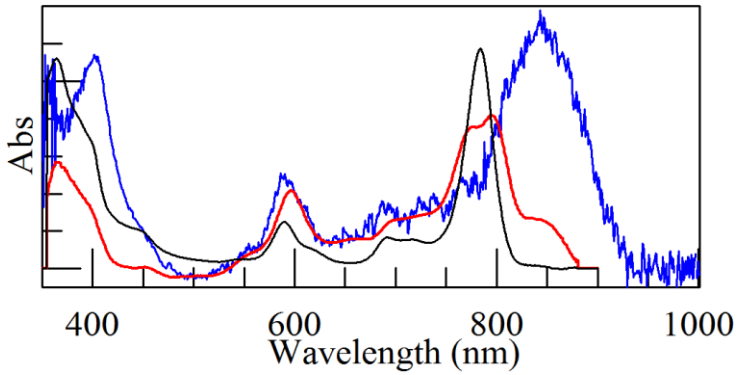

Figure 5.11: Extracted spectra from Figure 5.10A - monomer (BLACK) and aggregate (RED). Aggregate spectrum extracted from Figure 5.10C is shown in BLUE (extracted monomer not shown).

Applying the procedure described in section 5.1.3 to the spectra of Figure 5.10C produces a 100 nm wide near featureless band centered at 845 nm (Figure 5.11), supporting the large aggregate hypothesis. Analysis of the spectra of Figure 5.10A produces what appears to be three separate bands (Figure 5.11). It is unclear what these bands represent and there are a number of distinct possibilities. The bands at 775 and 795 could be an artifact of the procedure caused, for instance, by clipping of the absorbance spectra by the spectrometer. Spectrometers are known to round off of absorbance peaks in high density samples which is clearly evident in Figure 5.10D (obviously clipped

spectra were excluded from any calculations). These three bands could be the overlapping absorption peaks from a mixture of different absorbers like a dimer and a higher order aggregate or two different types of dimer. Finally, it could be the excitonic band structure of a single type of higher order aggregate such as a trimer or tetramer.

In addition to Chl *a* and BChl *a*, attempts were made to form dimers with BChl *c*. The only result achieved, using water saturated toluene and 2:1 (v/v) dichloromethane / toluene, were higher order aggregates which Olson et. al. suggest are tetrameric (Olson & Pedersen 1990; Olson & Cox 1991; Uehara & Olson 1992). While Olson et. al. showed evidence of BChl *c* dimer formation at room temperature, during freezing the equilibrium changes such that the aggregate becomes the dominant species. It may be possible to flash freeze the sample to trap the dimeric state, however obtaining the proper sample cells (thin enough to freeze quickly and clean enough for phosphorescence measurements) is problematic.

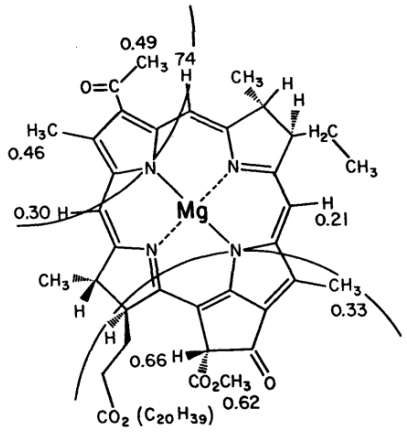

Figure 5.12: BChl *a* ^{1}H-NMR aggregation map produced by titration of a BChl *a* aggregate in benzene with pyridine (Katz & Brown 1983). Large partial circles indicate area of overlap with adjacent BChl macrocycles. Note the involvement of both the R_{13} and R_3 ketones.

The most likely reason for these difficulties originates from the fact that, unlike Chl *a*, both the BChl *a* and BChl *c* molecules have two sites that can serve as hydrogen bond acceptors or donors in dimer formation (Figure 5.12). Chl *a* possesses only one hydrogen bond acceptor, the ketone (R-CO-R') at R_{13}^{1}, that is involved in dimerization (discussed in the next section) while BChl *a* and BChl *c* possess two h-bonding sites capable of being involved in dimerization. Both BChl *a* and BChl *c* have the R_{13}^{1} ketone, like Chl *a*, in addition to a methyl ketone (R-$COCH_3$) at R_3 for BChl *a* or an alcohol (R-CHOH-CH_3) at R_3 for BChl *c* (see Figure 1.1). The presence of multiple sites capable of involvement in dimerization give BChl *a* and BChl *c* the ability to form multiple dimer types and makes aggregation more likely. This means that BChl *a* samples prepared in this way (like the Chl *a* dimers) will very likely contain an ambiguous mixture of multiple dimer types and higher order aggregates that is highly dependent on conditions just before and during freezing, while BChl *c* forms only aggregates. In fact, the only (B)Chl types having just one h-bond accepting site appropriate for dimerization, and thus capable of forming an unambiguous dimer, are Chl *a* and BChl *g* (see Figure 1.1).

5.2 Phosphorescence spectra: Dimeric Systems

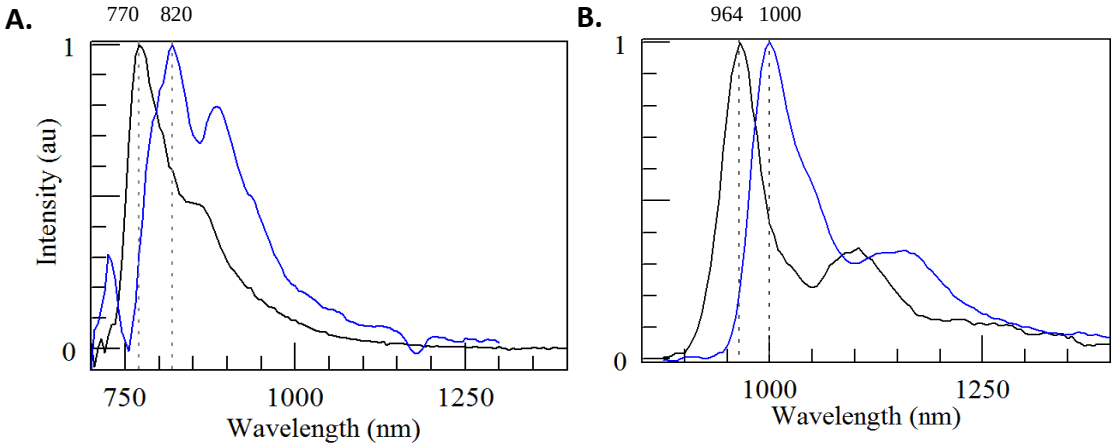

Figure 5.13: Phosphorescence emission spectra of monomers (BLACK) and dimers (BLUE) of: **A –** PPIX. **B –** Chl *a*

5.2.1 PPIX

The monomeric sample consisted of PPIX disodium salt in 40% NaOH (pH = 11.5) solution with 60% glycerin (by volume) at a temperature of 77K and was excited at 555 nm. The dimeric sample consisted of PPIX disodium salt in 40% HCl solution (pH = 1.2) with 15% MeOH and 45% glycerin (by volume) and was excited at 508 nm. The emission maxima lie at 770 nm for the monomer and 820 nm for the dimer, giving a monomer to dimer energy difference of 98 meV.

Because these samples were housed in different sample tubes, the alignment error (+/- half the monochromator bandwidth or +/- 6.4 nm in this case) affected each sample independently. This results in a monomer - dimer energy difference ranging from 73 meV to 123 meV, a spread of 50 meV. To reduce this relative error, an 800 nm LWP filter was placed just before the monochromator slits (as a wavelength reference) which reduced the

relative error to +/- half the wavelength step (+/- 2.5 nm). This results in a monomer - dimer energy difference ranging from 88 meV to 108 meV, a spread of 20 meV.

5.2.2 Chl *a*

The Chl *a* sample consisted of a mixture of monomers and dimers in water saturated toluene at 77K and the excitation wavelengths used were 660 nm and 700 nm. Exciting at 700 nm excited only the dimeric species (see Figure 5.3), producing the dimer phosphorescence emission spectrum in Figure 5.13B (BLUE). Exciting at 660 nm excited both the monomeric and dimeric species (see Figure 5.3), producing a combined phosphorescence emission spectrum (Figure 5.14).

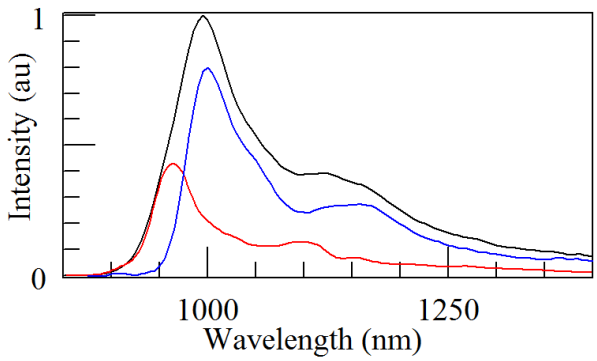

Figure 5.14: Relative contribution of monomer and dimer to combined emission spectrum. BLACK – Combined emissions spectrum (Excitation = 660 nm). BLUE – Dimer contribution. RED – Monomer contribution.

Using the dimer phosphorescence spectrum and a previous monomer spectrum (Figure 4.1) as fitting parameters, the relative contributions of the monomer and dimer to the combined emission spectrum could be determined (Figure 5.14). To perform the fit, the position of the dimer spectrum was fixed with only its amplitude allowed to vary while both the amplitude and position of the monomer spectrum were allowed to change.

Once the contribution of the dimer was determined (Figure 5.14, Blue), it was subtracted from the combined spectrum to produce the monomer phosphorescence spectrum in Figure 5.13B.

The alignment error (see Section 3.3.5) for this sample is +/- 10 nm, which places the emission maximum of the 6-coordinated monomer (973 nm, Table 4.1) within the error bounds of the monomer emission spectrum of Figure 5.13B (964 nm). The combined influence of solvent effects and alignment error (playing a large role) is the likely cause of this ~10 nm blue shift. Relative error, as discussed for the PPIX samples, is not a factor in this measurement because both the monomeric and dimeric species were contained in the same sample tube and measured during the same experiment without realignment. Since nothing was moved between measurements, the alignment errors are the same for both the monomer and dimer and thus the relative error is zero.

5.2.3 BChl *a*

As noted, producing a BChl *a* dimer with a known, unambiguous structure has proven difficult. The tendency for BChl *a* to aggregate together with the possibility of forming multiple dimer structures (Figure 5.12) severely complicates interpretation of emission spectra by allowing for a diverse population of phosphorescence emitting species to exist in a single sample. For instance, a 0.5 mM BChl *a* sample in water saturated toluene housed in a 4 mm diameter EPR tube produced a near featureless 225 nm wide phosphorescence emission band (FWHM) centered at approximately 1280 nm (Figure 5.15A). Compared to the emission band of a 5-coordineated monomer (BChl a in 2:1 toluene / trimethylamine, Figure 5.15A), the emission band of the aggregated sample

is over three times wider (225 vs. 70 nm), indicating a mixture of multiple phosphorescence emitters. Attempts to selectively excite individual species in the Q_x region (Figure 5.10A and B) failed due to either excitation saturation or a near absence of the 625 nm absorbing species (Figure 5.10) or a combination of both.

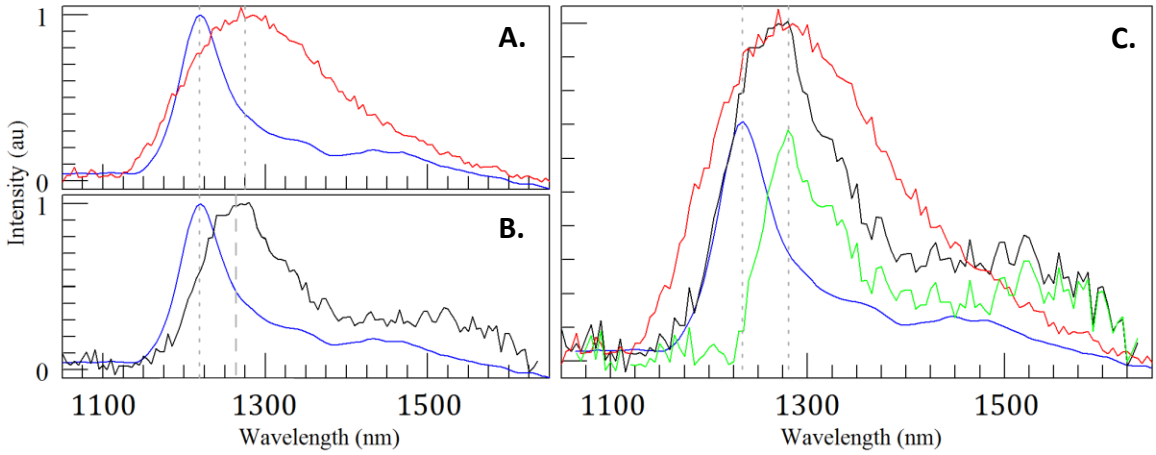

Figure 5.15: A – Comparison of 5-coordinate monomer (BLUE) and 0.5 mM combined spectrum (RED). B - Comparison of 5-coordinate monomer (BLUE) and 0.24 mM combined spectrum (BLACK). C - Relative contribution of monomers and dimers / aggregates of BChl *a* to emission spectrum of 0.24 mM sample. (NOTE: Maximum expected error = +/- 5 nm for all spectra)

Lowering the BChl a concentration by half (0.24 mM) gave significantly different results. The phosphorescence emission band in this case is 135 nm wide (FWHM) which is a factor of two larger than the monomer (Figure 5.15B). This spectrum was then fit from 1150-1400 nm using three copies of the 5-coordinated monomer spectrum (shown in blue in Figure 5.15) with each copy being allowed to vary in magnitude and position. Final peak positions for the three copies were 1234 nm (corresponding to the 6-coordinate monomer, Table 4.1, Figure 5.15C - BLUE), 1264 nm, and 1332 nm (not shown). The green curve in Figure 5.15C is the difference between the 1234 nm monomer (BLUE - Figure 5.15C) and 0.24 mM composite spectrum (BLACK - Figure

5.15C). It's likely this spectrum (green curve) is the phosphorescence emission of one or more dimer types, however, its exact origin is uncertain.

5.2.4 Emission Maxima

Table 5.1: A – Experimental error; PPIX = +/- 2.5 nm, Chl a = +/-10 nm, BChl a = +/- 5 nm. B – BChl *a* dimer structure unknown.

Molecule		Wavelength[A] nm	Energy eV (cm^{-1})	Difference meV (cm^{-1})
PPIX	Monomer	770	1.610 (12987)	98 (792)
	Dimer	820	1.512 (12195)	
Chl *a*	Monomer	964	1.285 (10363)	45 (363)
	Dimer	1000	1.240 (10000)	
BChl *a*	Monomer	1234	1.005 (8104)	36 (291)
	Dimer[B]	1280	0.969 (7813)	

5.2.5 Discussion – Dimeric Systems

The results of Table 5.1 show a consistent drop of the triplet state energy upon dimer formation, a trend predicted by excitonic theory. Furthermore, the lowering of the triplet state energies together with the structures of the PPIX and Chl *a* dimers (Figure 5.7) give evidence that the triplet-triplet coupling increases with the amount of direct contact between the molecules (specifically the conjugated π-systems). The monomers of the PPIX dimer are nearly in full face-to-face contact and the triplet state energy of the dimer is nearly 100 meV lower with respect to the uncoupled monomer. For the Chl *a* dimer, the monomers are significantly offset from one another (only overlapping at the C and E rings) and the triplet state for the dimer is nearly 50 meV lower compared to the uncoupled monomer.

5.2.5.1 Triplet Excitons

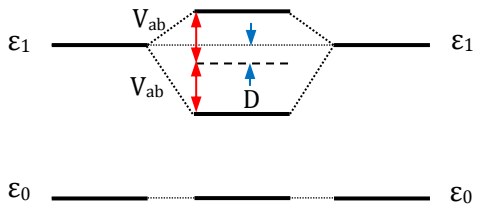

Figure 5.16: Excitonic energy levels of an identical dimer (center) showing the excitonic splitting equal to twice the coupling (V_{ab}) and the displacement energy (D). The original energy of the monomers are on the left and right.

With the two monomers in such close contact, as in the dimer, there should be a large overlap between adjacent molecular orbitals. This overlap should result in a large coupling for the triplet state (Equation 2.43) and produce a well-defined triplet exciton. To calculate that coupling we turn to excitonic theory, specifically Equation 2.38 which for a dimeric system becomes:

$$H = \begin{bmatrix} E_a + V_a & V_{ab} \\ V_{ab} & E_b + V_b \end{bmatrix}$$

Equation 5.6

Where V_a and V_b are the site energy offsets / displacement energies of the monomers (van Amerongen et al. 2000) and V_{ab} is the coupling. An identical dimer, where $E_a = E_b = \varepsilon_1$ and $V_a = V_b = D$, has solutions:

$$E_1 = \varepsilon_1 + D + V_{ab}$$
$$E_2 = \varepsilon_1 + D - V_{ab}$$

Equation 5.7

Thus the difference between the excitonic levels is twice the coupling ($E_1 - E_2 = 2V_{ab}$) and the difference between the uncoupled monomer (E_a) and the lowest energy excitonic level (E_2) is the coupling minus the displacement energy:

$$E_a - E_2 = V_{ab} - D$$

Equation 5.8

According to van Amerongen (van Amerongen et al. 2000), the displacement energy (D) is defined as the displacement of the average energy of the excitonic levels with respect to the ground state (Figure 5.16) and is comparable in magnitude to the solvation energy, i.e. the difference in energy between a molecule in solution and in the gas phase (usually negative). Recent work on the absorption spectrum of Chl *a* and Chl *b* in the gas phase (Milne et al. 2015; Stockett et al. 2015) shows the intrinsic (gas phase) Q_y absorption maximum of Chl *a* lies at 642 nm (1.93 eV) while solvated Chl *a* absorbs in the 660-680 nm (1.88-1.82 eV) range depending on the solvent, a 50 to 110 meV difference.

Also van Amerongen argues that since the displacement energy results from the interaction of the excited state electrons with all the electrons and nuclei of the other molecule, the displacement energy only slightly depends on the exact excited state of the exciton (specifically referring to doubly and singly excited singlet states, (van Amerongen et al. 2000)). Extending that line of reasoning to the triplet state, the results of the analysis in section 5.1.3 strongly suggest the displacement energy of the triplet exciton is approximately 44 meV (Figure 5.6B). If this is true, that means the coupling only plays a small role in the total energy difference between the monomer and the dimer.

5.3 Triplet Coupling in Linear Aggregates (Perylene Diimide)

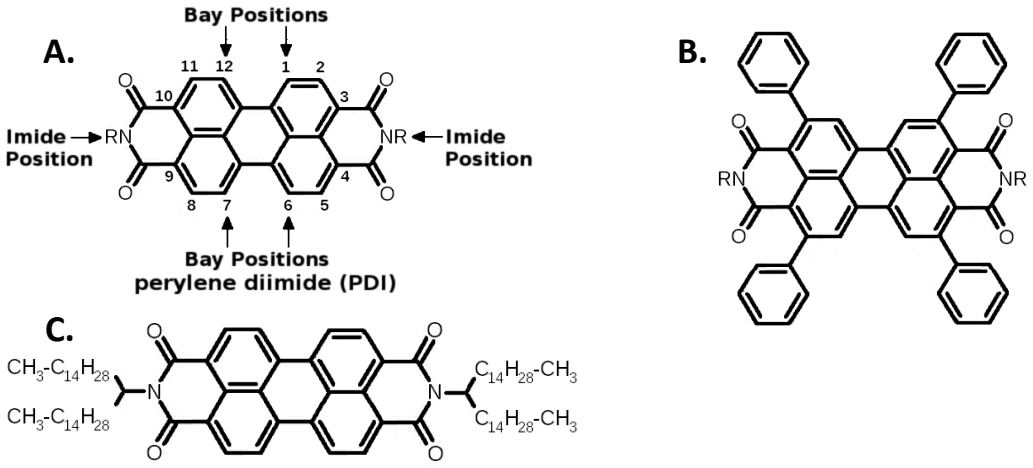

Figure 5.17: A. Structure and numbering convention of perylene diimide (PDI) monomer. B. Common molecular core of PDI-C5 and C8 consisting of a PDI monomer with phenyl groups at the 2,5,8,11 positions. C. PDI monomer with saturated, branched 31 carbon tails (PDI-1).

Perylene diimide (PDI) is an artificial dye found in red automotive paints that is being investigated for applications in artificial photosynthetic systems. Its relevance to natural photosynthetic systems comes from the fact that it is an organic molecule with its optical properties originating from an extended polycyclic conjugated π electron system. More importantly, derivatives of this molecule can be induced to form simple linear aggregates with similar π-π coupling that is found in natural aggregates of BChl *c*, *d*, and *e*. Phosphorescence measurements on monomers and aggregates of PDI have shown the formation of triplet state excitons resulting in a lowering of the triplet excited state energy, an effect hoped to be observable in aggregates of BChl *c*, *d*, and *e*.

5.3.1 Sample Preparation

Samples of three different perylene diimide (Figure 5.17A) derivatives were synthesized by the Wasielewski research group of Northwestern University. Two of these

samples consist of a common core of 2,5,8,11-tetraphenylperylene-3,4:9,10-bis(dicarboximide) (Figure 5.17B) with varying length alkyl chains attached at the imide positions; five carbon alkyl (PDI-C5) and an eight carbon alkyl (PDI-C8). The third sample, with molecular formula $C_{36}H_{134}N_2O_4$, is the quadruple tail molecule show in Figure 5.17C (PDI-1). The synthesis of PDI-C8 can be found in the supporting information of (Eaton et al. 2013). All samples were dissolved in 2-Methyl tetrahydrofuran (2-MeTHF).

5.3.2 PDI Singlet State Properties and Sample Aggregation

Absorption spectra were measured at room temperature where the PDI-C8 (Figure 5.17B) sample showed signs of aggregation both in the absorption spectrum (Figure 5.18B) and sample turbidity while PDI-1 and PDI-C5 showed no signs of aggregation at room temperature (Figure 5.18A, PDI-1). Fluorescence spectra were recorded with samples placed into quartz EPR tubes and frozen at 77K. Each sample experienced a significant red shift (visible to the naked eye) in the monomeric absorption spectrum upon freezing (~13nm for PDI-C8, Figure 5.18B_2). This shift was not an effect of aggregation and reversed upon thawing. PDI-1 and PDI-C8 showed signs of aggregation at 77K with two fluorescing species emitting with maxima at 538 and 605 nm respectively for the PDI-1 monomer and aggregate (Figure 5.18$A_{1,3}$) and 547 and 620 nm respectively for the PDI-C8 monomer and aggregate (Figure 5.18$B_{1,3}$). The PDI-C5 sample did not show signs of aggregation at any temperature. The fluorescence excitation spectra for the PDI-C8 shows the 547nm emitting species is consistent with the monomer while the 620 nm emitting species is consistent with slip-stack aggregate ((Eaton et al.

2013), Figure 5.18$B_{2,4}$). Fluorescence excitation spectra for the PDI-1 538 nm and 605 nm emitting species also demonstrated a similar monomer / aggregate character (Figure 5.18$A_{2,4}$).

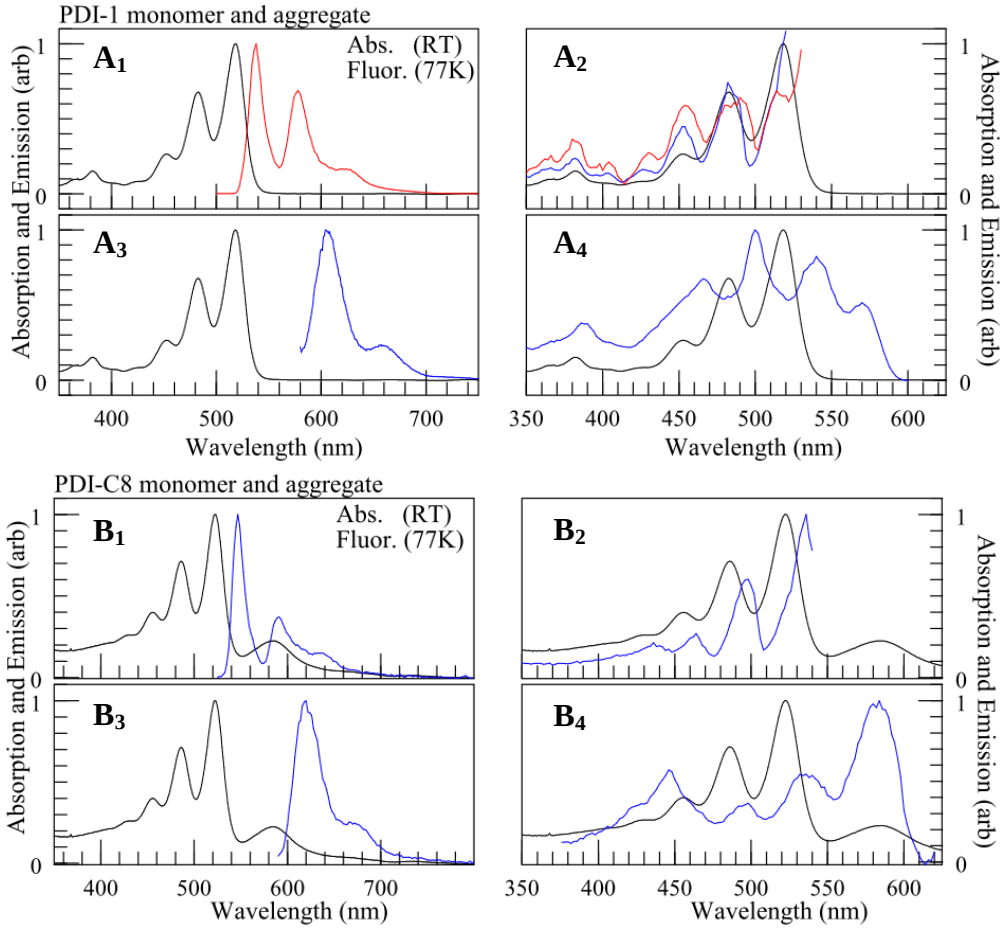

Figure 5.18: Room temperature (RT) absorption spectra and low temperature (77K) fluorescence emission and excitation spectra for the PDI-1 and PDI-C8 samples. A/B_1 – RT absorption and monomer 77K fluorescence emission spectra. A/B_2 – Absorption and monomer fluorescence excitation spectra. A/B_3 – RT absorption and aggregate 77K fluorescence emission spectra. A/B_4 – Absorption and aggregate fluorescence excitation spectra. PDI-C5 possess near identical absorbance and fluorescence properties as monomeric PDI-C8. No evidence was found of PDI-C5 aggregates.

In its aggregated state, PDI experiences strong pigment-pigment interactions resulting in a lowering of both the singlet and triplet excited state energies. The singlet state of the aggregate is clearly excitonic in nature due to the good alignment of the

pigment dipole moments (deduced from Figure 5.19) upon which the singlet excitonic coupling depends (Equation 2.37, Equation 2.22). Data from van Zandvoort et. al. (van Zandvoort et al. 1994) shows the absorption and emission dipole moments of a similar perylene molecule are orientated at 7º and 20º, respectively, relative to the symmetry axis connecting the nitrogen atoms shown in Figure 5.17A.

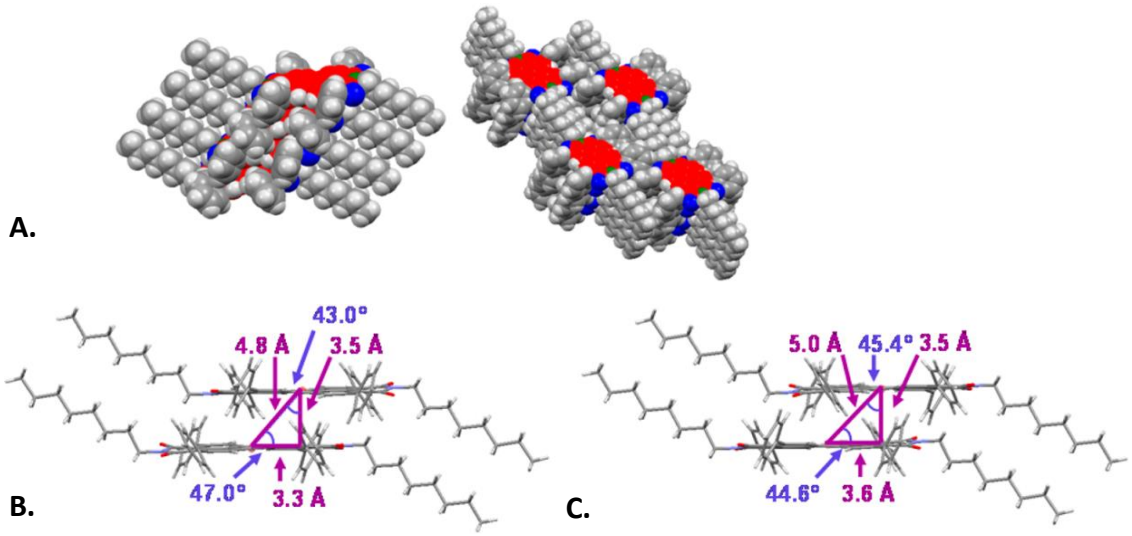

Figure 5.19: A. Space fill model of PCI-C8 slip stack aggregate. B. Monomer packing parameters within the slip-stack aggregate unit cell. C. Monomer packing between unit cells. (Eaton et al. 2013).

Taking the 13º difference between these dipole moments, and assuming an approximately 45º angle between each of these dipoles and a vector connecting the molecular centers (the approximately 5Å purple line in Figure 5.19B,C), the magnitude of the orientation factor (κ, Equation 2.23) is $|\cos(13°) - 3 \cdot \cos(45°)^2| \approx 0.5$. While less than the maximum magnitude of four, the orientation factor clearly shows the molecular orientation is appropriate for singlet exciton formation, although at a spacing of 3.5Å the dipole-dipole coupling model is likely invalid (You et al. 2006).

The left hand side of Equation 2.36, which comes from the Dexter exchange rate (Equation 2.35), is proportional to the square of the off diagonal matrix elements of Equation 2.37 (the V_{ij}, i.e. the triplet coupling strength). With a spacing of 3.5Å for a molecule with dimensions on the order of 10Å, the (square root of) the exponential of Equation 2.36 evaluates to $exp\left(-3.5\text{Å}/10\text{Å}\right) \sim 1$, which strongly suggest the possibility of triplet excitons in the PDI slip-stack aggregate.

5.3.3 PDI Triplet State Properties (Phosphorescence)

The triplet state energies of each of these three samples were investigated using the phosphorescence spectrometer described in Chapter 3. Samples were dissolved in 2-MeTHF, housed in quartz EPR tubes, and frozen at 77K for measurement. Due to the spectra separation of the monomers and aggregates, each species could be selectively excited and studied. Both the PDI-1 and PDI-C8 samples produced complex multiband emission spectra involving a variety of process including prompt fluorescence and phosphorescence from monomer and aggregate species as well as delayed fluorescence likely originating from the recombination of charge separated states which repopulated the singlet and triplet states.

Since PDI-C5 did not form aggregates, its spectra are the most simple to interpret. Exciting the sample produces a single long lived band with an approximate emission lifetime of 25-40μs and a maximum at 972nm with a broad shoulder (most likely a vibrational band) centered at approximately 1080nm (Figure 5.20).

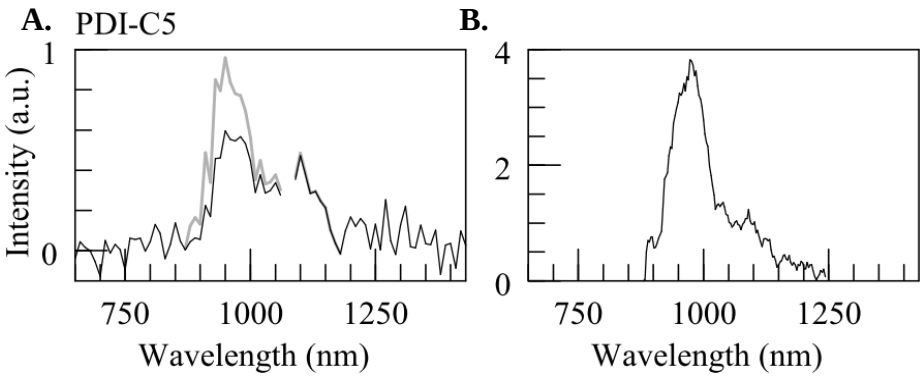

Figure 5.20: A. PDI-C5 phosphorescence emission spectrum with excitation at 530nm (note, OPO idler removed from 1070-1080nm) and 700nm LWP filter. Black spectrum is uncorrected for detector response; grey spectrum is corrected (870-1180nm). B. PDI-C5 phosphorescence emission (corrected) with excitation at 495nm. A 700nm LWP filter was used in both measurements. Note the lack of delayed fluorescence in 'A'.

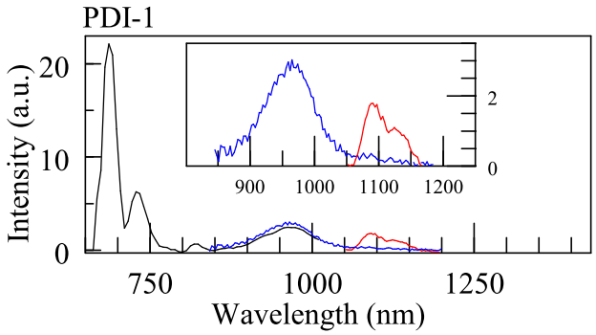

Figure 5.21: PDI-1 phosphorescence. Blue – Monomer phosphorescence, excitation at 500nm. Red – Aggregate phosphorescence, excitation at 580nm. Black - Long wavelength tail of delayed fluorescence. Note: a 700nm LWP filter was used for the blue and red curves.

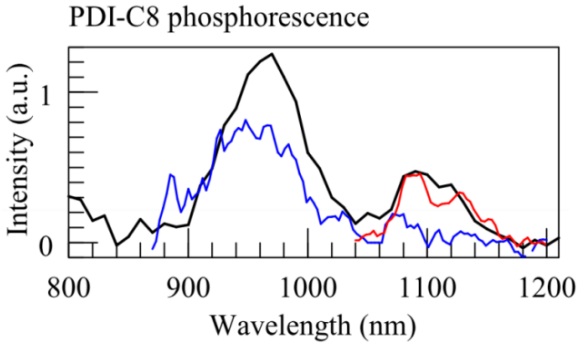

Figure 5.22: PDI-C8 phosphorescence emission (Eaton et al. 2013). Black – excitation at 500nm. Blue – excitation at 535nm. Red – excitation at 580nm. Note: a 700nm LWP filter was used for all measurements.

Both the PDI-1 and PDI-C8 samples produced significant aggregation in 2-MeTHF at 77K which resulted in significantly more complicated emission spectra (Figure 5.21 and Figure 5.22). Room temperature films of PDI (in a poly-styrene matrix) are known to produce delayed luminescence with the same spectral signature (i.e. same spectrum as the fluorescence) as the PDI aggregate (Keivanidis et al. 2010). This delayed fluorescence originates from the recombination of a charge separated state (Keivanidis et al. 2010; Keivanidis et al. 2012) which either repopulates the singlet state directly or indirectly via the triplet state by triplet-triplet annihilation.

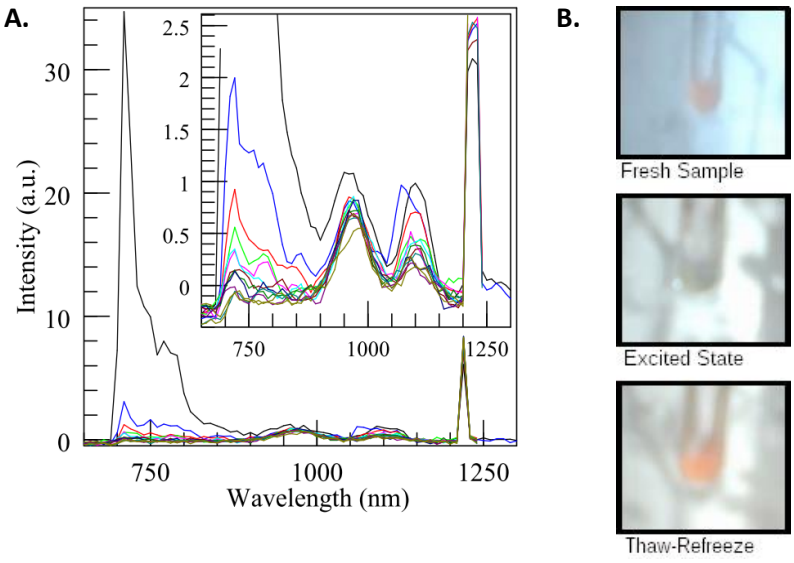

Figure 5.23: PDI-C8 long lived excited state. **A** – Sample luminescence as a function of illumination time. Black and blue ~16 minutes per scan (start to finish). Remainder ~9 min/scan. **B-** Reversible bleaching resulting from illumination for 5 min at 500nm (1mJ/pulse at 10Hz). Note: "Fresh Sample" image is back illuminated while other two are directly illuminated.

Additionally, a low temperature (77K) sample of PDI-C8 was shown to enter a long lived (>10 minutes) excited state that is characterized by significant photobleaching (Figure 5.23B) and reduction of the delayed fluorescence and phosphorescence emission

from the aggregate without affecting the phosphorescence emission from the monomer (Figure 5.23A). The photobleaching and loss of aggregate luminescence reverses upon thawing and refreezing (Figure 5.23B). This long living bleached state and the loss of luminescence is likely due to the aggregate entering a charge separated state which is stable at low temperature.

Table 5.2 - The singlet and triplet excited state energies and phosphorescence emission lifetime of three derivatives of PDI in both the monomeric and aggregated states.

Sample		**Fluorescence nm (eV)**		**Phosphorescence nm (eV)**		**Triplet Lifetime µs**
PDI-1	Monomer	538	(2.30)	962	(1.29)	35
	Aggregate	607	(2.04)	1091	(1.14)	520
PDI-C5	Monomer	549	(2.26)	972	(1.28)	25-40
PDI-C8	Monomer	547	(2.27)	970	(1.28)	35
	Aggregate	621	(2.00)	1090	(1.14)	--

5.3.4 Discussion – Linear Aggregate

5.3.4.1 Triplet excitons

The optical properties of monomeric PDI-C5 and C8 are nearly identical, with fluorescence and phosphorescence emission maxima occurring at the same wavelength to within experimental error while monomeric PDI-1 is also nearly the same, only shifted approximately 10 nm to shorter wavelengths in both fluorescence and phosphorescence (Table 5.2). Additionally, the singlet - triplet energy gap of all three monomeric species are nearly the same as well (~1 eV).

In the slip-stack aggregated state (Figure 5.19), the singlet states of both PDI-1 and PDI-C8 are lower by over 260 meV while the triplet states are lowered by over 140

meV. If we assume that, in the triplet state, molecules of PDI are only coupled to the nearest neighbor with identical couplings between all neighbors, then the system Hamiltonian (Equation 2.38) becomes a tridiagonal Toleplitz matrix (Equation 5.9) which has eigenvalues with closed form solutions (Equation 5.10) (Noschese et al. 2013):

$$H = \begin{bmatrix} \varepsilon + D & V & & 0 \\ V & \varepsilon + D & \ddots & \\ & \ddots & \ddots & V \\ 0 & & V & \varepsilon + D \end{bmatrix}$$

Equation 5.9

$$E_k = \varepsilon + D + 2V\cos\left(\frac{k\pi}{n+1}\right) \qquad k = 1, \cdots, n$$

Equation 5.10

Where ε is the monomeric triplet state energy, D is the displacement energy, V is the triplet-triplet (T-T) coupling, and n is the dimension of the Hamiltonian (i.e. the number of coupled pigments). Note that for large 'n', according to Equation 5.10, the lowest eigenvalue (k = n) becomes:

$$E_n \approx \varepsilon + D - 2V$$

Equation 5.11

Thus the difference between the triplet state of the uncoupled monomer and the large excitonic system is twice the coupling minus the displacement energy:

$$E_{mono.} - E_{aggreg.} = 2V - D$$

Equation 5.12

According to the data from Table 5.2, the T-T couplings for aggregated systems of both PDI-1 and PDI-C8 are both approximately 70 meV (half of 140 meV). This

value (70 meV) is consistent with the work of You et. al. who developed a computational model to predict T-T couplings between molecules containing conjugated π systems. For a system of linear polyene molecules with maximum π-π contact, similar to the PDI slip-stack (Figure 5.19), You calculated the magnitude of the T-T coupling at 3.5Å is 100 meV (You et al. 2006).

5.3.4.2 Singlet Fission

According to the theory of singlet fission (SF), a singlet state or singlet exciton will fission into two coupled triplet states or excitons (with total spin zero) via either a direct process where singlet states directly transform into triplet states or via a mediated process where an intermediate charge transfer (CT) state is involved (Berkelbach et al. 2013a). This process is spin-allowed and in systems with favorable state energies and couplings will occur with time constants on the order of picoseconds (Berkelbach et al. 2013a; Berkelbach et al. 2013b; Eaton et al. 2013).

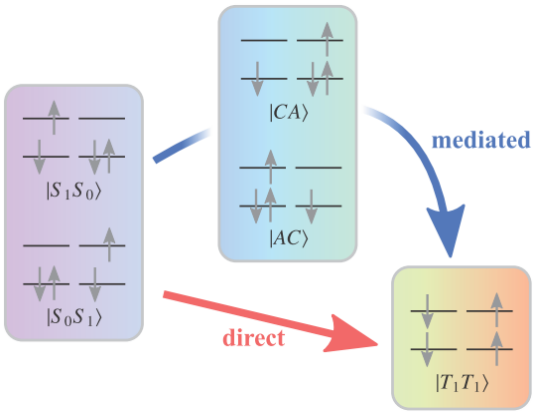

Figure 5.24: Schematic depiction of singlet fission via the direct route or the charge transfer state mediated route. (Berkelbach et al. 2013b)

Eaton et. al., investigated SF in slip-stack aggregate films of PDI-C8 at room temperature. Their findings show SF occurring with a time constant of ~180ps and a total triplet state quantum yield of ~140% (Eaton et al. 2013). Although phosphorescence measurements show that the final state consisting of two triplet excitons has higher total energy than the initial singlet exciton state ($E(S_1)$ = 2.0 eV and $2*E(T_1)$ = 2.28 eV, Table 5.2), thus making the fission process endothermic, the increase in entropy from gaining a second excitation likely results in an overall negative change in free energy and thus a spontaneous process.

5.4 Modeling Triplet-Triplet Coupling

5.4.1 General Model

Triplet-triplet (T-T) coupling can be calculated directly from the molecular orbitals by evaluating Equation 2.43 (You & Hsu 2010):

$$V_T = V_{exch} + V_{ovlp}$$

Equation 2.43

Where the electronic exchange energy, V_{exch} (Equation 2.33), and wavefunction overlap, V_{ovlp} (Equation 2.44), can be written:

$$V_{exch} = \int \frac{\varphi'_D(\boldsymbol{r_1})\varphi_A(\boldsymbol{r_2})\varphi_D(\boldsymbol{r_2})\varphi'_A(\boldsymbol{r_1})}{|\boldsymbol{r_1} - \boldsymbol{r_2}|} d\boldsymbol{r_1} d\boldsymbol{r_2}$$

Equation 5.13

$$V_{ovlp} = \omega_0 \int \varphi'_D(\boldsymbol{r})\varphi_D(\boldsymbol{r})\varphi_A(\boldsymbol{r})\varphi'_A(\boldsymbol{r})\, d\boldsymbol{r}$$

Equation 5.14

Where $\varphi'_{D(A)}(r)$and $\varphi_{D(A)}(r)$ are the excited state and ground state wavefunctions of the donor (acceptor) and ω_0 is the transition frequency.

A 2006 theoretical study by You et. al. (You et al. 2006) demonstrated that T-T coupling can be directly calculated (the direct coupling (DC) method) from the following coupling equation using unrestricted Hartree-Fock molecular (UHF) orbitals (as an approximation of "diabatic" molecular orbitals):

$$T_{rp} = \frac{H_{rp} - S_{rp}\left(H_{rr} + H_{pp}\right)/2}{\left(1 - {S_{rp}}^2\right)}$$

Equation 5.15

Where $H_{rp} = \langle \Psi_r | H | \Psi_p \rangle$ and $S_{rp} = \langle \Psi_r | \Psi_p \rangle$ and the $|\Psi_n>$ are the UHF orbitals of the reactant and product states (i.e. spin localized solutions with the triplet excited state located on either the donor ($|\varphi'_D\, \varphi_A\rangle$, the reactant) or located on the acceptor ($|\varphi_D\, \varphi'_A\rangle$, the product) where $\varphi'_{D(A)}$and $\varphi_{D(A)}$ are the excited state and ground state wavefunctions of the donor (acceptor)).

According to this triplet-triplet coupling theory (You et al. 2006), the magnitude of the coupling is independent of the sizes of the molecules involved and only depends on the inter-molecular distance and relative face-to-face contact area. The maximum predicted value of triplet-triplet coupling is expected to be 100 meV for full face-to-face contact (at a separation distance of 3.5 Å) with an approximately exponential dependence on the relative face-to-face contact area (Figure 5.25B).

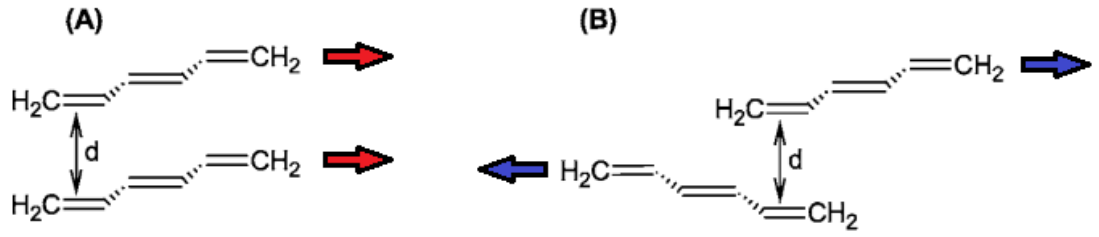

Figure 5.25: Geometry used by You et. al. to calculate triplet-triplet coupling (You et al. 2006). **A –** Full face-to-face contact. Increasing the length of the molecules (red arrows) does not change the magnitude of the coupling. **B –** End-to-end contact. Increasing the length of the molecules decreases the coupling exponentially with the molecule size.

Unfortunately, this work only involved carotenoid like molecules (linear polyenes) and only performed calculations with the molecules in full face-to-face contact OR minimal end only contact (Figure 5.25). The exponential dependence of the coupling strength was determined by keeping the end-to-end contact area constant and increasing the size of the molecule. This approach does not account for the fine details of the molecular structure and will miss oscillations in the coupling strength caused by the wave nature of the molecular orbitals (Figure 5.26).

A simple calculation of an overlap integral (Equation 5.17) was performed as a proof of concept test to determine if the oscillatory nature of the molecular wavefunction is an important factor for processes and calculations involving significant wavefunction overlap. Singlet state LUMO orbitals were chosen for this calculation because in the lowest energy triplet excited state this orbital is singly occupied (Weiss et al. 1965; Kay 2003) and, although most triplet electronic excited states are heavily mixed due to extensive configuration interaction (Weiss et al. 1965), the lowest energy triplet excited state is over 90% pure (Weiss et al. 1965). Since the intent of this calculation was as a

proof of concept, the calculation involved only the un-normalized and un-optimized $2p_z$ orbitals which were of the form given in Equation 5.16:

$$\varphi(r,\theta) = \pm\cos(\theta)\, e^{-r/r_0}$$

$$\varphi(r,z) = \frac{\pm z}{r}\, e^{-r/r_0}$$

Equation 5.16

$$S = \int \varphi_1(r,\theta)\varphi_2(r,\theta)dV$$

Equation 5.17

Where $\varphi_n(r,\theta)$ is the 2pz is atomic orbital of atom 'n', r is the radial distance from the atomic nucleus, ± denotes the appropriate phase (red and blue, Figure 5.26), and θ is the azimuthal angle between the z-axis (directed perpendicular out of the porphyrin macrocycle) and the vector **r**. Since cos(θ) can be written as z/r, and this form is computationally simpler, the second form of Equation 5.16 was used in the calculation of Equation 5.17. Calculating the overlap integral (Equation 5.17) of the (un-normalized and un-optimized) Gouterman LUMO orbitals (Gouterman 1961; Gouterman et al. 1963) only yielded the following results (Figure 5.27 and Figure 5.28):

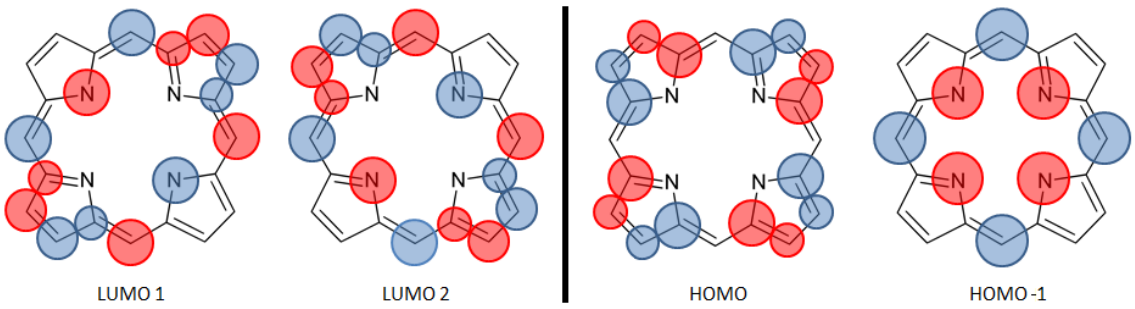

Figure 5.26: The orbitals of the Gouterman four orbital model of porphyrin. The degenerate LUMO, right, and the near degenerate HOMO, left. Color indicates phase.

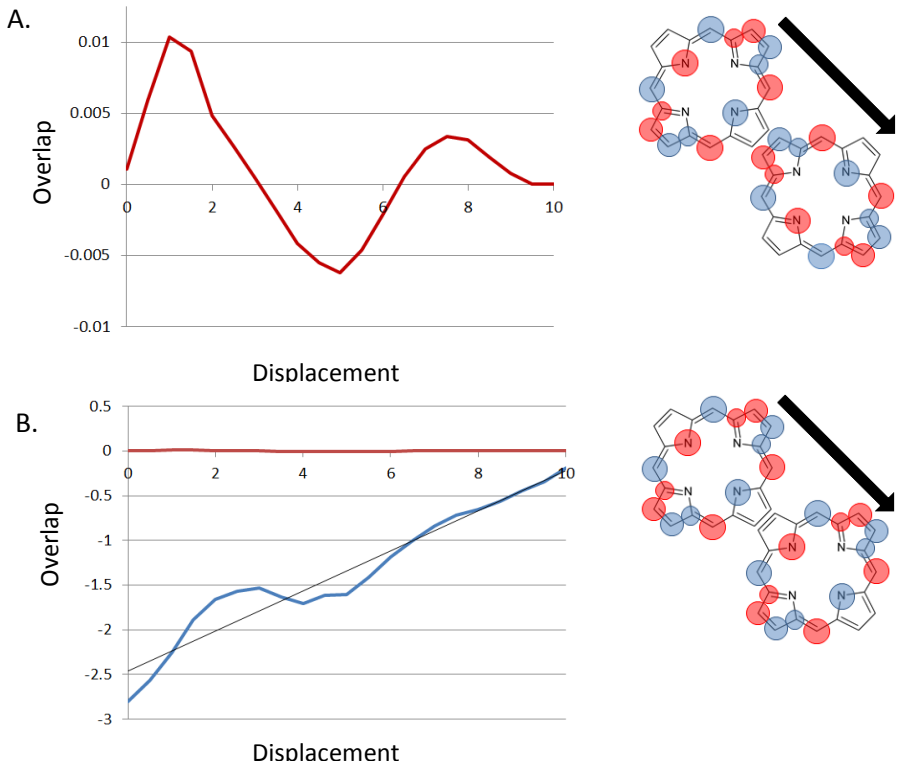

Figure 5.27: Overlap integral as a function of molecular contact for the two different (degenerate) LUMOs. **A** – Overlap of LUMO1 and LUMO2. **B** – Overlap of LUMO1 with LUMO1 (BLUE) plotted on the same scale as graph A. Vertical axis is the overlap integral while the horizontal axis is the center-center displacement. NOTE: vertical scale is arbitrary.

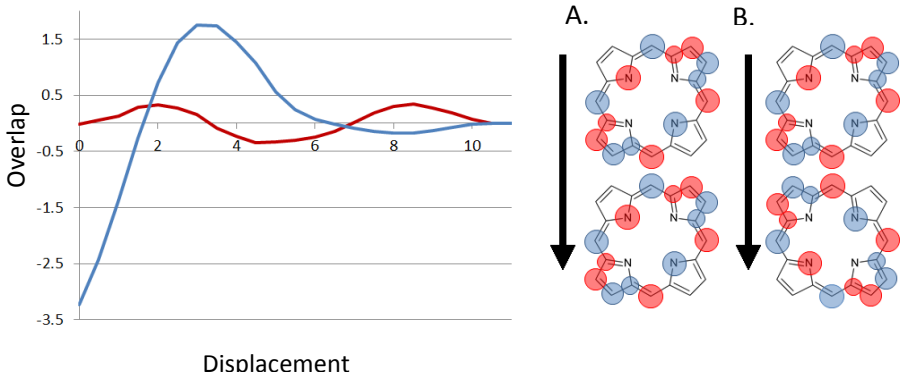

Figure 5.28: Overlap integral as a function of molecular contact for the two different (degenerate) LUMOs. BLUE - Overlap of LUMO1 and LUMO1 (A). RED - Overlap of LUMO1 with LUMO2 (B). NOTE: vertical scale is arbitrary.

In this simple calculation, the oscillatory nature of the molecular orbitals is seen to have a significant effect on the overlap integral. While the exact calculations performed to produce Figure 5.27 and Figure 5.28 are not physically realistic (due to the ad hoc orbitals), the implication is that for processes involving significant wavefunction overlap these oscillations will play a significant role. Since the T-T coupling depends on the wavefunction overlap, it can reasonably be assumed that this effect cannot be ignored.

Evaluation of the full T-T couplings for the geometries given in Figure 5.29 and Figure 5.30 is currently being performed by collaborator Professor Lyudmila Slipchenko utilizing the Fragment Spin Difference (FSD) method (You & Hsu 2010), a method developed by the same authors as the DC method (You et al. 2006) and implemented as a built-in feature of Q-Chem 4.1 (Shao et al. 2006). The results so far verify the oscillatory nature of the coupling as a function of center to center displacement and are presented in Figure 5.31 and Figure 5.32. Since the FSD method extracts the couplings from the triplet excited state of the dimer (You & Hsu 2010), this state must be created. First, the dimers of Figure 5.29 and Figure 5.30 were constructed from ground state optimized monomers (Gaussian 09, B3LYP 6-31G*). Next the singlet ground state orbitals for the dimer were computed with the unrestricted Hartree-Fock method (Q-Chem 4.1, UHF 6-31G*). Finally, the triplet excited state for the dimer was created from the singlet ground state orbitals using the CIS method (Q-Chem 4.1, CIS 6-31G*).

The FSD method has been shown to produce similar results to the DC method with the FSD couplings similar in both magnitude and the exponential decay constants (i.e. ‘α’ in Equation 5.18) compared to the results of the DC method (You & Hsu 2010).

The FSD method was also shown to reproduce the (B)Chl-carotenoid T-T couplings (computed from experimentally measured TET rates) in natural photosynthetic antenna to within a factor of 2 to 6 depending on the structure (You & Hsu 2011) and the T-T couplings in artificial porphyrin systems to within 30% (You & Hsu 2010).

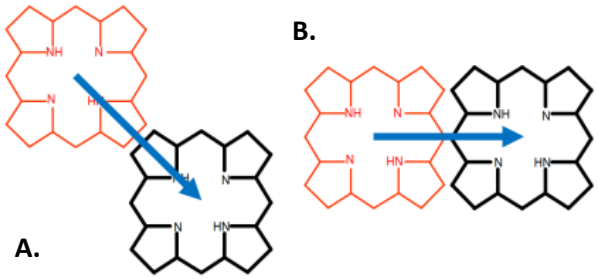

Figure 5.29: Geometry for evaluation of Equation 5.15 for free base porphyrin. NOTE: Displacement is in the direction of the arrow and the black pigment is on top.

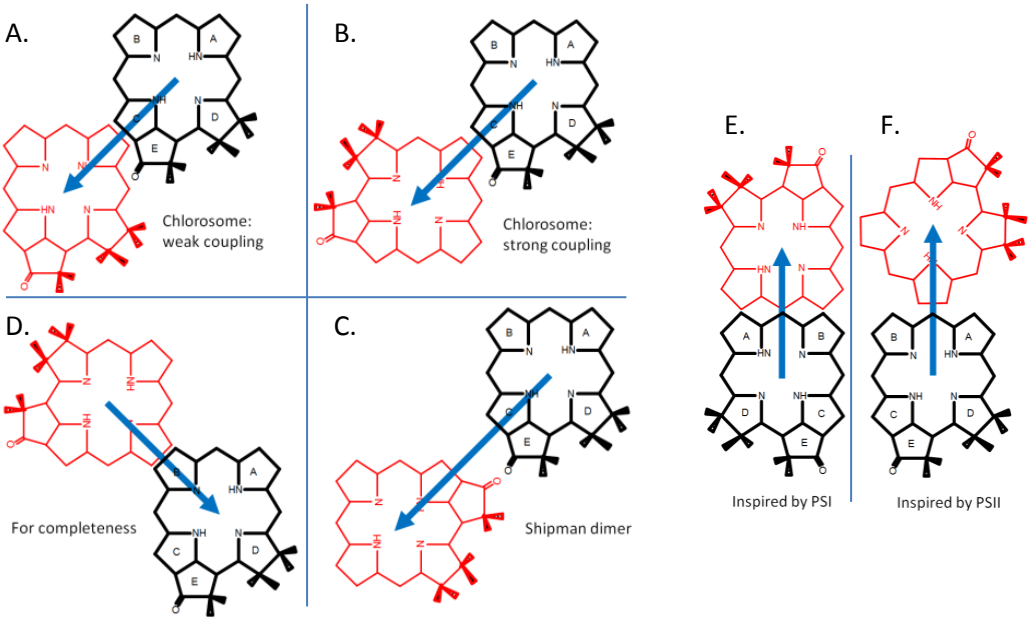

Figure 5.30: Geometries for evaluation of Equation 5.15 for the chlorin and the structures that inspired them (Note: Black is on top). **A** and **B** – Approximate pigment orientations found in the chlorosome. **C** – Approximate Shipman dimer. **D** – Included for completeness. **E** and **F** – Approximate orientations found in PSI and PSII RC dimers.

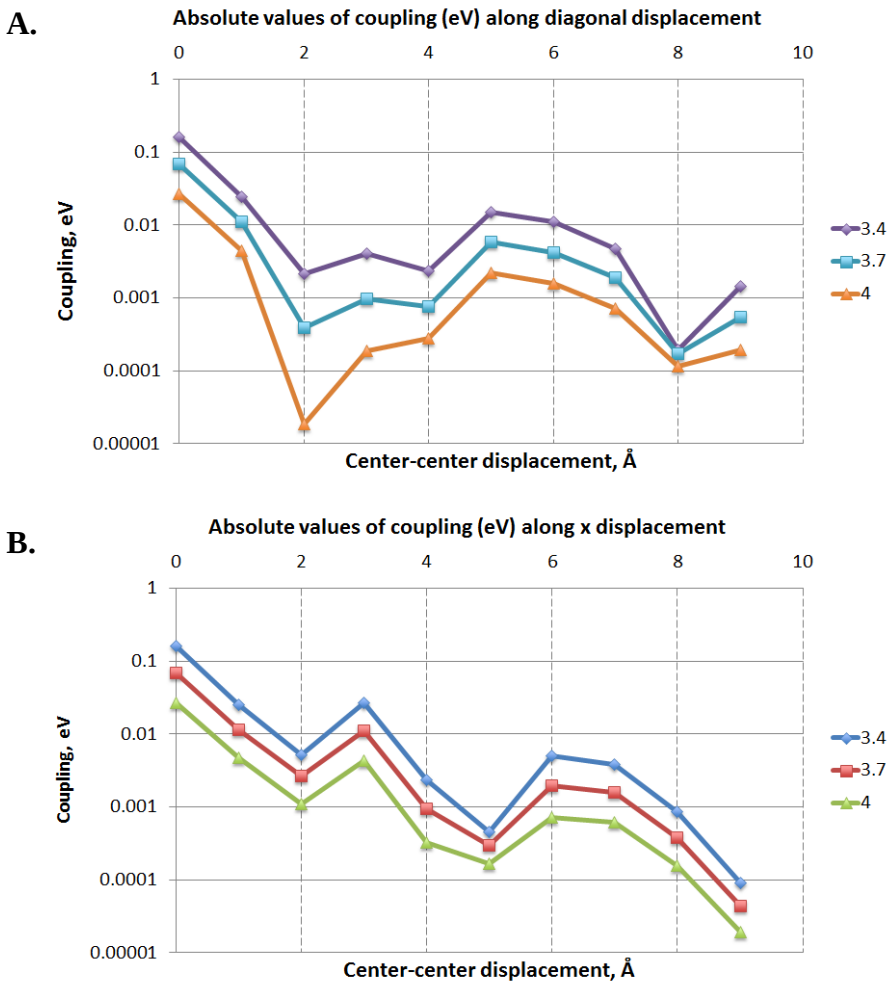

Figure 5.31: Triplet-triplet coupling of porphyrin dimer (Figure 5.29) as a function of center to center displacement for three vertical displacements (macrocycle plane to plane separations: 3.4, 3.7, and 4.0 Å). **A –** Diagonal displacement corresponding to Figure 5.29A. **B –** Horizontal displacement corresponding to Figure 5.29B. Note: vertical axis is a log scale unlike in Figure 5.27 and Figure 5.28. [In collaboration with Dr. Lyudmila Slipchenko]

It is expected that displacement in the vertical direction (i.e. out of the page in Figure 5.29 and Figure 5.30) will result in coupling that drops off exponentially (Equation 5.18) with distance as demonstrated by You et. al. using both the DC and FSD methods (You et al. 2006; You & Hsu 2010).

$$c = c_0 exp(-\alpha d)$$

Equation 5.18

Where *d* is the plane to plane separation distance in Å (out of the page displacement in Figure 5.29), c_0 is the zero distance coupling, and α is the "coupling exponent" in $Å^{-1}$. An exponential drop off is indeed the case as can be seen for most the points in Figure 5.31 A and B since the three evenly spaced vertical distances (3.4, 3.7, and 4Å) should always result in evenly spaced points on the log scale, obvious exceptions are the 2 Å and 8 Å diagonal displacements in Figure 5.31A. Using linear regression to fit the (natural log of the) coupling verses vertical displacement at each point in Figure 5.31A and B gives the following exponents (α in Equation 5.18) and coefficients of determination (R^2).

Table 5.3: Coupling exponents calculated from Figure 5.31. Significant outliers are flagged in **bold**.

Center-center displacement (Å)	**Diag. Displ. (Figure 5.31A)**		**Horiz. Disp. (Figure 5.31B)**	
	α_1 ($Å^{-1}$)	**R^2**	**α_2 ($Å^{-1}$)**	**R^2**
0	3.03	1.000	3.03	1.000
1	2.82	0.999	2.80	0.999
2	**7.92**	**0.973**	2.59	0.995
3	5.12	0.999	3.07	1.000
4	3.56	1.000	3.27	0.999
5	3.19	1.000	**1.67**	**0.992**
6	3.25	1.000	3.23	1.000
7	3.18	0.999	3.00	1.000
8	**0.86**	**0.908**	2.80	0.999
9	3.34	1.000	2.56	0.999

The results of the vertical displacement calculation conform to the results obtained by You et. al. (You et al. 2006; You & Hsu 2010) who computed coupling

exponents, α, that range from ~2.6 $Å^{-1}$ (full face to face contact, Figure 5.25A) to ~3.3 $Å^{-1}$ (end to end contact Figure 5.25B). Most of the calculated exponents in Table 5.3 fall within this range with three exceptions (in bold), two of which (α_1, d = 2 & 8 Å) show clear non-exponential behavior as indicated by the low R^2 values while the third (α_2, d = 5 Å) coincides with the lowest R^2 of the set. It's unknown if these deviations are the result of true non-exponential behavior for these geometries or error in the computational method. More points (perhaps a vertical step of 0.15 or 0.1Å from 3.4 to 4Å) would be needed to determine this since non-exponential behavior would be expected to occur at close distance while computational errors would be more likely to occur at larger distances due to the use of Gaussian type orbitals in the calculation (as opposed to Slater / exponential type). Note that use of Slater type orbitals is very computationally intensive.

A ground state DFT optimized structure of the PPIX dimer (rWB97XD, 6-31G* (Godbout et al. 1992)) with a water polarizable continuum solvent model) gives a center to center displacement in the diagonal direction (like Figure 5.29 A) of ~1.66 Å and a plane to plane separation distance of ~3.1 Å. Interpolating between the 1 and 2 Å displacements in Figure 5.31 B and extrapolating to a plane to plane separation distance of 3.1 Å, we arrive at a coupling of 62 meV, which is 26 meV smaller than (the lower range of) the observed 98±10 meV difference between the monomer and dimer (Table 5.1). A likely explanation for this large difference is the different chemical environment between the monomer (40% HCl solution of pH = 1.2 with 15% MeOH and 45% glycerin by volume) and the dimer (in 40% NaOH solution of pH = 11.5 with 60% glycerin by volume, see Section 5.2.1). The large difference in chemical environment, while necessary to form dimers and monomers, makes direct comparison of these two

samples difficult. Measuring a PPIX monomer in a less aggressive solvent would help reduce this uncertainty since at low pH the porphyrin exists in the di-protonated form (a 2+ cation). A solvent capable of completely dissolving PPIX as monomers at low temperature and with good optical properties would need to be found.

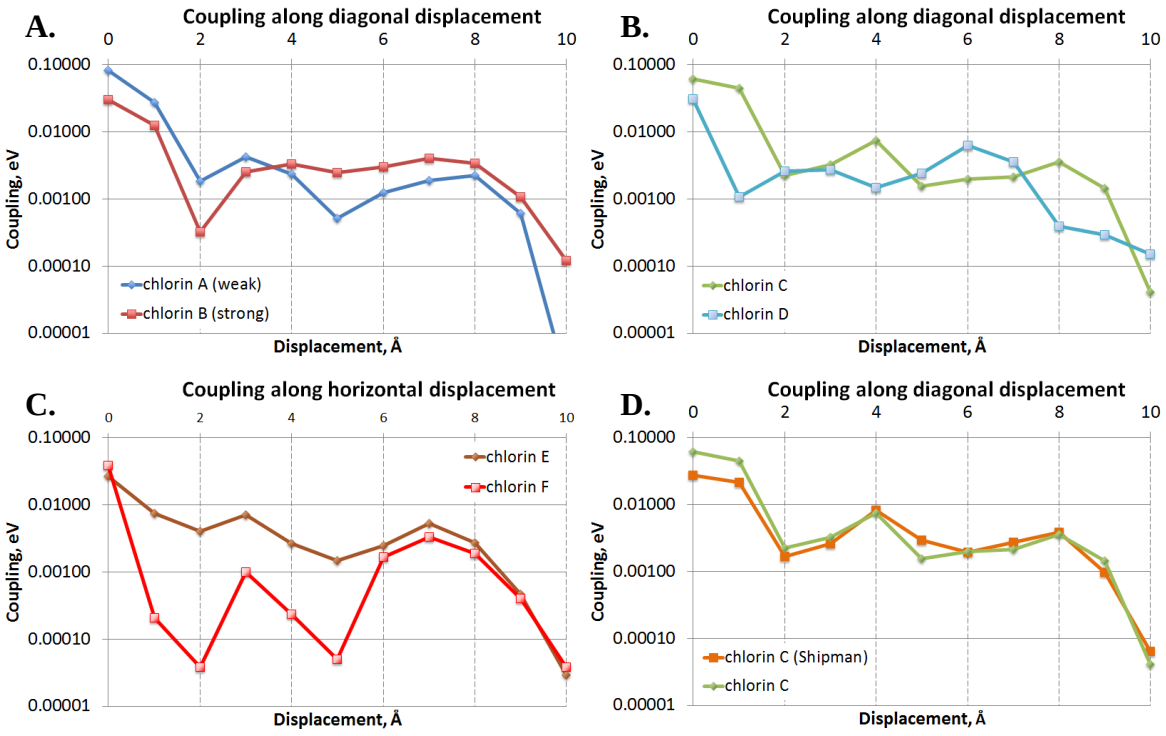

Figure 5.32: Triplet-Triplet coupling (eV) verses center-center displacement for chlorin geometries of Figure 5.30 (at 3.7 Å plane-plane separation). **A –** Figure 5.30 A and B. **B –** Figure 5.30 C and D. **C –** Figure 5.30 E and F. **D –** Comparison between geometry of Figure 5.30 C and ground state optimized (B3LYP, 6-31+G*) structure similar to Figure 5.7 B (waters removed for coupling calculation). [In collaboration with Dr. Lyudmila Slipchenko]

Couplings for the chlorin geometries of Figure 5.30 have been computed for a separation distance of 3.7 Å (Figure 5.32). Again we can see that the oscillatory nature of the molecular orbitals and relative pigment orientation plays a significant role in the coupling, which can change by two to three orders of magnitude with only a 1-2 Å center to center displacement. A careful examination of Figure 5.30 and Figure 5.32

demonstrates the coupling approaches a maximum value of ~100 meV for full face to face contact (i.e. zero center to center displacement) as calculated by You et. al. (You et al. 2006) but quickly deviates for non-zero displacements. The differences between the couplings at zero displacement (Figure 5.32) are easily explained by realizing the conjugated π system does not extend over the full molecule (skipping carbons 17 and 18 on the D ring and carbon 13^2 on the E ring) and is asymmetric (extending to oxygen of the R_{13}^1 ketone). Thus only the geometry of Figure 5.30A is in full face to face contact at zero center to center separation, the rest experience only partial contact.

In Figure 5.32 A the couplings for approximate pigment orientations found in the chlorosome (Figure 5.30 A and B, see also Ganapathy et. al. (Ganapathy et al. 2009)) are compared. These couplings are important for the possibility of triplet exciton formation in the chlorosome and will be discussed in detail in a subsequent chapter.

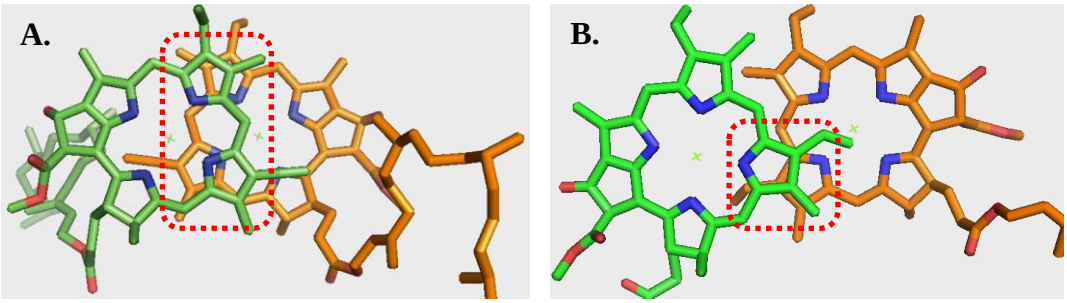

Figure 5.33: Reaction center special pairs. **A –** PSI of *Pisum sativum* (PDB ID = 3LW5, (Amunts et al. 2010)). **B –** PSII of *Thermosynechococcus vulcanus* (PDB ID = 4UB6, (Suga et al. 2014)). Area of overlap outlined in RED.

Figure 5.32 C compares couplings for pigment orientations (Figure 5.30 E and F) inspired by the reaction center special pairs of PSI and PSII (Figure 5.33). Using the structures of Figure 5.33, the approximate center to center displacement of the RC pigments is found to be 4.7 Å for PSI and 7.4 Å for PSII. Interpolating between the data

points of Figure 5.32 C for these two displacements yields T-T couplings of 1.8 meV for PSI and 2.8 meV for PSII, which surprisingly shows the T-T coupling found in the PSII reaction center is over 50% larger than the PSI RC despite the smaller contact area between the RC monomers (Figure 5.33). However, it can be seen by comparing Figure 5.30 and Figure 5.33 that the actual RC geometries deviate from the geometries assumed for the calculation by a rotation and perpendicular displacement (relative to the direction defined in Figure 5.30). Calculation of the couplings using the actual geometries (as determined by X-ray crystallography) may be necessary, but some insight can still be gained from Figure 5.32.

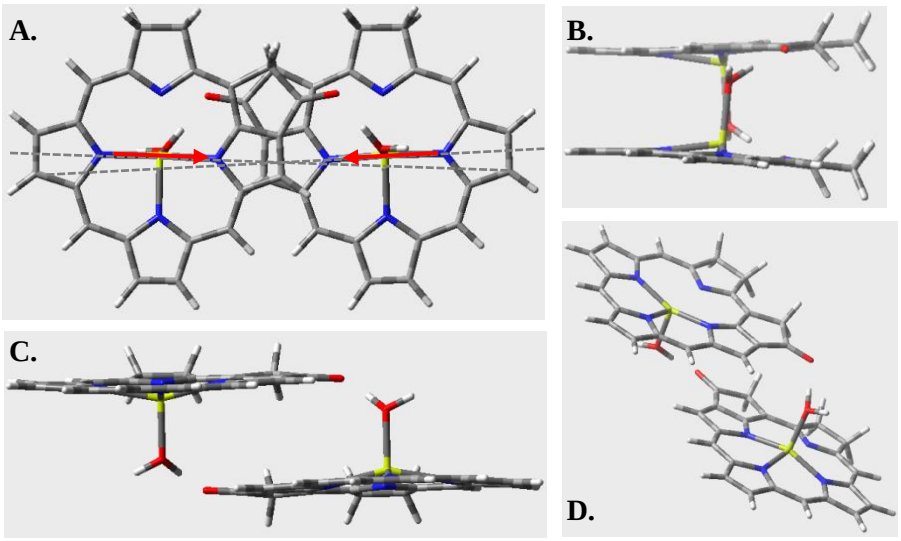

Figure 5.34: DFT optimized structure for stripped down version of Shipman dimer (B3LYP, 6-31*G+). Note: 4^{th} Mg^{2+} to N bond is present but not rendered.

Figure 5.32 D compares the coupling between the geometry of Figure 5.30 C (inspired by the Shipman dimer (Shipman et al. 1976b)) and the DFT ground state optimized structure of a Shipman like chlorin dimer (Figure 5.34). This chlorin dimer (Figure 5.34) consists of two stripped down Chl *a* molecules where all substituent groups

(e.g. R_3 vinyl, R_{17} tail, etc) have been replaced by hydrogens except for the R_{13}^1 ketone and with the monomers bound by coordination and hydrogen bonding interactions with two water molecules. The plane to plane separation distance is ~3.65 Å (at the Mg) and the center to center displacement is ~7 Å. Note that this optimized dimer differs from the orientation assumed in Figure 5.30 C by a slight angle between the Q_y transition dipole moments (Figure 5.34 A, red arrows) and an angle between the macrocycle planes (Figure 5.34 B). These slight differences do have an effect on the computed coupling, with the optimized structure having slightly higher coupling, 2.7 meV, at 7 Å displacement compared to the non-optimized dimer, 2.2 meV (Figure 5.35).

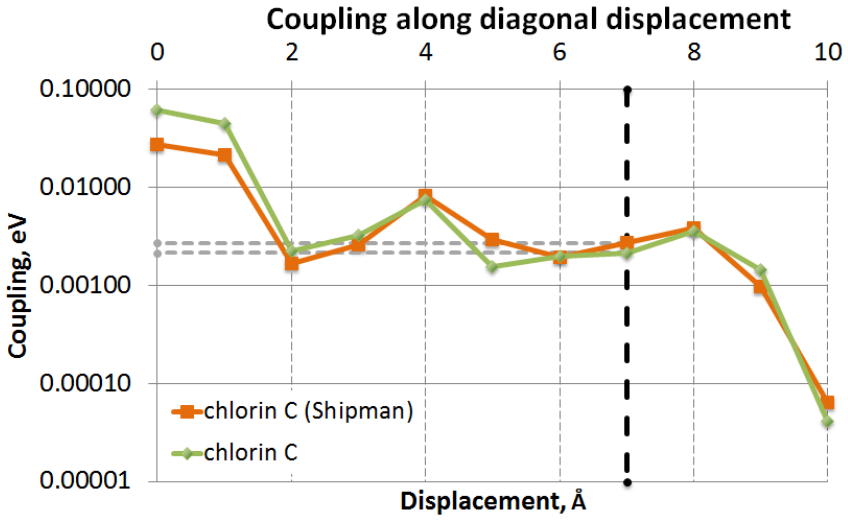

Figure 5.35: Comparison of couplings for the optimized dimer of Figure 5.34 and the unoptimized structure of Figure 5.30 C. Note: no waters were included in either calculation. [In collaboration with Dr. Lyudmila Slipchenko]

5.4.2 Displacement Energy and Effects of Micro-Solvation

A T-T coupling of 2 to 3 meV is far from sufficient to explain the experimentally observed 45 meV shift in the triplet state energy of the Chl *a* dimer relative to the

monomer (Table 5.1). In Equation 5.8 ($E_{monomer} - E_{dime} = V - D$) we see that the observed energy difference involves the both the T-T coupling, 'V', and the displacement energy, 'D', the energy shift resulting from bringing the monomers into close contact (as discussed in section 5.2.5.1). Note that "center to center displacement" will be used to refer to the center to center displacement as illustrated in Figure 5.30 unless stated otherwise and "displacement energy" will refer to the offset of the average energy of the excitonic bands with respect to the monomer energy (Figure 5.16).

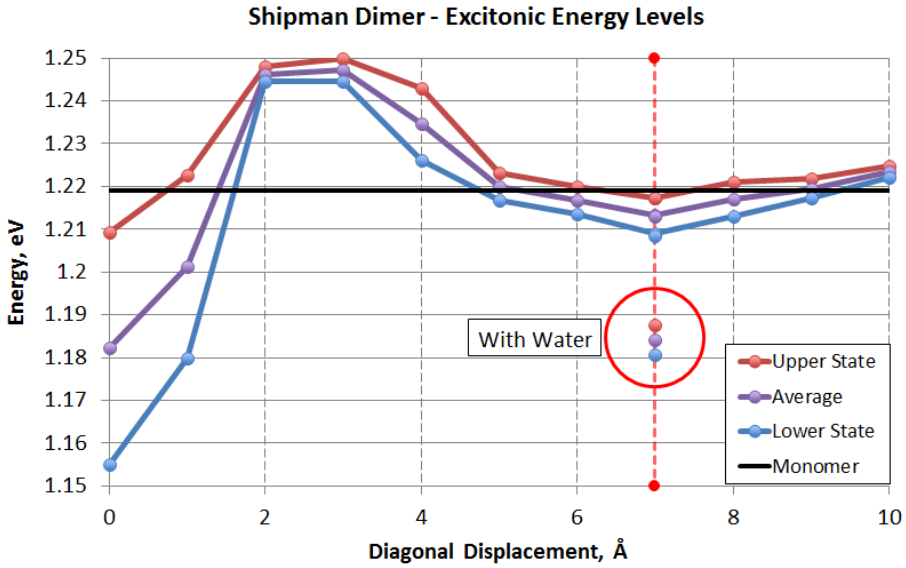

Figure 5.36: Energies of the upper and lower triplet state exciton for the Shipman like chlorin dimer as defined in Figure 5.34 (waters not included in calculation). The center to center displacement of the optimized dimer (7 Å) is marked with a vertical red line. Note the influence of adding the water molecules (i.e. micro-solvation) to the calculation (valid only at 7 Å displacement). Black horizontal line is the energy of the monomer. [In collaboration with Dr. Lyudmila Slipchenko]

To evaluate the effect of the displacement energy, the energies of the upper and lower triplet excitons were computed as a function of center to center displacement (Figure 5.36) for the chlorin dimer of Figure 5.34. The difference between the average of the upper and lower exciton energies and the monomer energy gives the displacement

energy (van Amerongen et al. 2000) and is show in Figure 5.37. At 7 Å center to center displacement the displacement energy is only approximately -5 meV, again far from the observed 45 meV energy shift in the Chl *a* dimer. The addition of the two water molecules incorporated into the dimer structure shifts the calculated triplet state energies downward by approximately 35 meV. This lowering of the triplet state energy by micro-solvation (plus the displacement energy) is much closer to the observed 45 meV. Based on these computational results it appears that micro-solvation, rather than triplet exciton formation, is responsible for the bulk of the experimentally observed energy difference between the Chl *a* monomer and dimer.

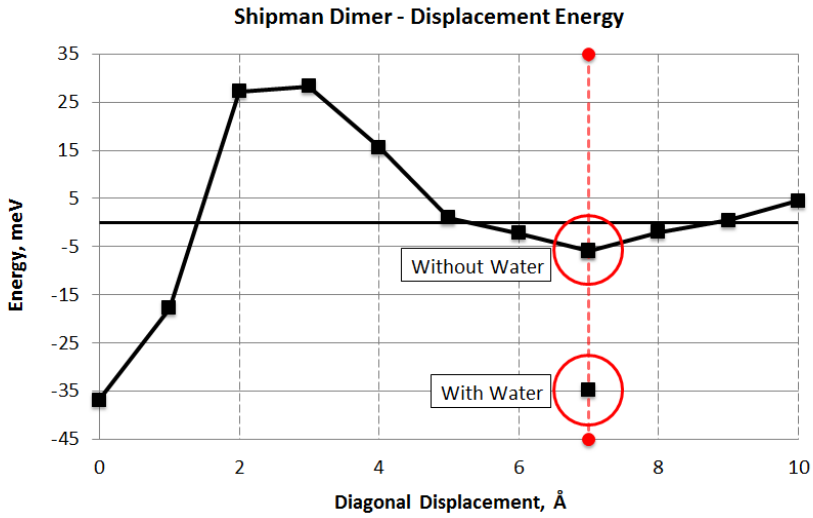

Figure 5.37: The displacement energy as computed from Figure 5.36. Again, note the influence of adding the water molecules to the calculation. [In collaboration with Dr. Lyudmila Slipchenko]

5.5 Conclusion

It's clear from Table 5.1 and Table 5.2 that triplet state energies are sensitive to the aggregation state while Table 4.4 shows the (B)Chl triplet state energies are sensitive to

solvation state. The question has been, how much of the experimentally observed energy shift is due to triplet exciton formation, the displacement energy, or other solvation effects. The approach used here was to attempt to independently evaluate the magnitude of the T-T coupling in order to estimate the relative contribution of the displacement energy and solvation effects. However, while the model of You et. al. (You et al. 2006) allowed for estimates of T-T coupling for certain geometries, the fine details of the molecular orbitals were ignored, which prevents extrapolation to molecules and dimer/aggregate geometries not explored in the 2006 study (You et al. 2006). Thus additional computational work was done to fill in this gap.

Both Figure 5.31 and Figure 5.32 show the importance of taking the structure of the molecular orbitals into account, with the coupling differing by over three orders of magnitude and depending strongly on monomer orientation and center to center displacement. The calculations allow us to estimate that the coupling, and thus triplet exciton formation, accounts for 2 to 3 meV of the observed 45 meV triplet state energy shift upon dimerization (Figure 5.35) and evaluation of the displacement energy accounts for another ~5 meV (Figure 5.37). Inclusion of the water molecules into the displacement energy calculation accounts for up to 35 meV of the observed 45 meV energy shift (Figure 5.37), showing that micro-solvation (involving both coordination and hydrogen bonding) is responsible for most of the observed change in the triplet state energy of the Chl *a* Shipman dimer. The ~7 meV difference between the calculated values and the measured value are likely due to computations being performed with the stripped down chlorin of Figure 5.34 and not Chl *a* and neglecting effects from the bulk solvent (toluene). Micro-solvation and bulk solvent effects could be investigated computationally

or experimentally by repeating the experiment in a variety of Shipman dimer forming solvent systems like carbon tetrachloride or toluene plus a small amount of water, ethanol (EtOH), or ethanethiol (EtSH, the sulfur analogue of ethanol) since the dimer absorption peak is known to be sensitive to combinations of these solvents (see Cotton et. al. (Cotton et al. 1978)).

While micro-solvation is responsible for most of the observed energy difference in the Shipman dimer, the same is not true of the PPIX dimer or the PDI aggregates because both these molecules lack the metal ions needed to form coordination complexes or hydrogen bond acceptors / donors that can affect the conjugated electron system responsible for the optical transitions. Thus the major contributors to the energy shift are the displacement energy and triplet exciton formation. In Figure 5.37 we see, in the right conditions, the displacement energy can contribute +/- tens of meV to the observed energy shift, however, the observed downward energy shift in the PPIX dimer is nearly 100 meV while the PDI aggregate it is lowered by 140 meV meaning that most of the observed shift is due to triplet exciton formation.

CHAPTER 6 – THE FENNA-MATTHEWS-OLSON COMPLEX

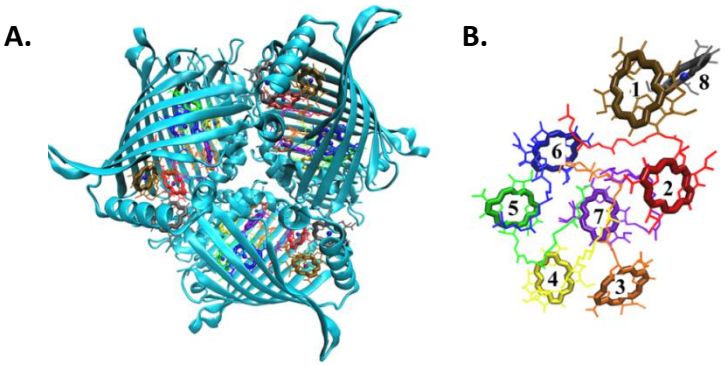

Figure 6.1: Fenna-Matthews-Olson (FMO) complex of *Chlorobaculum tepidum* (Kihara et. al. (Kihara et al. 2015)). **A –** FMO trimer. **B –** Arrangement of BChl *a* pigments within FMO monomer. Note that BChl #8 tends to be missing in many preparations.

6.1 Triplet State Energy

Experimental evidence from Kihara et. al. (Kihara et al. 2015) show that the triplet state of the Fenna-Matthews-Olson (FMO) complex is not quenched by oxygen. Room temperature measurements of the triplet state lifetime of FMO are independent of the presence of oxygen (Figure 6.2), which would be expected to significantly shorten the FMO triplet lifetime if triplet state quenching was occurring. It is likely that the lowest energy triplet state of FMO (localized on BChl #3, (Kihara et al. 2015)) lies below the energy of singlet oxygen, making quenching very unlikely or impossible. Phosphorescence spectroscopy could directly reveal the triplet state energy of FMO and verify this hypothesis.

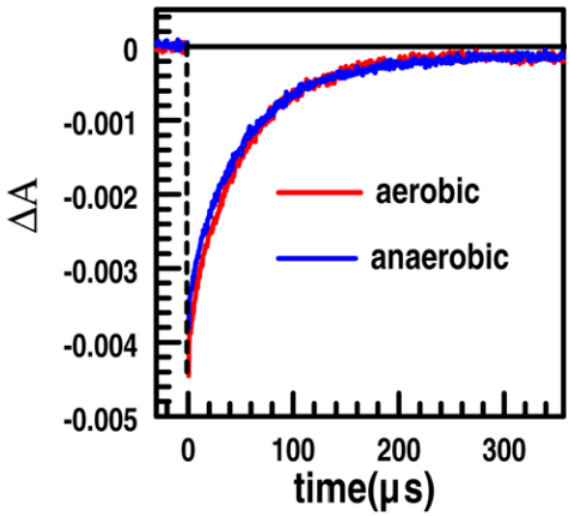

Figure 6.2: Room temperature triplet state dynamics of FMO (exited at 600 nm (Q_x band) and probed at 810 nm (Q_y band)) in aerobic and anaerobic conditions (Kihara et al. 2015). Note that the triplet state lifetime is unaffected by the presence of oxygen.

The phosphorescence from FMO is expected to peak at a wavelength longer than singlet oxygen (1270 nm) based on the inability of triplet FMO to be quenched by oxygen. An empirical model can be used to predict the expected triplet state energy of FMO given the predicted (singlet) site energy of BChl #3. By plotting the singlet excited state energy verses the triplet excited state energy (using the data of Table 4.1) a linear trend is revealed (Figure 6.3). Using the predicted singlet state site energy of BChl #3 (1.505 eV, (Kihara et al. 2015)), we can use the empirical trend to predict that the triplet state site energy of BChl #3 is 0.966 eV (Kihara et al. 2015) or 14 meV below the energy of singlet oxygen (0.98 eV, Table 4.1). This predicted energy corresponds to a phosphorescence peak of approximately 1283 nm.

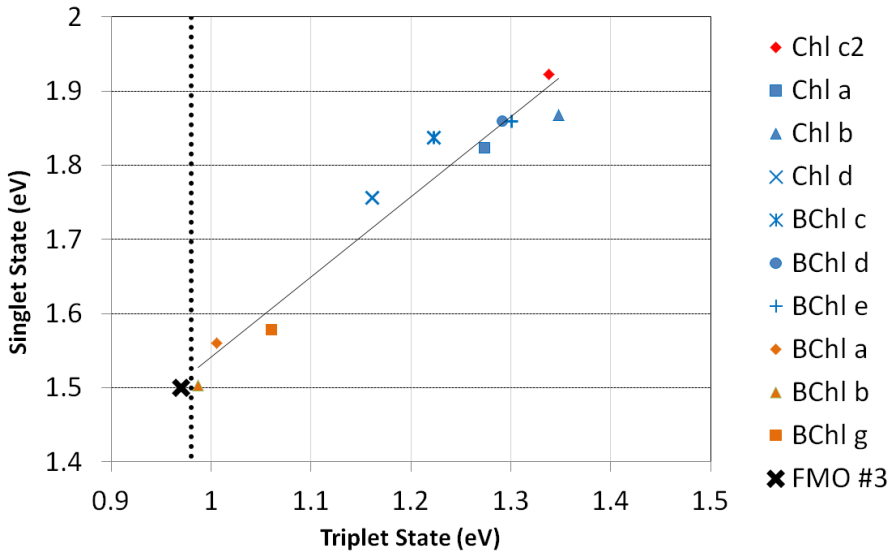

Figure 6.3: Singlet state energy (fluorescence maxima) verses triplet state energy (phosphorescence maxima) with empirical trend line. Black X is the predicted singlet and triplet state energy of FMO BChl #3. (Kihara et al. 2015)

Additionally, the spectral width of the FMO phosphorescence can be predicted from the width of its fluorescence. Examining Figure 4.4, we see that when plotted on an energy scale the fluorescence and phosphorescence possess the same spectra width, meaning the singlet and triplet radiative transitions experience the same inhomogeneous broadening. Using the FMO fluorescence spectrum published by Kell (Kell et al. 2014) and the predicted triplet state energy (0.966 eV) a prediction of the phosphorescence emission spectrum can be made by shifting the fluorescence peak while keeping the spectral FWHM constant on an energy scale. The resulting spectrum is show in Figure 6.4. Note the narrow spectral width of the measured (~4 nm FWHM) fluorescence and predicted phosphorescence (~10 nm FWHM) compared to Figure 4.1.

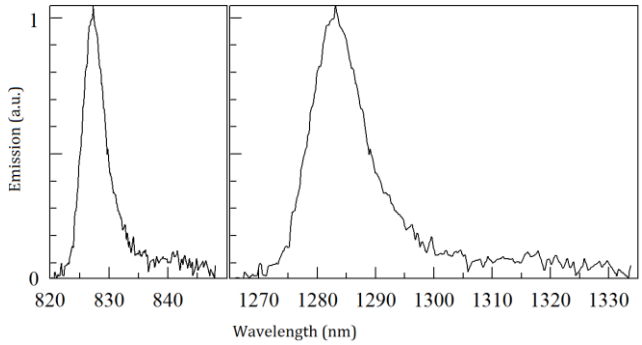

Figure 6.4: Fluorescence spectrum as measure by Kell et. al. (LEFT) (Kell et al. 2014) with predicted phosphorescence spectrum (RIGHT).

Samples of FMO were provided by Dr. Greg Orf of the Blankenship research group. The FMO complexes were isolated from *C. tepidum* and purified as described in (Orf et al. 2014). Before attempting the phosphorescence measurement, the sample was prepared in reducing conditions by addition of sodium dithionite (10 mM) which has been shown to extend the singlet state lifetime (~2ns in reducing conditions) and increase the triplet state quantum yield (up to ~11%) (Orf et al. 2014). During all phosphorescence measurements the sample was in a quartz EPR tube at a temperature of 77K and dissolved in 40%, 20 mM Tris-HCl buffer at pH 8.0 (with 10mM sodium dithionite) and 60% glycerin. The FMO monomer concentration was 4.3 uM (30-34 uM BChl *a* concentration) which corresponds to a Q_y peak absorption of ~0.5 with a 1 mm path length.

As shown in Figure 6.1, the FMO complex contains 8 BChl *a* monomers per protein monomer, however, the eighth BChl *a* is weakly bound and tends to wash out during protein preparation (Wen et al. 2011). One practical result of this weakly bound BChl is that FMO samples can be contaminated by free monomers of BChl *a* (as well as BPheo *a* and chlorin type molecules from the breakdown of BChl *a*) which can be exited

at wavelengths shorter than ~810nm. In experiments with FMO, care must be taken to avoid exciting these free monomers or account for their effects. Since the phosphorescence quantum yield of these monomers is potentially higher than the phosphorescence quantum yield of the FMO complexes, the samples were excited at 820 nm to avoid direct excitation of these free monomers and absorption spectra taken before and after the experiment show no degradation of the sample. However, exciting in this spectral range is problematic due to the ~800-810 nm absorption band of Nd^{3+} doped glass (Vijaya Kumar & Suresh Kumar 2012). Excitation of this band results in strong emissions at ~910, ~1060, and ~1330 nm from any Nd^{3+} contaminants.

Attempts to measure the phosphorescence emission from FMO (Figure 6.5) yielded no reliable results, even with integration times up to 1120 seconds per point (at ~20 nm bandwidth). When exciting at 820 nm a weak emission band was detected at ~1360 nm. However, based on its peak position and spectral width (~70nm) this band most likely is the result of an Nd^{3+} contaminant in the sample cell, cryostat windows, or system lenses. Future experiments can excite in the 825-830 nm range (near a minimum in the absorbance of Nd^{3+}, (Vijaya Kumar & Suresh Kumar 2012)) to reduce these emissions.

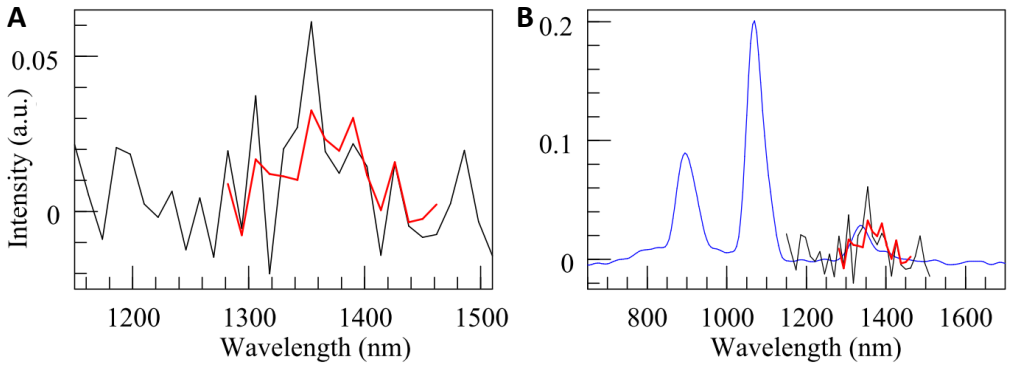

Figure 6.5: A – 1360 nm emission band. Integration time for BLACK spectrum was 360 sec/point and 1120 sec/point for RED spectrum (both RED and BLACK are from the same experiment). Excitation was 820nm. **B –** Overlay of spectra from A with emission spectrum from Nd^{3+} contaminated glass.

It is likely that the phosphorescence quantum yield of FMO is so low that it is beyond the reasonable detection limit. Each FMO monomer contains seven BChl *a* molecules and the triplet state dynamics, measured by nanosecond transient absorption (Kihara et al. 2015), show three distinct lifetimes of 1µs, 11µs, and 55µs. The 1µs and 11µs lifetimes originate from downhill triplet energy transfer (TET) between individual BChl *a* pigments within the complex. Specifically the 11µs component corresponds to TET from BChl #5 to BChl #4 and the 1µs component corresponds to TET from BChl #4 to BChl #3 (see Figure 6.1 for pigment numbering scheme). The 55µs component corresponds to the decay of the lowest energy triplet state of FMO which lies on BChl #3.

The longest living triplet state of FMO is 55µs, which is a factor of two to four shorter than the triplet state lifetime of monomeric BChl *a* in solution (see Table 4.1), which should reduce the expected phosphorescence quantum yield of FMO by a factor of two to four. Additionally, because the second longest living triplet state (11µs, BChl #4) is a factor of five shorter than the longest living state, we can assume that each FMO

monomer only emits phosphorescence from its lowest energy triplet state since the next highest state should be at least 5 times less intense. Therefore, since each FMO monomer contains seven BChl *a*, the total quantum yield will be an additional factor of seven lower than an equivalent amount of monomeric BChl *a* in solution (seven absorbers per one emitter). This simple analysis demonstrates that the expected phosphorescence quantum yield of FMO should be between 14-28 times less than an equivalent amount of BChl *a* in solution, which itself has a phosphorescence quantum yield of 10^{-7} (Table 4.1). However, phosphorescence is a forbidden transition and thus susceptible to small perturbations. It is possible that the pigment's surrounding chemical environment could have a significant effect on the quantum yield independent of the shortened triplet state lifetime.

The phosphorescence spectrum of BChl *a* in Figure 4.1 has a signal to noise ratio (S/N) of approximately 10:1 (at peak) and was measured at 10 nm spectral bandwidth (half the bandwidth used for the attempted measurement of FMO) and with an integration time of 56 seconds per point. With the expected intensity reduced by a factor of 14-28, to obtain a phosphorescence spectrum for FMO similar to that of BChl *a* in Figure 4.1 (at twice the spectral bandwidth) would require integration times between 49 ($(14/2)^2$) and 196 ($(28/2)^2$) times longer (S/N improves as the square root of the integration time). That is, integration times between ~2800 to 11000 seconds per point to reach the same S/N as in Figure 4.1, or ~250 to 1000 seconds per point to reach a S/N of three, which is equivalent to the integrations times used to produce the spectra in Figure 6.5A. It is possible that the phosphorescence emission of FMO is being masked by the emissions of Nd^{3+} contaminated glass; however, no clear sharp peaks are rising above the background level. With a predicted S/N of at least three, a monochromator bandwidth of 20 nm, and a

step size of 12 nm (as in Figure 6.5) one would expect a peak of two to three points standing well above the background like in Figure 6.6. No compelling candidates distinct from the Nd^{3+} band are visible in Figure 6.5.

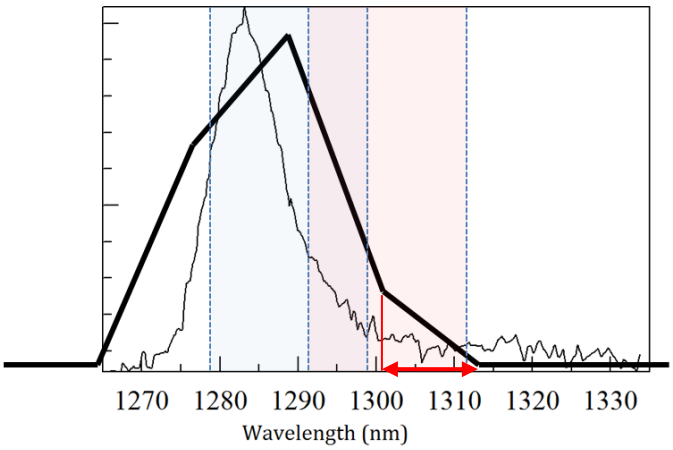

Figure 6.6: Simulated FMO phosphorescence spectrum with 12 nm step size and 20 nm monochromator bandwidth. Two adjacent 20 nm windows (BLUE and RED) are shown with the overlap in purple. Red arrow is the 12 nm step.

6.2 Triplet Energy Transfer and Couplings

As previously mentioned, TET was observed from FMO BChl #5 to #4 with a lifetime of 11 μs and from BChl #4 to #3 with a 1 μs lifetime. While Equation 2.35 allows for calculation of the triplet-triplet coupling between pigments, it assumes the transition occurs from a single vibronic state of the donor to a single vibronic state of the acceptor, both of known degeneracy. In reality, one must sum over all possible vibronic states of the donor and acceptor (You & Hsu 2011):

$$k_{IF} = \frac{2\pi}{\hbar}\sum_{\mu}\sum_{v} p(\varepsilon_{I\mu})\left|\langle \Phi_{I\mu}|H_{IF}|\Phi_{Fv}\rangle\right|^2 \delta(\varepsilon_{I\mu} - \varepsilon_{Fv})$$

Equation 6.1

Where $\langle \Phi_{I\mu}|$ is the 'μ' vibrational level of electronic state 'I' while $\varepsilon_{I\mu}$ and $p(\varepsilon_{I\mu})$ are the energy and Boltzmann population, respectively, of the same vibronic state (You & Hsu 2011). In the Condon Approximation and assuming no vibrational coupling between donor and acceptor, Equation 6.1 can be written as (see You and Hsu (You & Hsu 2011) for a derivation):

$$k_{IF} = \frac{2\pi}{\hbar}|H_{IF}|^2 \int_{-\infty}^{+\infty} f_D(E) f_A(E) dE$$

Equation 6.2

Where H_{IF} is the pure electronic coupling between states 'I' and 'F' and the integral is the Franck-Condon Weighted Density of states (FCWD). The functions $f_D(E)$ and $f_A(E)$ are related to the donor emission and acceptor absorption spectra by:

$$f_A(E) = \frac{\sigma_{IF}^A(E)/E}{\int dE\, \sigma_{IF}^A(E)/E}$$

$$f_D(E) = \frac{A_{IF}^D(E)/E^3}{\int dE\, A_{IF}^D(E)/E^3}$$

Equation 6.3

Where the acceptor absorption cross-section, σ_{IF}, and donor spontaneous emission coefficient, A_{IF}, can be replaced by the appropriate experimental absorption or emission spectrum.

Using the measured TET rates together with the predicted FMO phosphorescence spectrum (Figure 6.4) allows us to calculate the necessary coupling for the observed TET times. Solving Equation 6.2 for the coupling, $|H_{IF}|$, gives (where $k = 1/\tau$):

$$Coupling = \left(\frac{k}{\frac{2\pi}{\hbar} \int f_D(E) f_A(E) dE} \right)^{1/2}$$

Equation 6.4

Clearly we are not in possession of the triplet absorbance spectrum since the $S_0 \rightarrow T_1$ transition is spin forbidden and has a very low probability. However, as done by You and Hsu (You & Hsu 2011) it can be approximated by assuming the triplet absorption is the mirror of the phosphorescence spectrum with the same Stokes shift as the fluorescence (22 cm^{-1} (or 2.73 meV) according to Kell (Kell et al. 2014)).

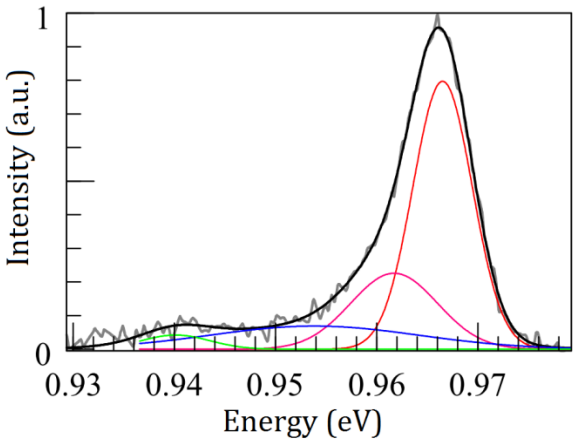

Figure 6.7: Simulated FMO phosphorescence spectrum (on energy scale) with Gaussian fit components.

The simulated phosphorescence spectrum (Figure 6.4) can be well fit with four Gaussian components, Figure 6.7. These fit components can be used, along with the BChl site energies and experimentally measured Stokes shift, to construct the donor emission

and acceptor absorption spectra needed to calculate the coupling using Equation 6.4. Using the estimated triplet excited state site energies of BChl #5, #4, and #3 (1.003 eV, 0.987 eV, and 0.967 eV respectively (see Kihara et. al. supporting info (Kihara et al. 2015)) the spectral overlap integral (i.e. FCWD) of Equation 6.4 was numerically evaluated and the couplings between BChl #5 and #4 and BChl #4 and #3 were calculated.

Table 6.1: Triplet energy transfer (TET) within FMO: Lifetime, spectral overlap of donor and acceptor (Figure 6.8), and triplet-triplet coupling

TET	**Lifetime** (μs)	**Overlap** (meV^{-1})	**Coupling** (meV)
BChl **#5** → BChl **#4**	11	0.0181	0.00073
BChl **#4** → BChl **#3**	1	0.0133	0.00281

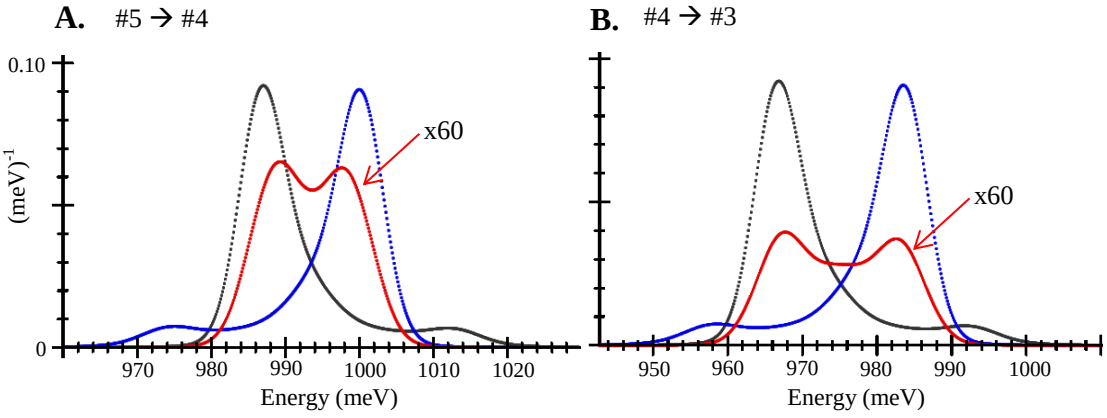

Figure 6.8: Simulated donor (BLUE) and acceptor (BLACK) spectra and product (RED, multiplied by 60 for display). **A –** Donor (BChl #5, blue), Acceptor (BChl #4, black). **B –** Donor (BChl #4, blue), Acceptor (BChl #3, black). Note: Donor and Acceptor spectra are normalized to an area of one and the vertical scale of **B** is the same as **A**.

The triplet-triplet coupling theory developed by You et al (You et al. 2006) can also be used to estimate these couplings. If the expression for full contact face to face

coupling (Figure 6.9 A) is used, as in Kihara et. al. (Kihara et al. 2015), then the coupling follows:

$$c = 895529\ meV * exp\left(-2.6\ \text{Å}^{-1} * d\right)$$

Equation 6.5

Where *d* is the carbon to carbon separation distance as depicted in Figure 6.9 A. If the expression for edge to edge coupling between two molecules (Figure 6.9 B) is used, then the coupling follows:

$$c = 1119\ meV * exp\left(-3\ \text{Å}^{-1} * d\right)$$

Equation 6.6

Where *d* is the hydrogen to hydrogen separation distance as depicted in Figure 6.9 B.

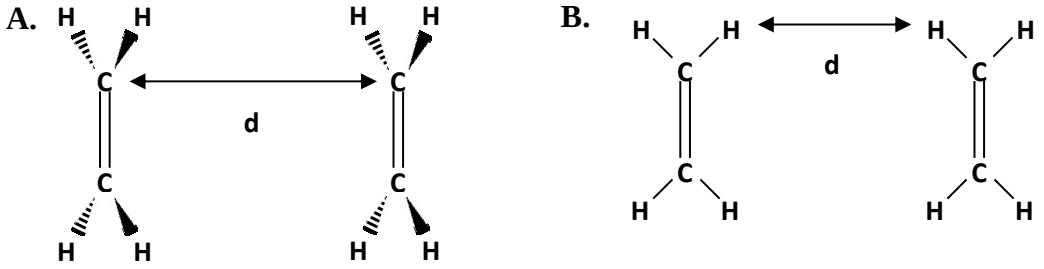

Figure 6.9: A - Geometry of full contact face to face coupling. **B -** Edge to edge coupling. See (You et al. 2006)

Taking the closest carbon to carbon distance (using only the carbons in the conjugated π system) between BChl #5 and BChl #4 to be 6.6 Å and between BChl #4 and BChl #3 to be 6 Å and the H-C bond length to be 1Å (needed for use of Equation 6.6) we get the couplings:

Table 6.2: Computed FMO T-T couplings using the method of You et. al. (Equation 6.5 and Equation 6.6) and Equation 6.4 (Table 6.1)

	Couplings		
BChl	**Equation 6.5** (meV)	**Equation 6.6** (meV)	**Table 6.1** (meV)
#5 → #4	0.0316	0.0011	0.000726
#4 → #3	0.1503	0.0069	0.002810

Note that the couplings calculated using Equation 6.5 are 20 - 30 times larger than the couplings obtained with Equation 6.6. Since Equation 6.6 accounts for the influence of the hydrogens while Equation 6.5 does not (Figure 6.9), it seems reasonable that Equation 6.5 would overestimate the couplings. Also note that the results from Equation 6.6 are only 1.5 - 2.5 times larger than the results obtained with Equation 6.4 (computed from measured TET lifetimes and simulated spectra).

6.3 Discussion

It appears unlikely that a direct measurement of the FMO triplet state energy will be made with the current phosphorescence spectrometer (Section 3.3), especially without eliminating all trace-sources of Nd^{3+} contamination since the ~1300 nm emission band overlaps the expected phosphorescence signal. However, inferences could still be made based on empirical trends obtained from the data of Chapter 0. Additional data (from Mg-porphyrins, Mg-chlorins, and Mg-bacteriochlorins) would be helpful in determining whether the observed trend in Figure 6.3 is a single trend as stated or each class of molecule has its own singlet state energy vs. triplet state energy trend. However, such data would be difficult to obtain because, excluding Chl *f*, all known natural (B)Chl

molecules have been measured and purely synthetic molecules would have to be obtained for the proposed measurements.

The experimentally measured TET rates offer an opportunity to calculate the T-T coupling independent of any computational modeling. However, the donor and acceptor spectra needed for such a calculation must be estimated because direct measurement is experimentally difficult. Fortunately, insights gained from monomer fluorescence and phosphorescence spectra together with the experimentally measured FMO fluorescence spectrum allow for estimation of the needed spectra and for an approximate calculation to be made. Better results can be obtained by better estimates of the BChl site energies and better estimation of the FMO phosphorescence spectrum (Figure 6.7) to account for the fact that phosphorescence vibrational bands are more intense relative to the emission peak than in fluorescence (see Figure 4.4).

CHAPTER 7 – THE *CHLOROBACULUM TEPIDUM* CHLOROSOME

The main antenna complex of C*hlorobaculum tepidum* (*C. tepidum*) is known as a chlorosome (Figure 1.6, Figure 7.1) and is described in brief in section 1.3.2. The major photosynthetic components of the chlorosome are the large BChl *c* (in *C. tepidum*) aggregates (which also contain a large amount of carotenoids, Pšencˇík 2013) and the membrane bound BChl *a* containing baseplate. It has been shown that, in spite of the large number of BChl molecules in these complexes (~100000 BChl), they are exceptionally photostable. Even the carotenoid free mutants show significantly enhanced photostability. In this section, we will analyze the triplet exciton formation as a possible mechanism responsible for the chlorosome's high photo stability.

Light energy absorbed by a BChl *c* in the chlorosome is rapidly transferred through the aggregates to the BChl *a* baseplate. From the baseplate the singlet excitation is transferred to the FMO complex (Chapter 0) which then transfers the excitation to the reaction center (Figure 7.1) where charge separation occurs.

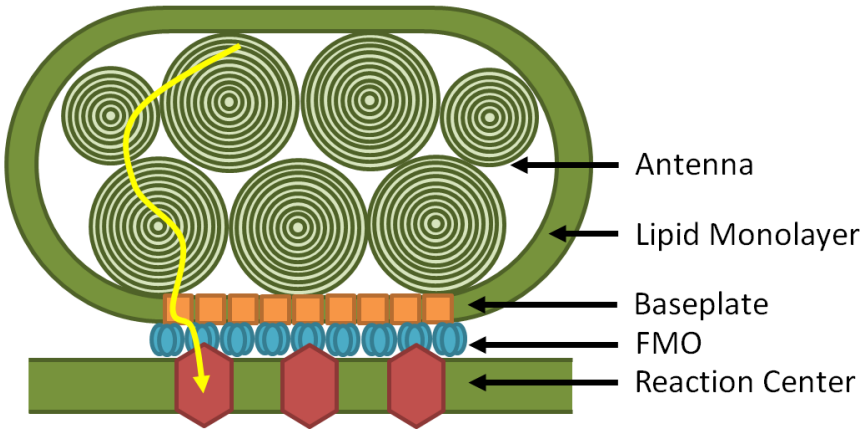

Figure 7.1: Chlorosome structure and function. Energy captured by the BChl *c* aggregate antenna is transferred to the BChl *a* containing base plate, to the FMO complex and then to the reaction center complex.

A model of BChl pigment organization within the aggregate antenna was developed by Ganapathy et. al. using data from NMR and cryoEM microscopy (Ganapathy et al. 2009) which has been used to explain the varied absorption and circular dichroism spectra of natural chlorosomes (Tang et al. 2013) and has additional experimental support from 2-D polarization fluorescence microscopy (Tian et al. 2011). In this model, the pigment-pigment organization is semi-crystalline with a unit cell consisting of six pigments (see the vectors 'a' and 'b' in Figure 7.2 A) and significant nearest neighbor T-T coupling along two distinct directions within the aggregate structure (see red and green arrows Figure 7.2 A). Spacing between nearest neighbors is examined in Figure 7.2 B where a pigment located at vertex V_1 has a plane to plane separation from pigments at vertices V_2 and V_3 of 3.67 Å (h_1) and center to center displacements of 5.06 Å (d_1) from the pigment at V_2 and 9.04 Å (d_2) from the pigment at V_3.

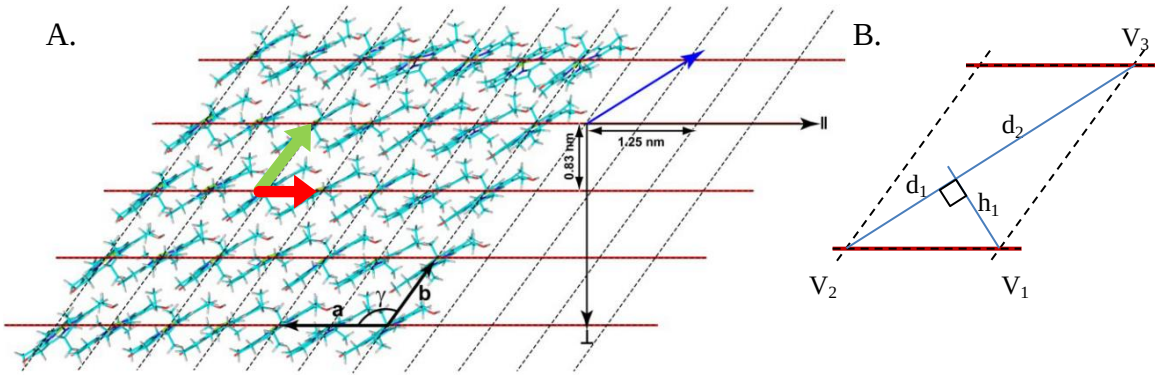

Figure 7.2: Model of chlorosome pigment packing proposed by Ganapathy et. al. (Ganapathy et al. 2009). **A –** Figure from Ganapathy showing unit cell parameters (a = 1.25 Å, b = 0.98 Å, γ = 122°) and inter-pigment spacing and orientation. Directions defined as "strong" and "weak" coupling are indicated with a green (weak) and red (strong) arrows. **B –** Inter-pigment plane to plane separation, "h_1", and center to center displacements, "d_1" and "d_2" for the "strong" and "weak" couplings respectively. Based on Ganapathy's parameters: $\mathbf{d_1}$ = 5.06 Å, $\mathbf{d_2}$ = 9.04 Å, $\mathbf{h_1}$ = 3.67 Å

Only the short range order as illustrated in Figure 7.2 matters for T-T interactions, unlike the singlet state interactions (absorption, CD, singlet exciton formation) where both the short range and long order matter, e.g. number and size of concentric and adjacent BChl tubular aggregates (Prokhorenko et al. 2003) and direction the 'a' vector of Figure 7.2 A wraps (Tang et al. 2013).

7.1 Singlet State Dynamics

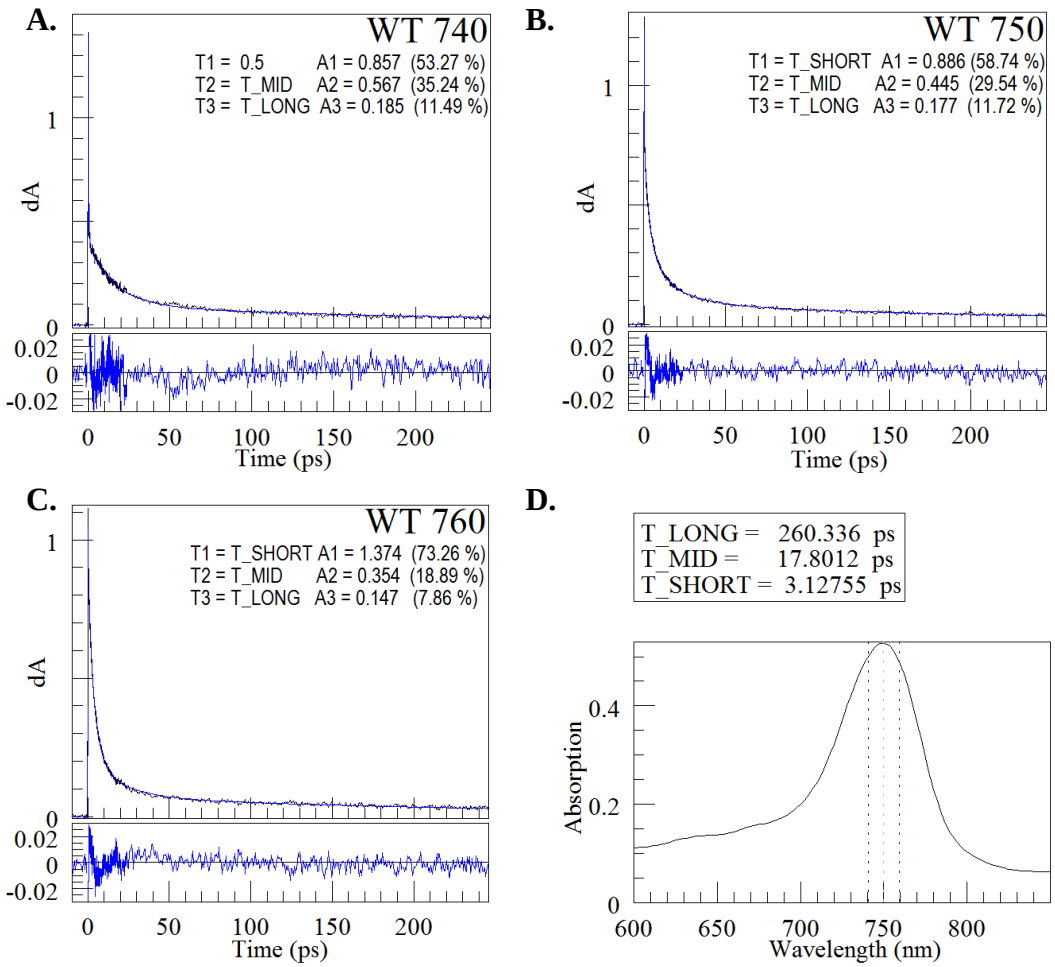

Figure 7.3: Single color ultrafast dynamics of wild type *C. tepidum* chlorosome. Black is the measured transient absorption trace, Blue is the fit (fit lifetimes and amplitudes given), and the lower box is the difference between the data and fit. **A thru C** – single color pump-probe measurements at 740, 750, and 760 nm. **D –** Absorption spectrum of sample (with pump-probe wavelengths marked) and global fit lifetimes.

Singlet state dynamics of wild type (WT) *C. tepidum* chlorosomes have been studied by a variety of means including ultrafast pump-probe transient absorption (Figure 7.3) and fluorescence lifetime experiments. These transient absorption and fluorescence lifetime experiments demonstrate that BChl *c* aggregates, both artificial and natural, have excited state lifetimes of only a few tens of picoseconds (Savikhin et al. 1995; van Noort et al. 1997). Single color (same wavelength for pump and probe) ultrafast pump-probe

transient absorption experiments using the system describe in Section 3.4.1 were performed on WT *C. tepidum* chlorosomes in phosphate buffer (Q_y OD = 0.4) (Figure 7.3) which closely matches the data obtained by Savikhin et. al. (Savikhin et al. 1995). These transient absorption experiments show that the dynamics of WT chlorosomes (*C. tepidum*) are dominated by three lifetime components (~0.5-3 ps, ~12-18 ps, ~200-500 ps, see Figure 7.3 and Savikhin et. al. (Savikhin et al. 1995)). While fluorescence lifetime spectroscopy suggests the singlet state lifetimes of WT *C. tepidum* chlorosomes are 9 ps and 40 ps (van Noort et al. 1997). The origin of this factor of ~3 difference between these techniques is likely due to the use of a photon counting system with an instrument response function of ~50 ps FWHM to measure lifetimes of ~3 and ~18 ps. The presence of three lifetimes in transient absorption data and only two in fluorescence lifetime data suggest that the short lifetimes are due to singlet state dynamics (since they are emissive) while the long lifetime component is a triplet or other long living non-emissive state.

In addition to WT chlorosomes, van Noort et. al. (van Noort et al. 1997) also measured the emissive lifetime of artificial aggregates of BChl *c* finding lifetime components of 12 ps and 52 ps (amplitudes of 95% and 5% total respectively). It's likely that these lifetimes also possess the factor of three discrepancy. However, it’s clear from this data that the short lifetime dominates the singlet state dynamics of the artificial aggregate much like in the WT chlorosome (Figure 7.3).

7.2 Triplet State Dynamics

Nanosecond pump-probe measurements of WT *C. tepidum* chlorosomes performed by Kim et. al. (Kim et al. 2007) demonstrate BChl *c* to carotenoid triplet state energy

transfer in WT chlorosomes, showing that BChl *c* triplet states form in chlorosomes and are quenched by carotenoids. Further experiments show that at high pump intensities, excited state absorbance reveals the existence of a long living excited state (possibly a triplet) with a lifetime exceeding the experimental detection window of 1 ms.

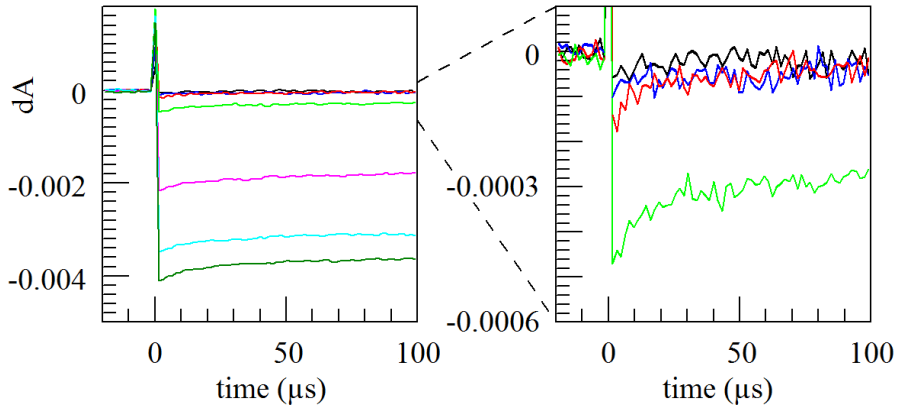

Figure 7.4: Nanosecond transient absorption measurements of BChl *c* artificial aggregates at different pump power densities. Pump = 426 nm. Probe = 738 nm. Pump energy densities were: 3.2 (black), 5.9 (blue), 15 (red), 25 (light green), 36 (magenta), 45 (cyan), 51 (dark green) mJ/cm^2. NOTE: initial positive spike is due to sample fluorescence [In collaboration with Valentyn Stadnytskyi]

Samples of BChl *c*, from WT *C. tepidum*, were extracted using the method described in Section 4.1 and mixed with tris-buffer to form aggregates according to the method of Miller (Miller et al. 1993). Nanosecond transient absorption experiments, performed with the spectrometer described in Section 3.4.2, show artificial aggregates of BChl *c* (Figure 7.4) have a strong non-linear response to the pump intensity. For a sample with an initial absorbance of 0.12 at the pump wavelength (426 nm), the non-linear response appears to start in the 15 to 25 mJ/cm^2 pump energy density range (Figure 7.5).

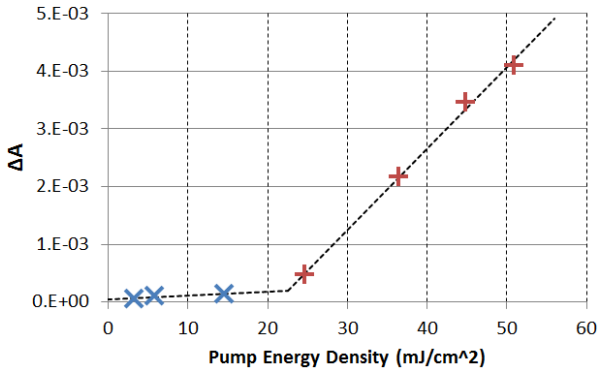

Figure 7.5: Initial |ΔA| amplitude (at t = 0, after the initial fluorescence spike) of nanosecond P-P traces from Figure 7.4 verses pump energy density. 'X' (Blue) and '+' (Red) points are measurements; black dashed lines are linear regression fits. Note that including the point at ~25 mJ/cm^2 with the '+' series was a semi arbitrary choice. However, the trend lines meet near ~25 mJ/cm^2 regardless of which choice is made.

Some understanding can be found by rescaling the x-axis so that, instead of energy density (mJ/cm^2), it's in units of excitations per exciton per exciton lifetime. Specifically, the number of absorbed photons per N-pigments per Δt, were N is the number of pigments a singlet exciton extends over and Δt is the expected lifetime of the exciton (Figure 7.6). Approximations can be made for the lifetime and physical size of a singlet exciton in these aggregated systems. Prokhorenko et. al. (Prokhorenko et al. 2003) estimates the size of the lowest energy singlet exciton on an isolated tubular aggregate to extend over 40-50 individual BChl *c* molecules while the data of van Noort (van Noort et al. 1997) shows the singlet state dynamics are dominated by the short (12 ps) lifetime component (~95% of total amplitude) with only a small contribution (~5% total amplitude) from the longer lifetime (52 ps). Assuming 100 pigments per exciton and a time interval of 10 ps (~1 lifetime) we see the start of the non-linearity beginning around one excitation per 100 pigments per 10 ps (Figure 7.6). This corresponds to the point where an aggregate has become near saturated with excitations or, to restate, at the point

of one excitation per exciton per exciton lifetime. However, the previous analysis is extremely simplistic and has ignored important phenomena such as singlet exciton annihilation which is known to shorten the singlet state lifetime (Engel et al. 2006).

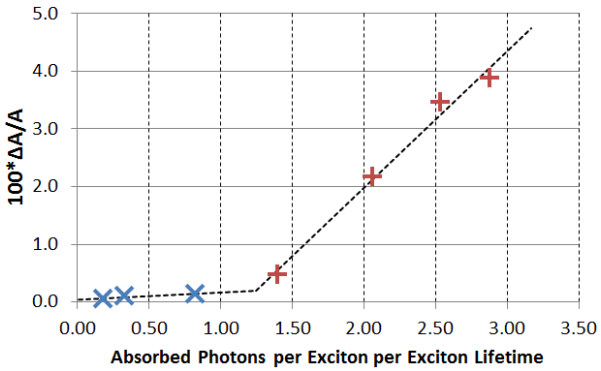

Figure 7.6: Percent change in absorption (vertical axis) verses excitations per exciton. Exciton size was assumed to be 100 BChl c pigments and exciton lifetime was assumed to be 10 ps. Horizontal axis could read "Absorbed photons per 100 pigments per 10 ps.

The origin of this long living excited state and nonlinear behavior is unknown. Additionally, it's unknown if the long living states produced in the 1st linear regime (Blue points, Figure 7.5 and Figure 7.6) are different from the long living states produced in the 2nd linear regime (Red points, Figure 7.5 and Figure 7.6). It is possible that absorption of an additional photon from the 1st excited excitonic state results in photoionization and this is the origin of the long living state observed in the nanosecond kinetics. Evidence for photoionization from EPR experiments will be presented in a later section.

As stated earlier, a similar non-linear response was observed by Kim et. al. (Kim et al. 2007) when investigating the microsecond dynamics of WT chlorosomes as a function of pump intensity (Figure 7.7). At pump energy densities of 17 and 5.9 mJ/cm^2 photobleaching with a lifetime exceeding 1 ms is the dominant signal while a pump energy density of 1 mJ/cm^2 produced no long living state. It was found that at pump

energy densities greater than 3 mJ/cm^2 the signal due to quenching of triplet BChl by carotenoids (excited state absorption) is superseded by the long living photobleaching. Plotting the amplitude of the long living component verses the pump intensity and rescaling the pump energy densities as done previously (assuming Δt = 10 ps and N_pigments = 1000) gives us Figure 7.7. Again, the beginning of the non-linear response is approximately at the point of one excitation per exciton per exciton lifetime. The choice to assume 1000 pigments to produce Figure 7.7 and 100 pigments to produce Figure 7.6 is discussed next.

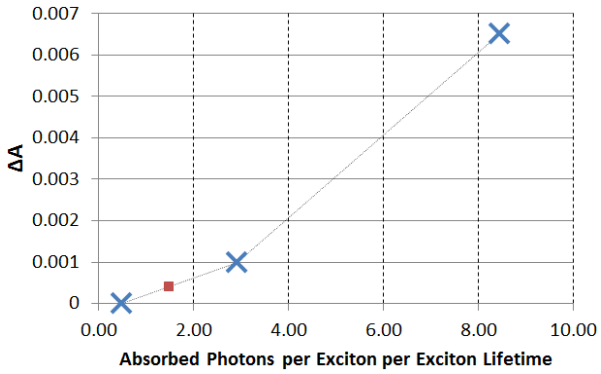

Figure 7.7: ΔA verses excitations per exciton for WT *C. tepidum* chlorosomes (data from Kim et. al. (Kim et al. 2007)). Exciton size was assumed to be 1000 BChl c pigments and exciton lifetime was assumed to be 10 ps. '■' (Red) point corresponds to pump energy density (3 mJ/cm^2) where Kim stated unexpected photobleaching began (no ΔA was given for this point).

The size of an exciton in a chlorosome is likely to be far larger than the isolated tubular rods assumed by Prokhorenko (Prokhorenko et al. 2003) due to the large number of closely packed pigments within the membrane bound organelle. In a chlorosome, the BChl aggregates form nested, concentric tube structures, "rods", with multiple closely spaced rods per chlorosome (see Ganapathy (Ganapathy et al. 2009)) allowing for strong tube to tube and rod to rod interactions, while an artificial aggregate lacks a membrane to

keep the individual tubular aggregates closely packed and the tubes self-assemble in a comparatively low concentration environment. The difference between a natural chlorosome and the artificial aggregate used in this experiment is easily understood by comparing the BChl *c* concentration. The concentration within a chlorosome is approximately 0.9 M (200,000 pigments in a 40X60X160 nm envelope, (Linnanto & Korppi-Tommola 2013)), a concentration ~60,000 times higher than the initial BChl concentration of 0.015 mM used in the experiment for Figure 7.4. Thus the artificial aggregate should, at least initially, exist mostly as isolated tubes. However, artificial aggregates have been known to clump and drop out of solution and its unknown if this process builds structures like those found in intact chlorosomes.

7.3 Electron Paramagnetic Resonance

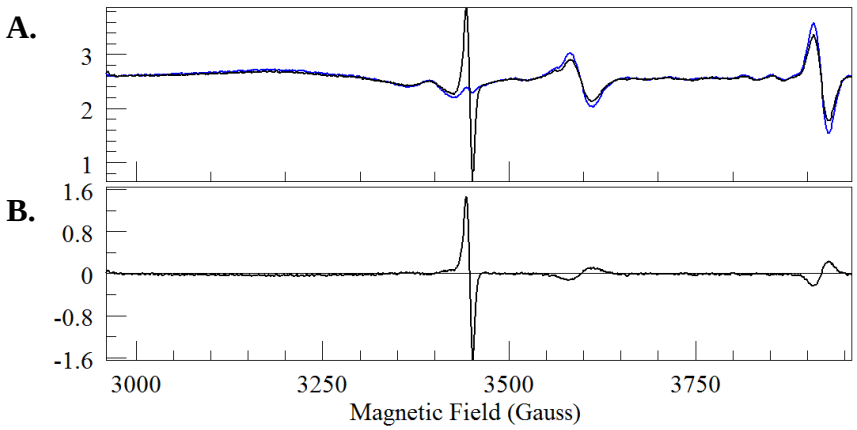

Figure 7.8: A - The EPR spectra of WT C. tepidum chlorosomes in the dark (BLUE) and under illumination by a xenon arc lamp (BLACK). **B –** The difference between the illuminated and dark measurements. Temperature was 20K and microwave frequency was 9.660807 GHz. [In collaboration with Dr. Oleg Poluektov and Dr. Jens Niklas]

In the last section it was mentioned that photoionization could occur when the chlorosome is exposed to intense light. Evidence of charge separation comes from

electron paramagnetic resonance (EPR) measurements performed on WT *C. tepidum* chlorosomes. An EPR spectrum of a chlorosome sample at 20K was measured in the dark, giving the blue spectrum in Figure 7.8 A. Another EPR spectrum was taken with the sample under the intense steady illumination of a xenon arc lamp, giving the black spectrum in Figure 7.8 A. Microwave frequency for both was 9.660807 GHz. The light induced EPR signal (black Figure 7.8 A) had a lifetime of many minutes (> 10 min) after illumination was removed, however thawing and refreezing the sample (in the dark) returned the sample to the dark state (blue Figure 7.8 A).

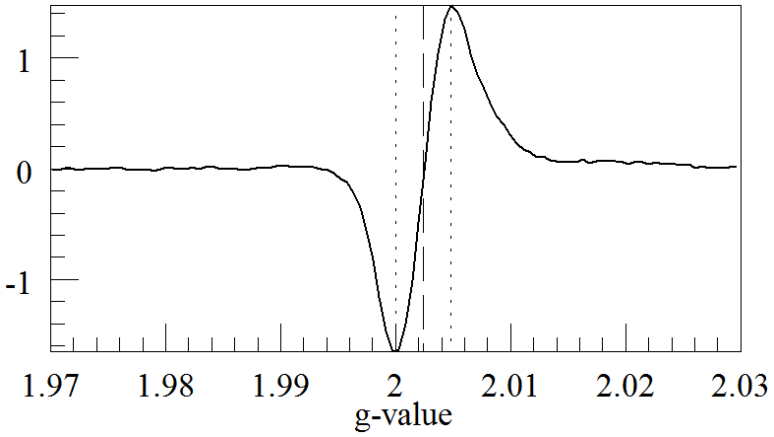

Figure 7.9: Radical signal of Figure 7.8 B converted to g-value.

Converting the light-dark difference spectrum (Figure 7.8 B) to g-value with Equation 3.8 we see a radical with a g-value of 2.0025 and a line width of 0.00483 (8.3 gauss) (Figure 7.9) which is nearly identical to the radical produced by chemically oxidizing the same type of chlorosome with potassium ferricyanide, center g-value = 2.0028(±0.0003) and a line width = 0.00485 (8.2 gauss) (Di Valentin et al. 2002). These g-values match the value for chemically oxidized BChl *c* monomers, 2.0025, with linewidths approximately 40% narrower compared to the monomer (line width of 0.0068

g-value or 11.5 gauss) (van Noort et al. 1997). Linewidth narrowing upon oligomerization was shown to happen in BChl *c* by van Noort et. al. (van Noort et al. 1997). From this data, i.e. identical line center and width compared to chemically oxidized chlorosomes and line center with oxidized monomers, it can be concluded that isolated chlorosomes under strong illumination undergo oxidation (without the need of a chemical oxidant).

Note that van Noort (van Noort et al. 1997) did not publish a microwave frequency and Valentin (Di Valentin et al. 2002) apparently published an incorrect frequency (9.5 GHz), so trial and error was used to determine the correct frequencies (needed to calculate line widths in g-value) from the published EPR spectra and published g-values. The frequencies used to calculate line widths were 9.5546 GHz for van Noort and 9.4064 GHz for Valentin. This process may have introduced errors.

An attempt was made to reproduce the effect seen in Figure 7.8 with aggregates of BChl *e* and BChl *f* which produced little to no response (i.e. difference from light to dark). It's possible that aggregates of BChl *e* or BChl *f* do not respond in the same way as WT BChl *c* containing chlorosomes and an additional experiment using the same type of sample as Figure 7.8 would need to be performed. Additionally a cryo-protectant (glycerin) was not added to the BChl *e* or *f* aggregates and its unknown if this affected the outcome. However, it's likely that the reason little to no response was observed was due to the different light sources used between the experiments. In the experiment for Figure 7.8, the sample was illuminated using a 300 W xenon arc lamp (filtered to remove UV and IR) that was well focused onto the sample. The later experiment used several light

sources, the strongest were an unfocused 1 W, 365 nm flashlight used to illuminate the sample before insertion into the spectrometer and a fiber bundle coupled tungsten lamp (measured output = 400 mW) focused into the spectrometer's resonator through a 50% obstructed window. The optical power delivered onto the sample was likely an order of magnitude or more less than the xenon lamp. Given the nonlinear response seen in nanosecond P-P experiments (see Figure 7.6 and Figure 7.7) it's unsurprising no response was observed in the second EPR experiment.

The EPR and nanosecond pump-probe data seem to strongly suggest photoionization as the origin of the long living state created under intense illumination in chlorosomes and artificial aggregates. This has implications for other optical experiments performed on chlorosomes and artificial aggregates since one must take care to avoid creation of this charge separated state. Also, the identity of the long living state created under less intense illumination (see Figure 7.4 and Figure 7.5) is currently unknown. Kim et. al. (Kim et al. 2007) showed that WT chlorosomes pumped in this regime produced triplet states that were quenched by carotenoids with no long living photobleaching observed. It's unknown if the same is true of artificial BChl *c* aggregates.

7.4 Enhanced Photostability

7.4.1 Experimental Evidence

Chlorosomes and artificial aggregates seem to possess photostability, that is resistance to degradation in the presence of light and oxygen, beyond what would be expected for such a system as seen in photodegration experiments performed by Kim et. al. (Kim et al. 2007). Natural and carotenoid free mutant chlorosomes of *C. tepidum* were

excited into their Q_y absorption maxima (at 0.23 W/cm^2, which falls well within the linear pumping regime) under aerobic conditions with their absorbance monitored as a function of exposure time. While the carotenoid free mutant degraded ~3 three times faster than the wild type (carotenoid protected) chlorosome, the apparently unprotected BChl molecules of the mutant still degrade over three orders of magnitude slower than monomeric BChl *c* in solution (under identical illumination and aerobic conditions). Part of this enhanced stability can be explained by the shortened singlet state lifetime of the aggregates, as a shortened singlet lifetime will reduce the triplet state quantum yield. In methanol, BChl *c* is known to have a singlet excited state lifetime of 2.7 ns which is ~50 to ~200 times longer than the measured singlet state lifetimes (52 and 12 ps) of the wild type chlorosome. This would lower the singlet oxygen formation rate by two orders of magnitude (relative to the monomer) while the photodegradation experiment implies a three order rate decrease.

Krasnovsky et. al. (Krasnovsky Jr et al. 1994) measured the singlet oxygen sensitizing ability of BChl *d* monomers, dimers, and oligomers (both in hexane and intact chlorosome) finding that the singlet oxygen quantum yield of the dimers was 5-7 times less than the monomer while the oligomers (both natural chlorosomes and aggregates in hexane) produced no detectable singlet oxygen. This is consistent with phosphorescence measurements of dimers and BChl *c* aggregates in that the dimer phosphorescence quantum yield was noticeably lower than monomers (maybe due to reduced triplet quantum yield or a shorter triplet state lifetime) while aggregates produced no measurable phosphorescence emission. Arellano et. al. (Arellano et al. 2002) obtained similar results

to Krasnovsky with BChl *e* monomers and aggregates (monomers sensitize singlet O_2 while aggregates do not) .

7.4.2 Possible Mechanisms

7.4.2.1 Exciton Formation

The protection mechanism proposed by Kim (Kim et al. 2007) is a lowering of the triplet state energy, below that of singlet oxygen, by formation of triplet excitons. Exciton formation (Section 2.4) results in a splitting of the monomeric excited states into excitonic states and the larger the T-T coupling and the greater the number of interacting pigments (for example compare Equation 5.8 and Equation 5.12), the lower the energy of the lowest triplet state (ignoring the displacement energy). The energy of the lowest triplet state exciton can be found by calculating the eigenvalues of Equation 2.37.

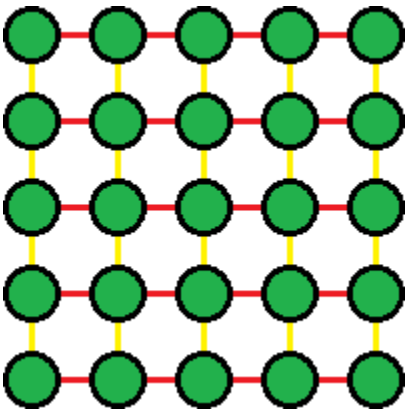

Figure 7.10: Flat sheet model of the BChl *c* aggregate assumed by Kim et. al. with equal coupling (RED and YELLOW lines) between all nearest neighbors.

By assuming an aggregate model of an N by N flat rectangular sheet with couplings of 100 meV between all nearest neighbors and taking the BChl *c* triplet state energy to be 1.29 eV, Kim calculates the lowest triplet state exciton to have an energy of 0.89 eV (Kim et al. 2007), which is 90 meV below the energy of singlet oxygen.

However, the structure by Ganapathy (see Figure 7.2) shows that the coupling cannot be the same in both directions and the work of Section 5.4, specifically Figure 5.32 A, shows that the expected coupling will be significantly less than 100 meV.

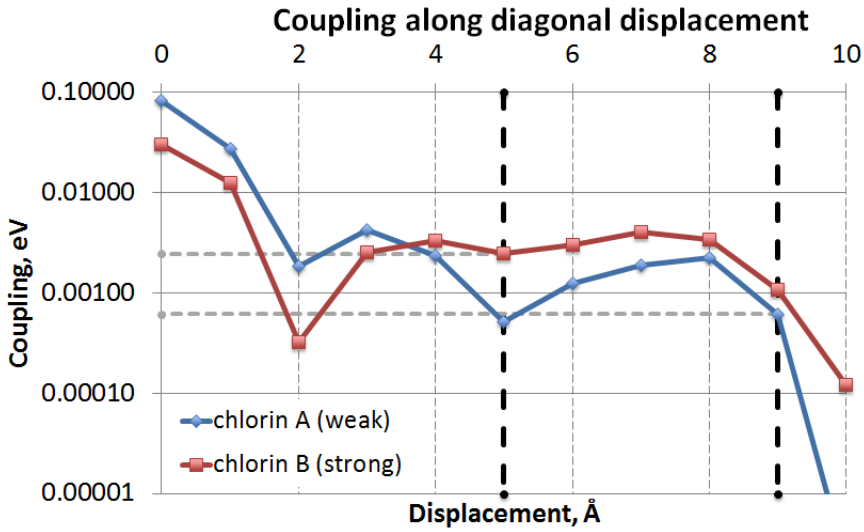

Figure 7.11: Computed couplings for pigment orientations similar to those found in the chlorosome (see Section 5.4) along the "weak" and "strong" coupling directions defined in Figure 7.2. [In collaboration with Dr. Lyudmila Slipchenko]

Based on Ganapathy's parameters, the center to center displacement in the strong coupling direction is 5.06 Å and the center to center displacement in the weak coupling direction is 9.04 Å (Figure 7.2). Thus the couplings in these directions are ~2.5 meV for the strong coupling and ~0.6 meV for the weak coupling (Figure 7.11). Using these couplings and the N by N rectangular model defined in Figure 7.10, we get the triplet state energies of Table 7.1. The lowest energy exciton achievable with these couplings is ~240 meV above the energy of singlet oxygen.

Table 7.1: Energy of lowest triplet exciton for different sized pigment arrays and its difference from the monomer energy. Convergence was achieved around 35x35 pigments

Array Size	Lowest Triplet Exciton (eV)	Difference (meV)
Monomer	1.223	--
3x3	1.2186	4.4
10x10	1.2171	5.9
35x35	1.2168	6.2
75x75	1.2168	6.2

It appears that triplet exciton formation cannot lower the chlorosome triplet state energy below singlet oxygen. Even the solvation energy is far from sufficient to make up the difference. This can be experimentally tested by determining the ability of oxygen to quench the triplet states of artificial aggregates. To do this one would determine the triplet excited state lifetime as a function of oxygen concentration. Since the BChl triplet quenching rate is linearly dependent on the oxygen concentration, evidence of quenching, and thus singlet oxygen sensitization, would come in the form of a decrease of the triplet state lifetime with increasing oxygen concentration as described by Fujimori (Fujimori & Livingston 1957).

$$\frac{dN_T}{dt} = -k_I N_T - k_q[O_2]N_T$$

Equation 7. 1

Where N_T is the triplet state population, $[O_2]$ the oxygen concentration and k_I and k_q are the intrinsic triplet decay and the oxygen quenching rate constants respectively.

Care must be taken to ensure the state created by photo excitation is an actual triplet and not a charge separated state as discussed earlier. This requires an investigation of the non-linear response of the aggregate and of the long living state created at high

pump intensities. Given the observed signal levels corresponding to "low" pump intensity, this may be difficult.

7.4.2.2 Excitation Quenching

Other possible reasons for the reduced chlorosome singlet oxygen yield are triplet-triplet or triplet-singlet annihilation. Due to the aggregate size and large coupling between adjacent chromophores, triplet excitations should be able to migrate through the aggregate structure where upon encountering another triplet excitation can combine to produce a single triplet or singlet excitation (i.e. triplet-triplet annihilation) (Saltiel et al. 1981). The net result is a reduction of the triplet state lifetime and thus a reduction of singlet oxygen yield. Additionally, triplet states are known to be quenchers of singlet excitations (Gruber et al. 2015; Steiner et al. 2014) and their long lifetime means they can persist long enough to interact with singlet excitations. An existing triplet state would further reduce the singlet excited state lifetime which in turn would reduce the triplet state quantum yield.

Clearly such a mechanism would only be active at relatively high light intensities where multiple excitations are present in the same antenna. Green sulfur bacteria grow in very low light intensities (e.g. 0.0005% surface sunlight intensity, (Overmann et al. 1992)). If excitation at surface intensities results in absorption of ~10 photons per chlorophyll per second (Nobel 2009), then 0.0005% surface intensity results in absorption of just over 4 photons per chlorophyll per day or 5-10 photons per chlorosome per second. Given the short lifetime of Chl singlet excited states, it is unlikely there are ever two excitations present in a single antenna at biologically relevant intensities.

7.4.2.3 Triplet State Evolution

It is also possible that the natural evolution of the triplet state in this highly coupled system is to a charge separated state or triplet excimer. If the triplet exciton has some charge transfer character (i.e. some degree of charge separation between the monomers), the state may evolve into a fully charge separated state. Another possibility is not the creation of a triplet exciton, but rather a triplet excimer - a special kind of a dimer with a covalent bond between two monomers that forms only if one molecule is in triplet excited state. Triplet excimers are known to exist and can have triplet state energies far below the monomeric triplet state energy (see Hoffmann et. al. for an example (Hoffmann et al. 2011)). It's unknown if a BChl *c* excimer would have a sufficient phosphorescence quantum yield to allow for detection.

7.5 Conclusion

The mechanism responsible for enhanced photostability of chlorosomes and aggregates is still an open question. As we demonstrate, triplet exciton formation, while present, is not sufficient to provide protection against singlet oxygen sensitization, so some other mechanism must be involved to explain the observed photo stability. Possible explanations include reduced triplet state quantum yield by excitation annihilation and triplet state lowering by triplet excimer formation. The next step in examining this phenomenon should be to establish if triplet states in chlorosomes or aggregates are capable of being quenched by oxygen, which will require carefully controlled

experimentation. Then the question of what kind of mechanism is active (triplet state lowering, carotenoid independent triplet state yield reduction, or other) can be pursued.

It's clear from Section 7.2 and Section 7.3 that any optical experiment on chlorosomes or artificial aggregates must take care not to over pump and cause photoionization. For instance, it's possible that Krasnovsky (Krasnovsky Jr et al. 1994) over pumped the samples when attempting to measure singlet oxygen sensitization by artificial aggregates and intact chlorosomes and it is likely that, in my own attempts to measure phosphorescence of artificial aggregates, the sample was over pumped. However, the pump intensities needed to produce a measurable phosphorescence signal are far beyond biologically relevant intensities and very likely to lie in the "over pump" regime.

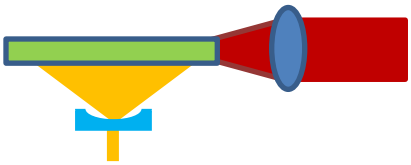

Figure 7.12: Proposed sample and pump geometry for concentration and pump power sensitive samples. Phosphorescence reabsorption (analogous to fluorescence reabsorption, see Figure 3.12) will not be an issue here, but IR absorption (analogous to an optical filter) will be an issue for this geometry and possibly introduce sharp spectral features.

Phosphorescence based experiments may not be possible without significant redesign of the experimental apparatus, specifically the optics and sample geometry. For example, a boost in signal for a low concentration sample was achieved by using a thin sample cell with a long pathlength and waveguide geometry similar to Figure 7.12, which can increase the signal while lowering the pump power density. Perhaps future experiments will be able to answers these questions.

REFERENCES

REFERENCES

Abraham, R.J. et al., 1989. N.M.R. Spectra of Porphyrins. Part 37. The Structure of the Methyl Pyrochlorophyllide a Dimer. *Journal of the Chemical Society, Perkin Transactions 2*, pp.1633–1641.

Abraham, R.J. & Rowan, A.E., 1991. Nuclear Magnetic Resonance Spectroscopy of Chlorophyll. In H. Scheer, ed. *Chlorophylls*. Boca Raton , USA: CRC Press, pp. 797 – 834.

Adar, F., 1978. Electronic Absorption Spectra of Hemes and Hemoproteins. In D. Dolphin, ed. *The Porphyrins*. Academic Press, pp. 167–209.

Ahrens, M.J. et al., 2007. Photoinduced charge separation in self-assembled cofacial pentamers of zinc-5,10,15,20-tetrakis(perylenediimide)porphyrin. *Physical chemistry chemical physics : PCCP*, 9(12), pp.1469–78.

Van Amerongen, H., Valkunas, L. & van Grondelle, R., 2000. *Photosynthetic Excitons*, World Scientific Pub Co Inc.

Amster, R.L. & Porter, G., 1967. Solvate and Dimer Equilibria in Solutions of Chlorophyll. *Proceedings of the Royal Society A: Mathematical, Physical and Engineering Sciences*, 296(1444), pp.38–44.

Amunts, A. et al., 2010. Structure determination and improved model of plant photosystem I. *Journal of Biological Chemistry*, 285(5), pp.3478–3486.

Arellano, J.B. et al., 2002. Bacteriochlorophyll e Monomers, but not Aggregates, Sensitize Singlet Oxygen: Implications for a Self-Photoprotection Mechanism in Chlorosomes. *Photochemistry and photobiology*, 76(4), pp.373–380.

Asano, M. & Koningstein, J.A., 1981. Probing of chlorophyll a with a pulsed tunable laser: Monomer and dimer excited state lifetimes and their time resolved fluorescence spectra. *Chemical Physics*, 57(1-2), pp.1–10.

Balzani, V. et al., 2011. Designing light harvesting antennas by luminescent dendrimers. *New Journal of Chemistry*, 35(10), p.1944.

Barber, J., 2004. Towards a full understanding of water splitting in photosynthesis. *International Journal of Photoenergy*, 6(2), pp.43–51.

Bassani, G.F. & Agranovich, V.M., 2003. *Electronic Excitations in Organic Based Nanostructures*, Academic Press.

Bauche, J. & Klapisch, M., 1972. Remarks on Brillouin's theorem in the atomic variational approach. *Journal of Physics B: Atomic and Molecular Physics*, 5(1), pp.29–36.

Beatty, J.T. et al., 2005. An obligately photosynthetic bacterial anaerobe from a deep-sea hydrothermal vent. *Proceedings of the National Academy of Sciences of the United States of America*, 102(26), pp.9306–10.

Berera, R., van Grondelle, R. & Kennis, J.T.M., 2009. Ultrafast transient absorption spectroscopy: principles and application to photosynthetic systems. *Photosynthesis Research*, 101(2-3), pp.105–118.

Berkelbach, T.C., Hybertsen, M.S. & Reichman, D.R., 2013a. Microscopic Theory of Singlet Exciton Fission. I. General Formulation. *Journal of Chemical Physics*, 138(11), p.114102.

Berkelbach, T.C., Hybertsen, M.S. & Reichman, D.R., 2013b. Microscopic Theory of Singlet Exciton Fission. II. Application to Pentacene Dimers and the Role of Superexchange. *The Journal of chemical physics*, 138(11), p.114103.

Blankenship, R.E., 2010. Early evolution of photosynthesis. *Plant physiology*, 154(2), pp.434–8.

Borland, C.F. et al., 1987. Photophysical Studies of Bacteriochlorophyll a and Bacteriopheophytin a—Singlet Oxygen Generation. *Journal of Photochemistry and Photobiology B: Biology*, 1, pp.93–101.

Bowers, P.G. & Porter, G., 1967. Quantum Yields of Triplet Formation in Solutions of Chlorophyll. *Proceedings of the Royal Society of London. Series A, Mathematical and Physical Sciences*, 296(1447), pp.435–441.

Briviba, K., Klotz, L.O. & Sies, H., 1997. Toxic And Signaling Effects of Photochemically or Chemically Generated Singlet Oxygen in Biological Systems. *Biological chemistry*, 378(November), pp.1259–1265.

Brockmann Jr., H. & Lipinski, A., 1983. Bacteriochlorophyll g. A New Bacteriochlorophyll from Heliobacterium Chlorum. *Archives of microbiology*, 136, pp.17–19.

Broyde, S.B. & Brody, S.S., 1967. Emission Spectra of Chlorophyll-a in Polar and Nonpolar Solvents. *The Journal of Chemical Physics*, 46(9), p.3334.

Brudvig, G.W., 1995. Electron paramagnetic resonance spectroscopy. In J. N. Abelson, M. I. Simon, & K. Sauer, eds. *Methods in Enzymology*. Academic Press, pp. 536–554.

Buick, R., 2008. When did oxygenic photosynthesis evolve? *Philosophical transactions of the Royal Society of London. Series B, Biological sciences*, 363(1504), pp.2731–43.

Callahan, P.M. & Cotton, T.M., 1987. Assignment of Bacteriochlorophyll a Ligation State from Absorption and Resonance Raman Spectra. *Journal of the American Chemical Society*, 109(23), pp.7001–7007.

Catling, D.C., 2014. The Great Oxidation Event Transition. In H. D. Holland & K. K. Turekian, eds. *Treatise on Geochemistry: Volume 6*. Elsevier, pp. 177–195.

Cotton, T.M. et al., 1978. Studies of Chlorophyll-Chlorophyll and Chlorophyll-Ligand Interactions by Visible Absorption and Infrared Spectroscopy at Low Temperatures. *Photochemistry and Photobiology*, 27, pp.735–749.

Croce, R. & van Amerongen, H., 2011. Light-harvesting and structural organization of Photosystem II: from individual complexes to thylakoid membrane. *Journal of photochemistry and photobiology. B, Biology*, 104(1-2), pp.142–53.

DeRosa, M.C. & Crutchley, R.J., 2002. Photosensitized singlet oxygen and its applications. *Coordination Chemistry Reviews*, 233-234, pp.351–371.

Desikachary, T. & Dweltz, N., 1961. The chemical composition of the diatom frustule. *Proceedings of the Indian Academy of Sciences B*, (1952).

Dexter, D.L., 1953. A Theory of Sensitized Luminescence in Solids. *The Journal of Chemical Physics*, 21(5), p.836.

Drzewiecka-Matuszek, A. et al., 2005. Effects of heavy central metal on the ground and excited states of chlorophyll. *Journal of biological inorganic chemistry : JBIC : a publication of the Society of Biological Inorganic Chemistry*, 10(5), pp.453–62.

Dvornikov, S.S. et al., 1979. Phosphorescence of Chlorophyllis a and b and Their Pheophytins. *Opt. Spectrosc. (USSR)*, 46(4), pp.385–388.

Eaton, S.W. et al., 2013. Singlet exciton fission in polycrystalline thin films of a slip-stacked perylenediimide. *Journal of the American Chemical Society*, 135(39), pp.14701–12.

EIA & United States Energy Infromation Administration, 2013. *International Energy Outlook 2013*,

Engel, E., Leo, K. & Hoffmann, M., 2006. Ultrafast relaxation and exciton-exciton annihilation in PTCDA thin films at high excitation densities. *Chemical Physics*, 325(1), pp.170–177.

Evans, T.A. & Katz, J.J., 1975. Evidence for 5- and 6-Coordinated Magnesium in Bacterio-Chlorophyll a from Visible Absorption Spectroscopy. *Biochimica et biophysica acta*, 396(3), pp.414–26.

F. P. Dwyer, 1964. *Chelating Agents and Metal Chelates*, Academic Press.

Fiedor, L., 2006. Hexacoordination of Bacteriochlorophyll in Photosynthetic Antenna LH1. *Biochemistry*, 45(6), pp.1910–8.

Field, C.B., 1998. Primary Production of the Biosphere: Integrating Terrestrial and Oceanic Components. *Science*, 281(5374), pp.237–240.

Fontana, P. & Meath, W., 1968. One- and Two- Center Expansions of the Breit-Pauli Hamiltonian. *Journal of Mathematical Physics*, 9(9), pp.1357–1364.

Frisch, M.J. et al., 2010. Gaussian 09, Revision C.01.

Fujimori, E. & Livingston, R., 1957. Interactions of Chlorophyll in its Triplet State With Oxygen, Carotene, Etc. *Nature*, 180, pp.1036–1038.

Fujiwara, M. & Tasumi, M., 1986. Resonance Raman and Infrared Studies on Axial Coordination to Chlorophylls a and b in Vitro. *The Journal of Physical Chemistry*, 90(2), pp.250–255.

Ganapathy, S. et al., 2009. Alternating syn-anti bacteriochlorophylls form concentric helical nanotubes in chlorosomes. *Proceedings of the National Academy of Sciences of the United States of America*, 106(21), pp.8525–30.

Glaeser, J. & Klug, G., 2005. Photo-oxidative stress in Rhodobacter sphaeroides: protective role of carotenoids and expression of selected genes. *Microbiology (Reading, England)*, 151(Pt 6), pp.1927–38.

Godbout, N. et al., 1992. Optimization of Gaussian-Type Basis Sets For Local Spin Density Functional Calculations. Part I. Boron through Neon, Optimization Technique and Validation. *Canadian Journal of Chemistry*, 70(2), pp.560–571.

Gomez Maqueo Chew, A., Frigaard, N.U. & Bryant, D.A., 2007. Bacteriochlorophyllide c C-8(2) and C-12(1) Methyltransferases are Essential for Adaptation to Low Light in Chlorobaculum Tepidum. *Journal of bacteriology*, 189(17), pp.6176–84.

Gong, J., Liang, J. & Sumathy, K., 2012. Review on dye-sensitized solar cells (DSSCs): Fundamental concepts and novel materials. *Renewable and Sustainable Energy Reviews*, 16(8), pp.5848–5860.

Gouterman, M., 1961. Spectra of Porphyrins. *Journal of Molecular Spectroscopy*, 6, pp.138–163.

Gouterman, M., Wagnière, G.H. & Snyder, L.C., 1963. Spectra of Porphyrins: Part II. Four Orbital Model. *Journal of molecular spectroscopy*, 11, pp.108–127.

Govindjee & Govindjee, R., 2000. Photosynthesis and the "Z"-scheme. *University of Illinois at Urbana-Champaign*.

Govindjee & Veit, W., 2010. Z-Scheme of Electron Transport in Photosynthesis.

Gruber, M. et al., 2015. Singlet–Triplet Annihilation in Single LHCII Complexes. *Phys. Chem. Chem. Phys.*, pp.19844–19853.

Hameka, H.F., 1967. Spin-Orbit Interactions in Organic Molecules. In A. B. Zahlan et al., eds. *The Triplet State*. Cambridge at the University Press, pp. 1–27.

Harris, D.C. & Bertolucci, M.D., 1978. *Symmetry and Spectroscopy: An Introduction to Vibrational and Electronic Spectroscopy*, New York: Oxford University Press.

Hartwich, G. et al., 1998. Metal-Substituted Bacteriochlorophylls. 1. Preparation and Influence of Metal and Coordination on Spectra. *Journal of the American Chemical Society*, 120(15), pp.3675–3683.

Hartzler, D.A. et al., 2014. *Triplet excited state energies and phosphorescence spectra of (bacterio)chlorophylls.*,

Herek, J.L. et al., 2002. Quantum control of energy flow in light harvesting. *Nature*, 417(6888), pp.533–535.

Hilborn, R.C., 2002. Einstein coefficients, cross sections, f values, dipole moments, and all that. , pp.1–12.

Hindman, J.C. et al., 1978. Coherent stimulated light emission (lasing) in covalently linked chlorophyll dimers. *Proceedings of the National Academy of Sciences*, 75(5), pp.2076–2079.

Hiraishi, A., 1997. Transfer of the bacteriochlorophyll b-containing phototrophic bacteria Rhodopseudomonas viridis and Rhodopseudomonas sulfoviridis to the genus Blastochloris gen. nov. *International journal of systematic bacteriology*, 47(1), pp.217–9.

Hoffmann, S.T. et al., 2011. Triplet Excimer Emission in a Series of 4,4′-Bis(N -carbazolyl)-2,2′-biphenyl Derivatives. *The Journal of Physical Chemistry B*, 115(3), pp.414–421.

Hofkens, J. et al., 2003. Revealing competitive Forster-type resonance energy-transfer pathways in single bichromophoric molecules. *Proceedings of the National Academy of Sciences of the United States of America*, 100(23), pp.13146–51.

Hollas, J.M., 2002. *Basic Atomic and Molecular Spectroscopy*, Cambridge: The Royal Society of Chemistry.

Hornback, J.M., 1998. *Organic Chemistry*, Brooks/Cole Publishing Company.

Hsu, C.P. et al., 2001. Excitation energy transfer in condensed media. *Journal of Chemical Physics*, 114(7), pp.3065–3072.

Ioanitescu, A.I. et al., 2009. Unusual flexibility of distal and proximal histidine residues in the haem pocket of Drosophila melanogaster haemoglobin. *Metallomics*, 1(3), p.256.

Iwai, M. et al., 2010. Live-cell imaging of photosystem II antenna dissociation during state transitions. *Proceedings of the National Academy of Sciences of the United States of America*, 107(5), pp.2337–42.

Janson, T.R. & Katz, J.J., 1972. An examination of the 220 MHz NMR spectra of mesoporphyrin IX dimethyl ester, deuteroporphyrin IX dimethyl ester, and protoporphyrin IX dimethyl ester. *Journal of Magnetic Resonance (1969)*, 6(2), pp.209–220.

Jockusch, S. et al., 2008. Singlet Molecular Oxygen by Direct Excitation. *Photochemical & Photobiological Sciences*, 7(2), pp.235–239.

Kania, A. & Fiedor, L., 2006. Steric control of bacteriochlorophyll ligation. *Journal of the American Chemical Society*, 128(6), pp.454–458.

Katz, J.J. & Brown, C.E., 1983. Nuclear Magnetic Resonance Spectroscopy of Chlorophylls and Corrins. In D. G. GORENSTEIN, ed. *Bulletin of Magnetic Resonance*. pp. 3–49.

Kay, C.W.M., 2003. The electronic structure of the photoexcited triplet state of free-base (tetraphenyl)porphyrin by time-resolved electron-nuclear double resonance and density functional theory. *Journal of the American Chemical Society*, 125(45), pp.13861–7.

Ke, B., 2001a. Light-Harvesting Pigment-Protein Complexes of Photosynthetic Bacteria. In *Photosynthesis: Photobiochemistry and Photobiophysics*. Springer, pp. 65–85.

Ke, B., 2001b. Oxygen Evolution - Introduction. In *Photosynthesis: Photobiochemistry and Photobiophysics*. Springer, pp. 323–336.

Ke, B., 2001c. Photosynthesis: An Overview. In *Photosynthesis: Photobiochemistry and Photobiophysics*. Springer, pp. 1–46.

Ke, B., 2001d. Photosystem I - Introduction. In *Photosynthesis: Photobiochemistry and Photobiophysics*. Springer, pp. 419–430.

Ke, B., 2001e. Photosystem II Introduction. In *Photosynthesis: Photobiochemistry and Photobiophysics*. Springer, pp. 199–214.

Ke, B., 2001f. Phycobiliproteins and Phycobilisomes. In *Photosynthesis: Photobiochemistry and Photobiophysics*. Springer, pp. 251–269.

Ke, B., 2001g. Role of Carotenoids in Photosynthesis. In *Photosynthesis: Photobiochemistry and Photobiophysics*. Springer, pp. 229–250.

Ke, B., 2001h. The Interphotosystem Cytochrome-b6f Complex and the Related Cytochrome-bc1 Complex. In *Photosynthesis: Photobiochemistry and Photobiophysics*. Springer, pp. 635–664.

Keivanidis, P.E. et al., 2012. Correlating Emissive Non-Geminate Charge Recombination with Photocurrent Generation Efficiency in Polymer/Perylene Diimide Organic Photovoltaic Blend Films. *Advanced Functional Materials*, 22(11), pp.2318–2326.

Keivanidis, P.E. et al., 2010. Delayed luminescence spectroscopy of organic photovoltaic binary blend films: Probing the emissive non-geminate charge recombination. *Advanced materials (Deerfield Beach, Fla.)*, 22(45), pp.5183–7.

Kell, A. et al., 2014. On destabilization of the Fenna-Matthews-Olson complex of Chlorobaculum tepidum. *Photosynthesis Research*, 120(3), pp.323–329.

Kiang, N.Y. et al., 2007. Spectral Signatures of Photosynthesis. I. Review of Earth Organisms. *Astrobiology*, 7(1), pp.222–251.

Kihara, S. et al., 2015. The Fate of the Triplet Excitations in the Fenna–Matthews–Olson Complex. *The Journal of Physical Chemistry B*, 119(18), pp.5765–5772.

Killops, S. & Killops, V., 2004. *Introduction to Organic Geochemistry*, Malden, MA USA: Blackwell Publishing Ltd.

Kim, H., 2007. *Discovery of Novel Photoprotection Mechanisms in Photosynthesis Using Optical Spectroscopy and Biosensor Development*. Purdue University, West Lafayette IN.

Kim, H. et al., 2007. Triplet Exciton Formation as a Novel Photoprotection Mechanism in Chlorosomes of Chlorobium Tepidum. *Biophysical journal*, 93(1), pp.192–201.

Kippelen, B. & Brédas, J.L., 2009. Organic photovoltaics. *Energy & Environmental Science*, 2(3), p.251.

Kissinger, P.T. & Heineman, W.R., 1983. Cyclic voltammetry. *Journal of Chemical Education*, 60(9), p.702.

Koyama, Y. et al., 2006. Effects of Axial Coordination, Electronic Excitation and Oxidation on Bond Orders in the Bacteriochlorin Macrocycle, and Generation of Radical Cation on Photo- Excitation of in Vitro and in Vivo Bacteriochlorophyll a Aggregates: Resonance Raman Studies. In B. Grimm et al., eds. *Chlorophylls and Bacteriochlorophylls*. Springer, pp. 324–335.

Krasnovsky Jr, A.A., 1982. Delayed Fluorescence and Phosphorescence of Plant Pigments. *Photochemistry and photobiology*, 36, pp.733–741.

Krasnovsky Jr, A.A. et al., 1994. Generation and quenching of singlet molecular oxygen by aggregated bacteriochlorophyll d in model systems and chlorosomes. *Photosynthesis Research*, 40(2), pp.191–198.

Krasnovsky Jr, A.A., 1979. Photoluminescence of Singlet Oxygen in Pigment Solutions. *Photochemistry and Photobiology*, 29(1), pp.29–36.

Krasnovsky Jr, A.A. et al., 1993. The Photophysics of Monomeric Bacteriochlorophylls c and d and Their Derivatives: Properties of the Triplet State and Singlet Oxygen Photogeneration and Quenching. *Photochemistry and Photobiology*, 57(2), pp.324–330.

Krawczyk, S., 1989. The Effects of Hydrogen Bonding and CoordinationInteraction in Visible Absorption and Vibrational Spectra of Chlorophyll a. *Biochimica et Biophysica Acta (BBA) - Bioenergetics*, 976(2-3), pp.140–149.

Kühlbrandt, W., 2003. Structural biology: dual approach to a light problem. *Nature*, 426(6965), pp.399–400.

Lang, F.S. & Oesterhelt, D., 1989. Microaerophilic Growth and Induction of the Photosynthetic Reaction Center in Rhodopseudomonas Viridis. *Journal of bacteriology*, 171(5), pp.2827–34.

Lauricella, R. et al., 2010. 5-Hydroxy-2,2,6,6-tetramethyl-4-(2-methylprop-1-en-yl)cyclohex-4-ene-1,3-dione, a novel cheletropic trap for nitric oxide EPR detection. *Chemical Communications*, 46(21), p.3675.

Lee, S.K. et al., 1999. Electrochemistry, Spectroscopy and Electrogenerated Chemiluminescence of Perylene, Terrylene, and Quaterrylene Diimides in Aprotic Solution. *Journal of the American Chemical Society*, 121(14), pp.3513–3520.

Li, Y.F. et al., 1997. Crystal Structure of the Bacteriochlorophyll a Protein from Chlorobium Tepidum. *Journal of molecular biology*, 271(3), pp.456–471.

Linnanto, J.M. & Korppi-Tommola, J.E.I., 2013. Exciton description of chlorosome to baseplate excitation energy transfer in filamentous anoxygenic phototrophs and green sulfur bacteria. *Journal of Physical Chemistry B*, 117(38), pp.11144–11161.

Livingston, R. & Weil, S., 1952. Activation of the Fluorescence of Chlorophyll Solutions. *Nature*, 170(4331), pp.750–751.

Maggiora, G.M. & Ingraham, L.L., 1967. Chlorophyll Triplet States. *Structure and Bonding*, 2, pp.126–159.

Marian, C.M., 2012. Spin-Orbit Coupling and Intersystem Crossing in Molecules. *Wiley Interdisciplinary Reviews: Computational Molecular Science*, 2(2), pp.187–203.

Michalski, T.J. et al., 1987. Bacteriopheophytin g: Properties and some Speculations on a Possible Primary Role for Bacteriochlorophylls b and g in the Biosynthesis of Chlorophylls. *Proceedings of the National Academy of Sciences of the United States of America*, 84(9), pp.2570–4.

Miller, M., Gillbro, T. & Olson, J.M., 1993. Aqueous Aggregates of Bacteriochlorophyll c as a Model for Pigment Organization in Chlorosomes. *Photochemistry and Photobiology*, 57(1), pp.98–102.

Milne, B.F. et al., 2015. Unraveling the Intrinsic Color of Chlorophyll. *Angewandte Chemie International Edition*, 54(7), pp.2170–2173.

Minaev, B., 2004. Theoretical study of the external heavy atom effect on phosphorescence of free-base porphin molecule. *Spectrochimica acta. Part A, Molecular and biomolecular spectroscopy*, 60(13), pp.3213–24.

Monsù Scolaro, L. et al., 2002. Aggregation behavior of protoporphyrin IX in aqueous solutions: Clear evidence of vesicle formation. *Journal of Physical Chemistry B*, 106, pp.2453–2459.

Moss, G.P., 1987. Nomenclature of Tetrapyrroles. *Pure and Applied Chemistry*, 59(6), pp.779–832.

Mulder, T.D., Scott, R.P. & Kolner, B.H., 2008. Amplitude and envelope phase noise of a modelocked laser predicted from its noise transfer function and the pump noise power spectrum. *Optics Express*, 16(18), p.14186.

Munnecke, A. & Samtleben, C., 1996. The formation of micritic limestones and the development of limestone-marl alternations in the Silurian of Gotland, Sweden. *Facies*, 34(1), pp.159–176.

Neverov, K.V., Santabarbara, S. & Krasnovsky Jr, A.A., 2011. Phosphorescence study of chlorophyll d photophysics. Determination of the energy and lifetime of the photo-excited triplet state. Evidence of singlet oxygen photosensitization. *Photosynthesis Research*, 108(2-3), pp.101–106.

Niedzwiedzki, D.M. & Blankenship, R.E., 2010. Singlet and Triplet Excited State Properties of Natural Chlorophylls and Bacteriochlorophylls. *Photosynthesis research*, 106(3), pp.227–38.

Nobel, P.S., 2009. *Physicochemical and Environmental Plant Physiology* 4th ed., Oxford: Academic Press.

Van Noort, P.I. et al., 1997. Redox effects on the excited-state lifetime in chlorosomes and bacteriochlorophyll c oligomers. *Biophysical journal*, 72(1), pp.316–325.

Noschese, S., Pasquini, L. & Reichel, L., 2013. Tridiagonal Toeplitz matrices: properties and novel applications. *Numerical Linear Algebra with Applications*, 20(2), pp.302–326.

Noy, D. et al., 2000. Optical Absorption and Computational Studies of [Ni]-Bacteriochlorophyll- a . New Insight into Charge Distribution between Metal and Ligands. *Journal of the American Chemical Society*, 122(16), pp.3937–3944.

Ohtomo, Y. et al., 2013. Evidence for biogenic graphite in early Archaean Isua metasedimentary rocks. *Nature Geoscience*, 7(1), pp.25–28.

Olson, J.M. & Cox, R.P., 1991. Monomers, dimers, and tetramers of 4-n-propyl-5-ethyl farnesyl bacteriochlorophyll c in dichloromethane and carbon tetrachloride. *Photosynthesis Research*, 30(1), pp.35–43.

Olson, J.M. & Pedersen, J.P., 1990. Bacteriochlorophyll c monomers, dimers, and higher aggregates in dichloromethane, chloroform, and carbon tetrachloride. *Photosynthesis Research*, 25, pp.25–37.

Orf, G.S. & Blankenship, R.E., 2013. Chlorosome Antenna Complexes from Green Photosynthetic Bacteria. *Photosynthesis research*, 116(2-3), pp.315–31.

Orf, G.S., Niedzwiedzki, D.M. & Blankenship, R.E., 2014. Intensity Dependence of the Excited State Lifetimes and Triplet Conversion Yield in the Fenna-Matthews-Olson Antenna Protein. *The journal of physical chemistry. B*, 118(8), pp.2058–69.

Overmann, J., Cypionka, H. & Pfennig, N., 1992. An extremely low-light adapted phototrophic sulfur bacterium from the Black Sea. *Limnology and Oceanography*, 37(1), pp.150–155.

Penzkofer, A. & Leupacher, W., 1987. Fluorescence Behaviour of Highly Concentrated Rhodamine 6G Solutions. *Journal of luminescence*, 37, pp.61–72.

Polívka, T. & Sundström, V., 2004. Ultrafast dynamics of carotenoid excited States-from solution to natural and artificial systems. *Chemical reviews*, 104(4), pp.2021–71.

Pospísil, P., 1998. Theoretical Simulation of Temperature Induced Increase of Quantum Yield of Minimum Chlorophyll Fluorescence ΦF(0). *Journal of Theoretical Biology*, 193(1), pp.125–130.

Prokhorenko, V.I., Steensgaard, D.B. & Holzwarth, A.R., 2003. Exciton theory for supramolecular chlorosomal aggregates: 1. Aggregate size dependence of the linear spectra. *Biophysical journal*, 85(5), pp.3173–3186.

Pšenčík, J., Butcher, S.J. & Tuma, R., 2014. Chlorosomes: Structure, Function and Assembly. In M. F. Hohmann-Marriott, ed. *The Structural Basis of Biological Energy Generation*. Springer, pp. 77–109.

Rätsep, M., Linnanto, J. & Freiberg, A., 2009. Mirror symmetry and vibrational structure in optical spectra of chlorophyll a. *The Journal of chemical physics*, 130(19), pp.194501–1 – 11.

Rohatgi, K.K. & Mukhopadhyay, A.K., 1971. Isolation of Unique Dimer Spectra of Dyes from the Composite Spectra of Aggregated Solutions. *Photochemistry and Photobiology*, 14(4), pp.551–559.

Sakuragi, Y. et al., 1999. Association of bacteriochlorophyll a with the CsmA protein in chlorosomes of the photosynthetic green filamentous bacterium Chloroflexus aurantiacus. *Biochimica et Biophysica Acta (BBA) - Bioenergetics*, 1413(3), pp.172–180.

Saltiel, J. et al., 1981. Spin-statistical factor in the triplet-triplet annihilation of anthracene triplets. *Journal of the American Chemical Society*, 103(24), pp.7159–7164.

Savikhin, S., 1995. Shot-noise-limited detection of absorbance changes induced by subpicojoule laser pulses in optical pump-probe experiments. *Review of Scientific Instruments*, 66(9), p.4470.

Savikhin, S. et al., 1995. Ultrafast energy transfer in light-harvesting chlorosomes from the green sulfur bacterium Chlorobium tepidum. *Chemical physics*, 194(2-3), pp.245–258.

Savikhin, S., Xu, W., et al., 1999. Ultrafast Primary Processes in Photosystem I of the Cyanobacterium Synechocystis Sp. PCC 6803. *Biophysical journal*, 76(6), pp.3278–88.

Savikhin, S., Buck, D.R. & Struve, W.S., 1999. The Fenna-Matthews-Olson Protein: A Strongly Coupled Photosynthetic Antenna. In D. L. Andrews & A. A. Demidov, eds. *Resonance Energy Transfer*. Wiley, pp. 399–434.

Schmidt am Busch, M. et al., 2011. The Eighth Bacteriochlorophyll Completes the Excitation Energy Funnel in the FMO Protein. *The Journal of Physical Chemistry Letters*, 2(2), pp.93–98.

Schödel, R. et al., 1998. Rate of carotenoid triplet formation in solubilized light-harvesting complex II (LHCII) from spinach. *Biophysical journal*, 75(6), pp.3143–53.

Scholes, G.D. et al., 2011. Lessons from nature about solar light harvesting. *Nature chemistry*, 3(10), pp.763–74.

Seely, G. & Connolly, J., 1986. Fluorescence of Photosynthetic Pigments in Vitro. In Govindjee, J. Amesz, & D. C. Fork, eds. *Light Emission by Plants and Bacteria*. Academic Press, pp. 99–133.

Shao, Y. et al., 2006. Advances in methods and algorithms in a modern quantum chemistry program package. *Physical Chemistry Chemical Physics*, 8(27), p.3172.

Shipman, L.L. et al., 1976a. An analysis of the visible absorption spectrum of chlorophyll a monomer, dimer,and oligomers in solution. *Journal of the American Chemical Society*, 98, pp.8222–8230.

Shipman, L.L. et al., 1976b. New proposal for structure of special-pair chlorophyll. *Proceedings of the National Academy of Sciences of the United States of America*, 73(6), pp.1791–1794.

Solov'ev, K.N. et al., 1983. Phosphorence and State of Chlorophyll in Solutions. *Journal of Applied Spectroscopy*, 38(1), pp.73–79.

Steiner, F., Vogelsang, J. & Lupton, J.M., 2014. Singlet-triplet annihilation limits exciton yield in poly(3-hexylthiophene). *Physical Review Letters*, 112(13), pp.1–5.

Steiner, R., Cmiel, E. & Scheer, H., 1983. Chemistry of Bacteriochlorophyll b: Identification of some (Photo)Oxidation Products. *Zeitschrift für Naturforschung*, 38 c, pp.748–752.

Stockett, M.H. et al., 2015. The Soret absorption band of isolated chlorophyll a and b tagged with quaternary ammonium ions. *Phys. Chem. Chem. Phys.*

Strouse, C.E., 1974. The Crystal and Molecular Structure of Ethyl Chlorophyllide a.2H(2)O and Its Relationship to the Structure and Aggregation of Chlorophyll a. *Proceedings of the National Academy of Sciences of the United States of America*, 71(2), pp.325–328.

Struve, W.S., 1995. Theory of Electronic Energy Transfer. In R. E. Blankenship, M. T. Madigan, & C. E. Bauer, eds. *Anoxygenic Photosynthetic Bacteria*. Springer, pp. 297–313.

Stryer, L., 1995. *Biochemistry* 4th ed., W.H. Freeman & Company.

Suga, M. et al., 2014. Native structure of photosystem II at 1.95 Å resolution viewed by femtosecond X-ray pulses. *Nature*, 517(7532), pp.99–103.

Szalay, L., Tombácz, E. & Singhal, G.S., 1974. Effect of Solvent on the Absorption Spectra and Stokes' Shift of Absorption and Fluorescence of Chlorophylls. *Acta Physica Academiae Scientiarum Hungaricae*, 35(1-4), pp.29–36.

Takaichi, S. & Oh-oka, H., 1999. Pigment Composition in the Reaction Center Complex from the Thermophilic Green Sulfur Bacterium, Chlorobium tepidum: Carotenoid Glucoside Esters, Menaquinone and Chlorophylls. *Plant and Cell Physiology*, 40(7), pp.691–694.

Takiff, L. & Boxer, S.G., 1988a. Phosphorescence from the Primary Electron Donor in Rhodobacter Sphaeroides and Rhodopseudomonas Viridis Reaction Centers. *Biochimica et Biophysica Acta (BBA)-Bioenergetics*, 932, pp.325–334.

Takiff, L. & Boxer, S.G., 1988b. Phosphorescence Spectra of Bacteriochlorophylls. *Journal of the American Chemical Society*, 110(13), pp.4425–4426.

Tang, J.K.H. et al., 2013. Temperature and carbon assimilation regulate the chlorosome biogenesis in green sulfur bacteria. *Biophysical Journal*, 105(6), pp.1346–1356.

Telfer, A. et al., 2010. Fluorescence Line Narrowing Studies on Isolated Chlorophyll Molecules. *The journal of physical chemistry. B*, 114(6), pp.2255–60.

Terazono, Y., Patrick, B.O. & Dolphin, D.H., 2002. Synthesis, Crystal Structures, and Redox Potentials of 2,3,12,13-Tetrasubstituted 5,10,15,20-Tetraphenylporphyrin Zinc(II) Complexes. *Inorganic Chemistry*, 41(25), pp.6703–6710.

Tian, Y. et al., 2011. Organization of Bacteriochlorophylls in Individual Chlorosomes from Chlorobaculum tepidum Studied by 2-Dimensional Polarization Fluorescence Microscopy. *Journal of the American Chemical Society*, 133(43), pp.17192–17199.

Turina, P., Samoray, D. & Gräber, P., 2003. H+/ATP ratio of proton transport-coupled ATP synthesis and hydrolysis catalysed by CF0F1-liposomes. *The EMBO journal*, 22(3), pp.418–26.

Uehara, K. & Olson, J.M., 1992. Aggregation of bacteriochlorophyll c homologs to dimers, tetramers, and polymers in water-saturated carbon tetrachloride. *Photosynthesis Research*, 33, pp.251–257.

Di Valentin, M. et al., 2002. Structural investigation of oxidized chlorosomes from green bacteria using multifrequency electron paramagnetic resonance up to 330 GHz. *Photosynthesis Research*, 71(1-2), pp.33–44.

Vijaya Kumar, K. & Suresh Kumar, A., 2012. Spectroscopic properties of Nd3+ doped borate glasses. *Optical Materials*, 35(1), pp.12–17.

Vogl, K. et al., 2012. Bacteriochlorophyll f: Properties of chlorosomes containing the "forbidden chlorophyll." *Frontiers in Microbiology*, 3(AUG), pp.1–12.

Van der Waals, J.H. & de Groot, M.S., 1967. Magnetic Interactions Related to Phosphorescence. In A. B. Zahlan et al., eds. *The Triplet State*. Cambridge at the University Press, pp. 101–132.

Wakao, N. et al., 1996. Discovery of Natural Photosynthesis using Zn-Containing Bacteriochlorophyll in an Aerobic Bacterium Acidiphilium Rubrum. *Plant and Cell Physiology*, 37(6), pp.889–893.

Weiss, C., Kobayashi, H. & Gouterman, M., 1965. Spectra of porphyrins Part III. Self-consistent molecular orbital calculations of porphyrin and related ring systems. *Journal of Molecular Spectroscopy*, pp.415–450.

Wen, J. et al., 2011. Native electrospray mass spectrometry reveals the nature and stoichiometry of pigments in the FMO photosynthetic antenna protein. *Biochemistry*, 50(17), pp.3502–3511.

West, W. & Pearce, S., 1965. The dimeric state of cyanine dyes. *The Journal of Physical Chemistry*, 566(1956), pp.1894–1903.

You, Z.Q. & Hsu, C.P., 2011. Ab inito study on triplet excitation energy transfer in photosynthetic light-harvesting complexes. *Journal of Physical Chemistry A*, 115(16), pp.4092–4100.

You, Z.Q. & Hsu, C.P., 2010. The fragment spin difference scheme for triplet-triplet energy transfer coupling. *Journal of Chemical Physics*, 133(7).

You, Z.Q., Hsu, C.P. & Fleming, G.R., 2006. Triplet-triplet energy-transfer coupling: theory and calculation. *The Journal of chemical physics*, 124(4), p.044506.

Van Zandvoort, M. a et al., 1994. Determination of the directions of the transition dipoles in tetrabutylperylene in stretched polymers. *Journal of fluorescence*, 4(1), pp.83–6.

Zhang, H., Huang, D. & Cramer, W.A., 1999. Stoichiometrically Bound Beta -Carotene in the Cytochrome b6f Complex of Oxygenic Photosynthesis Protects Against Oxygen Damage. *Journal of Biological Chemistry*, 274(3), pp.1581–1587.

Ziegelhoffer, E.C. & Donohue, T.J., 2009. Bacterial responses to photo-oxidative stress. *Nature reviews. Microbiology*, 7(12), pp.856–863.

APPENDIX

APPENDIX

SpectraScript code for extraction of the unique dimer absorption spectrum from the combined dimer + monomer absorption spectra based on the method described by West & Pearce and Rohatgi & Mukhopadhyay (West & Pearce 1965; Rohatgi & Mukhopadhyay 1971).

```
from = 395              //start wavelength
to = 950                //end wavelength
N_spect = 4             //number of absorption spectra
startSpect = 583        //dump window number of 1st spectrum
dim c(N_spect)          //initial total chl concentration for each spectrum
c(1) = 0.231// mM
c(2) = 0.185// mM
c(3) = 0.131// mM
c(4) = 0.073// mM

dim X_cm(N_spect)           //monomer concentration (mM) for each spectrum
dim dX_cm(N_spect)          //change in monomer concentration (for simplex method)

//set initial guess for monomer conc from total Chl conc (for Simplex fit)
for i=1, N_spect
        X_cm(i) = c(i)*(1-0.75*(c(i)/c(1))^2)       // initial guess for monomer conc
        dX_cm(i) = X_cm(i)/10.0                     // change in monomer conc
next

s_Sx = 901     // spectra for linear least squares parameters
s_Sy = 902
s_Sxx = 903
s_Sxy = 904
s_Syy = 905
s_slope = 906
s_intercept = 907
s_rSq = 908

//set initial linear regression parameters (before Simplex fit starts)
GOSUB linearReg
// call to simplex method
simplex error,key,1e-7,chi2,X_cm(1),dX_cm(2),X_cm(2),dX_cm(2),X_cm(3),dX_cm(3)
```

```
print "\nChi2=",chi2
for i=1,N_spect
        //final monomer concetrations (normalized to c(1))
        print "\ncm(",i,")=",X_cm(i)
next
stopp

// linear regression calculation (compute slope, intercept, and R^2)
linearReg:
        GOSUB zeroSpect
        spec0 = startSpect
        L0 = len0
        n = N_spect

        for i=1, L0
                Sx = 0
                Sy = 0
                Sxx = 0
                Sxy = 0
                Syy = 0
                slope = 0
                intercept = 0
                rSq = 0
                if specx0(i) < from; GOTO SKIP
                if specx0(i) > to; GOTO SKIP

                for j=1,N_spect
                        spec0 = startSpect + j-1
                        ei = spec0(i) / c(j)        // "reduced" absorption
                        xj = X_cm(j) / c(j)         // normalized monomer conc
                        Sx = Sx + xj
                        Sy = Sy + ei
                        Sxx = Sxx + xj*xj
                        Sxy = Sxy +ei*xj
                        Syy = Syy + ei*ei
                next

                spec1(i) = Sx
                spec2(i) = Sy
                spec3(i) = Sxx
                spec4(i) = Sxy
                spec5(i) = Syy
                // COMPUTE SLOPE, INTERCEPT, AND R^2
                // SLOPE = (A_mono - 0.5*A_dimer) -- note A = "reduced" abs
                spec6(i) = (n*Sxy - Sx*Sy) / (n*Sxx - Sx*Sx)

                // INTERCEPT = 0.5*A_dimer -- see above note
                spec7(i) = (Sy - spec6(i)*Sx) / n

                // R^2
                spec8(i) = spec6(i) * (n*Sxy - Sx*Sy) / (n*Syy - Sy*Sy)

                SKIP:
        next
```

```
        comment6$ = "slope"
        comment7$ = "intercept"
        comment8$ = "R^2"
RETURN

// Chi^2 is calculated from difference between data and linear regression fit
error:
        spec0 = startSpect
        L0 = len0
        chi_2 = 0
        for i=1, L0
                slope = spec6(i)
                intercept = spec7(i)
                for j=1,N_spect
                        spec0 = startSpect + j-1
                        spectra spec0 = spec0
                        xi = X_cm(j)/c(j)
                        yi_0 = spec0(i)/c(j)
                        yi_1 = c(j)*(slope*xi + intercept)
                        dyi = yi_0 - yi_1
                        chi_2 = chi_2 + dyi*dyi
                next
        next
        chi2 = sqrt(chi_2)
RETURN

key:
if simplex_improved>0;refresh;print simplex_iteration,": ",,X_cm(1), " ", X_cm(2), " ",
X_cm(3),"  ",chi2,"\n"
if inkey()=27;simplex_break=1
return

calculate:
gosub linearReg
return

// zero all spectra needed for linear regression and simplex fit
zeroSpect:
        spec0 = startSpect
        spectra spec0 = spec0

        spec1 = s_Sx
        spectra spec1 = spec0*0
        COMMENT1$ = " "
        spec2 = s_Sy
        spectra spec2 = spec0*0
        COMMENT1$ = " "
        spec3 = s_Sxx
        spectra spec3 = spec0*0
        COMMENT1$ = " "
        spec4 = s_Sxy
        spectra spec4 = spec0*0
        COMMENT1$ = " "
```

```
        spec5 = s_Syy
        spectra spec5 = spec0*0
        COMMENT1$ = " "
        spec6= s_intercept
        spectra spec6 = spec0*0
        COMMENT1$ = " "
        spec7= s_slope
        spectra spec7 = spec0*0
        COMMENT1$ = " "
        spec8= s_rSq
        spectra spec8 = spec0*0
        COMMENT1$ = " "

RETURN
```

VITA

VITA

Daniel A. Hartzler

EDUCATION

Ph.D., Physics, Purdue University, West Lafayette, IN 2015
Thesis - Triplet Excitons in Natural Photosynthetic and Artificial Light Harvesting Systems: Measurement and Modeling
Advisor - Professor Sergei Savikhin

B.S., Applied Physics, Purdue University, West Lafayette, IN 2003
Minor - Computer Science

RESEARCH EXPERIENCE

Research Assistant, Department of Physics, (Sergei Savikhin), Purdue University 2008-2015

- Built a high sensitivity time gated phosphorescence spectrometer to directly measure triplet state energies.
- Utilized phosphorescence spectroscopy to measure the triplet state energies of ten naturally occurring (Bacterio)Chlorophyll ((B)Chl) pigments.
- Studied triplet-triplet coupling and triplet exciton formation in dimeric and aggregated organic pigments using phosphorescence spectroscopy.
- Developed a quantum mechanical model of triplet-triplet coupling between organic pigments.
- Modeled excitonic spectra in dimeric and aggregated pigment systems.
- Investigated singlet state dynamics in natural photosynthetic antenna by means of a high sensitivity ultrafast pump-probe spectrometer.
- Upgraded the spectral range of a home built ultrafast pump-probe spectrometer into the near ultra violet (UV).
- Investigated photoinduced electron transfer for use in photovoltaic applications by means of UV upgraded ultrafast pump-probe spectrometer.
- Built an optical autocorrelator for characterization of ultrafast laser pulses (100 femtosecond).

TECHNICAL SKILLS

Computer

- Software Packages: Gaussian 09, SpectraSolve, LTSpice, Maple, Standard office software
- Programming: C, C++, Python, Java, SpectraSolve SpectraScript
- Examples: Have written programs for creation and manipulation of molecular models for quantum chemical calculations, Modeling excitonic systems, Spectral analysis, Data handling, Interfacing with equipment

Electronic

- Circuit design and construction, Ultrasensitive light detectors, Programmable microcontrollers
- Examples: Have built frequency dividers, Line driver and conditioner (TTL signals), Circuit for laser synchronization and triggering, Controller for an optical autocorrelator

Optical

- Optical system design, Layout, and Alignment
- Examples: Designed optics for a phosphorescence spectrometer and an optical autocorrelator, Alignment and modification of a home built 1 kHz ultrafast transient absorption spectrometer

Mechanical

- Component design and construction, Machining, Welding, Soldering
- Examples: Have made custom equipment mounts, Optical mounts, Optical slits, Cryogenic sample cells, Equipment for use of cryostat (e.g. nitrogen gas purging, cryogen filling, mounting and transport)

Scientific

- Scientific Instruments and Techniques
    - Phosphorescence Spectroscopy
    - Ultrafast Transient Absorption Pump-Probe Spectroscopy
    - Nanosecond Transient Absorption Pump-Probe Spectroscopy
    - Time Correlated Single Photon Counting
    - Fluorescence Spectroscopy
    - Absorption Spectroscopy
    - Quantum Mechanical Modeling
    - Data Fitting and Analysis
    - Closed Cycle and Liquid Cryogen Cryostats
    - Handling of Light and Oxygen Sensitive Biological Samples
    - Flash Chromatography
    - EPR Spectroscopy

Editorial

- Scientific Document Proofreading and Technical Editing

TEACHING EXPERIENCE

Teaching Assistant

- Modern Physics (Recitation)
  Textbook: Six Ideas that Shaped Physics: Unit Q and R – Moore
- Introductory Modern Mechanics (Lab and Recitation)
  Textbook: Matter and Interactions – Chabay and Sherwood
- Honors Introductory Modern Mechanics (Lab and Recitation)
  Textbook: Matter and Interactions – Chabay and Sherwood

Lecture

- Introductory Modern Mechanics (summer semester)
  Textbook: Matter and Interactions – Chabay and Sherwood

PUBLICATIONS

- The Fate of the Triplet Excitations in the Fenna–Matthews–Olson Complex
  Shigeharu Kihara, **Daniel A. Hartzler**, Gregory S. Orf, Robert E. Blankenship, and Sergei Savikhin
  The Journal of Physical Chemistry B ***2015*** *119 (18), 5765-5772*

Triplet Excited State Energies and Phosphorescence Spectra of (Bacterio)Chlorophylls
Daniel A. Hartzler, Dariusz M. Niedzwiedzki, Donald A. Bryant, Robert E. Blankenship, Yulia Pushkar, and Sergei Savikhin
The Journal of Physical Chemistry B **2014** *118* (26), 7221-7232

Oxygen Concentration Inside a Functioning Photosynthetic Cell
Shigeharu Kihara, **Daniel A. Hartzler**, and Sergei Savikhin
Biophysical Journal **2014** *106* (9), 1882–1889

Singlet Exciton Fission in Polycrystalline Thin Films of a Slip-Stacked Perylenediimide
Samuel W. Eaton, Leah E. Shoer, Steven D. Karlen, Scott M. Dyar, Eric A. Margulies, Brad S. Veldkamp, Charusheela Ramanan, **Daniel A. Hartzler**, Sergei Savikhin, Tobin J. Marks, and Michael R. Wasielewski
Journal of the American Chemical Society **2013** *135* (39), 14701-14712

MANUSCRIPT IN PREPARATION

- Experimental and Theoretical Evaluation of Triplet-Triplet Coupling in Dimeric and Aggregated Dyes, **Daniel A. Hartzler**, Shigeharu Kihara, Lyudmila V. Slipchenko, Sergei Savikhin

CONFERENCE PRESENTATION

- Unconventional Photoprotection Mechanisms in Photosynthetic Systems
  Daniel A. Hartzler, Shigeharu Kihara, Jens Niklas, Gregory Orf, Donald Bryant, Robert Blankenship, Oleg Poluektov, Yulia Pushkar, and Sergei Savikhin
  Presented at the *40th Midwest/Southeast Regional Photosynthesis Conference*
  2014

AWARDS

- **Best Graduate Student Talk** – 2014 Midwest/Southeast Regional Photosynthesis Conference
- **AAPT Outstanding Teaching Assistant Award** – 2010 Purdue University